

INFORMATION TO USERS

This manuscript has been reproduced from the microfilm master. UMI films the text directly from the original or copy submitted. Thus, some thesis and dissertation copies are in typewriter face, while others may be from any type of computer printer.

The quality of this reproduction is dependent upon the quality of the copy submitted. Broken or indistinct print, colored or poor quality illustrations and photographs, print bleedthrough, substandard margins, and improper alignment can adversely affect reproduction.

In the unlikely event that the author did not send UMI a complete manuscript and there are missing pages, these will be noted. Also, if unauthorized copyright material had to be removed, a note will indicate the deletion.

Oversize materials (e.g., maps, drawings, charts) are reproduced by sectioning the original, beginning at the upper left-hand corner and continuing from left to right in equal sections with small overlaps. Each original is also photographed in one exposure and is included in reduced form at the back of the book.

Photographs included in the original manuscript have been reproduced xerographically in this copy. Higher quality 6" x 9" black and white photographic prints are available for any photographs or illustrations appearing in this copy for an additional charge. Contact UMI directly to order.

UMI[®]

Bell & Howell Information and Learning
300 North Zeeb Road, Ann Arbor, MI 48106-1346 USA
800-521-0600

UNIVERSITY OF ALBERTA

**BIAXIAL FATIGUE AND LEAKAGE CHARACTERISTICS OF
FIBER REINFORCED COMPOSITE TUBES**

BY

JOHN D. WOŁODKO 

A thesis submitted to the Faculty of Graduate Studies and Research
in partial fulfillment of the requirements for the degree
of Doctor of Philosophy

Department of Mechanical Engineering

Edmonton, Alberta

Spring 1999



National Library
of Canada

Acquisitions and
Bibliographic Services

395 Wellington Street
Ottawa ON K1A 0N4
Canada

Bibliothèque nationale
du Canada

Acquisitions et
services bibliographiques

395, rue Wellington
Ottawa ON K1A 0N4
Canada

Your file Votre référence

Our file Notre référence

The author has granted a non-exclusive licence allowing the National Library of Canada to reproduce, loan, distribute or sell copies of this thesis in microform, paper or electronic formats.

The author retains ownership of the copyright in this thesis. Neither the thesis nor substantial extracts from it may be printed or otherwise reproduced without the author's permission.

L'auteur a accordé une licence non exclusive permettant à la Bibliothèque nationale du Canada de reproduire, prêter, distribuer ou vendre des copies de cette thèse sous la forme de microfiche/film, de reproduction sur papier ou sur format électronique.

L'auteur conserve la propriété du droit d'auteur qui protège cette thèse. Ni la thèse ni des extraits substantiels de celle-ci ne doivent être imprimés ou autrement reproduits sans son autorisation.

0-612-39608-8

UNIVERSITY OF ALBERTA

LIBRARY RELEASE FORM

Name of Author: **John David Wolodko**


Title of Thesis: **Biaxial Fatigue and Leakage Characteristics of
Fiber Reinforced Composite Tubes**

Degree: **Doctor of Philosophy**

Year this Degree Granted: **1999**

Permission is hereby granted to the University of Alberta Library to reproduce single copies of this thesis and to lend or sell such copies for private, scholarly, or scientific research purposes only.

The author reserves all other publication and other rights in association with the copyright in the thesis, and except as hereinbefore provided, neither the thesis nor any substantial portion thereof may be printed or otherwise reproduced in any material form whatever without the author's prior written permission.



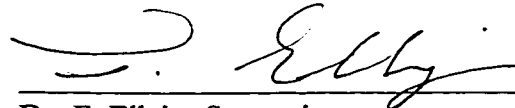
John D. Wolodko
1607 - 152 Street
Edmonton, AB
CANADA T5R 1K6

Feb 1, 1999

UNIVERSITY OF ALBERTA

FACULTY OF GRADUATE STUDIES AND RESEARCH

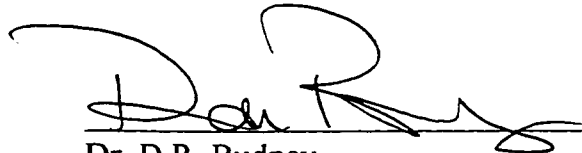
The undersigned certify that they have read, and recommend to the Faculty of Graduate Studies and Research for acceptance, a thesis entitled **Biaxial Fatigue and Leakage Characteristics of Fiber Reinforced Composite Tubes** submitted by John D. Wolodko in partial fulfillment of the requirements for the degree of Doctor of Philosophy



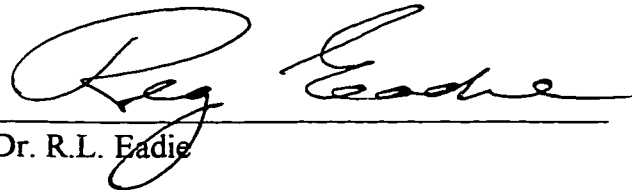
Dr. F. Ellyin, Supervisor



Dr. K.W. Neale



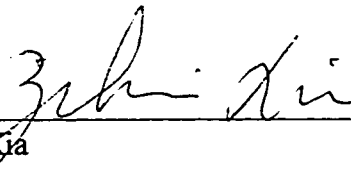
Dr. D.R. Budney



Dr. R.L. Eadie



Dr. W.A. Lipsett



Dr. Z. Xia

January 29, 1999

ABSTRACT

Fiber reinforced composites used in pressure containment structures (e.g. piping and downhole tubing) are seen as an attractive alternative to conventional materials due to their corrosion resistance and light weight. The reluctance in adopting composite materials, however, is due to a limited understanding of their long-term behaviour and failure characteristics.

The purpose of this study is to investigate the leakage behaviour of glass fiber reinforced epoxy tubes under monotonic and cyclic biaxial loading. A unique biaxial testing apparatus and specimen fabrication methodology was developed. Specimens were fabricated from pre-impregnated composite tapes using a tube rolling method, in conjunction with an inflatable mandrel molding process.

By using Darcy's Law for flow through a permeable medium, a relation which defines the fluid flow characteristics in a damaged composite tube was developed. The resulting permeability characteristics are calculated using the experimentally determined fluid volume loss measurements. The relation is useful in explaining observed leakage behaviour since it takes into account fluid and geometrical considerations.

Biaxial monotonic and cyclic tests were performed on $[\pm 71^\circ]_S$ and $[\pm 45^\circ]_S$ tubular specimen geometries in the tensile-tensile biaxial regime. Leakage failure stress, failure locations, and macroscopic failure modes were found to be dependent upon the lay-up geometry, applied biaxial loading ratio and loading type (monotonic versus cyclic). While monotonic tests were seen to fail by abrupt leakage (burst), all cyclic tests failed by weepage. For the $[\pm 45^\circ]_S$ specimens, matrix damage accumulation (as measured by cyclic creep strain and elastic stiffness reduction) was compared to leakage initiation life. Although leakage was seen to occur after the initial crack saturation, no distinct correlation was found between leakage initiation life and the

measured damage parameters.

A finite element analysis of the tubular specimens was conducted to verify the observed failures. By invoking the maximum strain failure criteria and using a through wall failure definition, the leakage failure mode and location under cyclic loading conditions were accurately predicted. The prediction of applied failure stresses, however, was inconsistent. The predicted long-term failure envelope based on the monotonic linear elastic limit was also determined, but was found to be very conservative.

ACKNOWLEDGEMENTS

I would like to extend my gratitude to Dr. F. Ellyin for his support, guidance and unwavering confidence throughout the years, and for providing me with the opportunity to pursue my many thoughts and ideas. I also wish to thank the technical staff at the Department of Mechanical Engineering for their assistance and contribution to this work.

Finally, I owe a debt of gratitude to my wife, Renie, and my family for their everlasting encouragement and patience.

John Wolodko
Edmonton, Alberta
January 1999

TABLE OF CONTENTS

1	Introduction to Composite Materials	1
1.1	Background	1
1.1.1	Introduction	1
1.1.2	Manufacturing Methods	3
1.2	Damage Development in Composite Materials	5
1.2.1	Microstructural Damage and Effect of Constituents	6
1.2.2	Manufacturing Induced Effects	8
1.2.3	Macrostructural Damage Modes	10
1.2.4	Effect of Cyclic Loading	12
1.2.5	Effect of Environment	13
1.3	Biaxial Characterization of Composite Materials	14
1.4	Functional Failure in Composite Tubulars	17
1.5	Overview of the Current Study	24
2	Development of the Multiaxial Testing Facility	27
2.1	Review of Tubular Testing Apparatus	27
2.2	Apparatus Description	30
2.2.1	Structural Components	31
2.2.2	Servo-hydraulic System	36
2.2.3	Feedback and Control System	38
2.2.4	Computer Data Acquisition and Control	42
3	Tubular Specimen Design and Manufacturing Methodology	46
3.1	Design Objectives	46
3.2	Specimen Loading Considerations	47
3.3	Specimen Design and Assembly	49
3.3.1	Initial Specimen Designs	50
3.3.2	Current Specimen Design	53
3.3.3	Aspects of the Tube Rolling Procedure	58

TABLE OF CONTENTS

3.3.4	Computer Controlled Tubular Molding Techniques	61
4	Leakage Characterization of Composite Tubular Specimens	69
4.1	Definitions of Functional Failure	69
4.1.1	Introduction	69
4.1.2	Leakage Failure Criteria	71
4.2	Critical Permeability Criterion	75
4.2.1	Application of Darcy's Law	75
4.2.2	Permeability as a Damage Parameter	77
4.3	Considerations for Measuring Leakage in Tubular Specimens	79
4.3.1	Calculation of Fluid Volume Lost	79
4.3.2	Fluid Volume Loss Profiles for Monotonic Tests	82
5	Biaxial Testing of $[\pm 71^\circ]_S$ Tubular Specimens	85
5.1	Monotonic Behaviour	85
5.1.1	Experimental Method	85
5.1.2	Pure Hoop Loading	85
5.1.3	Pure Axial Loading	86
5.1.4	Loading Based on Netting Analysis	91
5.2	Cyclic Behaviour	93
5.2.1	Experimental Method	93
5.2.2	Pure Hoop Loading	94
5.2.3	Pure Axial Loading	97
5.2.4	Loading Based on Netting Analysis	104
5.3	Biaxial Failure Envelopes	106
6	Biaxial Testing of $[\pm 45^\circ]_S$ Tubular Specimens	110
6.1	Monotonic Behaviour	110
6.1.1	Experimental Method	110
6.1.2	Pure Hoop Loading	110
6.1.3	Pure Axial Loading	111
6.1.4	Loading Based on Netting Analysis (Equi-biaxial)	114
6.2	Cyclic Behaviour	119
6.2.1	Experimental Method	119
6.2.2	Pure Hoop Loading	122
6.2.3	Axial Dominated Loading	138
6.2.4	Loading Based on Netting Analysis (Equi-biaxial)	149
6.3	Biaxial Failure Envelopes	154

TABLE OF CONTENTS

7	Stress-Strain Distributions and Failure Analysis of Tubular Specimens	160
7.1	Methodology	160
7.1.1	Description of the Finite Element Model	160
7.1.2	Description of the Failure Analysis	165
7.2	Analysis of $[\pm 71^\circ]_S$ Tubular Specimens	168
7.2.1	Pure Hoop Loading	168
7.2.2	Pure Axial Loading	170
7.2.3	Loading Based on Netting Analysis	173
7.3	Analysis of $[\pm 45^\circ]_S$ Tubular Specimens	174
7.3.1	Pure Hoop Loading	174
7.3.2	Axial Dominated Loading	177
7.3.3	Loading Based on Netting Analysis (Equi-biaxial)	177
7.4	Prediction of Biaxial Failure Envelopes	179
8	Conclusions	189
	References	193
	Appendix A	220
	Appendix B	223
	Appendix C	235
	Appendix D	263
	Appendix E	270
	Appendix F	272

LIST OF TABLES

1.1	<i>Summary of biaxial tests on fiber reinforced polymeric tubular specimens.</i>	18
2.1	<i>Operational characteristics of feedback transducers.</i>	40
5.1	<i>Experimentally and analytically derived elastic laminate constants for $[\pm 71^\circ]_S$ glass-fiber reinforced epoxy tubular specimens.</i>	93
5.2	<i>Average applied stresses and strains at failure (leakage) for $[\pm 71^\circ]_S$ glass-fiber reinforced epoxy tubular specimens under monotonic loading.</i>	109
6.1	<i>Experimentally and analytically derived elastic laminate constants for $[\pm 45^\circ]_S$ glass-fiber reinforced epoxy tubular specimens.</i>	114
6.2	<i>Average applied stresses and strains at failure (leakage) for $[\pm 45^\circ]_S$ glass-fiber reinforced epoxy tubular specimens under monotonic loading.</i>	158
7.1	<i>Elastic properties for tubular specimen components.</i>	163
7.2	<i>In-plane residual thermal strains for the $[\pm 71^\circ]_S$ and $[\pm 45^\circ]_S$ glass-fiber reinforced epoxy tubular specimens as determined at the inner and outer layer ($\Delta T = -139^\circ C$ or $-250^\circ F$).</i>	165
7.3	<i>Critical failure strains for use with maximum strain failure criterion (3M-1003 Scotchply Glass-fiber Epoxy).</i>	167
7.4	<i>Summary of experimental and predicted failure results for $[\pm 71^\circ]_S$ glass-fiber reinforced epoxy tubular specimens under biaxial loading.</i>	186
7.5	<i>Summary of experimental and predicted failure results for $[\pm 45^\circ]_S$ glass-fiber reinforced epoxy tubular specimens under biaxial loading.</i>	187

LIST OF FIGURES

1.1	<i>Definitions for fiber reinforced laminated composites (where θ is the fiber angle orientation with respect to the structural or loading axis).</i>	3
1.2	<i>Applied loading conditions and definition of fiber angle orientation (θ) in a fiber reinforced laminated tubular specimen.</i>	16
2.1	<i>In-plane biaxiality regimes in terms of the principal stress and strain for various applied loading configurations: (a) axial-torsion, and (b) axial-pressure, where ν is the Poisson ratio.</i>	28
2.2	<i>View of the multiaxial testing machine.</i>	30
2.3	<i>Description of the multiaxial testing machine components.</i>	31
2.4	<i>Gripping system assembly.</i>	33
2.5	<i>Schematic of the bladder system for use in environmental studies.</i>	34
2.6	<i>Block diagram of the servo-hydraulic system.</i>	36
2.7	<i>Block diagram of the feedback and control system.</i>	38
2.8	<i>Mounted clip gage extensometers, (a) axial and (b) diametral.</i>	41
2.9	<i>Simplified flowchart of the multiaxial testing machine acquisition and control software operation.</i>	44
3.1	<i>Specimens with integrated connections; (left) (a) threaded end connections, (b) conical wedge end connections, (c) failure at conical wedge, (right) specimen dimensions.</i>	51
3.2	<i>Specimens with bonded aluminum threaded connections; (a) inner and outer tabs prior to assembly, (b) specimen failure by fiber pull-out, and (c) assembled specimen prior to testing.</i>	52
3.3	<i>Current specimen design; (top) $[\pm 45^\circ]_S$ glass-fiber reinforced epoxy tubular specimen with optional internal bladder, (bottom) tubular specimen dimensions.</i>	54
3.4	<i>Summary of tubular specimen manufacturing procedure.</i>	55
3.5	<i>Application of prepreg pattern onto mandrel using rolling table assembly.</i>	57

LIST OF FIGURES

3.6	<i>Assembled specimen alignment stands; (left) first tab bonded, and (right) second tab bonded.</i>	57
3.7	<i>Failure of 0° unidirectional glass-fiber reinforced epoxy tubular specimens under monotonic and cyclic axial loading (collet gripping system); (top) macroscopic failure mode, and (bottom) fatigue-life curve.</i>	59
3.8	<i>Prepreg pattern (template) geometry and applied orientation.</i>	60
3.9	<i>Schematic of the tubular molding press.</i>	63
3.10	<i>Schematic of the inflatable mandrel method.</i>	64
3.11	<i>Thermal distributions in the mold, part and mandrel during curing using inflatable mandrel technique; (left) setpoint and measured temperature profiles, and (right) thermocouple (TC) locations.</i>	65
3.12	<i>Average dimensions and fiber volume fraction variation along the length of post-cured $[\pm 45^\circ]_S$ glass-fiber reinforced epoxy tubes, where d_o and d_i are the outside and inside diameters, respectively.</i>	67
3.13	<i>Micrographs from an un-tested $[\pm 45^\circ]_S$ glass-fiber reinforced epoxy tube; (top) tube wall (sectioned at 45° with respect to the tube axis), and (bottom) typical void.</i>	68
4.1	<i>Typical fluid volume loss (leakage) profiles for (a) Burst and (b) Weepage failure modes in fiber reinforced composite pressure containment structures</i>	71
4.2	<i>Example of a biaxial loading state in a downhole tubular and the corresponding biaxial failure points for an improperly designed tubular.</i>	72
4.3	<i>Determination of leakage failure point based on the following criteria: (a) Initiation of Leakage (t_1), (b) Intersecting Tangent Curve Method (t_2), and (c) Loss of a Fixed Volume of Fluid (t_3).</i>	73
4.4	<i>Assumed deformation shape for the calculation of specimen volume.</i>	80
4.5	<i>Apparent volume loss due to compression of hydraulic oil (closed system - internal pressure intensifier and connection hose only).</i>	82
4.6	<i>Representative monotonic fluid loss (leakage) profile for a $[\pm 45^\circ]_S$ glass-fiber reinforced epoxy tubular specimen under pure hoop loading (1H:0A).</i>	83
5.1	<i>Monotonic stress-strain response of a $[\pm 71^\circ]_S$ glass-fiber reinforced epoxy tubular specimen under pure hoop loading (1H:0A); (a) stress-strain response to failure, (b) stress-strain response at the initial stages of loading.</i>	87
5.2	<i>Hoop and axial strain response of a $[\pm 71^\circ]_S$ glass-fiber reinforced epoxy tubular specimen under pure hoop loading (1H:0A).</i>	88

LIST OF FIGURES

5.3	<i>Macroscopic failure modes for $[\pm 71^\circ]_S$ glass-fiber reinforced epoxy tubular specimen under pure hoop (1H:0A) monotonic loading; (top) front view, (bottom) surface map.</i>	89
5.4	<i>Monotonic stress-strain response of a $[\pm 71^\circ]_S$ glass-fiber reinforced epoxy tubular specimen under pure axial loading (0H:1A); (a) stress-strain response to failure, (b) stress-strain response at the initial stages of loading.</i>	90
5.5	<i>Hoop and axial strain response of a $[\pm 71^\circ]_S$ glass-fiber reinforced epoxy tubular specimen under pure axial loading (0H:1A).</i>	91
5.6	<i>Macroscopic failure modes for $[\pm 71^\circ]_S$ glass-fiber reinforced epoxy tubular specimen under pure axial (0H:1A) monotonic loading; (top) front view, (bottom) surface map.</i>	92
5.7	<i>Monotonic stress-strain response of a $[\pm 71^\circ]_S$ glass-fiber reinforced epoxy tubular specimen under biaxial loading (17H:2A).</i>	94
5.8	<i>Macroscopic failure modes for $[\pm 71^\circ]_S$ glass-fiber reinforced epoxy tubular specimen under biaxial (17H:2A) monotonic loading; (top) front view, (bottom) surface map.</i>	95
5.9	<i>Representative cyclic stress-strain curves for $[\pm 71^\circ]_S$ glass-fiber reinforced epoxy tubular specimens under pure hoop loading (1H:0A); (a) short-term test ($\sigma_{h \max} = 230$ MPa), (b) long-term test ($\sigma_{h \max} = 206.8$ MPa).</i>	98
5.10	<i>Representative cyclic fluid loss (leakage) profiles for $[\pm 71^\circ]_S$ glass-fiber reinforced epoxy tubular specimens under pure hoop loading (1H:0A); (a) short-term test ($\sigma_{h \max} = 230$ MPa), (b) long-term test ($\sigma_{h \max} = 206.8$ MPa).</i>	99
5.11	<i>Fatigue-life relationships based on critical volume loss for $[\pm 71^\circ]_S$ glass-fiber reinforced epoxy tubular specimens under pure hoop loading (1H:0A).</i>	100
5.12	<i>Representative cyclic stress-strain curves for $[\pm 71^\circ]_S$ glass-fiber reinforced epoxy tubular specimens under pure axial loading (0H:1A); (a) short-term test ($\sigma_{a \max} = 36$ MPa), (b) long-term test ($\sigma_{a \max} = 20$ MPa).</i>	101
5.13	<i>Macroscopic failure modes for $[\pm 71^\circ]_S$ glass-fiber reinforced epoxy tubular specimen under pure axial (0H:1A) cyclic loading; (top) front view, (bottom) surface map.</i>	102
5.14	<i>Representative cyclic fluid loss (leakage) profiles for $[\pm 71^\circ]_S$ glass-fiber reinforced epoxy tubular specimens under pure axial loading (0H:1A); (a) short-term test $\sigma_{a \max} = 36$ MPa, (b) long-term test $\sigma_{a \max} = 20$ MPa.</i>	103

LIST OF FIGURES

5.15	<i>Fatigue-life relationships based on critical volume loss for $[\pm 71^\circ]_S$ glass-fiber reinforced epoxy tubular specimens under pure axial loading (0H:1A)</i>	104
5.16	<i>Representative cyclic stress-strain curve for $[\pm 71^\circ]_S$ glass-fiber reinforced epoxy tubular specimens under biaxial loading (17H:2A) - ($\sigma_{h \max} = 212.5 \text{ MPa}$)</i>	105
5.17	<i>Leakage failure mode for $[\pm 71^\circ]_S$ glass-fiber reinforced epoxy tubular specimen under biaxial (17H:2A) cyclic loading</i>	106
5.18	<i>Representative cyclic fluid loss (leakage) profile for $[\pm 71^\circ]_S$ glass-fiber reinforced epoxy tubular specimens under biaxial loading (17H:2A) - ($\sigma_{h \max} = 212.5 \text{ MPa}$)</i>	107
5.19	<i>Fatigue-life relationships based on critical volume loss for $[\pm 71^\circ]_S$ glass-fiber reinforced epoxy tubular specimens under biaxial loading (17H:2A)</i>	107
5.20	<i>Biaxial monotonic and cyclic failure (leakage) envelopes for $[\pm 71^\circ]_S$ glass-fiber reinforced epoxy tubular specimens in applied stress space</i>	108
6.1	<i>Monotonic stress-strain response of a $[\pm 45^\circ]_S$ glass-fiber reinforced epoxy tubular specimen under pure hoop loading (1H:0A); (a) stress-strain response to failure, (b) stress-strain response at the initial stages of loading</i>	112
6.2	<i>Hoop and axial strain response of a $[\pm 45^\circ]_S$ glass-fiber reinforced epoxy tubular specimen under pure hoop loading (1H:0A)</i>	113
6.3	<i>Burst failure mode for a $[\pm 45^\circ]_S$ glass-fiber reinforced epoxy tubular specimen under pure hoop (1H:0A) monotonic loading</i>	114
6.4	<i>Monotonic stress-strain response of a $[\pm 45^\circ]_S$ glass-fiber reinforced epoxy tubular specimen under pure axial loading (0H:1A); (a) stress-strain response to failure, (b) stress-strain response at the initial stages of loading</i>	115
6.5	<i>Hoop and axial strain response of a $[\pm 45^\circ]_S$ glass-fiber reinforced epoxy tubular specimen under pure axial loading (0H:1A)</i>	116
6.6	<i>Macroscopic failure modes for $[\pm 45^\circ]_S$ glass-fiber reinforced epoxy tubular specimen under pure axial (0H:1A) monotonic loading; (top) front view, (bottom) surface map</i>	117
6.7	<i>Monotonic stress-strain response of a $[\pm 45^\circ]_S$ glass-fiber reinforced epoxy tubular specimen under equi-biaxial loading (1H:1A); (a) stress-strain response to failure, (b) stress-strain response at the initial stages of loading</i>	118
6.8	<i>Hoop and axial strain response of a $[\pm 45^\circ]_S$ glass-fiber reinforced epoxy tubular specimen under equi-biaxial loading (1H:1A)</i>	119

LIST OF FIGURES

6.9	<i>Macroscopic failure modes for $[\pm 45^\circ]_S$ glass-fiber reinforced epoxy tubular specimen under equi-biaxial (1H:1A) monotonic loading; (top) front view, (bottom) surface map.</i>	120
6.10	<i>Representative cyclic stress-strain curve for $[\pm 45^\circ]_S$ glass-fiber reinforced epoxy tubular specimens under pure hoop loading (1H:0A) - ($\sigma_{h \max} = 115$ MPa).</i>	123
6.11	<i>Measured surface temperature of a $[\pm 45^\circ]_S$ glass-fiber reinforced epoxy tubular specimens under pure hoop (1H:0A) cyclic loading - ($\sigma_{h \max} = 115$ MPa).</i>	124
6.12	<i>Macroscopic failure modes for $[\pm 45^\circ]_S$ glass-fiber reinforced epoxy tubular specimen under pure hoop (1H:0A) cyclic loading; (top) front view, (bottom) surface map.</i>	125
6.13	<i>Weepage failure mode for $[\pm 45^\circ]_S$ glass-fiber reinforced epoxy tubular specimen under pure hoop (1H:0A) cyclic loading.</i>	126
6.14	<i>Fluid loss characteristics of a $[\pm 45^\circ]_S$ glass-fiber reinforced epoxy tubular specimen under pure hoop loading (1H:0A) - ($\sigma_{h \max} = 115$ MPa); (a) fluid volume loss (leakage) profile, (b) derived permeability curve.</i>	127
6.15	<i>Fluid loss characteristics of a $[\pm 45^\circ]_S$ glass-fiber reinforced epoxy tubular specimen under pure hoop loading (1H:0A) - ($\sigma_{h \max} = 100$ MPa); (a) fluid volume loss (leakage) profile, (b) derived permeability curve.</i>	128
6.16	<i>Fluid loss characteristics of a $[\pm 45^\circ]_S$ glass-fiber reinforced epoxy tubular specimen under pure hoop loading (1H:0A) - ($\sigma_{h \max} = 70$ MPa); (a) fluid volume loss (leakage) profile, (b) derived permeability curve.</i>	129
6.17	<i>Fatigue-life relationships for $[\pm 45^\circ]_S$ glass-fiber reinforced epoxy tubular specimens under pure hoop loading (1H:0A) based on critical permeability criterion.</i>	130
6.18	<i>Measured cyclic creep strain curves for $[\pm 45^\circ]_S$ glass-fiber reinforced epoxy tubular specimens under pure hoop loading (1H:0A) - short-term test ($\sigma_{h \max} = 115$ MPa); (a) in global coordinates (loading directions), (b) in material coordinates.</i>	131
6.19	<i>Measured cyclic creep strain curves for $[\pm 45^\circ]_S$ glass-fiber reinforced epoxy tubular specimens under pure hoop loading (1H:0A) - long-term test ($\sigma_{h \max} = 70$ MPa); (a) in global coordinates (loading directions), (b) in material coordinates.</i>	132

LIST OF FIGURES

6.20	<i>Relationship between the permeability and cyclic creep (shear) strain for $[\pm 45^\circ]_S$ glass-fiber reinforced epoxy tubular specimens under pure hoop loading (1H:0A); (open symbols) maximum cyclic shear strain value, and (closed symbols) minimum cyclic shear strain value.</i>	133
6.21	<i>Measured axial laminate stiffness reduction of a $[\pm 45^\circ]_S$ glass-fiber reinforced epoxy tubular specimen under pure hoop (1H:0A) cyclic loading - ($\sigma_{h \max} = 115$ MPa); (a) stiffness reduction evolution for selected monotonic ramps at indicated cycle numbers, (b) derived stiffness reduction curve.</i>	134
6.22	<i>Measured hoop laminate stiffness reduction of a $[\pm 45^\circ]_S$ glass-fiber reinforced epoxy tubular specimen under pure hoop (1H:0A) cyclic loading - ($\sigma_{h \max} = 115$ MPa); (a) stiffness reduction evolution for selected monotonic ramps at indicated cycle numbers, (b) derived stiffness reduction curve.</i>	135
6.23	<i>Measured shear laminate stiffness reduction of a $[\pm 45^\circ]_S$ glass-fiber reinforced epoxy tubular specimen under pure hoop (1H:0A) cyclic loading - ($\sigma_{h \max} = 115$ MPa); (a) stiffness reduction evolution for selected monotonic ramps at indicated cycle numbers, (b) derived stiffness reduction curve.</i>	136
6.24	<i>Measured axial laminate stiffness reduction of a $[\pm 45^\circ]_S$ glass-fiber reinforced epoxy tubular specimen under pure hoop (1H:0A) cyclic loading - ($\sigma_{h \max} = 70$ MPa).</i>	138
6.25	<i>Representative cyclic stress-strain curve for $[\pm 45^\circ]_S$ glass-fiber reinforced epoxy tubular specimens under axial dominated loading (1H:8A) - ($\sigma_{h \max} = 110$ MPa).</i>	139
6.26	<i>Measured surface temperature of a $[\pm 45^\circ]_S$ glass-fiber reinforced epoxy tubular specimens under axial dominated (1H:8A) cyclic loading - ($\sigma_{h \max} = 110$ MPa).</i>	139
6.27	<i>Macroscopic failure modes for $[\pm 45^\circ]_S$ glass-fiber reinforced epoxy tubular specimen under axial dominant (1H:8A) cyclic loading; (top) front view, (bottom) surface map.</i>	141
6.28	<i>Contraction of fibers on the inside of a $[\pm 45^\circ]_S$ glass-fiber reinforced epoxy tubular specimen under axial dominated (1H:8A) cyclic loading at failure.</i>	142

LIST OF FIGURES

6.29	<i>Fluid loss characteristics of a $[\pm 45^\circ]_S$ glass-fiber reinforced epoxy tubular specimen under axial dominated loading (1H:8A) - ($\sigma_{a \max} = 100$ MPa); (a) fluid volume loss (leakage) profile, (b) derived permeability curve.</i>	143
6.30	<i>Fluid loss characteristics of a $[\pm 45^\circ]_S$ glass-fiber reinforced epoxy tubular specimen under axial dominated loading (1H:8A) - ($\sigma_{a \max} = 75$ MPa); (a) fluid volume loss (leakage) profile, (b) derived permeability curve.</i>	144
6.31	<i>Fluid loss characteristics of a $[\pm 45^\circ]_S$ glass-fiber reinforced epoxy tubular specimen under axial dominated loading (1H:8A) - ($\sigma_{a \max} = 60$ MPa); (a) fluid volume loss (leakage) profile, (b) derived permeability curve.</i>	145
6.32	<i>Fatigue-life relationships for $[\pm 45^\circ]_S$ glass-fiber reinforced epoxy tubular specimens under axial dominated loading (1H:8A) based on critical permeability criterion.</i>	146
6.33	<i>Measured cyclic creep strain curves in the material coordinate system for $[\pm 45^\circ]_S$ glass-fiber reinforced epoxy tubular specimens under axial dominated loading (1H:8A).</i>	146
6.34	<i>Relationship between the permeability and cyclic creep (shear) strain for $[\pm 45^\circ]_S$ glass-fiber reinforced epoxy tubular specimens under axial dominated loading (1H:8A).</i>	147
6.35	<i>Measured axial laminate stiffness reduction of a $[\pm 45^\circ]_S$ glass-fiber reinforced epoxy tubular specimen under axial dominated (1H:8A) cyclic loading - ($\sigma_{a \max} = 100$ MPa).</i>	148
6.36	<i>Measured shear laminate stiffness reduction of a $[\pm 45^\circ]_S$ glass-fiber reinforced epoxy tubular specimen under axial dominated (1H:8A) cyclic loading - ($\sigma_{a \max} = 100$ MPa).</i>	148
6.37	<i>Measured axial laminate stiffness reduction of a $[\pm 45^\circ]_S$ glass-fiber reinforced epoxy tubular specimen under axial dominated (1H:8A) cyclic loading - ($\sigma_{a \max} = 60$ MPa).</i>	149
6.38	<i>Representative cyclic stress-strain curve for $[\pm 45^\circ]_S$ glass-fiber reinforced epoxy tubular specimens under equi-biaxial loading (1H:1A) - ($\sigma_{h \max} = 130$ MPa).</i>	150
6.39	<i>Weepage failure mode for a $[\pm 45^\circ]_S$ glass-fiber reinforced epoxy tubular specimen under equi-biaxial (1H:1A) cyclic loading.</i>	151

LIST OF FIGURES

6.40	<i>Scanning electron micrographs of matrix damage for a $[\pm 45^\circ]_S$ glass-fiber reinforced epoxy tubular specimen under equi-biaxial (1H:1A) cyclic loading (sectioned at 45° with respect to the tube axis); (top) through width section, (bottom) local transverse cracking and delamination failure.</i>	152
6.41	<i>Fluid loss characteristics of a $[\pm 45^\circ]_S$ glass-fiber reinforced epoxy tubular specimen under equi-biaxial loading (1H:1A) - ($\sigma_{h \max} = 145$ MPa); (a) fluid volume loss (leakage) profile, (b) derived permeability curve.</i>	153
6.42	<i>Permeability profile for $[\pm 45^\circ]_S$ glass-fiber reinforced epoxy tubular specimens under equi-biaxial loading (1H:1A) - ($\sigma_{h \max} = 110$ MPa).</i>	154
6.43	<i>Fatigue-life relationships for $[\pm 45^\circ]_S$ glass-fiber reinforced epoxy tubular specimens under equi-biaxial loading (1H:1A) based on critical permeability criterion.</i>	155
6.44	<i>Measured axial laminate stiffness reduction of a $[\pm 45^\circ]_S$ glass-fiber reinforced epoxy tubular specimen under equi-biaxial (1H:1A) cyclic loading - ($\sigma_{h \max} = 145$ MPa).</i>	156
6.45	<i>Measured shear laminate stiffness reduction of a $[\pm 45^\circ]_S$ glass-fiber reinforced epoxy tubular specimen under equi-biaxial (1H:1A) cyclic loading - ($\sigma_{h \max} = 145$ MPa).</i>	156
6.46	<i>Biaxial monotonic and cyclic failure (leakage) envelopes for $[\pm 45^\circ]_S$ glass-fiber reinforced epoxy tubular specimens in applied stress space.</i>	157
7.1	<i>Finite element mesh of glass-fiber reinforced epoxy tubular specimens.</i>	162
7.2	<i>Non-dimensional stress (a) and strain (b) distributions along the half gage length of a $[\pm 71^\circ]_S$ glass-fiber reinforced epoxy tubular specimen under pure hoop loading (1H:0A).</i>	169
7.3	<i>In-plane failure strain ratios based on through wall failure for a $[\pm 71^\circ]_S$ glass-fiber reinforced epoxy tubular specimen under pure hoop loading (1H:0A) - ($\sigma_{h \text{ applied}} = 310.1$ MPa); (a) along half gage length, (b) concentration effects at the tab ($\epsilon_1/\epsilon_{1f}^+$ was omitted for clarity).</i>	171
7.4	<i>Non-dimensional stress (a) and strain (b) distributions along the half gage length of a $[\pm 71^\circ]_S$ glass-fiber reinforced epoxy tubular specimen under pure axial loading (0H:1A).</i>	172
7.5	<i>In-plane failure strain ratios based on through wall failure for a $[\pm 71^\circ]_S$ glass-fiber reinforced epoxy tubular specimen under pure axial loading (0H:1A) - ($\sigma_{a \text{ applied}} = 64.0$ MPa).</i>	173

LIST OF FIGURES

7.6	<i>Non-dimensional stress (a) and strain (b) distributions along the half gage length of a $[\pm 71^\circ]_S$ glass-fiber reinforced epoxy tubular specimen under (17H:2A) biaxial loading.</i>	175
7.7	<i>In-plane failure strain ratios based on through wall failure for a $[\pm 71^\circ]_S$ glass-fiber reinforced epoxy tubular specimen under (17H:2A) biaxial loading - (σ_h applied = 393.3 MPa); (a) along half gage length, (b) concentration effects at the tab ($\epsilon_1/\epsilon_{1f}^+$ was omitted for clarity).</i>	176
7.8	<i>Non-dimensional stress (a) and strain (b) distributions along the half gage length of a $[\pm 45^\circ]_S$ glass-fiber reinforced epoxy tubular specimen under pure hoop loading (1H:0A).</i>	178
7.9	<i>In-plane failure strain ratios based on through wall failure for a $[\pm 45^\circ]_S$ glass-fiber reinforced epoxy tubular specimen under pure hoop loading (1H:0A) - (σ_h applied = 88.3 MPa).</i>	179
7.10	<i>Non-dimensional stress (a) and strain (b) distributions along the half gage length of a $[\pm 45^\circ]_S$ glass-fiber reinforced epoxy tubular specimen under axial dominated loading (1H:8A).</i>	180
7.11	<i>In-plane failure strain ratios based on through wall failure for a $[\pm 45^\circ]_S$ glass-fiber reinforced epoxy tubular specimen under axial dominated biaxial loading (1H:8A) - (σ_h applied = 100.7 MPa).</i>	181
7.12	<i>Non-dimensional stress (a) and strain (b) distributions along the half gage length of a $[\pm 45^\circ]_S$ glass-fiber reinforced epoxy tubular specimen under equi-biaxial loading (1H:1A).</i>	182
7.13	<i>In-plane failure strain ratios based on through wall failure for a $[\pm 45^\circ]_S$ glass-fiber reinforced epoxy tubular specimen under equi-biaxial loading (1H:1A) - (σ_h applied = 117.1 MPa).</i>	183
7.14	<i>Predicted and experimental biaxial failure (leakage) envelopes for $[\pm 71^\circ]_S$ glass-fiber reinforced epoxy tubular specimens in applied stress space. .</i>	184
7.15	<i>Predicted and experimental biaxial failure (leakage) envelopes for $[\pm 45^\circ]_S$ glass-fiber reinforced epoxy tubular specimens in applied stress space. .</i>	185

LIST OF SYMBOLS

β	prescribed nodal rotations
C	compressibility
d_i	inside specimen diameter
d_m	mean specimen diameter
d_o	outside specimen diameter
E_A	global axial laminate modulus
E_H	global hoop laminate modulus
ϵ_a	measured axial strain
ϵ_h	measured hoop strain
$\epsilon_1, \epsilon_2, \gamma_{12}$	derived strain components in the material coordinate system
$\epsilon_{1f}, \epsilon_{2f}, \gamma_{12f}$	critical failure strains in the material coordinate system
F	applied axial force
f_c	cyclic frequency
K	permeability
l_g	specimen gage length
μ	dynamic (absolute) fluid viscosity
ν_{AH}, ν_{HA}	global laminate Poisson's ratio
P_i	applied internal pressure
Q	volumetric flow rate
r_m	mean specimen radius
σ_a	applied axial stress
σ_h	applied hoop stress
T	applied torque
θ	fiber angle orientation with respect to the structural (loading) axis
V_h	volume in hoses and connections
V_i	intensifier volume
V_p	apparent volume lost due to compression of fluid
V_s	internal specimen volume
V_t	total system volume (corrected)
u	prescribed nodal displacements
w	specimen wall thickness

CHAPTER 1

Introduction to Composite Materials

1.1 BACKGROUND

1.1.1 Introduction

Composite materials are material forms which consist of two or more distinct constituents which are combined macroscopically to obtain specific properties or performance characteristics. By combining material types, advantageous properties from each constituent can be exploited to create properties unique to the composite form. Composite materials are defined by their constituent material type and form. Binary (or two-phase) composite forms are the most common, and typically consist of a discontinuous phase (reinforcement) embedded in a continuous one (matrix). Commonly available reinforcement types include continuous and short fibers (glass, carbon, graphite, aramid, boron), and particles (SiC, Al_2O_3). Common matrix materials include thermosetting (epoxies, vinylesters, polyesters) and thermoplastic (PEEK, Nylons, Polyethelynes) polymers, metals (aluminium, titanium) and ceramics (SiC, carbon). The use of a particular reinforcement/matrix combination ultimately depends upon the intended application. In most cases, the reinforcement phase is used to provide structural integrity to the composite structure (especially under tensile type loading conditions).

Fiber reinforced polymeric composites are probably the most predominant form of structural composite material in use today. Applications are found in many areas including aerospace, transportation, oil and gas production, chemical processing, consumer goods and infrastructure rehabilitation. Polymeric composites are displacing metals in a number of applications because of two primary advantages: a) a

high strength (and stiffness) to weight ratio, and b) corrosion resistance in common environments.

Because of their high strength to weight ratio, fiber reinforced polymeric composites have been extensively investigated and used in the aerospace industry over the last four decades. Their use as a primary structural material in *industrial applications*, however, has been limited. When compared to conventional metals, the use of composites in structural design is restrictive due to: a) higher material and processing costs, b) limited manufacturing options, c) difficulty in joining, d) lack of available infrastructure (manufacturing and servicing) and e) lack of validated design methodologies. Although the breadth of potential material combinations is overwhelming from a research point of view, only limited material types and forms are readily available in the marketplace. The use of composite materials in a particular application is usually justified by long-term or value added economic savings.

In fiber reinforced composites, continuous fibers, made of glass, carbon and graphite, have exceptionally high strength compared to their material in bulk form. This apparent strengthening is attributed to the atomic composition of these materials (high molecular or atomic bonding strengths), and to the reduction of debilitating microstructural defects in the (small diameter) fiber form. When these fibers are bound together by a matrix substrate in a parallel orientation, very high strength and stiffnesses in the unified composite structure can be achieved in the fiber direction. When fabricated in a planar form, the resulting composite structure is referred to as a *lamina*. This material form has orthotropic properties (stiffness and strength) with respect to the fiber direction. In most practical applications, the lamina form is rarely used by itself since the transverse strength and stiffness (perpendicular to the fiber direction) is typically orders of magnitude smaller than that in the fiber direction. By combining (stacking) many lamina at various orientations (as shown in figure 1.1), a *laminate* with improved multi-directional strength properties can be produced.

Referring to figure 1.1, the laminate geometry is defined by the fiber angle orientations of each layer with respect to a global structural or loading reference frame. Laminate geometries are coded by a sequence representing the layer order from top to bottom (for example $[+\theta_1, -\theta_1, +\theta_2, -\theta_2]_T$ is a four layer laminate with $+\theta_1$ at the top and $-\theta_2$ at the bottom). If the laminate is symmetric with respect to its midplane, only one half of the sequence is coded with symmetry being distinguished by the subscript 's' (see figure 1.1).

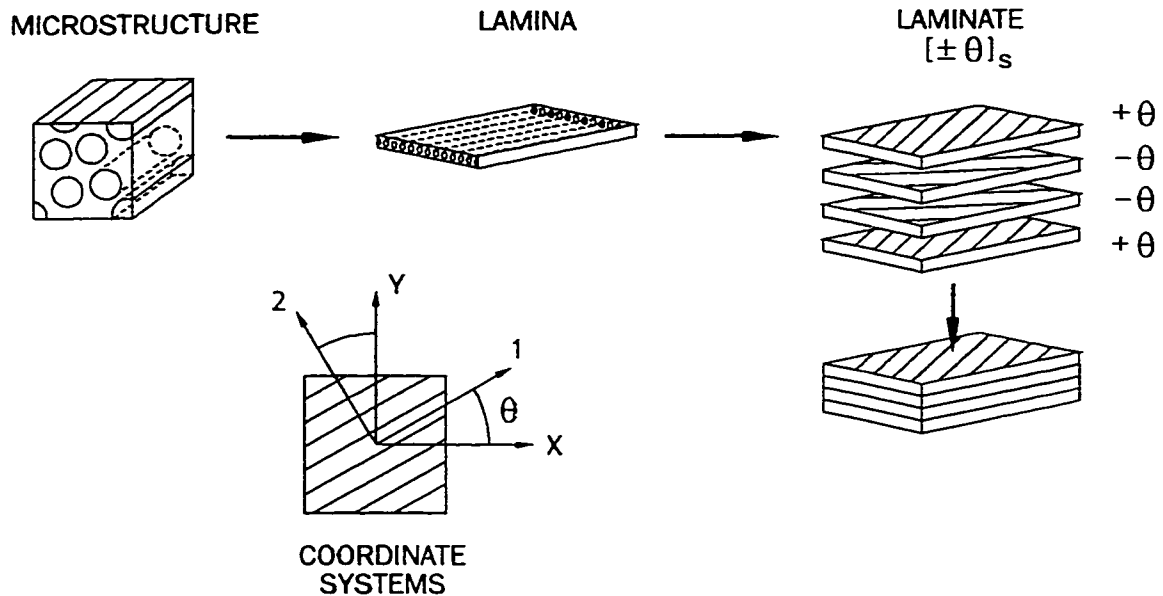


Figure 1.1: Definitions for fiber reinforced laminated composites (where θ is the fiber angle orientation with respect to the structural or loading axis).

1.1.2 Manufacturing Methods

Selection and useage of a composite material in a particular application will ultimately depend upon its cost effectiveness and its ability to be fabricated. Various methods have been developed to manufacture fiber reinforced composite structures (see review in reference [1]). The most common methods for fabricating tubular structures are a) hand lay-up, b) filament winding, c) braiding, and d) tape laying.

The oldest and simplest manufacturing method is the *hand lay-up method*. With this method, flat, contoured or cylindrical shapes are created by placing layers of resin soaked mat reinforcement (chopped strand or woven fabric) onto a mold surface. Multiple layers are placed on top of one another with joints typically staggered in order to reduce stress concentrations. Excess resin is removed from the system by manual “squeegee” operations. This method is popular due to its low cost and infrastructure requirements, and is commonly used to manufacture fluid containment structures. Since the paths of fibers are not continuous through the circumference, however, vessels made by hand lay-up are typically restricted to low pressure service.

The most common method of fabricating shells of revolution is *filament winding*. The method consists of winding continuous fiber rovings (glass or carbon fibers)

onto a solid rotating mandrel. As the mandrel is rotated, the fiber delivery system traverses along the axis of the mandrel and dispenses the fiber/resin combination. The relationship between the mandrel rotation and traversing speeds determine the angle at which fibers are placed with respect to the rotating axis. In *wet filament winding*, fiber rovings are run through a bath of liquid resin before being deposited on the surface of the mandrel. Tensioning of the fibers is required to ensure proper fiber/resin ratios and consolidation of the layers. In *dry filament winding*, fiber rovings are pre-impregnated with solidified resins (i.e. tow-pregs) which allows for better control of constituent distribution and a much cleaner process. For both methods, heat and pressure are often applied after the winding operation in order to fully consolidate the layers. The precise placement of fibers, regulation of resin wetting, and fiber tensioning are critical factors in ensuring high quality, filament wound parts [2]. Precision filament winding infrastructure, however, is expensive.

Braiding is a relatively new but promising technology where the fiber/resin system is applied to a mandrel by an intricate inter-weaving process using dry or pre-impregnated (tow-preg) fibers. If dry reinforcement is used, low viscosity resin must be injected into the preformed fiber network using a technique known as *resin transfer molding*. Although somewhat similar to filament winding, the braiding process produces much more inter-weaving in the structure. Braiding has a greater advantage in that it can apply reinforcement in three-dimensions, and can produce very intricate “near net” shapes. Due to this 3D inter-weaving, braided structures have been shown to be extremely damage tolerant (i.e. impact resistant) [3].

The final fabrication process reviewed is the *tape laying method*. In this method, the basic material system consists of pre-impregnated (continuous) fiber reinforced polymer sheets (also referred to as *prepreg*). Similar to the hand lay-up method, flat, contoured or cylindrical shapes are created by laying patterns of prepreg onto a mold surface. The laying process can be performed manually or by automated methods [4]. Since the resin system is typically in a “B-stage” form (i.e. solidified but only partly cross-linked), heat and pressure are required to properly consolidate the layers. This is most commonly accomplished using vacuum bagging techniques in conjunction with autoclave curing systems. The main advantage of this method is that parts can be fabricated with exceptionally high quality (i.e. highly uniform fiber distributions and low void content). The main disadvantage, however, with prepreg based techniques is the high material and large scale production costs.

1.2 DAMAGE DEVELOPMENT IN COMPOSITE MATERIALS

Damage development in composite materials is characterized by the initiation and accumulation of multiple, interacting damage events over a number of geometric length scales. This complex damage progression is attributed to the heterogeneous and anisotropic nature of the composite material at the micro- and macro-structural scale. This multiplicity of interacting and competing failure modes is in contrast to the initiation and self-similar propagation of a singular damage event typically found in isotropic, homogeneous materials (e.g. metals).

Damage begins (initiates) at the micro-scale in the form of inter-fiber matrix cracking, fiber/matrix debonding, fiber breakage and fiber buckling. These events often occur simultaneously at multiple initiation sites, and coalesce to form macroscopic failure modes such as intralaminar cracking (transverse matrix cracking), interlaminar cracking (delamination), continuous fiber failure, and global instability (buckling). Although the number of failure modes is small, their multiplicity and interaction can result in highly complex failures. Over the past four decades, these individual failure modes have been well documented and modeled individually, but their combined effects and interaction are still not fully understood.

Because of the progressive nature of damage, the definition of failure in composites is not straightforward, and is often based on functional aspects of the intended application. Common definitions include point of damage initiation (first ply failure), ultimate failure (complete fracture and separation), loss of required stiffness, loss of residual strength or leakage of fluid (for fluid containment applications). Hence, depending upon its definition, the failure of a composite structure can be quite unique.

In general, the highest strength and stiffness of a lamina is achieved when the fibers are oriented in the direction of the applied load. Unfortunately, most real loading conditions are multiaxial in nature, and, as such, laminates must be designed with multi-directional fiber orientations. The main consequence of lamination is the resultant structural dependence on the material response. As opposed to isotropic or orthotropic material forms (e.g. metals, uni-directional lamina), the stress state of a material element within a laminate is inherently multiaxial. If the contribution of matrix dominated layers to the global response is significant, the stress-strain behaviour of a laminate is typically non-linear as a result of progressive damage and

matrix visco-elasticity.

The linear elastic response of general laminate geometries can be successfully predicted using properties of the individual laminae in conjunction with homogenization techniques such as classical laminate theory [5,6]. In these macro-mechanical models, the composite is treated as a continuum with effective material properties being determined through macroscopic characterization tests, or predicted from the constituent material properties using micro-mechanical models.

Prediction of non-linear response and ultimate laminate failure, on the other hand, has proven to be difficult due to the complex nature of progressive damage found in laminates. Although there has been significant research in this area, there still is no universal methodology which can accurately predict failure (functional or structural) in laminated structures (see reviews in references [7–9]). The generally disappointing correlation between experiments and predictions using the multitude of failure criteria available (see for example [10–12]), has been attributed to two key factors: 1) the inability to properly model the stress-strain behaviour, and 2) the inappropriate characterization of some failure properties. Recent attempts, however, to create progressive damage models, which include the prediction and accumulation of individual failure modes, have shown some promise in a limited number of cases [13–15].

In general, the initiation and accumulation of the aforementioned damage modes in composites is influenced by a number of factors: 1) constituent material types and properties (matrix, fiber and interface), 2) manufacturing method (micro- and macro-defects, and residual stresses), 3) lay-up geometry (fiber angle orientation, stacking sequence, number of layers, ply thicknesses, and free edge conditions), 4) loading conditions (monotonic, cyclic, time dependent and multiaxial), and 5) environment.

These effects are briefly examined in the following sections.

1.2.1 Microstructural Damage and Effect of Constituents

The global failure of composite materials is initiated at the micro-scale in the form of fiber fracture, inter-fiber matrix cracking, and fiber/matrix debonding. The distributed nature of damage at this scale is due to the statistical strength and non-homogeneous variation of the constituent fiber phase and inherent defects.

The progression of damage at this scale has been well documented experimentally. When tensile loads are applied parallel to the fibers (fiber dominated), the first observable sign of damage is the development of distributed fiber fractures and short matrix cracks perpendicular to the fiber direction [16]. Growth of these short matrix cracks is arrested by the constraint effect of the fiber phase. After further loading, the short perpendicular cracks transform into macrocracks along the fiber direction (splitting behaviour) which ultimately leads to massive fiber failure.

Under compression loading, fiber and matrix shearing, and fiber microbuckling are the most common microstructural failure modes observed [17, 18]. Fiber microbuckling occurs as a result of the loss of matrix constraint and stiffness due to the formation of small-scale matrix damage (brittle mode), or due to non-linear shear deformation (ductile behaviour). Compared to the tensile loading case, the failure of unidirectional fiber composites under compression is highly dependent upon the properties of the supporting matrix system.

Under matrix dominated loading conditions (i.e. loads transverse to the fiber direction), the initiation and development of microcracks is seen to occur at both inter-fiber and interface locations, typically at sites where local fiber non-homogeneity occurs (either as fiber clustering or matrix rich areas) [19, 20]. Crack propagation is again restricted due to variations in local stress fields caused by the random distribution of the fiber phase. As load is increased, these micro-crack features coalesce around fibers to form a dominant intra-laminar or inter-laminar macro-crack.

In the development of transverse macro-cracks, the relative dominance of inter-fiber cracking or debonding is dependent upon the multi-axial characteristics of the matrix and the strength of the fiber/matrix interface. The local stress conditions in the matrix phase is highly multi-axial due to the presence and constraint of the non-homogeneous fiber phase [21, 22]. The global behaviour of the composite is reflected by these multi-axial properties of the matrix. Under multi-axial loading, thermoset polymers have been shown to exhibit a combination of brittle behaviour under normal tensile loading, and ductile behaviour under shear and compressive loads [23]. When thermoset polymers are reinforced with fibers, the brittle behaviour is enhanced by the local stress concentration effect of the fiber phase. This is ultimately responsible for the lower matrix strains observed in composites as compared to neat resins. The matrix response under shear loading is responsible for the observed macroscopic

non-linear, large deformation, and time dependent behaviour of shear dominated laminates [24–26] (for example, $[\pm 45^\circ]$ laminates under uniaxial loading).

In general, the failure of both fiber and matrix dominated lay-ups has been shown to be affected by matrix toughness [27–29], interface strength [30–32], fiber/matrix distribution [33] and fiber volume fraction [34, 35]. Because the transverse cracking mode can occur early in the loading of a general laminate, the use of toughened resin systems to increase composite strength has been explored. Experimental results, however, have shown mixed results in terms of the benefits of toughened resin systems. Increasing matrix toughness has been shown to provide little improvement in transverse tensile strength when the interface failure mode is dominant [21, 30]. Conversely, by using toughened matrices, improvements in compressive properties and impact resistance of laminates have been shown due to the increased resistance to shear and delamination failures [36].

The prediction of global failure events (e.g. macro-crack formation) based on micro-mechanics is an extremely difficult problem. This is primarily due to the various length-scales encountered in laminated composites [37], and the intractability of defining and modeling true representative material elements. Micro-mechanical models are further hampered by the statistical variation of the constituent phases (i.e. fibers and micro-defects), and by the inability to properly characterize all failure properties at the micro-scale. Percolation type models, using simple spring elements, have been developed to study the effect of non-homogeneous phase distribution on macro-crack formation [33]. Due to the discrete nature of these models, however, direct correlation with experiments is not possible.

1.2.2 *Manufacturing Induced Effects*

Manufacturing induced effects such as non-homogeneous phase distributions, defects, and residual stresses can substantially reduce material strength. The presence of microstructural anomalies such as fiber clustering, matrix rich areas, voids, fiber waviness, and fiber crossover (inter-weaving) is highly dependent upon the manufacturing method used. These inherent flaws are assumed to be responsible for the observed *scaling effects* found in composite materials (i.e. macroscopic strength is seen to decrease as the bulk volume of material tested is increased) [38–41]. In gen-

eral, the basic objective during manufacturing is to create a uniform microstructural distribution and reduce the presence of associated defects.

Voids are formed in composite laminates as a result of physical air entrapment during the lamination process (tape placement or filament winding), or due to the evolution of volatile gases as the matrix phase is cured [42,43]. Due to stress concentration effects, voids have been observed to be crack initiation sites for both intralaminar and inter-laminar matrix cracking [44,45]. Many studies have correlated an increase in void content with reduced macroscopic strength under both monotonic and cyclic loadings [42,46]. The effect of void content, however, has been shown to be critical only if large quantities are present (i.e. > 5%) [35,47]. Furthermore, the impact of voids is dependent upon their size and distribution within the laminate [48].

Fiber waviness can occur locally or globally in composite layers as a result of manufacturing processes or material handling. The effect of fiber and layer waviness on the mechanical behaviour of laminates has been studied extensively. In-plane fiber waviness has been shown to have a detrimental effect on the compressive strength of laminates [49–51], but tends to increase in-plane shear strength and delamination resistance [52]. The effect of out-of-plane (radial) layer waviness, common in many tubular manufacturing processes, was found to be dependent upon the severity and location in the tube wall [53,54]. Mild waviness was shown to have no substantial global effect. Localized fiber undulations due to fiber crossover or interweaving (which occurs in filament wound structures) has also been shown to be detrimental to monotonic failure strength in tubular specimens [55,56].

A common result of elevated temperature curing processes, found in most composite fabrication methods, is the creation of thermal residual stress states within the composite laminate at the micro- and macro-scales. The formation of residual stresses at the micro-scale is due to the mismatch between the coefficients of thermal expansion of the constituent phases. At the macro-scale, global residual stresses form in each layer as a result of ply anisotropy (i.e. coefficient of thermal expansion and stiffness). Since the polymer phase is consolidated at elevated temperatures, shrinkage and constraint by neighbouring phases or plies results in the development of residual stresses as the laminate is cooled to room temperature. Residual stress gradients can also occur within a ply as a result of processing induced variations in the fiber/resin ratio [57,58], or non-uniform temperature distributions during cure [59,60].

The state of residual thermal stress in a composite part is a function of a) the material system (resin cure temperature, coefficients of thermal expansion, and relative stiffnesses), b) laminate geometry (fiber angle orientation and stacking sequence), and c) uniformity of heat application. The presence of thermal residual stress gradients during and after curing has been linked to the formation of defects such as fiber waviness (due to compressive residual stresses in the fiber direction) [61] and matrix cracking (due to tensile residual stresses in the transverse direction) [62].

1.2.3 Macrostructural Damage Modes

A consequence of the lamination process is the observed development of two unique macroscopic failure modes: a) transverse matrix cracking (intralaminar) and b) delamination (interlaminar). Although these failure modes may not be catastrophic, their presence plays a significant role in the functional behaviour of composite structures (e.g. stiffness reduction and leakage), and can affect the ultimate strength of a laminate due to local load redistribution and stress concentration effects.

Transverse matrix cracking in a laminated ply is characterized by planar cracks running parallel to the fiber direction and through the ply thickness. In unidirectional lamina, the first occurrence of a dominant macro-crack will ultimately result in specimen separation. In multidirectional laminates, however, the development of transverse cracks is not catastrophic due to the load carrying capacity of the neighbouring constraining plies. This results in the unique formation of an evenly distributed crack field throughout the laminate.

Since transverse cracking is often the first visible sign of observable macro-damage, it has been extensively studied for monotonic [29, 63–66], cyclic fatigue [64, 67, 68], and static fatigue loading conditions [66, 69]. Although extensive experimental and analytical work has been directed towards this mode of failure, studies have been restricted to that of mode I cracking in cross-ply ($[0^\circ, 90_n^\circ]_s$) coupon specimens under uniaxial loading.

In these studies, the initiation of transverse cracking has been shown to be responsible for the initial change in global stiffness and observed non-linearity in the stress-strain curve. The distributed nature of the transverse crack field is due to a combination of the statistical variation of material strength, and to the changing

stress field within the ply as a result of the formation of cracks. Load redistribution and stress concentration effects at the tips of these transverse cracks have also been shown to cause localized failure in the neighbouring constraining plies [70]. The initiation of transverse cracking within a laminate is significantly affected by the ply thickness [71–73]. Due to the enhanced effect of layer constraint, the transverse (in-situ) strength of a ply can be effectively increased by reducing its thickness.

Another common macrostructural failure mode observed in laminated structures is *delamination*. Delamination is characterized by the two-dimensional separation of layers along an inter-ply boundary within a laminated structure. Delamination failure has been observed to initiate: a) at geometric boundaries (edge effect) [74–76], b) from transverse cracks [77–79], c) due to lateral impact loading [80–82] and d) due to in-plane compressive loading [36, 80]. In all these cases, delamination occurs as a result of generated interlaminar tensile and shear stresses (which form due to the anisotropic mismatch in neighbouring ply properties), and to the general weakness of the interlaminar interface.

The most common example of this failure mode is as a result of the *free edge effect* found in multi-directional laminated coupon specimens. This phenomenon has been extensively studied due to the use of coupon type specimens in materials characterization. The dominance of free-edge failure is a function of the laminate stacking sequence, fiber angle orientation, and specimen width [74, 75, 83].

Lateral impact damage is characterized by the localized formation of concentric delaminations through the thickness of the laminate at the point of impact. These stratified delaminations are coupled together by transverse matrix cracks, and are formed due to localized out-of-plane shear stresses imposed by the lateral impact forces.

The presence of delaminations has been shown to reduce global stiffness [76] and in-plane compressive strength due to buckling behaviour [80]. Effect and growth of imposed delaminations have been studied under monotonic and fatigue loading conditions [84, 85]. Whereas fracture mechanics has been unsuccessful in predicting crack growth in notched laminates due to the lack of a singular, self-similar fracture event, it has been successfully applied in characterizing delamination propagation [86–89].

1.2.4 *Effect of Cyclic Loading*

The behaviour of fiber reinforced composites under cyclic loading conditions has been studied extensively for a wide range of material systems and geometries (see reviews in references [90–92]).

In general, the micro- and macro-structural damage events observed during cyclic loading are the same as those observed under monotonic loading [93]. The sequence and dominance of particular failure modes, however, can be substantially different depending upon their unique fatigue characteristics. Fiber dominated lay-ups tend to exhibit better fatigue resistance due to the inherent strength of the constituent fiber phase [94,95]. By comparison, the fatigue strength of off-axis plies are typically more than an order of magnitude less with a much steeper slope in their fatigue-life curves [35,96].

In multi-directional laminates, the failure progression under tensile fatigue loading occurs in three distinct phases [67,97–100]. The first phase is characterized by a rapid increase in matrix damage accumulation, in particular, the formation of transverse matrix cracks in the off-axis plies. The crack formation is seen to initiate and saturate quite early in the life of the laminate, and is marked by a significant drop in global stiffness.

The second phase begins at the point of transverse crack saturation, and is characterized by a slower rate of damage accumulation. During this phase, the initiation of other damage modes begins to occur (i.e. matrix splitting in the fiber dominated plies, delamination and local fiber failure). The reduction in damage accumulation rate is reflected by a much slower reduction in global stiffness. It is also during this stage that the residual strength of the laminate begins to decrease. This phase often represents a significant portion of the specimen life.

In the last stage, damage in the fiber dominated layers (due to extensive fiber fracture and delamination) is seen to dominate, resulting in a high rate of damage accumulation (and a large drop in global stiffness) leading up to ultimate failure.

Under compressive cyclic loading, initiation and propagation of delamination damage is dominant due to development of high interlaminar stresses and the resulting propensity for ply buckling [36,99,101,102]. Delamination first occurs at the outer layers due to lack of lateral constraint, followed by the inner plies. The compressive

fatigue strength is highly dependent upon the laminate geometry (stacking sequence) and fracture properties of the matrix [36].

Due to its time dependent effects, the cyclic shear behaviour of unidirectional laminae and matrix dominated laminates has received considerable attention [83, 103–105]. The cyclic response for shear dominated loading is characterized by extensive ratcheting behaviour (cyclic creep) and large strains at failure. The $[\pm 45^\circ]$ angle-ply laminate, commonly used as a sub-laminate group, is seen to possess this shear dominated behaviour under uniaxial loading.

Similar to that observed in metals, the effect of cyclic loading ratio (or mean stress effect) has been shown to significantly affect the fatigue life of unidirectional laminae [96] and multidirectional laminates [106–109]. However, this effect in composites is not straightforward due to the multiplicity, interaction and competition between failure modes. In general, fully reversed tension-compression loading ($R = \sigma_{min}/\sigma_{max} = -1$) has been shown to be the worst case due to the combined interaction of tensile and compressive failure modes [96, 110]. For matrix dominated tension-tension cyclic loading, a tensile mean stress is seen to reduce fatigue lives due to the acceleration of cyclic creep [103].

The effect of frequency on the fatigue behaviour of composite materials has been also shown to be quite contradictory and not well understood. Increases [103, 111, 112], decreases [113, 114] and plateaus [115] in fatigue life with increasing frequency have been observed. This indicates that the effect of frequency is rather complex and depends upon the material system, laminate geometry, and loading conditions. It has been observed, however, that matrix dominated lay-ups tend to be more sensitive to changes in frequency [116].

1.2.5 *Effect of Environment*

Although polymeric composites are resistant to corrosion in the traditional sense (i.e. degradation by oxidation), they are not immune to environmental effects. Absorption of water in polymeric composites and its effect on mechanical behaviour has been studied extensively in the literature (see review in [117]). While in some studies, water absorption has been shown to have a detrimental effect on composite strength and stiffness [118–120], other studies have demonstrated no effect at all [121, 122]. This

implies that the effect of environment is critically dependent upon the specific chemistry of the material system. Although all microstructural phases have been shown to be affected by water absorption including the matrix [123], glass fibers [124–126] and interface [126–128], the mechanisms behind these effects are not clear.

In the matrix phase, changes in material response have been attributed to two different phenomena: a) moisture induced expansion (swelling) and b) matrix plasticisation. Swelling occurs due to the expansion caused by the ingress of water molecules into the cross-linked polymer microstructure. This results in an alteration in the internal residual stress state in the laminate, countering the previously mentioned thermal residual stresses. As such, for matrix cracking modes, expansion due to moisture absorption has been observed to increase the stress at crack initiation [62].

The plasticisation phenomenon, however, is much more complicated. It is seen to affect the crack-tip characteristics in fractured polymer matrices resulting in reduced long-term resistance to crack growth [20, 129]. Plasticisation is inherently affected by the properties of the polymer (in particular, toughness) and the hygrothermal aging period (amount of water intake).

In order to predict long-term environmental effects, the diffusion characteristics of water in thermoset composites have been extensively studied [119, 121, 130]. Diffusion characteristics are seen to depend upon the material system and laminate geometry. Cyclic loading has been observed to accelerate transport as a result of fatigue induced matrix cracking [127, 131–133].

1.3 BIAXIAL CHARACTERIZATION OF COMPOSITE MATERIALS

Applied biaxial loading plays a significant role in the behaviour and failure of laminated composite structures. Due to the biaxiality of most real loading conditions and the material anisotropy in composites (i.e. directional dependence), characterization under biaxial loading is enormously important.

Biaxial tests on composites are not commonly performed due to their difficulty, expense (in specimen fabrication and testing), and requirement for complex and costly infrastructure. Of the biaxial studies cited in the literature, only a limited number of tests are usually performed due to the time consuming nature of these experiments. As such, the vast majority of studies on composites have been performed on laminated

coupon specimens under uniaxial loading conditions.

Biaxial tests have been performed on composite laminates in order to determine material properties (elastic, inelastic, and failure), and to study structural effects (laminated geometry, imposed cracks and notches) under complex loading conditions. Biaxial testing, however, is most commonly used to generate biaxial failure envelopes for use in design or verification of available failure models. Depending upon the specimen geometry, the envelopes can be defined with respect to a number of applied or material (in-situ) coordinates, and by various failure criteria. The failure points are generated by specialized tests which provide the required state of biaxiality in applied stress or strain space.

Biaxial testing machines are inherently designed around the geometry and loading requirements of the test specimen. The majority and most successful of these testing facilities can be classified by one of two main test specimen geometries, a) the cruciform (planar) specimen, and b) the thin-walled tubular specimen.

Cruciform testing machines typically consist of two sets of orthogonal actuating mechanisms which apply biaxial loads directly to a flat cruciform specimen in a single plane. The cruciform specimen is the preferred choice for crack growth studies as 1) the surface is accessible and visible, 2) long crack formation can be accomplished, and 3) there are no curvature effects. The disadvantage with cruciform testing techniques is the difficulty in accurately determining the distribution of stresses in the specimen. This stress distribution is often determined using empirical or numerical methods, and is largely dependent upon the specimen design, configuration of the loading frame, specimen attachment, and actuation method. This accounts for the large number of variations in the reported specimen designs [134, 135] and testing apparatus [136, 137]. For composite materials, grip attachment and free edge effects further tend to limit the testing to specific laminate geometries and loading conditions [138]. Cruciform type specimens have been used to characterize biaxial failure of notched [138–140] and unnotched [102, 141–143] laminates under monotonic and cyclic loading.

The thin-walled tubular specimen has been shown to be the most versatile geometry available for characterizing biaxial properties in materials. As shown in figure 1.2, an applied biaxial stress or strain field can be introduced into the specimen through the application of a pressure differential (internal and external pressure), axial force

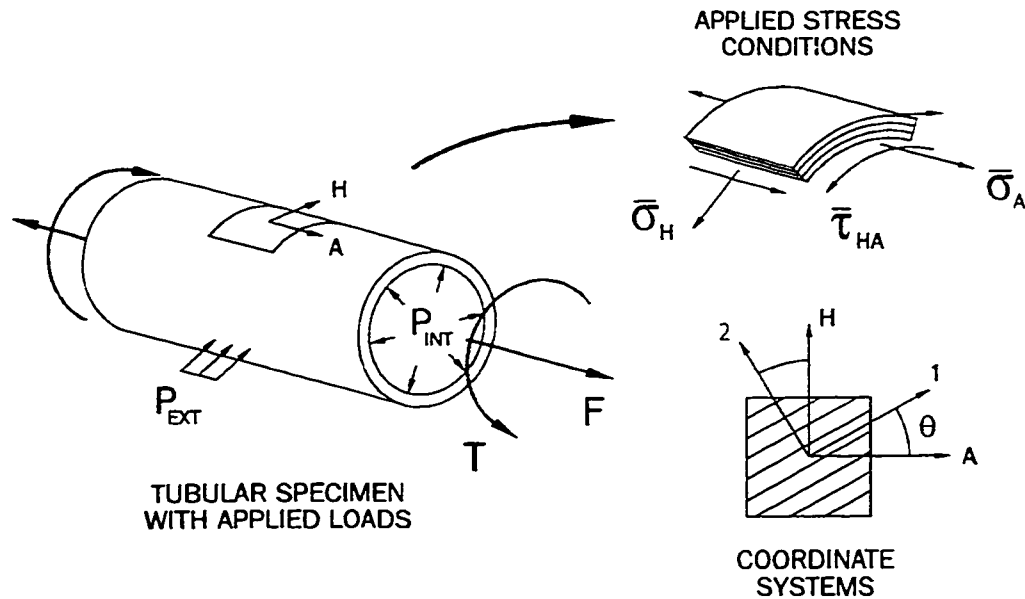


Figure 1.2: Applied loading conditions and definition of fiber angle orientation (θ) in a fiber reinforced laminated tubular specimen.

and torsion (for further discussion of loading configurations, see chapter 2). Lay-up geometry, applied loading, and failure envelopes are usually defined with respect to the cylindrical coordinates of the tube (i.e. axial, hoop and radial directions). The fiber angle orientation within each layer is defined with respect to the axial direction.

Unidirectional tubular geometries ($[0^\circ]$ or $[90^\circ]$) are often used to determine lamina material properties under applied axial and shear loading [144–149]. When compared to isotropic materials, the stress distribution in unidirectional laminae are found to be less uniform through the wall thickness and, as such, higher diameter to thickness ratios are typically required [150]. Early attempts were made to use helically wound unidirectional tubes $[\theta]_n$ in an effort to test theoretical transformation laws [151, 152]. These specimens, however, were found to be very susceptible to end buckling effects as a result of the lamina shear-extension-bending coupling.

Un-notched multidirectional tubular geometries have been extensively tested with a wide range of material systems, geometries, and loading configurations. A summary of studies is provided in table 1.1. While a vast majority of these tests have been concerned with characterizing the ultimate failure strength under monotonic loading, relatively few biaxial fatigue studies have been conducted [10, 153–157]. Of the monotonic studies, generation of failure envelopes has typically been restricted to the

tension-tension biaxial regime. Only a few have been able to generate the complete biaxial failure envelope in all hoop/axial loading quadrants [12,145,158].

In addition to its predominant use in determining the failure properties of un-notched geometries, composite tubular specimens have also been used to characterize failure under lateral impact loading [215–220] and axial impact loading [221–225], and in studies involving damage tolerance (i.e. notched specimens) [226–232].

1.4 FUNCTIONAL FAILURE IN COMPOSITE TUBULARS

For pressurized containment structures (i.e. piping, down-hole tubulars and pressure vessels), failure is defined as the inability of the structure to contain its fluid (leakage). The ability to predict and understand leakage failure is, therefore, a necessary requirement for a successful design. For metallic structures, there exists a well established background and understanding of their behaviour under a wide range of applied conditions. This understanding is translated into the wealth of available codes and standards of practise which enable engineers to design safe and reliable structures. For fiber reinforced composites, however, there is a general lack of knowledge and understanding of these materials, particularly, in terms of their long term behaviour. To date, there exists a limited body of published work on leakage failure characterization of fiber reinforced composite pipe and tubing. Most have dealt with characterizing leakage failure under monotonic loading [159,160,165–167,178,182,198,204,214] but few have dealt, explicitly, with the long-term cyclic performance [160,170,198,205]. Of the studies conducted under cyclic loading conditions, only the pure hoop (1H:0A) [205] and (2H:1A) [160,170,198,199] biaxial loading ratios were investigated.

Hull and co-workers studied the monotonic behaviour of angle-ply ($\pm\theta$) filament wound glass-fiber polyester pipe for pure hoop (1H:0A), pure axial (0H:1A) and (2H:1A) loading ratios [165–167]. In general, fiber dominated loading cases exhibited much stiffer responses with higher applied stresses at failure (leakage and ultimate failure). Based on microscopic examination of tested specimens, it was noted that the relationship between winding angle and loading ratio had a significant effect on the crack distribution in the tubes. It was also observed that the preferred site of transverse crack initiation were regions of high fiber volume fraction.

Table 1.1: Summary of Biaxial Tests on Fiber Reinforced Polymeric Tubular Specimens

Author	Refs	Material *	Lay-up Geometry	Loading †	Analysis Method/ Failure Criteria ‡
Bax (1970)	[159]	GF-EP,PR [WFW]	[±50], [±55]	MONO,STF [LC] (+2σ _h :+1σ _a)	
Mieras (1973)	[160]	GF-EP,PR [WFW]	[±55]	MONO,STF,CYCF [LC] (+2σ _h :+1σ _a)	
Hütter et al. (1975)	[145]	GF-EP [WFW]	[90], [90, ±30, 90]	MONO [LC] (±σ _h :±σ _a :τ)	Linear AM [UF:TH,PU,OTHER]
Owen and co-workers (1975-82)	[10,34,161,162]	GF-PR [WHL]	[0, 90]	MONO,CYCF [LC] (±σ _h :±σ _a)	[UF:TW,TH,OTHER]
Guess et al. (1977-80)	[163,164]	CF,AF-EP [WFW]	[90], [±30, 90],	MONO [LC] (+σ _h :+σ _a)	Linear CLT,FEA [UF:MXS,OTHER]
Hull and co-workers (1978-79)	[165-167]	GF-PR [WFW]	[±35], [±45] [±55], [±65] [±75]	MONO [LC] (+σ _h :+σ _a)	Linear CLT [DI:NA,OTHER]
Soden and co-workers (1978)	[168,169]	GF-PR [WFW]	[±35], [±55], [±72.5]	MONO [LC] (+σ _h :±σ _a)	Non-linear CLT [DI,UF:OTHER]

(continued)

Table 1.1: Summary of Biaxial Tests on Fiber Reinforced Polymeric Tubular Specimens (continued)

Author	Refs	Material *	Lay-up Geometry	Loading †	Analysis Method/ Failure Criteria ‡
Swanson and co-workers (1986-93)	[146,183-189]	CF-EP [TR,DFW]	[90], [90, ±45, 0] _s , [0, ±60, 0] _s , [±45] _s	MONO [LC] (+σ _h :±σ _a)	Linear CLT,FEA [UF:MXN,TW,HA,NA]
Dersine et al. (1990)	[155]	CF-EP [TR]	[15, 0, ±10, 0, -15] _s	MONO, CYCF [LC] (±σ _a :τ)	Non-linear AM [DI:TW]
Fujii and co-workers (1991-96)	[156,157, 190-193]	GF-PR [WHL]	[0, 90]	MONO, CYCF [LC] (+2σ _h :+1σ _a)	Non-linear AM [UF:TW]
Cazeneuve et al. (1992)	[194]	CF,AF-EP [WFW]	[90], [±55], [±70] [90, ±55, 90], [90, ±70, 90]	MONO [LC] (+σ _h :+σ _a ,τ)	Linear CLT,AM [DI:TH,TW,HA]
Mistry and co-workers (1992)	[195,196]	GF-EP [WFW]	[±55]	MONO [LC] (-σ _h : -σ _a)	Linear CLT,AM [UF:TH]
Norman and co-workers (1992)	[197]	CF-EP [TR]	[0, ±45, 90] _s	CYCF [LC] (+σ _a)	Non-linear AM [UF:OTHER]
Frost et al. (1994-95)	[198,199]	GF-EP [WFW]	[±55]	MONO, CYCF, STF [LC] (+2σ _h :+1σ _a)	Linear CLT,FEA [DI:OTHER]

(continued)

Table 1.1: Summary of Biaxial Tests on Fiber Reinforced Polymeric Tubular Specimens (continued)

Author	Refs	Material *	Lay-up Geometry	Loading †	Analysis Method/ Failure Criteria ‡
Perreux and co-workers (1994-98)	[131,133, 200-203]	GF-EP [WFW]	[±55] ₃	MONO,CYCF,STF,ENV [LC] (+σ _h ;+σ _a)	Linear FEM,AM [DI:MXS,MICRO]
Ellyin and co-workers (1995-98)	[204,205]	GF-EP [WFW]	[±55] ₁ , [±70,±45 ₂ , -70, 0, +45, ±45 ₄]	MONO,CYCF [LC] (+σ _h ;±σ _a)	
Ishai and co-workers (1995)	[206-207]	CF,GF-EP [WFW]	[±θ], [90, ±θ ₂ , 90]	MONO [LC] (0;±σ _a)	Non-linear CLT [DI,UF:TW]
Swanson and co-workers (1995-96)	[208,209]	CF-EP [BR]	[±θ]	MONO [LC] (+σ _h ;+σ _a)	Linear CLT,AM [UF:MXN]
Zocher et al. (1995)	[11]	CF-EP [WFW]	[±1.5, ±45, ±89] ₇	MONO [LC] (+σ _h ;±σ _a ;τ)	Linear FEA [UF:MXS,MXN, TH,TW,OTHER]
Gargiulo et al. (1996)	[158]	CF-EP [WFW]	[±35 ₂] ₁ , [±45 ₂] ₃ , [±75 ₂] ₃	MONO [LC] (±σ _h ;±σ _a)	Linear FEM,CLT [UF:MXS,TW,TH,OTHER]
Ghorbel and co-workers (1996)	[132,210]	GF-PR,VR [WFW]	[±55]	MONO,STF,ENV [LC] (+2σ _h ;+1σ _a)	Linear CLT [UF:NA,DM]

(continued)

Table 1.1: Summary of Biaxial Tests on Fiber Reinforced Polymeric Tubular Specimens (continued)

Author	Refs	Material *	Lay-up Geometry	Loading †	Analysis Method/ Failure Criteria ‡
Bai and co-workers (1997-98)	[45,211-213]	GF-EP [WFW]	$[\pm 55]_3$	MONO [LC,DC] ($+\sigma_h; +\sigma_a$)	Linear FEM, AM [DI;MXS,MICRO]
Wang et al. (1997)	[214]	GF-EP [WFW]	$[\pm 55]_2$, $[\pm(66)_2, (0)_3]$, $\pm(66)_3, (0)$	MONO, STF [LC] ($+\sigma_h; +\sigma_a$)	Non-linear [DI,UF;OTHER]

* [CF] carbon fiber, [GF] glass fiber, [AF] aramid fiber
[EP] epoxy, [PR] polyester, [VN] vinyl ester

[WFW] wet filament wound, [DFW] dry filament wound (towpregs), [TR] tape rolled (prepregs), [WHL] wet hand lay-up (woven mat fabric), [BR] braided

† [MONO] monotonic, [CYCF] cyclic fatigue, [STF] static fatigue, [ENV] environmental effects
[LC] load control, [DC] displacement control

Multiaxial Regimes: $[\pm\sigma_h]$ applied hoop stress (tensile and compressive), $[\pm\sigma_a]$ applied axial stress, $[\tau]$ applied shear stress
 $[\pm\epsilon_d]$ applied diametral strain, $[\pm\epsilon_o]$ applied axial strain, $[\gamma]$ applied shear strain

‡ [CLT] classical laminate theory, [FEM] finite element modelling, [AM] analytical modelling
[DI] damage initiation (first ply failure), [UF] ultimate failure

Failure Criteria: [MXS] max. stress, [MNS] max. strain, [TW] Tsai-Wu, [TH] Tsai-Hill, [HA] Hashin, [PU] Puck, [DM] Damage Mechanics, [NA] Netting Analysis

Soden and co-workers performed a much more extensive series of monotonic biaxial tests on filament wound glass-fiber composite pipe with epoxy [182] and polyester [168, 169] matrices. Both leakage and ultimate failure envelopes were determined in the entire tension-tension biaxial regime for $[\pm 45^\circ]$, $[\pm 55^\circ]$ and $[\pm 75^\circ]$ angle-ply geometries. In general, the relationship between leakage and ultimate failure stresses was seen to depend upon laminate geometry and applied biaxial loading ratio.

Carroll et al. [204] investigated the effect of loading rate on the leakage failure characteristics of $[\pm 55^\circ]$ filament wound, glass-fiber epoxy pipes. It was demonstrated that under the matrix dominated loading ratios, a prevalent rate effect was observed. The failure mode and damage accumulation exhibited by short and long-term tests were also found to be different.

In predicting the long-term performance of tubular products, it has been suggested by a number of authors [144, 159, 160, 166, 198, 233] that the monotonic stress or strain at the limit of linear elastic response may be used as a conservative estimate for the onset of leakage in composite tubulars both under monotonic and cyclic loading. In these studies, leakage was seen to occur after the observed kneepoint in the monotonic stress-strain curve. The exact relation between the leakage failure (monotonic and cyclic) and the departure from linearity, however, is not fully understood.

Mieras [160] found that the applied stress at the linear elastic limit was approximately 70 to 80% of the applied stress at weepage under monotonic loading for a variety of $[\pm 55^\circ]$ filament wound glass-fiber/epoxy pipes with different resin formulations. Using the same pipes, Mieras also showed that the linear elastic limit point corresponded to failure lives of 10^4 for tests conducted under cyclic loading. Spencer and Hull [166] found that the applied stress at the linear elastic limit was approximately 40% of the applied stress at weepage under monotonic loading for a number of angle-ply glass-fiber polyester resin pipes with different winding angles. Frost and Cervenka [198] showed that the linear elastic limit corresponded to a failure life in excess of 10^8 for cyclic tests on $[\pm 55^\circ]$ filament wound, glass-fiber epoxy pipes.

1.5 OVERVIEW OF THE CURRENT STUDY

It can be seen from the previous section, that investigations of biaxial leakage characteristics of composite tubular specimens under cyclic loading are virtually non-existent. This is surprising since the long-term cyclic behaviour represents the predominant loading case in actual tubular applications, and is important in determining long-term economic viability. Furthermore, actual loading conditions in pressurized fluid containment applications are typically multiaxial in nature.

The purpose of the current study, therefore, is to investigate the leakage behaviour of glass-fiber reinforced epoxy tubular specimens under biaxial monotonic and cyclic loading conditions. Two symmetric angle-ply geometries* were tested: a) $[\pm 45^\circ]_S$ and b) $[\pm 71^\circ]_S$. These lay-up geometries were selected since they are representative of sub-laminate groups currently found in commercial composite tubulars products. The $[\pm 71^\circ]_S$ geometry is representative of high angle groups used to sustain hoop dominated loads. The $[\pm 45^\circ]_S$ geometry, on the other hand, is used to provide strength under biaxial loading conditions. The $[\pm 45^\circ]_S$ lay-up is also unique since it has been shown to exhibit highly ductile behaviour [103, 178, 182, 234, 235].

The material system used in this study is 3M-1003 Scotchply E-glass fiber reinforced epoxy. This general purpose prepreg system has a long service history in a number of applications, and has been extensively investigated in a variety of studies [24, 25, 64, 66, 96, 236–242]. Elastic and failure properties for this material system are provided in chapter 7.

Since leakage failure only occurs under pressurized environments, tests were restricted to the tensile-tensile biaxial regime (see figure 2.1). Monotonic and cyclic tests were conducted for three biaxial loading ratios: a) pure hoop (1H:0A), b) pure axial (0H:1A), and c) the biaxial ratio determined by “netting analysis”. For angle-ply laminates ($\pm\theta$), the shape of the biaxial failure envelope in the tensile-tensile regime has been shown to be adequately represented by these three biaxial ratios [182]. *Netting analysis* assumes that the strength of the laminate is governed solely by the fibers (i.e. the contribution of the matrix is negligible), and, as such, the maximum load

*The actual designations for these 8 ply geometries are $[\pm 45^\circ]_S$ and $[\pm 71^\circ]_S$. For convenience, these will be written as $[\pm 45^\circ]_S$ and $[\pm 71^\circ]_S$.

carrying efficiency is assumed to occur for the biaxial stress ratio (i.e. $\sigma_h:\sigma_a$) defined by [19],

$$\frac{\sigma_h}{\sigma_a} = \tan^2 \theta$$

where, σ_h is the applied hoop stress, σ_a is the applied axial stress, and θ is the fiber angle orientation with respect to the axial direction (see figure 1.2). Although this is an enormous over-simplification, it is particularly useful for reducing the total number of tests required to define the trends in the failure envelopes. For the $[\pm 45^\circ]_S$ and $[\pm 71^\circ]_S$ geometries, the loading ratios based on netting analysis are (1H:1A) and (17H:2A), respectively.

In the following chapters, details of the experimental apparatus, results and analysis are provided. General testing methodologies used for tubular specimens are summarized in chapter 2, along with details of the specialized biaxial testing apparatus developed for this study. This biaxial testing machine, developed for use with tubular specimens, can impose a complex biaxial state of stress (or strain) through the application of internal pressure, external pressure, axial force, and torsion. Unique features for testing composite materials and leakage behaviour are discussed.

In chapter 3, the design and development of the tubular composite specimens are examined. Specimens are fabricated from prepreg tapes using a tube rolling method, in conjunction with an inflatable mandrel molding process. Design and fabrication aspects, including effects of processing variables and end connections, are reviewed. An unabridged description of the manufacturing method is provided in Appendix C.

Methods used to characterize leakage failure in composite tubular structures are examined in chapter 4. By using Darcy's Law for flow through a permeable medium, a relation which defines the fluid flow characteristics in a damaged composite tube is developed. Based on this relation, a new damage parameter (permeability) can be specified which defines functional failure for weepage type behaviour. The permeability can be calculated from the experimentally determined fluid loss (leakage) profiles. The utility of this parameter is that it is inherently independent of fluid type and specimen size.

In chapters 5 and 6, monotonic and cyclic test results are presented for the $[\pm 71^\circ]_S$ and $[\pm 45^\circ]_S$ tubular specimens. The experimental behaviour is compared to the linear elastic response predicted by classical laminate theory. Macroscopic failure modes,

leakage profiles and fatigue-life curves are given for each biaxial stress ratio tested. For the $[\pm 45^\circ]_S$ tubular specimens, damage accumulation is quantified by measuring the elastic stiffness reduction and cyclic creep strains. The monotonic failure stresses and the fatigue-life curves are used to generate biaxial failure envelopes. A predicted long-term failure envelope based on the monotonic stresses at the linear elastic limit is compared to the experimental results. A discussion regarding the observed behaviour is provided.

Finally, in chapter 7, failure analysis of the tubular specimens is performed using the finite element method in conjunction with the maximum strain failure criteria. For each test geometry and loading ratio, the failure mode, failure location and the applied stress at failure are predicted for initiation and through wall failure conditions. Comparisons are made to the experimental results from the previous chapters.

CHAPTER 2

Development of the Multiaxial Testing Facility

2.1 REVIEW OF TUBULAR TESTING APPARATUS

The general requirement of a biaxial testing apparatus is to impose a controlled biaxial stress or strain state in a material by applying boundary tractions and/or displacements to the test specimen. For tubular specimens, this can be achieved through the simultaneous application of axial force, differential pressure and/or torsion (see figure 1.2). Of these actuation methods, three main loading combinations are commonly found in the literature: a) axial force (tension-compression) and torsion, b) axial force and differential pressure (internal-external), and c) axial force, differential pressure, and torsion.

Axial-Torsion

Testing facilities which provide axial-torsion capabilities are most common, due to their relatively low cost and availability from commercial vendors. A biaxial state of stress or strain is generated by the simultaneous application of shear (torsion) and normal stresses (axial force) in the material element. Since the biaxial state is created by a superposition of shear and normal loading components, the direction of the principal stresses and strains will change as the biaxiality ratio changes. This may be insignificant for tests on isotropic materials, but may be limiting for materials with directional properties (anisotropic). The tube surface is readily accessible during testing which is extremely beneficial for investigating crack growth phenomena [243, 244] and high temperature material response under fatigue loading [245–247].

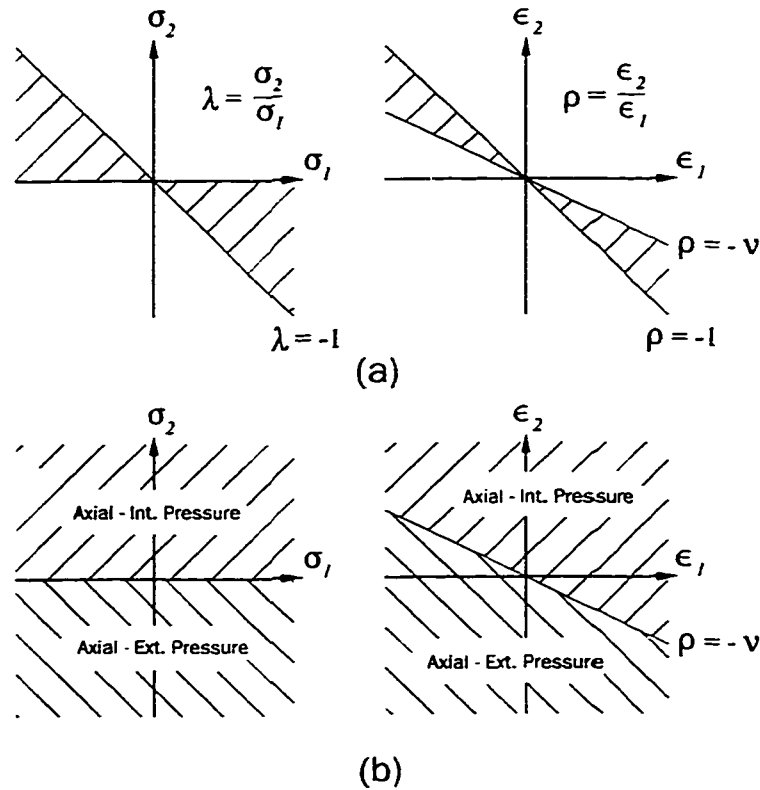


Figure 2.1: *In-plane biaxiality regimes in terms of the principal stress and strain for various applied loading configurations: (a) axial-torsion, and (b) axial-pressure, where ν is the Poisson ratio.*

The major disadvantage of axial-torsion testing is its limited range of attainable principal stress and strain ratios (see figure 2.1a). A thorough review of fatigue life investigations using axial-torsion fatigue is given by Kalluri and Bonacuse [248].

Axial-Differential Pressure

Differential pressurization of a thin-walled tubular specimen induces a circumferential and radial stress component in the test material. Because of the thin-walled geometry, the radial component is typically much smaller than the in-plane components and can be ignored. By independently varying the applied axial load and differential pressure, a biaxial state of stress or strain with any biaxiality ratio can be attained (see figure 2.1b). Since the applied loading is parallel and perpendicular to the specimen axis, the principal loading direction is fixed for all biaxiality ratios.

Axial-differential pressure testing apparatus are not common since they are typically more expensive to implement and require a controlled (safe) pressurized environment. Access to the specimen surface is not available during the test, and due to the pressurizing media, high temperature testing is difficult.

The use of thick-walled tubular specimens provides the ability to perform limited triaxial testing. The radial stress component is dependent on the specimen geometry and the applied pressure. The radial-to-circumferential loading ratios are fixed by the specimen wall thickness and diameter with the resulting states of stress being non-uniform.

Crack studies using internally pressurized tubular specimens can only be accomplished with the use of liners or pressure containment sleeves to bridge crack formation. The use of liners is a common practice in the testing of tubular specimens made of fiber-reinforced polymeric composites [182, 249]. These materials often possess brittle matrices which experience extensive cracking under multiaxial loading.

In biaxial testing machines with pressure capabilities, dependent and independent load control capabilities have been reported. Testing apparatus with dependent loading schemes have been built in which the axial force applied to the specimen is serviced by the same pressure source supplied internally or externally to the specimen [161, 182]. Though these systems are relatively simple to develop and require only one control system, the applied biaxiality ratio is fixed by the relation between specimen diameters and axial actuating piston sizes. Furthermore, high pressures, resulting in a significant out-of-plane stress component, may be required to achieve adequate axial forces.

Investigations using testing machines with strictly independent axial and differential pressure capabilities can be found in the literature [250–252].

Axial-Differential Pressure-Torsion

The combination of axial load, differential pressure, and torsion results in the most versatile testing apparatus for tubular specimens. This combination offers the advantages of the two previous loading schemes described. Due to the axial load and differential pressure, all principal stress or strain ratios are attainable (see figure 2.1b). Due to the addition of an applied shear component (torsion), the direction of the applied principal stresses and strains can now be varied. This is extremely advanta-



Figure 2.2: *View of the multi-axial testing machine.*

geous for testing of anisotropic materials where material properties are directionally dependent.

A large number of testing machines capable of axial, torsion and pressure loading have been reported in the literature [145, 148, 174, 226, 253–258]. These have been used to conduct studies on a wide range of metallic [253, 256, 257] and non-metallic [145, 148, 174, 226, 254, 255, 258] materials. Even though most testing machines reported have extended loading capabilities, very limited loading schemes have been implemented to date.

The development of a multi-axial testing machine with the capability of applying monotonic and cyclic axial load, differential pressure, and torsion to a tubular specimen under independent control is described in the remainder of this chapter.

2.2 APPARATUS DESCRIPTION

The rationale for developing the testing machine is to provide a precise, yet flexible environment to conduct complex multi-axial tests on tubular specimens. A photograph of the servo-hydraulic multi-axial testing machine, described herein, is shown in figure 2.2.

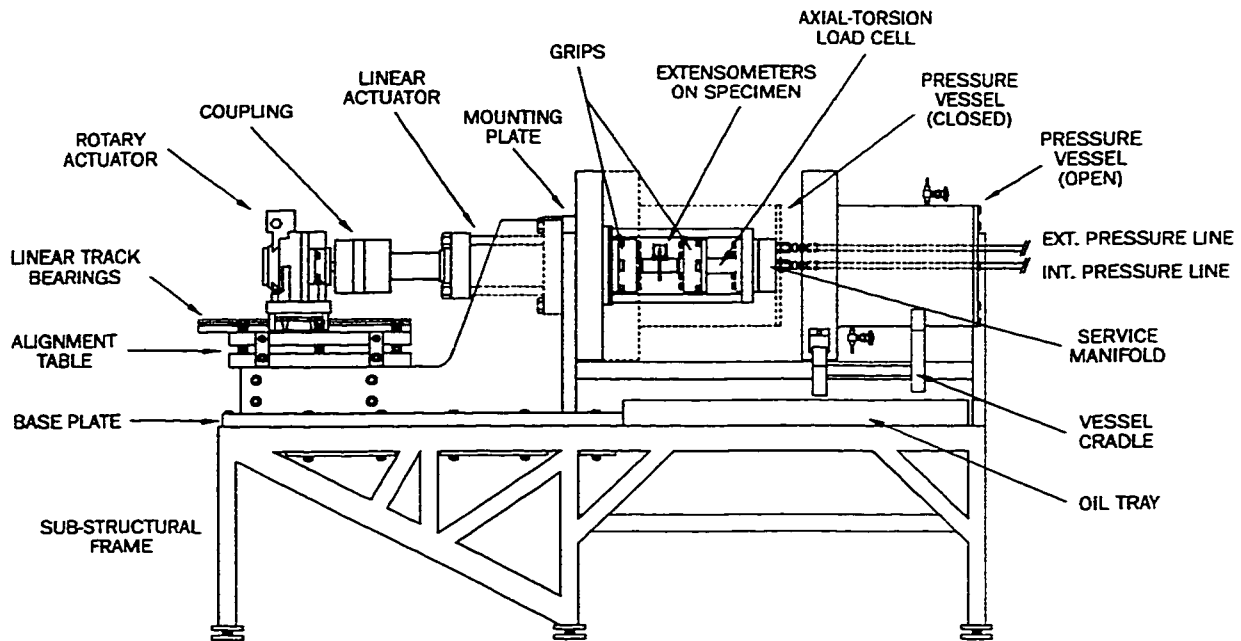


Figure 2.3: Description of the multi-axial testing machine components.

The main elements in the testing machine design are: 1) the structural components, 2) the servo-hydraulic system, 3) the feedback and control system, and 4) computer data acquisition and control. These elements will be described in the following sections.

2.2.1 Structural Components

Referring to figure 2.3, the testing machine structure is comprised of three sub-systems: 1) the load train, 2) external pressure containment, and 3) the support structure.

Load Train

The load train consists of a linear series of components whose purpose is to provide axial force and torque to the specimen while maintaining transverse constraint. It consists of the rotary and linear hydraulic actuators in series with the grips, the

specimen, and the load cell. The rotary actuator is connected to the linear actuator rod with a keyed compression coupling.

The actuated portion of the load train assembly is supported at two locations by separate bearing systems. At the entrance to the chamber, a bronze bushing bearing located in the mounting plate supports the actuator rod. At the other end, a pair of linear track bearings supports the rotary actuator assembly. Linear track bearings provide excellent lateral stiffness, good maintainability, easy installation and relatively low friction.

The grip assembly transfers axial and in-plane shear forces to the specimen without slippage, and supplies pressure to the interior of the specimen. The gripping system consists of two independent gripping units, one for each opposite end of the specimen. The units are identical except for the addition of a check valve mechanism in the grip attached to the load cell. This mechanism is required to facilitate internal pressurization of the specimen. Referring to figure 2.4, the gripping units consist of three parts: 1) the tapered collet, 2) the flanged hub, and 3) the pre-loading plug.

The purpose of the tapered collet is to provide the necessary clamping force to the specimen during testing. The flanged conical hub provides the restraining force necessary to activate the collet, and is used to locate and attach the grips to the testing machine. Matching pairs of the tapered collets and hubs were machined with the same tool set-up to ensure compatibility between the mating parts. The hubs can accommodate specimen end sizes up to 64 mm (2.5 in.) in diameter.

The purpose of the pre-load plug is to apply the necessary force to activate the collet, and to lock the collet into place. The pre-load plug consists of a cylindrical plug integrated onto a flat plate with extending teeth. These extending sections are used to bolt the plug to the flange hub. Torsional forces are transferred to the specimen by collet friction and by a key located in the plug.

Internal pressure is supplied to the specimen through a specially designed tube assembly. The tube assembly is inserted into the grip assembly through the center of the load cell, and is sealed and threaded externally to the vessel service manifold. Insertion of the tube into the grip cavity forces the check valve to open, resulting in direct and sealed pressurization of the inside of the specimen (see figure 2.4).

The test specimen is installed into the grips using a separate loading frame which provides for secure installation and removal without extraneous loading or damage.

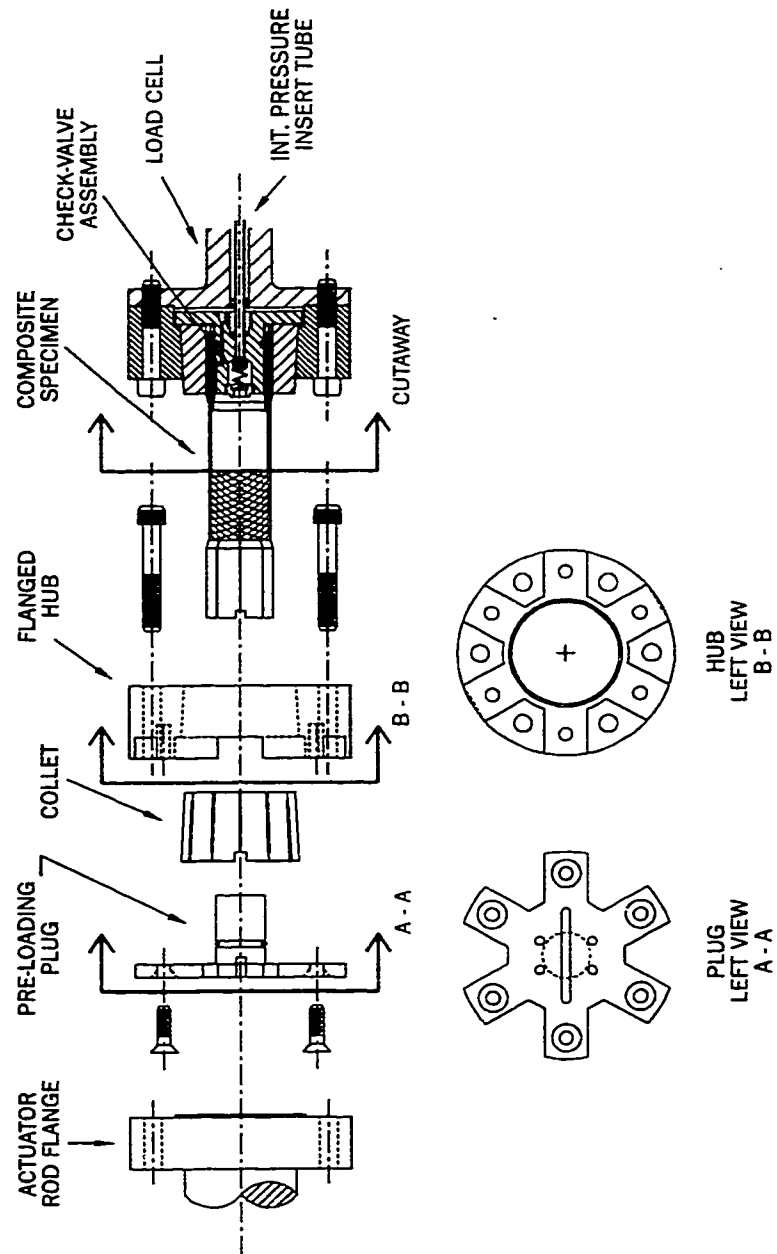


Figure 2.4: *Gripping system assembly.*

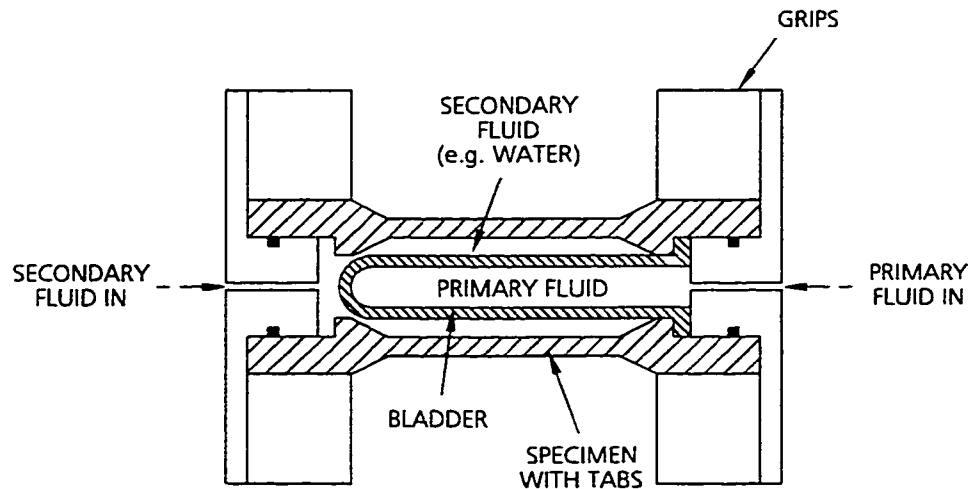


Figure 2.5: *Schematic of the bladder system for use in environmental studies.*

The grip collet is pre-loaded in order to prevent any slippage during the test. This is particularly important for fully reversed loading conditions (i.e. tension-compression). Since the specimen is mounted horizontally, the specimen-grip assembly must be filled with fluid and bled prior to mounting in the testing machine. Once the specimen and grips have been assembled and pre-loaded, the unit is mounted on locators in the testing machine and bolted into place.

For conducting experiments with various fluid environments, an expendable elastomeric bladder can be installed as shown in figure 2.5 (also see figure 3.3). The internal bladder acts to separate the hydraulic system (primary fluid system) from the testing fluid environment (secondary fluid). In addition to environmental testing, the bladder system can be used to investigate both leakage and ultimate failure characteristics using a single specimen.

External Pressure Containment

The pressure vessel provides three functions: 1) to contain the pressure applied externally to the specimen, 2) to provide a safety barrier for internal pressure tests, and 3) to provide stiffness for torsional loading. This thick-walled vessel is made from low-temperature A350-LF3 pressure vessel steel and was machined from a solid

forged piece so as to eliminate any welded joints in the vessel structure. The vessel has an inside diameter of 242 mm (9.5 in.) and a wall thickness of 57 mm (2.25 in.). Filling, bleeding, and draining of the approximately 13.0 L (790 in³) of fluid is done by manipulating two valves located at the top and bottom of the vessel.

The vessel is supported on a cradle to facilitate its opening and closing, providing access to the test area for installation, inspection, or removal of the specimen (see figure 2.3). The cradle houses two roller bearings and is mounted on two parallel guide rods. The vessel is sealed by two o-rings at both ends of the chamber and by a dynamic rod seal at the actuator rod opening. Rods extending from the pressure vessel flange provide support to the load cell when the vessel is opened. When closed, the vessel is attached to the main structure with two series of bolt circles at each end respectively. Pressure and transducer wiring is introduced into the system through specially sealed ports in the pressure vessel service manifold.

Support Structure

The purpose of the support structure is 1) to provide stiffness for all loading conditions, 2) to provide a location to house the actuator elements and support the containment chamber, and 3) to allow for alignment capabilities. As shown in figure 2.3, the testing machine is comprised of two structural systems a) the super-structure and b) the sub-structural frame.

The purpose of the super-structure is to provide a mounting frame, and a closed loop loading path for the linear and rotary actuators. The super-structure consists of a series of thick plates pinned and bolted together to form an extremely rigid box structure. Pinning and bolting was a necessary precaution to ensure that any future dis-assembly due to maintenance or modifications would not alter the alignment of the plates. The carbon-steel base plate and mounting plate were surface ground to a flatness of 0.05 mm over 2.0 m. They provide the necessary surfaces for proper mounting and alignment of subsequent components.

To ensure the linear bearing tracks run parallel to the load train, adjustment is provided by the alignment table unit. The alignment table consists of two plates separated by 8 standing bolt assemblies (see figure 2.3). The standing bolt assemblies each consist of two concentric bolt elements. The outer bolts are threaded through the top plate and sit atop the bottom plate inside a countersunk hole. These outer

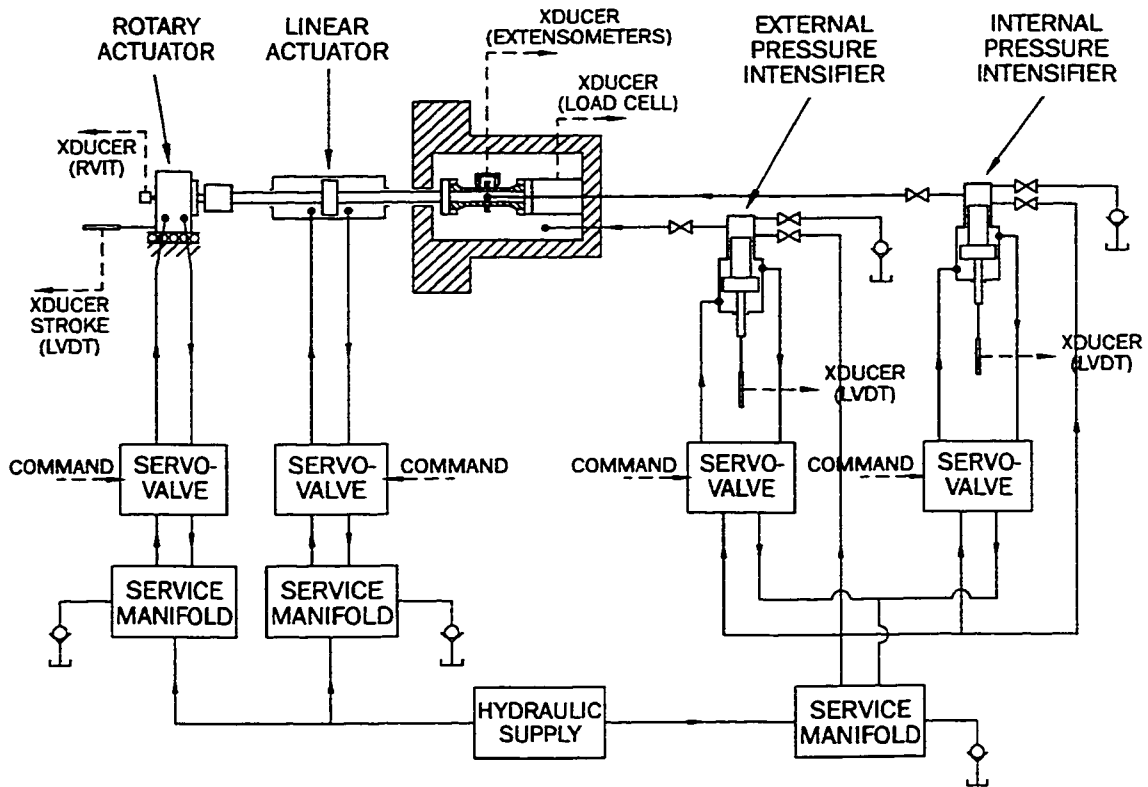


Figure 2.6: Block diagram of the servo-hydraulic system.

bolts are used to adjust the relative spacing between the plates. The inner bolts are threaded into the bottom plate and are used to rigidly clamp the outer bolts into place once final alignment has been achieved. By adjusting the standing bolts, vertical translation and small rotations in three planes can be achieved. The final alignment of the load train was verified using a flanged strain gaged specimen in a procedure outlined by Baten, et al. [259]. From this procedure, it was determined that the calculated bending strains in the specimen due to misalignment of the load train were small and can be neglected.

2.2.2 Servo-hydraulic System

A block diagram of the servo-hydraulic system is shown in figure 2.6. Loads to the specimen are provided by four independent hydraulic components: 1) linear actuator (axial force), 2) rotary actuator (torsion), 3) internal pressure intensifier and 4) external pressure intensifier.

The axial force is provided by a double rod, double acting linear actuator with a rated static capacity of ± 267 kN (± 60000 lbf) and stroke of 165 mm (6.5 in.). Torsion is provided by a double vane rotary actuator with a rated static capacity of ± 2780 N.m (± 24700 lbf.in.) and a rotational capability of $\pm 55^\circ$.

Internal and external pressure is provided by a 4:1 and 2:1 double acting pressure intensifier with a rated output pressure of 82.7 MPa (12000 psi) and 41.4 MPa (6000 psi), respectively. The secondary fluid volume of both intensifiers is 170 mL (10.2 in³). Fluid is ported from both units to the pressure vessel manifold through high pressure flexible hoses. This allows for easy connection and disconnection of the pressure systems when the chamber is being opened and closed. Each line contains a shut-off valve to isolate the specimen during charging of the intensifiers, preventing inadvertent damage to the specimen. The secondaries of both intensifiers have valved send and return lines which allow for manual charging. Both intensifiers were constructed with a rod extending from the primary cylinder in order to measure intensifier stroke (i.e. volume).

The hydraulic system is serviced by an MTS 506.02 power supply unit. This skid mounted unit contains a fixed displacement pump with constant pressure and flow control components. The hydraulic power unit supplies a constant flow rate of 22.7 L/min (6 gal/min) at a pressure of 20.7 MPa (3000 psi).

Fluid is ported from the power unit through a shut-off manifold to the service manifolds of each independent servo-hydraulic system. The purpose of the service manifolds is to provide controlled pressure application upon start-up, independent low-high pressure switching, and independent on-off flow switching. Controlled pressure application upon start-up ensures that the actuators are under control during initialization and prevents inadvertent damage to the specimen from instantaneous pressure overloading.

The service manifolds supply fluid to the actuating components via four electro-hydraulic servo-valves. The servo-valves have a full-flow rating of 9.5 L/min (2.5 gal/min) at a pressure drop of 6.9 MPa (1000 psi). The servo-valves regulate flow to the actuating components, and are controlled by command signal inputs from the control system.

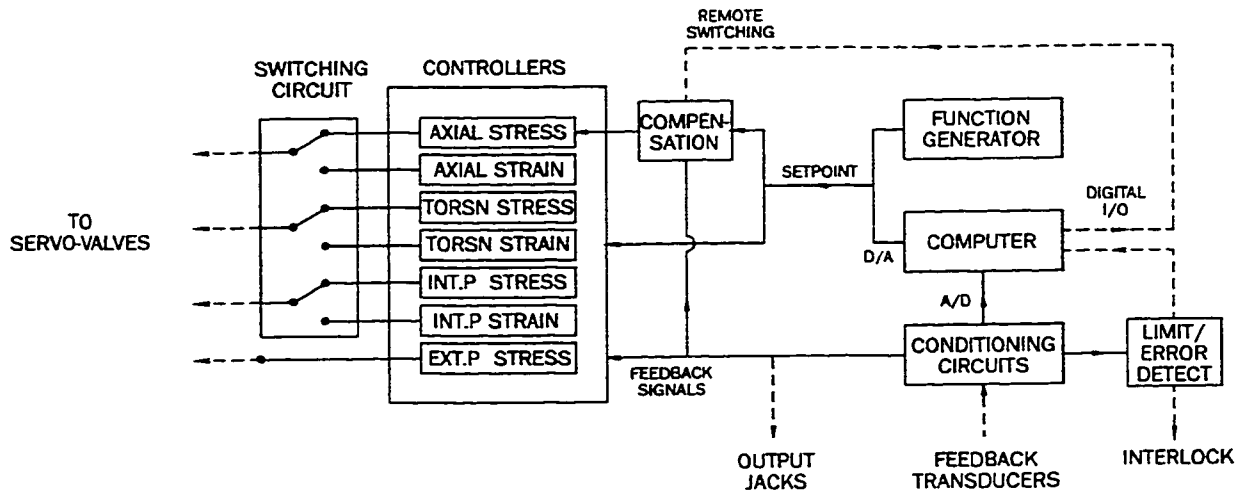


Figure 2.7: Block diagram of the feedback and control system.

2.2.3 Feedback and Control System

A block diagram of the feedback and control system is shown in figure 2.7. Control of the hydraulic systems is provided by seven P.I.D. analog controller modules and their associated hardware. The control modules are responsible for providing stable response based on the given feedback signal (transducer measurement) and required command signal (function generator or computer). Two control modes (stress and strain control) are available for each of the axial, torsion and internal pressure systems. Cyclic tests requiring negative hoop stresses or strains are achieved by superimposing a static external pressure with a cyclic internal pressure. All controller modules are housed in the MTS 458.10 control console which provides interlock and emergency on/off switching for all controller modules, and low/high pressure switching for the linear actuator.

A switching circuit was developed to prevent uncontrolled switching between stress and strain control modes. The circuit will only allow mode switching when the command and feedback signals from the stress and strain controllers are within a finite bandwidth.

For tests with internal or external pressurization and under axial stress control, an active compensation circuit provides real-time axial load compensation based on the applied pressure feedback signals. Compensation factors are determined by the specimen inside and outside diameters, and are set on the circuit control panel. Passive compensation methods, whereby an in-line actuator with interchangeable pistons of fixed diameters is used to produce a counteracting axial force, have been reported [258]. The major disadvantage of this method is the uncertainty in the resulting frictional force in the compensating piston.

The average applied stresses can be determined from the measured pressure, axial force, or torque, as follows:

$$\text{for hoop stress, } \sigma_h = \frac{P_i d_m}{d_o - d_i} \quad (2.1)$$

$$\text{for axial stress, } \sigma_a = \frac{4F}{\pi (d_o^2 - d_i^2)} + \frac{\pi P_i d_i^2}{4} \quad (2.2)$$

and

$$\text{for shear stress, } \tau_{ha} = \frac{16T d_o}{\pi (d_o^4 - d_i^4)} \quad (2.3)$$

where, P_i is the internal pressure, F is the axial force, T is the torque, d_m is the mean specimen diameter, d_o is the outside specimen diameter, and d_i is the inside specimen diameter. The far right term in equation 2.2 represents the axial force resultant due to internal pressure which is not directly measured by the load cell.

Feedback is provided by an extensive array of displacement and force measuring transducers. Low frequency operational characteristics of these transducers are shown in table 2.1.

As shown in figure 2.8, separate clip gage extensometers are used for the measurement of diametral and axial strains. The light-weight extensometers are attached directly to the specimen with knife edges (axial) or pins (diametral), and are held on the specimen with a set of springs. Mounting of the extensometers is coordinated by the computer data acquisition and control software, which ensures accurate determination of the mounted gage lengths after extensometer initialization with gage blocks. The knife edges are typically bonded to the surface of the specimen to prevent slippage at the point of attachment. Torsional strains are currently being measured

Table 2.1: *Operational characteristics of feedback transducers.*

Transducer	Operating Range	Calibration Constant	Linearity (%) [*]	Hysteresis (%) [*]	Precision (%) [†]
Axial Extensometer	±10% (25 mm GL [‡])	1.00% ϵ/V	0.15	0.18	0.29
Diametral Extensometer	±10% (41 mm GL [‡])	1.00% ϵ/V	0.21	0.16	0.22
Load Cell (Axial)	±267 kN	26.6 kN/V	0.10	0.08	0.18
Load Cell (Torsional)	±1125 N.m	112.5 N.m/V	0.13	0.14	0.21
Int. Pressure Transducer	0-68.9 MPa	6889 kPa/V	0.10	0.13	0.20
Ext. Pressure Transducer	0-34.5 MPa	3442 kPa/V	0.07	0.06	0.09
Axial Stroke (LDVT [§])	0-101.6 mm	5.06 mm/V	0.18	0.18	0.22
Intensifier Stroke (LDVT [§])	0-152.4 mm	7.46 mm/V	0.10	0.12	0.14
Torsional Rotation (RVIT [¶])	±50°	5.00°/V	0.12	0.13	0.15

^{*}Based on percent of full scale output.

[†]Based on percent of full scale output at 99.7% confidence.

[‡]Gage Length.

[§]Linear variable differential transformer.

[¶]Rotary variable induction transformer.

using either strain gages mounted to the specimen, or are derived from the actuator rotation (i.e. RVIT). Fabrication drawings of the extensometers are provided in Appendix A.

The use of independent extensometers has two distinct advantages: 1) independent extensometers in various combinations can be used to achieve maximum resolution in each particular loading direction, and 2) independent extensometers can be easily designed to eliminate cross-talk response due to loads in opposite directions. These features are particularly useful for testing fiber reinforced composite materials where the strain response of the material is directionally dependent. For these materials, the strain difference between loading axes can often be an order of magnitude or greater.

The output from strain gages bonded to the specimen and extensometers are affected by external pressurization. Since the differential pressure on the specimen

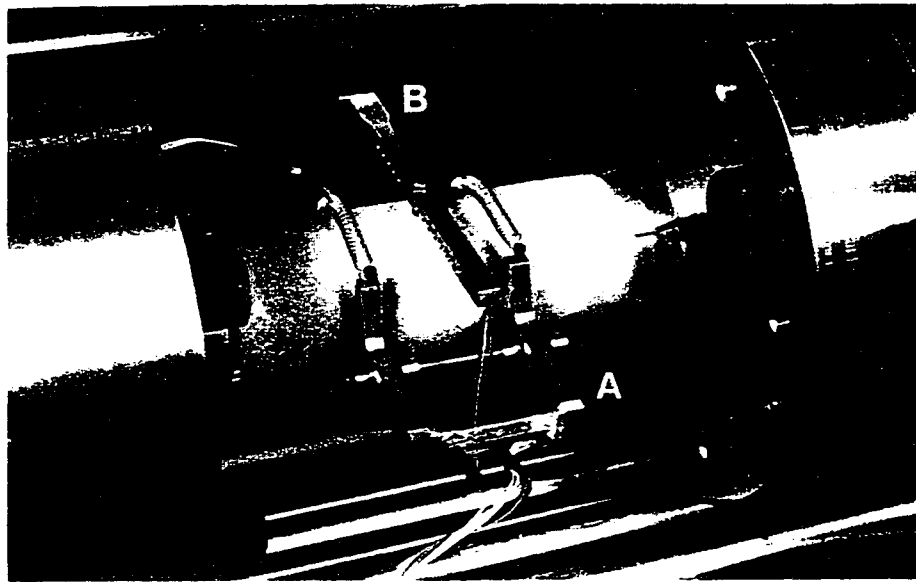


Figure 2.8: *Mounted clip gage extensometers. (a) axial and (b) diametral.*

wall is typically generated by fluctuating the internal pressure while maintaining a constant external pressure, the resulting strain gage error due to external hydrostatic pressure can be compensated through calibration or empirical relations provided by the strain gage manufacturer.

Displacement limit detect circuits are available for the axial stroke linear variable differential transformer (LVDT) and the internal pressure intensifier LVDT. These can be set to generate an interlock (manual) or to generate a signal for use by the computer control system. Limit detection of the pressure intensifiers is critical for long-term tests where leakage or weepage of hydraulic fluid may fully discharge the intensifier secondary.

The testing machine can be operated manually, or with the assistance of the computer data acquisition and control system (described in the next section). For manual operation, external function generators are used to generate a cyclic or monotonic command signal. The front control panel allows the setting of command mean, span, and error detect levels for each system independently. Auxiliary requirements such as axial load compensation, control mode switching, and error/limit detect are available to the user.

2.2.4 Computer Data Acquisition and Control

The enhanced testing capabilities of the testing machine are primarily due to the computer control hardware and software. For biaxial testing, computer assisted operation provides extensive supervisory control, complex function generation and enhanced data acquisition capabilities. Due to the extensive amount of data sampled and the complexity of control requirements, coordination of activities can only be performed in this manner.

The computer hardware consists of a 80486/33 PC with two peripheral cards for analog-to-digital (A/D) data acquisition (16 channels), and digital-to-analog (D/A) command signal generation (4 channels). The A/D and D/A cards are interfaced to the transducer conditioning circuits and analog controllers, as shown in figure 2.7. In order to efficiently sample all transducer channels, an A/D card with burst mode acquisition and Direct Memory Access (DMA) capabilities was chosen. This provides for high speed acquisition rates of up to 100 kHz.

The data acquisition and control software (MTM30.EXE) is used to initiate and execute cyclic/monotonic, in-phase/out-of-phase, proportional/non-proportional tests for fixed biaxiality ratios or for independent control of each hydraulic system. A wide range of flexibility is provided to the user in terms of test set-up, data sampling, control features, and test monitoring. The software provides seven main services: 1) function generation (command signals), 2) data acquisition (feedback signals), 3) system failure detection (limit error or interlock), 4) controlled system start-up and shut-down, 5) input data validation and conversion, 6) an interactive user interface for command specifications (start, stop, initialization, etc.), and 7) output data management (on-line graphics and output data storage).

Referring to figure 2.9, operation of the data acquisition and control software is quite complex. The software was programmed in 'C' in order to improve execution speed and provide low-level programming functions. Test and system control parameters are input as a set of ASCII textfiles, which are described as follows:

1. *test datafile* - This file specifies all the required parameters for monotonic and cyclic testing, including: a) specimen information and dimensions, b) general test parameters (initialization ramp rates, hold period status and sample trigger levels), c) controller status (load/displacement and span setting), d) cyclic

test data (cyclic frequency, waveform type, samples per cycle, data buffer sizes and automatic set-point adjustment), e) monotonic test data (step frequency, sampling frequency and data buffer sizes), f) sequence filenames, and g) loading parameters for pressure, axial and torsion controllers (mean, amplitude, phase angle, and/or ramp rates).

2. *sequence files* - These files are responsible for triggering various events during a test at user defined cycle numbers (cyclic tests) or times (monotonic tests). The following events can be instigated using these files: a) test stoppage, b) write current cycle to buffer, c) purge buffers to disk, d) external hardware triggering (8 bit word), e) automatic waveform (set-point) adjustment, and f) initiate monotonic ramps (for stiffness measurements).
3. *calibration datafile* - This file provides the software with transducer calibration constants, fluid system parameters and load train compliances (for deriving specimen displacements from load train stroke or rotation).
4. *graphics datafile* - This file controls the screen graph parameters including axis data type, axis limits and update status.

Test execution is handled by a set of interrupt based routines which provide precise timing for output waveform generation and data-acquisition. The interrupt routine is triggered by a variable frequency timer circuit located on the A/D card. When a trigger is given, program execution in the foreground loop is temporarily halted and handed over to the interrupt routine. At these regular intervals, the interrupt routine is called into service in order to provide error and interlock checking, command signal output and data acquisition. In the foreground loop, functions which are less timing critical are performed.

Two output data buffering schemes are used: a) a sequential buffer, and b) a circular buffer. The sequential buffer provides storage space for transducer data at pre-determined intervals. Data from this buffer is regularly written to disk, minimizing the chance of lost data due to power failure. Since the exact point of failure is not known, a priori, data just prior to stoppage of the test can be saved using the circular buffer. This buffer continually stores data from the latest available cycles or steps, and its size (i.e. number of cycles or steps) is defined by the user.

The output files contain all relevant input data and transducer output from a given test. Transducer data is stored in its native hexadecimal format to increase writing speed and save file memory. Since massive output files are often generated

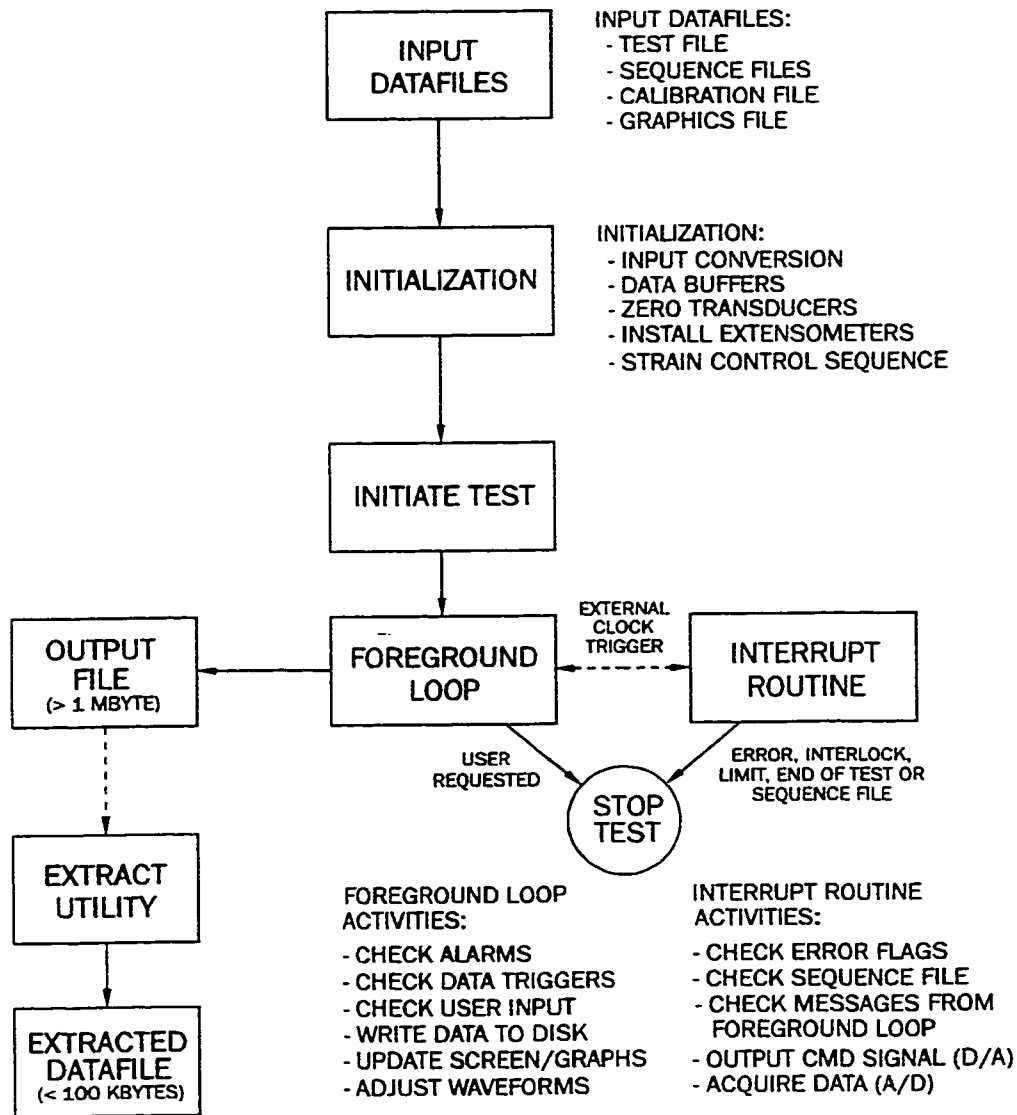


Figure 2.9: Simplified flowchart of the multi-axial testing machine acquisition and control software operation.

during testing, an extraction utility program (EXTRA30.EXE) was developed to manage and selectively extract limited data sets for further analysis. In this program, the user can selectively choose the appropriate data type, output columns required, cycle numbers, and output units using an input configuration datafile. Elementary statistical functions (e.g. mean, maximum, minimum, linear regression), hysteresis loop generation, units conversion, and calculation of permeability profiles are available. A sample of all datafiles and associated indexes are provided in Appendix B.

The data-acquisition and control software has two specific features for composite materials testing: a) elastic stiffness measurement capabilities during cyclic tests, and b) automatic adjustment of command signal waveforms (automatic set-point adjust). The elastic stiffness reduction is an important parameter for characterizing damage in composite materials. The testing machine software provides the ability to measure this parameter by performing a series of monotonic ramps at regular intervals during cyclic tests. Hold periods can be specified before the execution of each ramp in order to eliminate visco-elastic relaxation effects. Independent biaxial loading ratios, ramp rates and maximum load limits can be specified for each series of monotonic ramps.

Automatic waveform adjustment is necessary for performing biaxial cyclic tests on composite specimens using analog control systems. Composites often exhibit a significant decrease in elastic modulus during cyclic testing, resulting in increased actuator displacements. This can result in command signal phase shifts and loss of amplitude as the test progresses. Phase shift between loading axis is particularly troublesome due to the general path dependency of anisotropic materials. In order to alleviate this problem, the software is equipped with an algorithm which monitors the feedback signals, and makes the necessary phase and amplitude adjustments to the output waveform.

CHAPTER 3

Tubular Specimen Design and Manufacturing Methodology

3.1 DESIGN OBJECTIVES

Proper design and repeatable manufacturing techniques for composite test specimens are important to ensure valid results with reduced experimental scatter. A specimen fabrication method suitable for laboratory use should encompass the following requirements: 1) the specimen should be relatively easy and inexpensive to manufacture, 2) the method should allow for a wide variation in specimen geometries (lay-up sequence, fiber orientations, and end grip transitions) and material systems, and 3) the specimen should provide a representative material/structural unit based on the test objectives. For a particular application, the specimen should be fabricated so that it represents the inherent material quality with all salient features of the in-situ material system (including representative defects).

The influence of manufacturing anomalies on the resulting mechanical properties was examined in chapter 1. Based on these effects, the following general objectives for achieving quality specimens made from composite materials can be summarized:

- reduction of microstructural anomalies (fiber clustering/bridging, matrix rich areas, and voids)
- reduction of macrostructural anomalies (fiber waviness, surface crevasses and dimensional inaccuracies)
- proper matrix consolidation and degree of cure

- reduction of thermal residual stress gradients
- repeatable fiber/resin ratio and part dimensions

The curing process governs the thermal and consolidation aspects of specimen quality including degree of cure, fiber/resin ratio, void content and thermal residual stresses. The overall degree of cure in the part (i.e. the amount of fully cross-linked polymer) is dictated by the time and temperature to which the part is subject. Full cure is typically assured by following the manufacturers' recommended post-cure procedures. The reduction of thermal residual stress gradients can be accomplished by ensuring a uniform temperature distribution during the cure process. Repeatable part sizes and fiber/resin ratios can be achieved by using automated processing techniques, precision tooling components (templates, mandrels and molds), and proper secondary tooling materials (release films, peel plies and bleeder cloth).

Part consolidation, fiber/resin ratio, and void content are governed by a) the magnitude and distribution of applied pressure during the cure cycle, b) the permeability of the mold system and consumables (bleeders and cloth layers), and c) the flow characteristics of the resin system. Insufficient pressure during the cure cycle can result in poor matrix consolidation (particularly poor interlaminar adhesion) and high void content. Voids are formed in the resin by physical trapping of air during fabrication, and by the evolution of resin volatiles during cure. Applied pressure acts to collapse voids (in the case of physically trapped species), or prevent their formation (in the case of those formed by resin reactions).

3.2 SPECIMEN LOADING CONSIDERATIONS

An important consideration in the design of any tubular specimen is the effect of end connections. The end connections are responsible for transmitting the applied tractions or displacements from the testing machine to the gage section of the specimen. Due to the radially clamped end conditions imposed by most grip systems, significant bending stresses can be introduced into the specimen under applied pressure or axial loading. In most specimen designs, geometrical transitions are used to reduce the cross-sectional area from the grips to the gage section in order to: a) reduce the effect of end constraint on the measured response (St. Venant's effects), and

b) increase the probability of failure in the gage section.

In most metallic tubular specimens, precise geometries with complex profiles can be incorporated directly by machining operations [251,260]. For continuous fiber reinforced composites, however, fabrication of a specimen profile by machining is prohibitive due to the potential for fiber damage. As such, alternative methods have been used to create successful composite tubular designs. The most common method of creating a profile is by applying tapered reinforcement at the specimen ends. For filament wound specimens, tapered conical sections (in the form of steps) can be directly wound onto the ends during the fabrication process [261,262]. For straight tubular forms fabricated using other methods, profiles have been created by bonding or potting tapered conical joints to the ends of the specimen [200,249,262–264].

The main disadvantages with adding end reinforcement, however, are the increased fabrication costs and time. In addition, the inability to machine the profile directly, severely limits the ability to create complex transitional shapes. Fortunately, end reinforcement may not be necessary for the leakage testing of certain laminate geometries. Uniformly distributed leakage patterns have been observed for composite tubular specimens with unreinforced ends under a variety of loading conditions [160,166,167,198,204]. The effect of geometry and loading conditions on the leakage behaviour in tubular specimens without reinforced ends, however, has not been fully studied.

Methods of attaching the specimen to the testing machine must be also considered. Due to the variety of testing apparatus, a large number of unique specimen and grip designs have been reported in the literature. In all cases, axial loads are transferred to the specimen via shear, either through cylindrical clamps (friction), adhesively bonded tabs, integral conical wedges or collet gripping systems. Gripping methods using only friction [155] or adhesive bonding [249,263,265,266] have been found to be insufficient for applying large axial loads due to fiber pull-out from the ends. Using conical wedge [182,200,262,264] or collet [153,204] type gripping systems, axial load capabilities are increased since fiber pull-out is suppressed by large radial clamping forces.

In addition to restrictions imposed by the fabrication methods, the actual design of end geometries in fiber reinforced specimens is extremely difficult due to the effects of material anisotropy, multiplicity of failure modes, and the progressive nature

of damage. Most tubular specimen designs cited in the literature have been developed by iterative experimental testing due to a general lack of validated predictive methodologies.

3.3 SPECIMEN DESIGN AND ASSEMBLY

In the following sections, specimen designs and manufacturing methodologies developed during the course of this study are documented. The general method used to fabricate the specimens was the *tape rolling method*. In this method, prepreg tape is wrapped onto a cylindrical mandrel at specific fiber orientations to create a laminated tubular structure. Since the polymer phase in the prepreg material is only partially cross-linked, heat and pressure are required to consolidate and cure the part. In this study, all specimens were manufactured using the 3M type 1003 (Scotchply) E-glass fiber/epoxy unidirectional prepreg system.

The use of prepreg materials, in conjunction with the tape rolling method, have a number of advantages for small scale laboratory testing:

1. structures manufactured using prepreg based systems typically possess less microstructural variability throughout the part (i.e. fiber/resin ratio and void content),
2. specimens with a wide range of laminate geometries (fiber angle orientations and stacking sequences) and material systems can be manufactured in small runs without requiring costly filament winding facilities,
3. the manufacturing process is much cleaner and is relatively easy to master, and
4. prepreg systems can be used in fabrication of a wide range of specimen types (e.g. coupon, Iosepescu, cruciform) which allows for full property characterization of the material system, and comparative studies between specimen types.

As alluded to in the previous section, current fiber reinforced tubular specimen designs are developed, primarily, by experimental iteration. In this study, three generations of specimen/grip combinations were developed and tested: 1) specimens with integrated connections (threaded ends and conical wedges), 2) specimens with threaded bonded tabs (with internal potted wedges), and 3) specimens with bonded

tabs used in conjunction with a collet type gripping system. The last option was the one chosen for use in the testing phase of this study. In the following section, the first two specimen/grip designs are briefly outlined along with the problems encountered in their implementation. A detailed description of the manufacturing procedure, quality determination and experimental validation of the final design is provided in the remaining sections.

3.3.1 Initial Specimen Designs

The objective of the initial specimen design trials was to develop a specimen capable of resisting fiber pull-out in the grips under axial loading. This mode of failure severely limits the range of possible lay-up geometries which can be successfully tested, and has been a source of difficulty for a number of specimen designs cited in the literature [263,265]. This mode of failure is particularly troublesome for axial "fiber dominated" geometries (i.e. low fiber angles with respect to the axial direction). As such, a $[0^\circ]$ unidirectional tubular geometry was used in the trials since this was deemed to represent the worst case condition.

The first series of specimens investigated were ones in which end connections were directly integrated into the specimen geometry (i.e. all composite design). These specimens were manufactured by simply rolling prepreg material onto a 31.8 mm (1.25 in.) diameter split steel mandrel. The lay-up consisted of 4 layers of $[0^\circ]$ unidirectional prepreg for the main tube body followed by a build up of 20 layers of $[0^\circ]$ or $[90^\circ]$ prepreg strips at the ends. In order to provide a molded exterior surface, three sets of sectioned aluminum shells were placed on the outside of the specimen at the reduced gage section and at the built-up ends. To prevent mold seams along the length of the specimen, shim stock material was used to bridge the gap formed by the external shells. Hose clamps were used to hold the shells in place, and to provide some initial consolidating pressure. The specimens were then cured in an oven at $300^\circ F$ for 12 hours. After removal of the exterior shells and mandrel, the built-up specimen ends were machined to the required form.

Threaded and conical wedge end connections were both tested as shown in figure 3.1. Threaded ends were initially tested due to the availability of threaded mounts. Machining of the threads was found to be successful only for the $[90^\circ]$ built-up ends.

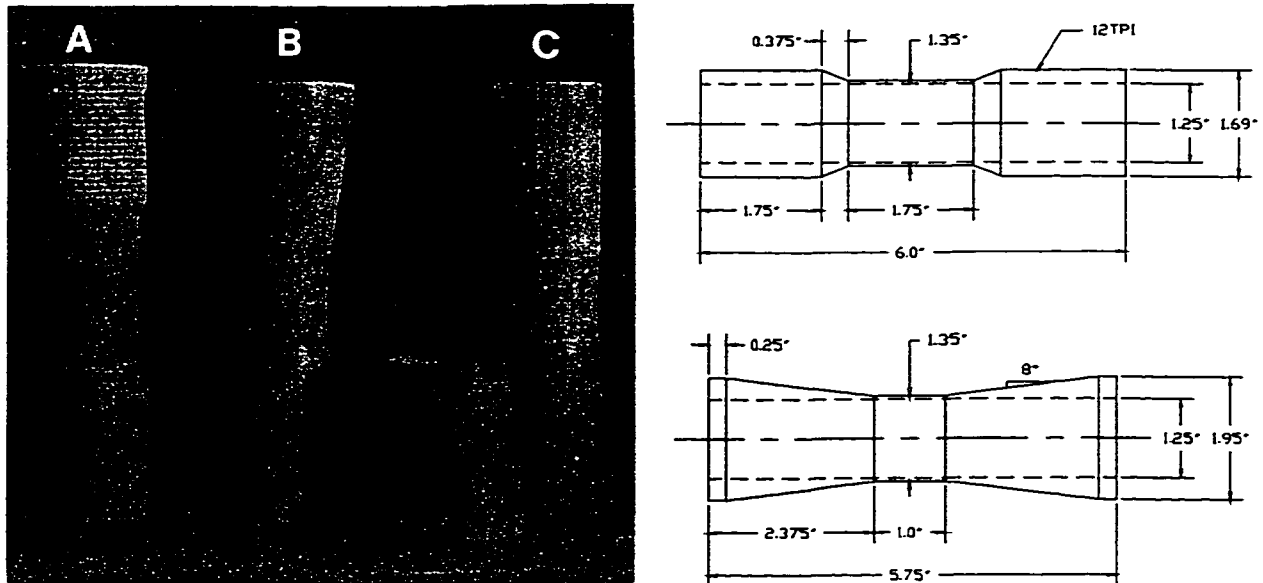


Figure 3.1: *Specimens with integrated connections; (left) (a) threaded end connections, (b) conical wedge end connections, (c) failure at conical wedge, (right) specimen dimensions.*

Due to the low transverse strength of the $[90^\circ]$ lay-up, however, failure occurred at the root of the threads when the specimen was placed under axial load. For the $[0^\circ]$ ends, the machining operation resulted in excessive fiber pull-out and surface damage (see figure 3.1a).

Due to the problems associated with integral threads, a conical wedge end connection based on the grip design by Highton and Soden [261] was investigated (refer to figure 3.1). Compared to the threaded design, a longer grip section was used in order to provide more shear transfer area at the ends. A matching flanged conical hub was used to attach the specimen to the testing machine. Although the tapered sections were easy to machine, it was difficult to prevent undercutting at the start of the gage section. As such, the entire surface of the gage section had to be machined to ensure a smooth geometrical transition. Under applied axial loading, these specimens failed by fiber pull-out in the taper as shown in figure 3.1c.

In order to eliminate the machining problems associated with the first series of specimens, a bonded aluminum connection was developed as shown in figure 3.2.

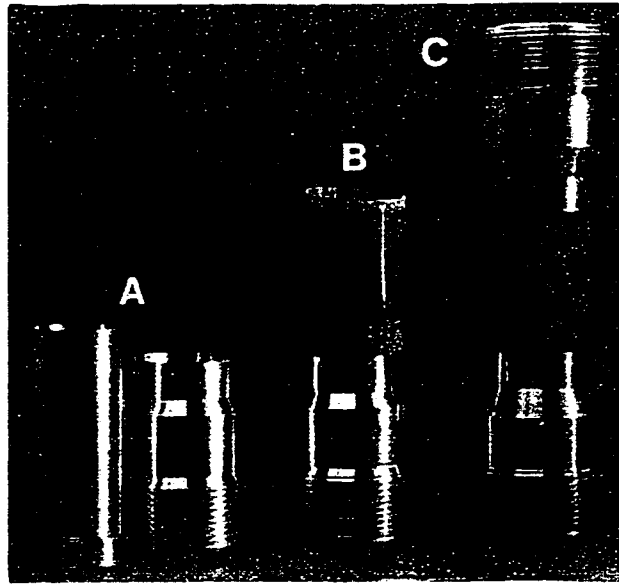


Figure 3.2: *Specimens with bonded aluminum threaded connections; (a) inner and outer tabs prior to assembly, (b) specimen failure by fiber pull-out, and (c) assembled specimen prior to testing.*

Combinations of the first two designs were subsequently incorporated. Internal wedges formed by the potting adhesive was intended to provide some radial clamping force on the tube during axial extension, while the threaded tabs allowed for easy specimen installation. This second generation of specimens proved to be much simpler to fabricate for two reasons: a) a straight tubular form was easier to mold than one with built-up ends, and b) the end connections could be manufactured using a CNC lathe. By using a “near-net” tubular shape, the possibility of fiber damage in the gage section due to machining was eliminated. Since this design was the prototype for the current specimen used in the testing phase of this study, details of the specimen assembly procedure are similar to that given in section 3.3.2.

Similar to the previous specimens tested, pull-out failure was seen to occur for all tests under axial loading. Tests were conducted for a number of epoxy adhesive systems and internal wedge profiles. Depending upon the surface preparation and adhesive system used, bond line failure was seen to occur either between the adhesive and tab, or between the adhesive and specimen.

The general problem with all the initial prototypes was the weakness of the various shear transfer mechanisms. Although successful application of similar designs have

been cited in the literature, most tests have been limited to laminates with matrix dominated or quasi-isotropic lay-ups (in the axial direction) [262,264,266]. For these laminates, judicious selection of an appropriate adhesive system and end geometry may be required for each laminate geometry tested.

In summary, a number of deficiencies with the initial prototypes were identified:

- Fiber pull-out (in various forms) was seen to occur for all prototypes tested. This is due to the general lack of radial (compressive) clamping force on the specimen.
- The void content in the gage section of all specimens was found to be quite high ($\sim 5-10\%$) (as determined by micrographic examination). This was attributed to insufficient consolidation pressure applied during the cure process.
- Dimensional inconsistencies and surface anomalies were also noted for most specimens due to the nature of the molding method.
- The inability to properly align the prepreg sheets during tube rolling operation resulted in observed gaps and overlaps at the termination points.
- While the specimens were relatively easy to install into the testing machine, they were difficult to remove after failure.

3.3.2 Current Specimen Design

The current tubular specimen design consists of a straight fiber reinforced composite tube with adhesively bonded aluminum end tabs, as shown in figure 3.3. This is a variation of the tabbed specimen described earlier. Instead of relying on adhesive bonding only, improved fiber constraint and axial load transfer at the ends is achieved by mechanical clamping using the collet type gripping system described in section 2.2.1.

Referring to the outline in figure 3.4, the specimen manufacturing procedure consists of three phases: a) composite tube fabrication, b) aluminum tab fabrication and assembly, and c) integration of the tube and tab components (an unabridged description of the procedure is provided in Appendix C).

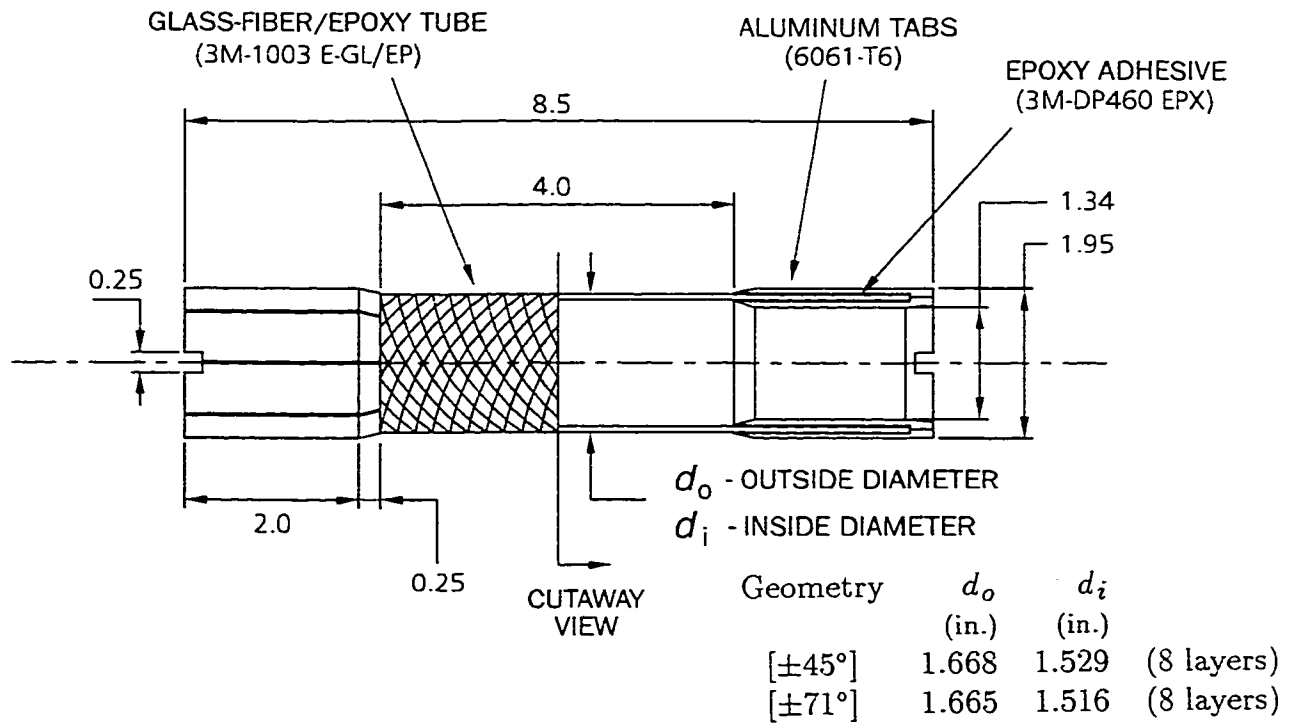
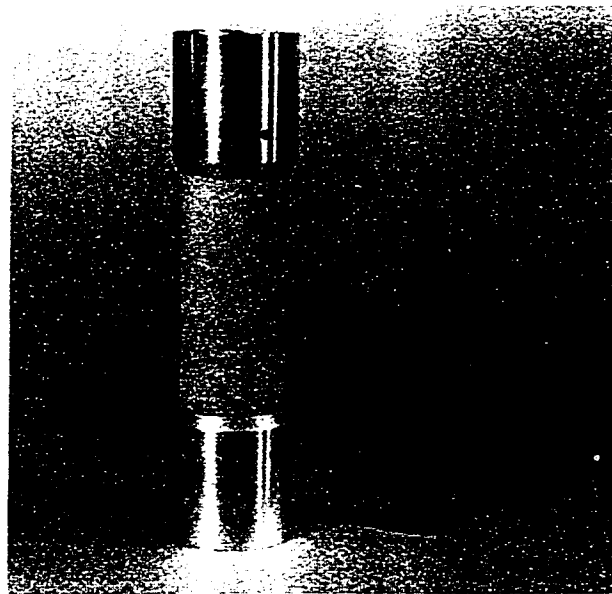


Figure 3.3: Current specimen design; (top) $[\pm 45^\circ]_S$ glass-fiber reinforced epoxy tubular specimen with optional internal bladder, (bottom) tubular specimen dimensions.

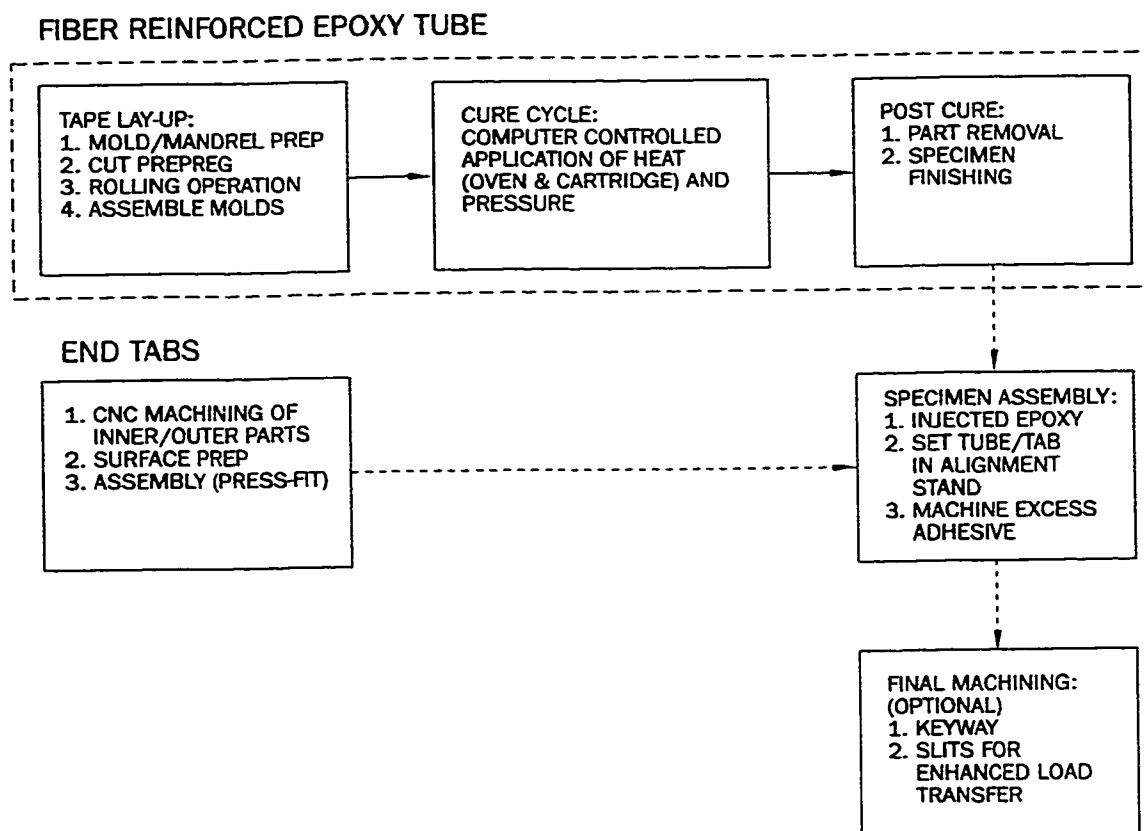


Figure 3.4: Summary of tubular specimen manufacturing procedure.

The composite tubular part is manufactured by rolling uni-directional prepreg tapes onto an inflatable mandrel using a specially designed rolling table. Varying lay-up angles for each successive layer are achieved by precise orientation of the prepreg tape pattern with respect to the mandrel rolling direction (see figure 3.5). Prepreg patterns are cut by hand from stock rolls using precision machined templates. Upon completion of the rolling procedure, the lay-up is placed in a two-part cylindrical (female) mold, and is consolidated and cured by computer controlled application of heat and pressure. Auxiliary release layers are used in the lay-up to ensure a good surface finish, and to facilitate easy part removal.

The aluminum tabs are manufactured in two annular sections on a CNC lathe which provides for precise and inexpensive production. After proper surface preparation, the inner and outer tab parts are press-fit together using a precision spacer to form an annular cavity for the encapsulation of the tube. For this specimen/grip

design, the aluminum tabs provide a number of important functions:

1. The tabs provide for a consistently precise and smooth internal and external surface for improved specimen alignment, accurate locating in the grips, and high pressure sealing. Seals mounted directly on composite surfaces have been found to be problematic due to inherent dimensional variability and surface irregularities.
2. By altering the tab diametral dimensions, a large range of tubular specimen diameters and wall thickness can be tested with the current system (for the given collet sizes available). This provides the flexibility to test or evaluate many specimen transition geometries without a complete re-design of the gripping system. Tubes manufactured by any method (e.g. filament winding or hand lay-up) can be tested with little modification.
3. The tabs provide an efficient and easy means of anchoring an internal specimen bladder used for testing ultimate failure properties under pressure loading, and for testing specimens under environmental conditions (see section 2.2.1).
4. Deformation in the tabs prevents damage to the specimen when the collet is contracted. For composite specimens mounted directly into collet type grips, extensive grip damage in the form of localized transverse cracking and delamination has been observed [267].
5. Keyways (or any other geometrical feature) can be machined into the tabs to improve the transfer of shear loads under applied torsion. Due to the poor machining characteristics of fiber reinforced composites, adding keyways directly to composite tubes is difficult.

For final specimen assembly, potting adhesive is injected into the tab cavity, and the fiber reinforced composite tube is forced into the tab annulus, fully displacing the potting material. Excess adhesive is removed, and the tab/tube configuration is placed in a concentric alignment stand until the potting adhesive is fully cured (see figure 3.6). When bonding is complete, keyways and longitudinal slits can be machined into the tabs to improve load transfer capabilities.

In order to test the effectiveness in preventing fiber pull-out, $[0^\circ]$ unidirectional specimens were tested under monotonic and cyclic loading. Referring to figure 3.7, it can be seen that the failure mode is uniformly distributed fiber fracture, and extensive matrix cracking along the fiber direction (brush type failure). In all tests, fiber



Figure 3.5: *Application of prepreg pattern onto mandrel using rolling table assembly.*

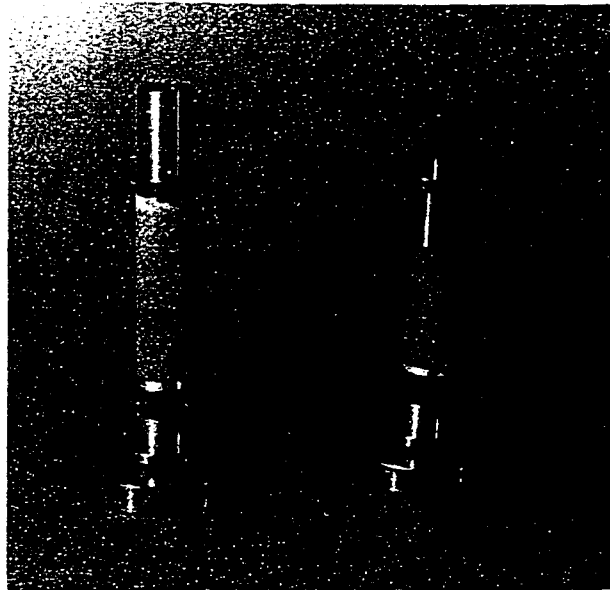


Figure 3.6: *Assembled specimen alignment stands; (left) first tab bonded, and (right) second tab bonded.*

pull-out was effectively suppressed. Compared to equivalent tests on coupon specimens [268], the resulting monotonic and low cycle failure strength for the tubular specimens is seen to be higher, most likely, due to improved quality control.

3.3.3 Aspects of the Tube Rolling Procedure

The tube rolling procedure represents the most critical step in the tube manufacturing process. This procedure is used to apply the required number of prepreg layers on to the mandrel, and apply compaction to the lay-up in order to eliminate trapped voids. The prepreg pattern is cut and oriented in such a way that, as it is wrapped around the mandrel, it forms a continuous surface of a particular fiber angle without gaps or over-laps (butt joined). Free fiber ends are located only at the specimen ends which are subsequently encapsulated by the end tab.

Since the outer diameter of the lay-up increases as successive layers are applied, each layer must be cut from templates of different sizes. Referring to figure 3.8, the geometry of each template is determined from the required fiber angle orientation, the current diameter of the lay-up, and the length of the specimen as follows:

$$D_i = D_{mandrel} + 2(i - 1) t_p,$$

$$h_i = \pi D_i \cos \theta_i,$$

$$l_{circ} = \pi D_i$$

and

$$l_{roll} = l_{spec} \tan \theta_i + l_{circ} \quad \text{for } i = 1 \text{ to } n \quad (3.1)$$

where, θ_i is the current fiber angle orientation with respect to the tube axis, D_i is the current lay-up diameter, $D_{mandrel}$ is the outside diameter of the mandrel, t_p is the prepreg thickness, h_i is the width of the current template, l_{circ} is the current circumference, l_{roll} is the required rolling length, l_{spec} is the specimen length, and n is the total number of layers.

The sizing of new templates is an iterative process. Based on measurements of the mandrel diameter and prepreg thickness, initial estimates of template dimensions can be determined using equations 3.1. During the rolling process, however, the in-situ

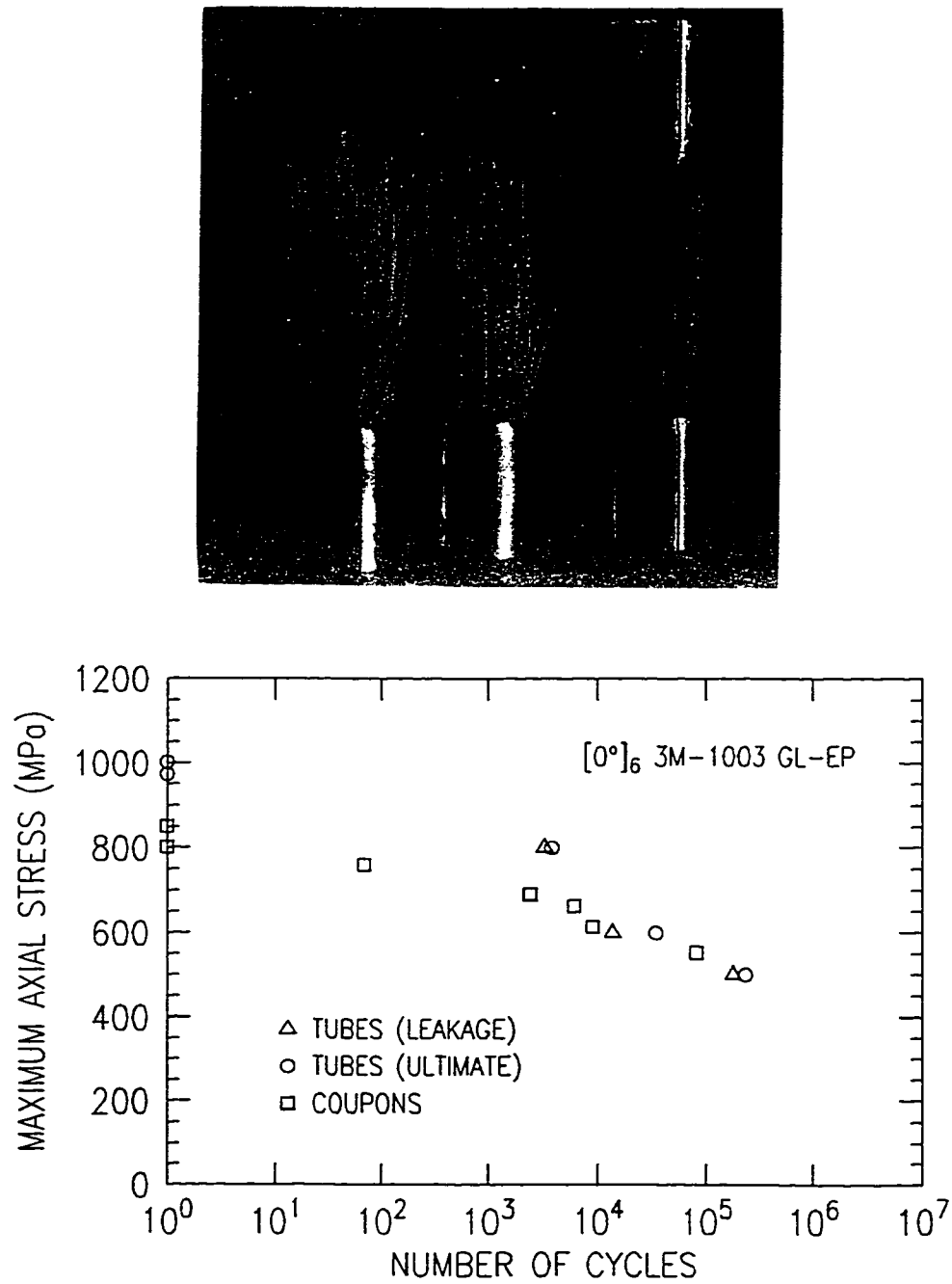


Figure 3.7: Failure of 0° unidirectional glass-fiber reinforced epoxy tubular specimens under monotonic and cyclic axial loading (collet gripping system); (top) macroscopic failure mode, and (bottom) fatigue-life curve.

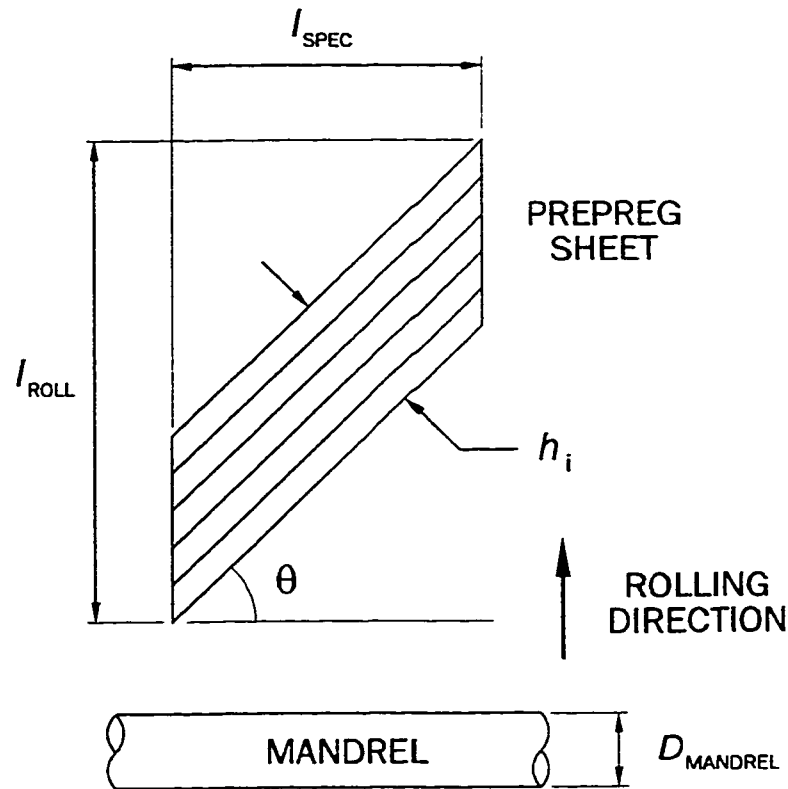


Figure 3.8: Prepreg pattern (template) geometry and applied orientation.

prepreg thickness (or total lay-up diameter) will vary due to the compaction characteristics of the particular material system and fiber angle orientation. By measuring the diameter of the lay-up and the gap (or overlap) as the layer is applied, the template widths can be corrected by re-machining (i.e. if a gap occurs, the template width must be increased; if an overlap occurs, the width must be decreased).

When compared to filament winding, the tape rolling procedure produces a laminate without fiber crossover or banding, and can be used to generate true fiber angle orientations between 0° and 75° . A disadvantage of the tube rolling method, however, is the inability to roll layers with high fiber angles ($> 75^\circ$) due to the long template lengths required. As the fiber angle or desired tube length increases, the length of the template increases. Hoop wound specimens [90°] cannot be achieved using this method without allowing for free fiber ends inside the specimen (which is not desirable).

One difficulty which has been observed during the rolling process is the tendency of *off-axis* prepreg layers to wrinkle out of plane when wrapped onto a small diam-

eter mandrel. This effect occurs due to the extension-bending coupling present in unidirectional off-axis lamina when deformed in a cylindrical manner. This wrinkling action severely distorts the lay-up, and prevents proper compaction and addition of further layers. In general, the prevention of out-of-plane wrinkling can be achieved by increasing the mandrel diameter, or by using material systems with smaller prepreg thicknesses. It is for this reason that the current specimen design uses a larger diameter mandrel (38.1 mm or 1.5 in.) than that of the prototypes discussed in section 3.3.1.

3.3.4 Computer Controlled Tubular Molding Techniques

A major objective in fabricating the composite tubular section is the ability to ensure proper cure and consolidation of the prepreg layers. In addressing this point, automation of the cure process was seen as an essential requirement. By automating the curing process, repeatable dimensional and microstructural characteristics (fiber/resin ratio and degree of cure) in the final parts can be achieved. Furthermore, automation allows for easy modification to cure cycle parameters and implementation of a wide number of resin systems.

The purpose of the curing process is to provide heat and pressure to the part in order to promote resin flow, inter-layer consolidation and final polymer cross-linking. The *cure cycle* is the programmed sequence of heating and pressure steps required to properly cure and consolidate the part. In comparison to flat laminates, the curing process for prepreg based tubular parts is much more arduous due to the difficulty in applying consolidation pressure to cylindrical geometries.

In this study, two automated processing systems were developed: a) *tubular molding press* and b) *inflatable mandrel system*.

Tubular Molding Press

The first system developed was the *tubular molding press* which is shown schematically in figure 3.9. This system is a self-contained unit which provides heat, mold pressure and vacuum to the tubular laminate. Heat is supplied by an electric heater cartridge inserted inside the mandrel unit. The temperature is measured using a thermocouple located within the mandrel, close to the surface of the part. A fixed consolidation pressure is applied externally to the composite lay-up using three pneumatic actuators

in conjunction with a set of split external shells. The temperature and pressure cycles are controlled by computer using specially designed control software (see below for description).

Although the tubular molding press was found to produce repeatable tubular dimensions, the external pressurization resulted in significant localized fiber wrinkling along the length of the part at the shell edges. The wrinkling phenomena occurs due to fiber buckling imposed by the lateral pressure during the polymer liquification phase of the cure cycle. The wrinkling anomaly was reduced by using various consumable layers, shim stock and shrink wrap materials, but could not be eliminated. The significance of this macroscopic defect was demonstrated during initial testing of tubular specimens under pressure loading. Leakage failure was seen to occur at the defect locations at very low loading levels. Ultimate (monotonic) failure strengths of $[\pm 45^\circ]_S$ specimens under pure hoop (1H:0A) biaxial loading were approximately half of those reported for specimens without this surface defect (see chapter 6).

Inflatable Mandrel System

In order to eliminate the problem of localized fiber wrinkling, a molding system using an *inflatable mandrel* was developed as shown in figure 3.10. The inflatable mandrel technique has been shown to have a number of advantages over other methods examined, including 1) superior dimensioning with minimal micro- and macroscopic anomalies, 2) simple and easily fabricated tooling, 3) the ability to fabricate multiple tubular parts simultaneously, and 5) uniform temperature distribution during cure. Although fabrication techniques using this method have been proposed in the literature [152, 269, 270], only cursory discussions of the methodology are typically given.

Uniformly distributed pressure is applied to the tubular part from the inside by inflating the air-tight membrane (bladder) on the mandrel. The resulting hoop expansion eliminates any possibility of fiber buckling. The external mold is sized so that a small gap exists between the lay-up and mold surface to allow for part expansion and fiber tensioning. The appropriate gap must be determined by iteration. An excessive gap between the part and mold will result in an irregular part surface due to excess resin build-up.

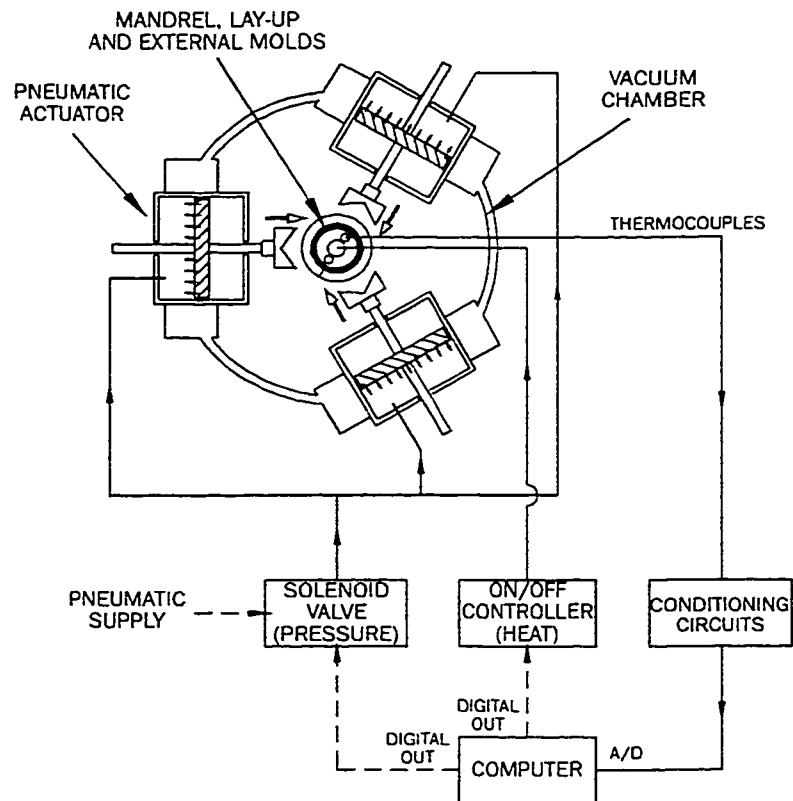


Figure 3.9: Schematic of the tubular molding press.

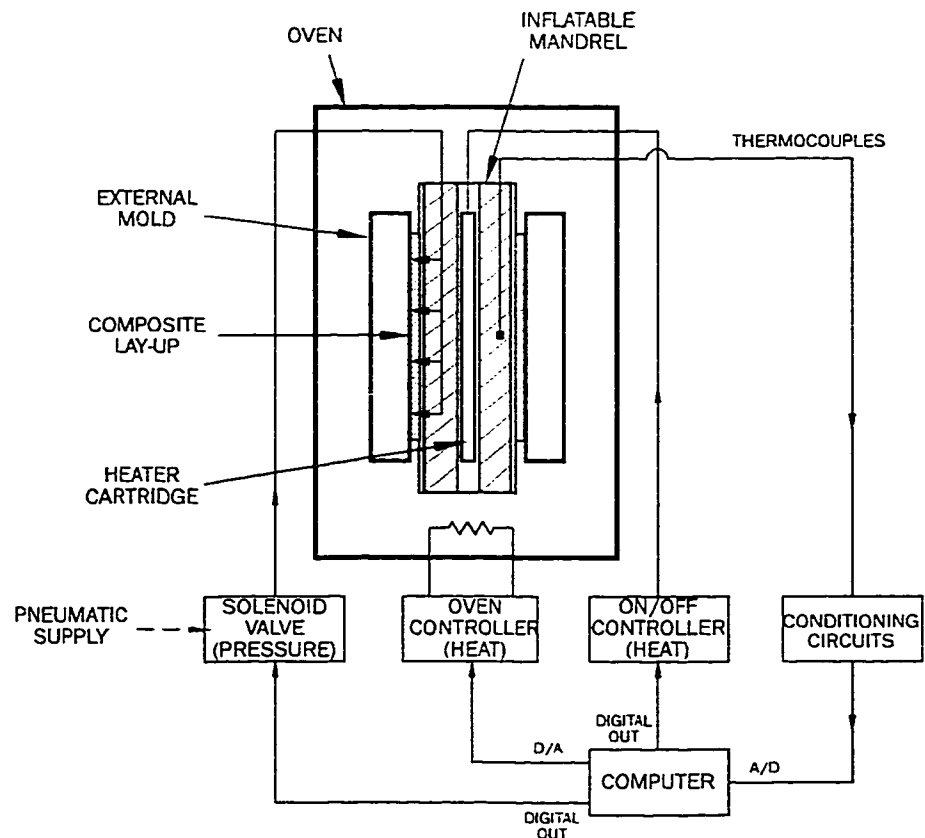
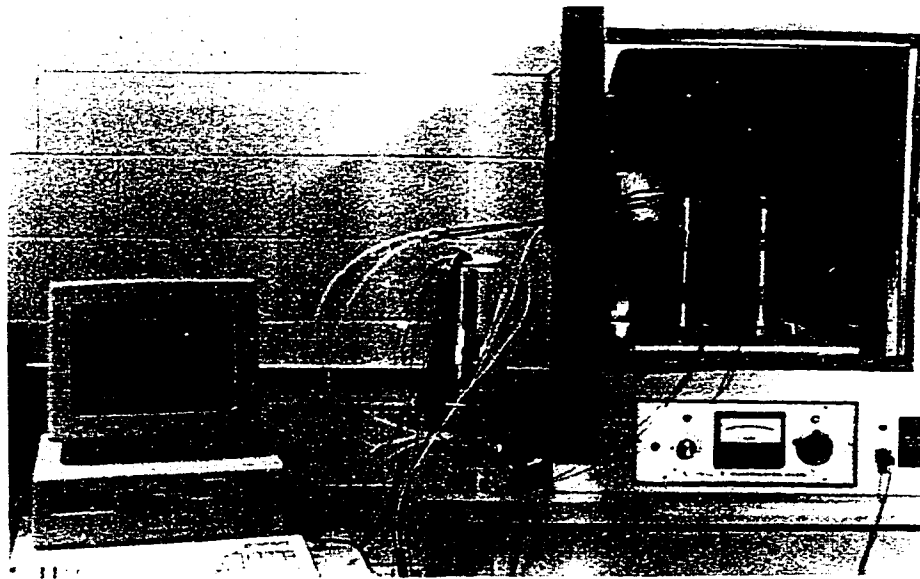


Figure 3.10: Schematic of the inflatable mandrel method.

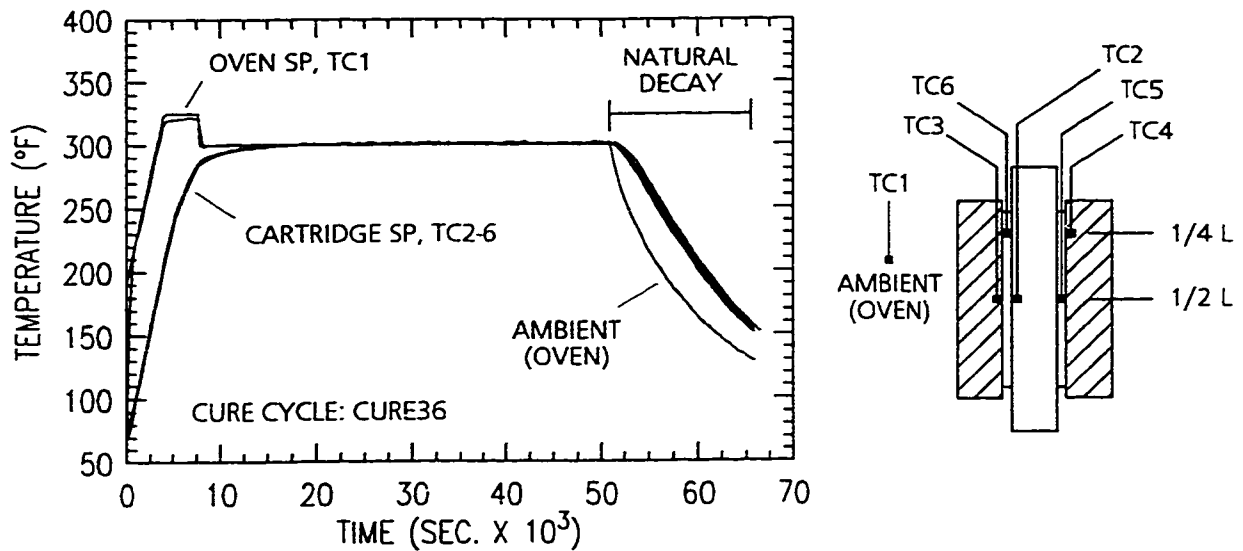


Figure 3.11: Thermal distributions in the mold, part and mandrel during curing using inflatable mandrel technique; (left) setpoint and measured temperature profiles, and (right) thermocouple (TC) locations.

The inflatable mandrel consists of a steel mandrel with a fitted silicone rubber tube (for high temperature use). The steel mandrel provides rigid support during the rolling operation, and is equipped with pathways for installing a pressurized air line, thermocouples and heater cartridge. Shallow grooves, machined onto the steel mandrel surface, ensures that supplied air is evenly distributed over the entire bladder.

In order to reduce thermal gradients, heat is supplied to the part both internally and externally using a combination of heater cartridge and oven. Since the thermal characteristics of the oven and cartridge heaters are different, a separate cure cycle must be specified for each system. As shown in figure 3.11, an optimal cure cycle which produces minimal thermal differentials can be determined by adjusting the applied internal and external temperature profiles.

Temperature and pressure is controlled by a computer and specialized cure cycle control software. The modest hardware requirements consist of a PC (80286 processor) with an eight channel analog-to-digital (A/D) data acquisition card and a two channel digital-to-analog (D/A) peripheral card. The A/D card is connected to a multiplexed conditioning circuit for reading up to seven thermocouples. The heater

cartridges are activated by solid state relays connected to the digital out ports on the A/D card. The heat output from these cartridges are regulated using pulsed ON/OFF control. The D/A card is used to supply an analog setpoint value to the oven control system. The air pressure level is set manually using an adjustable regulator, but is activated by the computer using a solenoid valve.

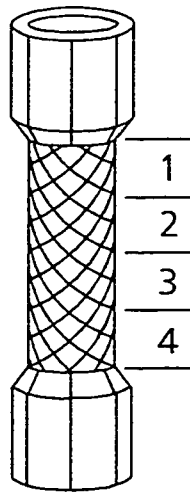
The cure cycle control program (CCCP.EXE) provides data acquisition and control facilities for curing up to seven specimens simultaneously. The software provides six main services: 1) independent cure cycle specification (temperature ramp rates and hold periods, and activation of pressure), 2) closed loop feedback control of heater cartridges, 3) open loop supervisory control of oven temperature, 4) alarm trigger in the event of excessive temperature rise (with system shut down), 5) input data validation, 6) on-line cycle monitoring and output data storage (in english or metric units).

The required cure cycle and hardware setup are input as a set of ASCII textfiles, which are described as follows:

1. *master datafile* - This file is responsible for specifying: a) the status of the various heaters and thermocouples, b) the appropriate cure cycle for the oven and cartridge heating systems, and c) the output datafiles to record the cure cycle process (important for identifying and trouble shooting system failures).
2. *cure cycle datafile* - This file contains the sequential steps necessary to create the temperature profile (ramps and hold periods), and to activate the pressure source.
3. *control and calibration datafiles* - These files are responsible for setting the temperature alarm levels, heater output, and calibration constants for the thermocouples and oven controller.

The datafiles used in this study are provided in appendix D.

The inflatable mandrel technique, presented, is seen to produce cylindrical parts with repeatable dimensions and exceptional microstructural characteristics. As shown in figure 3.12, the average dimensions measured along the gage section are seen to be quite consistent (based on measurements of 10 specimens). In addition, the absolute variation of the mean diameters between specimens is very low ($< \pm 0.0015$). Fiber



Position	d_o (in.)	d_i (in.)	V_f (%)
1	1.6682 ± 0.0006	1.5298 ± 0.0009	54.0
2	1.6677 ± 0.0009	1.5289 ± 0.0011	53.0
3	1.6677 ± 0.0006	1.5291 ± 0.0014	53.1
4	1.6680 ± 0.0006	1.5303 ± 0.0009	53.7

Figure 3.12: Average dimensions and fiber volume fraction variation along the length of post-cured $[\pm 45^\circ]_S$ glass-fiber reinforced epoxy tubes, where d_o and d_i are the outside and inside diameters, respectively.

volume fraction and void content were destructively measured on two specimens using ignition loss techniques (see ASTM standards D2584 and D2734). Referring to figure 3.12, the distribution of fiber volume fraction is also seen to be consistent. The void content was found to be $< 1\%$ throughout the tube length, which was corroborated by micrographic examination (see figure 3.13). A sample calculation sheet for determining the fiber volume fraction and void content is provided in Appendix E.

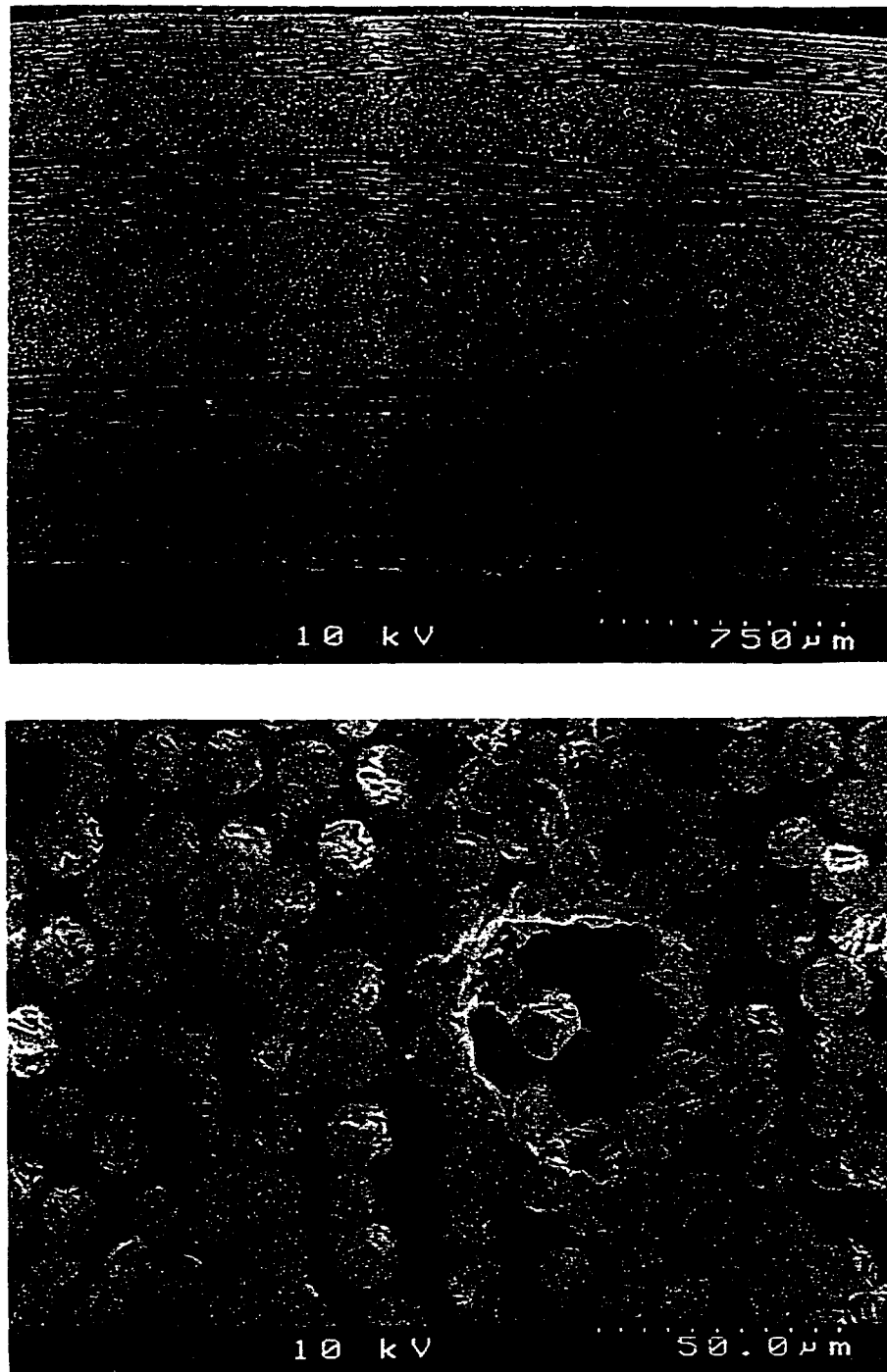


Figure 3.13: Micrographs from an un-tested $[\pm 45^\circ]_S$ glass-fiber reinforced epoxy tube; (top) tube wall (sectioned at 45° with respect to the tube axis), and (bottom) typical void.

CHAPTER 4

Leakage Characterization of Composite Tubular Specimens

4.1 DEFINITIONS OF FUNCTIONAL FAILURE

4.1.1 Introduction

Leakage failures can be classified into two categories: a). *Burst Failures* and b). *Weepage Failures*. Burst failures are characterized by an abrupt or fast loss of contained fluid volume, typically, in association with excessive structural damage (fiber breakage and/or localized matrix cracking). The failure point (load, time or number of cycles) is well defined, marked by the excessive fluid loss, and often coincides with the loss of structural load carrying capability. Burst failures most commonly occur under monotonic loading situations, with catastrophic failures being associated with fiber-dominated pressure loadings.

Weepage failure, on the other hand, is characterized by a gradual or slow (stable) loss in fluid volume due to localized or distributed matrix cracking. It is a result of the initiation and coalescence of intralaminar and interlaminar cracks forming a continuous pathway through the wall thickness. The failure (load, time or number of cycles) is *not* a well defined point. Under monotonic loading, weepage failures have been observed prior to burst. Under cyclic or long-term static fatigue (creep), weepage failures predominate.

From an engineering design perspective, weepage failures are preferred over burst failures for safety and environmental concerns. With regular inspection, weepage type failures can be monitored, detected, and repaired without excessive loss of fluid

or harm. Current designs based on the prevention of weepage failure, however, are very conservative in nature due to a general lack of validated predictive methods. The characterization of damage interaction and progression is not fully understood and, as such, the ability to predict when a structure will leak, without empirical determination, is difficult.

Liner structures (integrated or retrofitted) are often used to provide an impermeable membrane to increase the life of composite fluid containment systems which exhibit weepage type failure modes. Liners, however, are not suitable for all applications, and add a premium to the cost of the structure. In addition, liners are often difficult to incorporate during installation especially at geometric transitions (e.g. pipe elbows/tees) and joints, and have been shown to fail due to blistering, cracking, creep (elevated temperature applications) and buckling collapse (spoolable products). Even if a suitable liner material is used in the design, understanding pipe wall failure is crucial for developing fail safe designs in the event of liner failure.

The fluid volume loss or leakage profile of a pressure containment structure, represents the loss of fluid as a function of time (or load) for monotonic tests, or number of cycles for cyclic tests. Typical leakage profiles for burst and weepage failures are shown in figure 4.1. The leakage profile of a composite tubular product is a function of geometry (lay-up angles, lay-up sequence, number of layers, and constituent material properties), loading (biaxiality, cyclic/monotonic, and rate dependency), and environment (hygrothermal effects).

For design purposes, a *leakage failure envelope* defines the limits of usage of a tubular structure or material system under a defined set of loads. For pressurized tubular products, the applied loading is typically defined in terms of the hoop (or circumferential) and axial (or longitudinal) loads. The hoop loads are the result of internal and external pressurization of the tube, and are generated due to constraint of the radial pressure forces in a closed body. The axial loads can be generated by superimposed bending moments (pipe supports), applied pressure (for closed end structures) and by constrained thermal stresses.

Once the failure envelope has been determined, a given material form or structure can be evaluated for a given application. A failure envelope can be used by the designer to determine if the structure will fail (and possibly how), and can also provide insight as to how the design can be improved. As an illustrative example, the failure

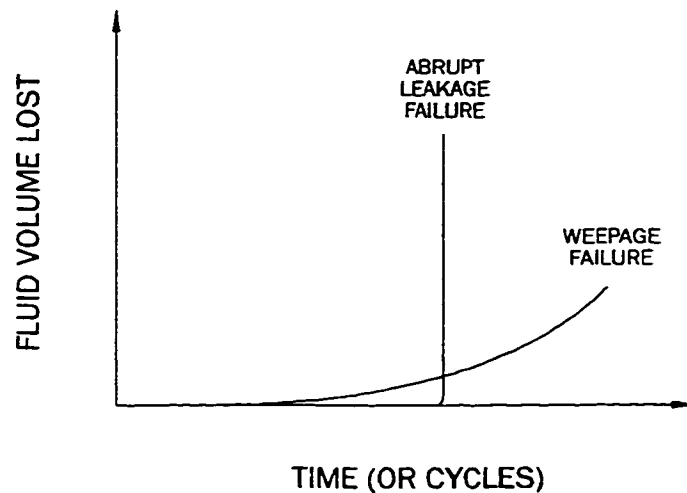


Figure 4.1: *Typical fluid volume loss (leakage) profiles for (a) Burst and (b) Weepage failure modes in fiber reinforced composite pressure containment structures*

envelope and the predicted failure points of a downhole tubular application, typical in oil and gas production, is shown in figure 4.2. This example is an extremely difficult design problem since there exists a wide range of applied biaxial loading conditions in a single structure. The hoop loading gradient is a result of the fluid pressure differential from the bottom of the well bore (high pressure) to the top (low pressure). The axial loading gradient is due to the weight of the tubular at various points along the string. If a down-hole pump is used to transfer fluid to the surface, a cyclic loading situation results, further complicating the analysis. As can be seen in the figure, failure is predicted to occur at the top of the tubular due to axial loads, and at the bottom due to pressure loading. The design can be modified by increasing the wall thickness at the ends of the tubular (effectively moving the envelope outwards), or changing the geometry of the lay-up (effectively changing the shape of the envelope).

4.1.2 Leakage Failure Criteria

In previous studies, a number of criteria have been used to specify the leakage failure point of a composite tubular structure:

1. Initiation of Leakage
2. Intersecting Tangent Curve Method
3. Loss of a Fixed Volume of Fluid

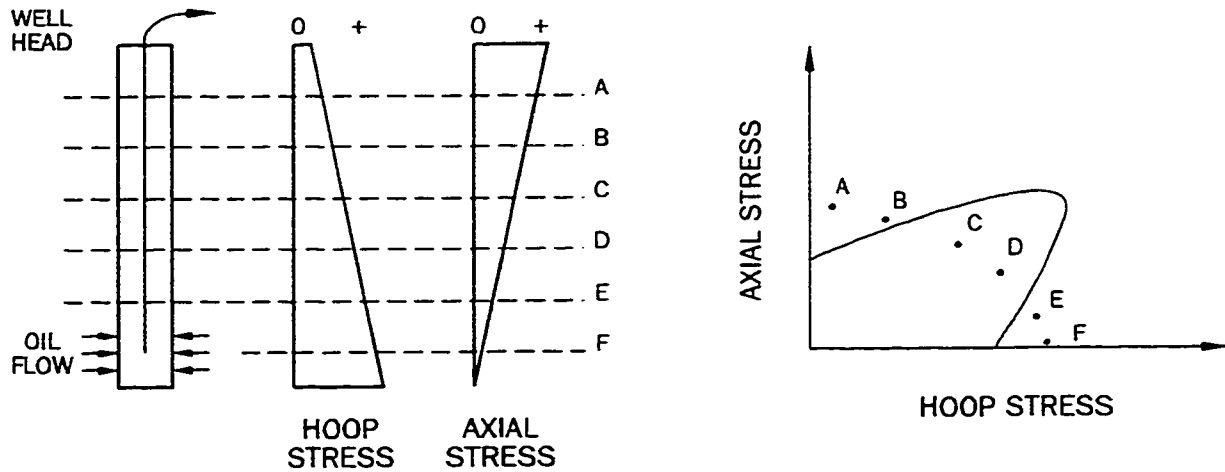


Figure 4.2: Example of a biaxial loading state in a downhole tubular and the corresponding biaxial failure points for an improperly designed tubular.

The determination of the failure point based on each of these criteria is shown graphically in figure 4.3. It should be mentioned that for abrupt failure (burst) modes for which no observable sign of weepage occurs, all three criteria collapse to the same point. Their differentiation occurs only for weepage type failures, as shown.

Failure based on the **initiation of leakage** is the most common criterion used in experimental studies. The initiation point is a very important parameter especially for designs that must be fail safe. Testing for just the initiation, though, does not provide useful information on the rate and characteristics of fluid loss which are important factors for safe design in the event of leakage. In spite of this, it is beneficial to examine the methods used to detect the onset of leakage. The point at which initiation occurs can be determined using a number of experimental techniques.

The easiest method to identify initiation is by physical observation of the specimen surface. Although this method is good in that it physically confirms the presence of fluid loss, it can be subjective (especially when only a limited area of the tube is observed), dangerous due to the presence of pressurized media, and time consuming for long-term tests.

Frost [198] detected the initiation of leakage by changes in the resistance of a wire mesh wrapped around the specimen. This method, however, will work only if water

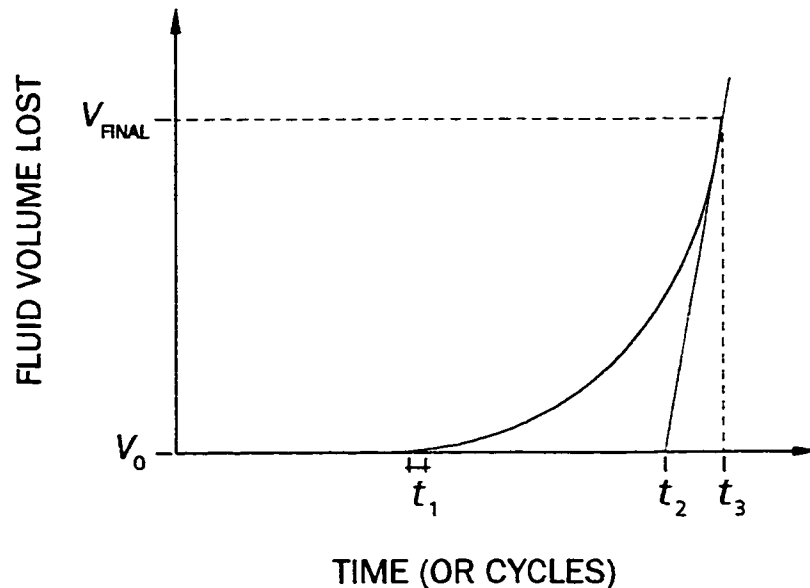


Figure 4.3: *Determination of leakage failure point based on the following criteria: (a) Initiation of Leakage (t_1), (b) Intersecting Tangent Curve Method (t_2), and (c) Loss of a Fixed Volume of Fluid (t_3).*

is used as the pressurizing medium. Due to the possible degradation effects of water on epoxy matrices, this method may not be appropriate for long-term testing.

The third method of detecting initiation is by using an intensifier based pressurization system. Intensifiers supply fluid pressure to the containment structure via displacement of a staged piston. By measuring the displacement of this piston, the total volume of the system, and, hence, the fluid loss can be monitored. This has the benefit of detecting not only initiation but generating a leakage profile for the test (see figure 4.1). The determination of the initiation point from a given volume loss (leakage) profile, however, can be subjective since the change in slope of the volume loss curve at the start of leakage can be quite small. This method is also prone to errors unless proper correction of the fluid loss data is performed to take into account effects such as fluid compression and change of specimen size due to strain (see section 4.3.1).

To reduce the subjectivity in selecting the point of initiation from the leakage profile, the intersecting tangent curve method can be used [205]. In this method, tangent lines representing the initial slope of the curve (typically the baseline at zero) and the final slope of the curve are drawn such that they intersect. The point of

intersection represents the failure point (initiation). For cyclic test profiles, the data can be plotted using a semi-log axis which tends to straighten the slope of the fluid loss curve at the end of the test, making the tangent line easier to draw. The drawback of the intersecting tangent method is that the final slope can vary depending on when the test is stopped. Since stoppage is usually at point where a fixed volume of fluid is lost (i.e. volumetric capacity of the intensifier), the failure point will vary depending upon the volume capacity of the fluid system. Testing machines with different capacities may yield different failure points.

Another method which can be used to determine the leakage initiation point from volume loss (leakage) profiles is a criterion based on the **loss of a fixed volume of fluid** [204]. If the volume loss profiles are generated during a test, this method is easy to implement and can even be used to trigger the stoppage of the testing machine (see section 2.2.3). The deficiency of this criterion stems from its inability to take into account a number of factors which affect the leakage profile of the test, including the fluid driving force (pressure), fluid viscosity, damage area and pipe wall thickness. If these factors are not accounted for, the results may be deceptive. To illustrate this, consider a tubular specimen which has been loaded such that sufficient damage has occurred to allow fluid to permeate through its wall. Now, assume that pressure can be introduced without imparting further damage. As the pressure is increased, the rate of fluid loss will naturally increase. If a failure criterion based on a fixed volume lost is used, the time to failure at the lower pressure will be longer than that at the higher pressure. As such, two different failure points are observed but the actual damage state is the same.

As an alternative to the above methods, the **Critical Permeability Criterion** is presented in the following section. By experimentally measuring the volume loss profiles (versus time or number of cycles) and using Darcy's Law for flow through a porous media, one can experimentally determine the permeability conditions at any point in time. By setting a critical value for the permeability constant, the corresponding leakage life for a given specimen geometry and loading condition can be obtained.

4.2 CRITICAL PERMEABILITY CRITERION

4.2.1 Application of Darcy's Law

The flow of a fluid through a porous media which contains uniformly distributed, small scale pathways is indicative of a class of fluid mechanics problems known as "Darcy Flows". The transportation of fluids via this type of phenomenon is seen to occur in a number of important engineering applications including oil/gas reservoir geology, composites manufacturing (RTM) and building science. As such, there exists a plethora of experimental and analytical research in this area.

As discussed earlier, weepage type failures in composite fluid containment structures are observed under most loading conditions. This mode of failure manifests itself as a slow, evenly distributed loss of fluid at the surface of the structure, and is the result of distributed intralaminar and interlaminar matrix cracking [166,167,204]. This physical observation of weepage failure indicates that "Darcy Flows" may be present. Darcy flow assumptions are valid for flow situations where the inertial effects of fluid flow are small and can be neglected. Since weepage failure results in a slow, progressive (stable) loss in fluid, the basic premise for Darcy flow is assumed to apply.

The cornerstone for characterizing fluid transport through a porous media is the empirical relation developed by Darcy [271],

$$\bar{u} = -\frac{K}{\mu}(\nabla P) \quad (4.1)$$

where, \bar{u} is the apparent macroscopic (average) velocity of the fluid through the media, K is the permeability (in units of $length^2$), μ is the dynamic (or absolute) viscosity, and ∇P is the pressure gradient through the media in question.

The permeability (K) is a material property which reflects the ability of a given fluid to flow through that material. An increase in permeability implies a decrease in the resistance of fluid flow. Since this resistance is governed by the quantity, size and distribution of small scale cracks and pathways, the permeability provides a quantitative measure of the damage state for pressure containment structures which exhibit weepage type failure.

The general form of Darcy's Law (equation 4.1) can be applied to the case of a cylindrical tubular structure subjected to an internal pressure loading. Assuming

that the pressure gradients in the axial and circumferential directions are negligible, equation 4.1 can be written in cylindrical coordinates as,

$$u_r \bar{e}_r = -\frac{K}{\mu} \left(\frac{dP}{dr} \bar{e}_r \right)$$

or,

$$u_r = -\frac{K}{\mu} \left(\frac{dP}{dr} \right) \quad (4.2)$$

where, \bar{e}_r is a unit vector in the radial direction.

Assuming that the pressure distribution across the wall thickness is approximately linear (thin-wall condition) and that only internal pressure is applied ($P_{ext} = 0$), equation 4.2 becomes,

$$u_r = -\frac{K}{\mu} \left(\frac{-P_i}{w} \right) = \frac{K P_i}{\mu w} \quad (4.3)$$

where, P_i is the applied internal pressure and w is the wall thickness of the specimen.

The averaged radial fluid velocities can be integrated along the axial and circumferential directions to obtain the total volumetric flow rate, Q ,

$$Q = \int_S \bar{u} \cdot \bar{e}_r ds \quad (4.4)$$

Assuming that \bar{u} is constant along θ and z (which indicates uniform weepage along the tube), equation 4.4 becomes,

$$Q = u_r A_s = \pi d_o l_g u_r \quad (4.5)$$

where, A_s is the total surface area of the tube, d_o is the outside diameter, and l_g is the specimen gage length.

Combining equations 4.3 and 4.5, the radial weepage flow rate through a tubular specimen with evenly distributed cracking along its length is defined as,

$$Q = \frac{\pi d_o l_g P_i K}{\mu w} \quad (4.6)$$

The permeability K of a composite tubular specimen is a direct measure of the total crack area (reflected in the units of permeability, $length^2$) and the connectivity

between these cracks. Since the damage accumulation and the observed flow rate is seen to increase with monotonic and cyclic loading, the flow rate, permeability and pressure are all functions of time (monotonic loading) or number of cycles (cyclic loading).

By inverting equation 4.6, the permeability, $K(t)$, for a composite tubular specimen is,

$$K(t) = \frac{\mu w}{\pi d_o l_g P_i(t)} Q(t) \quad (4.7)$$

By experimentally determining the rate of fluid loss, $Q(t)$, internal pressure, $P_i(t)$, and the length over which the weepage is distributed, l , the changing permeability characteristics during a test can be quantified.

The flow rate is found by differentiating the experimentally determined volume loss (leakage) profiles with respect to time, i.e.,

$$Q(t) = \frac{dV(t)}{dt} \quad (4.8)$$

where, $V(t)$ is the total volume loss of fluid.

For cyclic tests, the permeability should be explicitly solved in terms of the time, t , to ensure proper balance of units. This can be accomplished using the transformation,

$$t = \frac{N}{f_c}$$

where, N is the current number of cycles, and f_c is the cyclic frequency.

Also for cyclic tests, the mean value of volume loss, $V_m(t)$, and internal pressure, $P_m(t)$, for each cycle is used in equations 4.7 and 4.8. This approximation is justified by the observation that volume loss changes occur gradually over a number of cycles. For load controlled cyclic tests, the mean internal pressure will be a constant.

4.2.2 Permeability as a Damage Parameter

In the previous section, a method for determining the permeability of a composite tubular specimen was derived. The relation defined by equation 4.6 demonstrates that the damage state, fluid viscosity, applied pressure, and specimen size (diameter, length and wall thickness) all influence the measured leakage characteristics of a

given tubular specimen. The functional failure based on leakage can, therefore, be effectively characterized by the permeability.

By experimentally determining the permeability evolution for a given specimen and loading (equation 4.7), a leakage failure load (monotonic tests) or life (cyclic tests) can be determined by defining a critical permeability value,

$$K(t) = K_{critical} \quad (4.9)$$

For monotonic tests, the failure points for various critical values of permeability could be used to generate constant damage failure envelopes, which would demonstrate the relationship between leakage initiation and burst. For cyclic tests, a family of fatigue-life curves based on constant permeability could be generated for different critical values. For the leakage initiation curve, a nominally small critical value is used. For fail safe designs, the fatigue-life curves give an indication of the fluid loss behaviour after initiation (i.e. whether slow stable or abrupt fluid loss will occur). In applications where some weepage can be tolerated, a design based on the (leakage) initiation failure life may be unnecessarily conservative. A case in point is the down-hole tubular example discussed in section 4.1.1. The loss of fluid through the tubular wall will ultimately be contained in the well bore. Therefore, fluid loss is tolerable as long as the loss rate is small compared to the rate of fluid being transported through the tubular. By selecting an allowable range of fluid loss rates, a critical permeability could be determined. Based on this value and using the fatigue-life curves, the working life of the tubular could be predicted.

The utility of using critical permeability as a failure criterion is that it is independent of loading, fluid and specimen factors, and, as such, may be useful in predicting the leakage performance of large scale structures based on small scale tests. Even though the critical permeability criterion is best suited in characterizing weepage type behaviour, it can still be used to identify burst type failures since its value will change abruptly as a result of an abrupt fluid rate increase. In this case, however, the permeability has no advantage over any of the previous methods discussed.

Since the permeability is an indirect measure of the damage state, its use as a damage parameter is analagous to that of stiffness. It has been extensively shown that global stiffness reduction in a composite laminate is a result of the accumulation of matrix cracking and delamination [64,67,76,272,273]. The use of stiffness (reduction)

as a fatigue damage parameter is quite extensive [157, 274–276]. Permeability and stiffness are both global (macromechanical) measures of damage, and, therefore, the evolution of either parameter is unique for a given material system, geometry and applied loading.

4.3 CONSIDERATIONS FOR MEASURING LEAKAGE IN TUBULAR SPECIMENS

4.3.1 Calculation of Fluid Volume Lost

In order to effectively quantify the permeability or the onset of leakage, an accurate measurement of volume loss is required. During a test, the volume change as measured directly from the intensifier piston displacement is not necessarily due to fluid leakage alone. Two other effects, namely, fluid compressibility and specimen volumetric changes, must also be accounted for if proper leakage profiles are to be generated. In this section, the methodology required to determine the actual volume loss during a test is derived.

The specimen internal pressurization system consists of a pressure intensifier, connecting hoses and the test specimen. The intensifier generates pressures upto 82.7 MPa (12000 psi) by using a two stage piston (4:1) in conjunction with a hydraulic pump. As the system is pressurized, the intensifier exhibits a drop in volume due to compression of the hydraulic fluid, expansion of the specimen and fluid loss due to leakage. In order to separate each effect, the total volume of fluid in the system at any point in time can be calculated by,

$$V_t(t) = V_i(t) + V_s(\epsilon_h(t), \epsilon_a(t)) + V_p(P(t)) + V_h \quad (4.10)$$

where, $V_t(t)$ is the total system volume (corrected), $V_i(t)$ is the intensifier volume, $V_s(\epsilon_h(t), \epsilon_a(t))$ is the specimen volume, $V_p(P(t))$ is the apparent volume lost due to compression of the fluid, and V_h is the volume in the hoses and connection (constant value of approximately 50 cm^3).

The intensifier volume is determined by multiplying the measured piston stroke (LVDT) and the cross-sectional area of the secondary piston. When full, the intensifier has a maximum volume of 170.2 cm^3 (10.4 in^3).

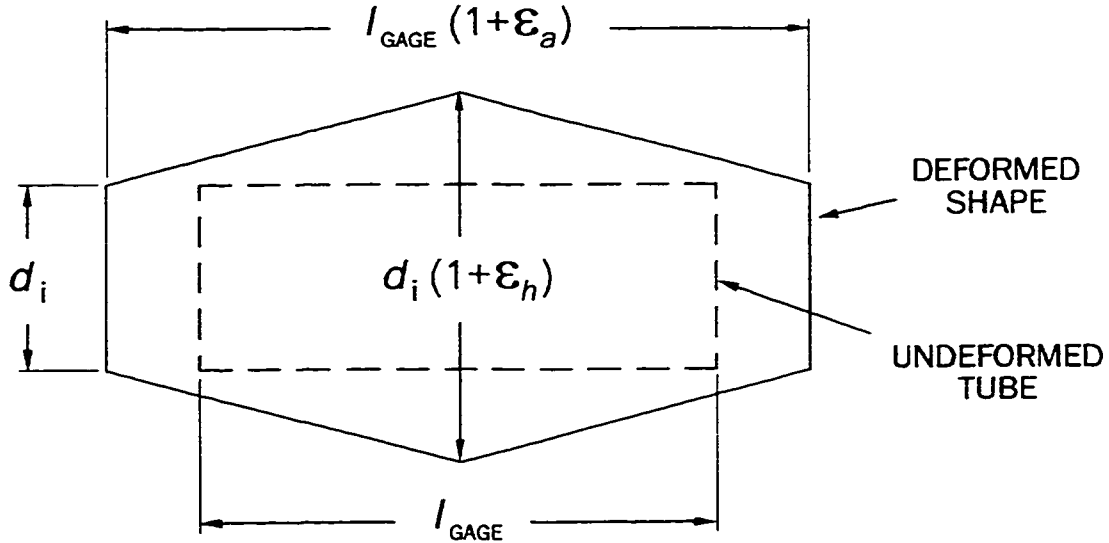


Figure 4.4: Assumed deformation shape for the calculation of specimen volume.

The change in specimen volume is due to the deformation as a result of applied loads. For fiber reinforced composites which may exhibit large strains, the changes in dimensions during a test can be significant. This will depend upon the specimen geometry (lay-up), size of the specimen (length and diameter), and the applied loading. The undeformed specimens in this study had an internal volume of approximately 131 cm^3 (8 in^3). Using the measured hoop and axial strains, the specimen volume can be approximated by assuming the deformed specimen shape shown in figure 4.4 (conical deformation). Based on this deformed geometry, the specimen volume can be calculated using,

$$V_s(\epsilon_h(t), \epsilon_a(t)) = \frac{1}{3} \pi h (a^2 + ab + b^2) \tag{4.11}$$

where,

$$h = l_g (1 + \epsilon_a), \quad a = \frac{d_i}{2}, \quad b = \frac{d_i}{2} (1 + \epsilon_h),$$

and l_g is the specimen gage length, d_i is the inside diameter of the specimen, ϵ_a is the measured axial strain, and ϵ_h is the measured hoop strain.

The apparent volume loss due to compression of the hydraulic fluid is determined by performing ramped pressure tests on the closed supply system (i.e. intensifier and

connection hose only). For this test, the change in intensifier volume is measured as the pressure is ramped to maximum value. As shown in figure 4.5, the generated curve represents the compression characteristics of the hydraulic oil for the closed system. The sharp rise in the curve is, most likely, due to air entrapment in the system and in the hydraulic oil itself.

In order to find the compressed fluid volume in the *total system* (i.e. specimen included), the compressibility function must be determined using the compression curve in figure 4.5. For a given total volume, the compressibility function (at isothermal conditions) relates the change in volume due to a change in the pressure, i.e.,

$$C(P) = \frac{1}{V_{cs}} \left(\frac{\partial V_p(P)}{\partial P} \right)_T \approx \frac{1}{V_{cs}} \left(\frac{\Delta V_p}{\Delta P} \right) \quad (4.12)$$

where, $C(P)$ is the compressibility, V_{cs} is the closed system volume (intensifier and connection hoses), ΔV_p is the compressed volume, and ΔP is the change in pressure.

The compressibility function, $C(P)$, is determined by numerical differentiation of the compression curve in figure 4.5. This was done by linearizing segments of the compression curve and implementing the approximate form of equation 4.12. Once the compressibility function is known, the compressed volume, $V_p(P)$, for the *total system* can be found by substituting the control system volume with the total system volume, and numerically integrating equation 4.12. As shown in figure 4.5, when the above function is used to correct for compressible effects, the apparent volume lost for the closed system ramp test is eliminated.

Using equations 4.10 - 4.12, the volume lost due to leakage can be determined by,

$$V_l(t) = V_t(t) - V_t(0) \quad (4.13)$$

where, $V_l(t)$ is the volume lost due to leakage, $V_t(t)$ is the total system volume at any point in time (corrected), and $V_t(0)$ is the total system volume at initialization.

When a test has stopped due to a loss in the total intensifier volume, the test can be continued by re-filling the intensifier. The volume lost before re-filling must be recorded and added to future volume loss values (i.e. cumulative loss). The initialization volume in equation 4.13 must be re-determined after the intensifier is filled. For the testing machine used in this study, this complex housekeeping task is performed by the data acquisition and control software (see section 2.2.4).

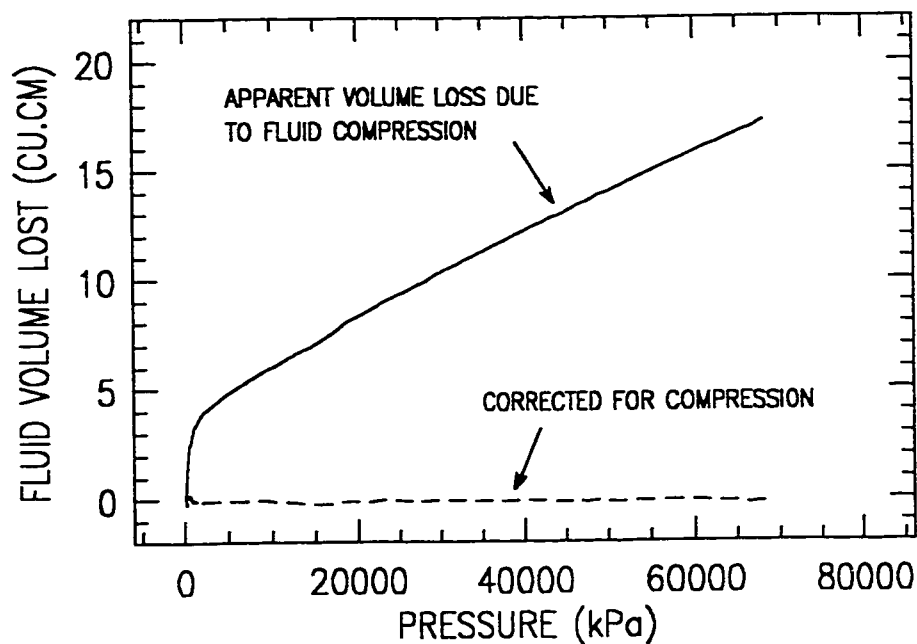


Figure 4.5: *Apparent volume loss due to compression of hydraulic oil (closed system - internal pressure intensifier and connection hose only).*

4.3.2 Fluid Volume Loss Profiles for Monotonic Tests

As will be discussed in the following chapters, there exists a common difference between the observable functional failure mode for the monotonic and cyclic tests. In this study, all monotonic tests failed by abrupt leakage (burst) while for the cyclic tests, weepage was the failure mode observed. For the monotonic tests, though, the (corrected) volume loss profiles indicated that weepage failure had occurred prior to burst. Since all tests were conducted in a closed vessel configuration (for safety purposes), verification of this weepage mode was not possible by physical examination.

In order to determine whether weepage was actually occurring prior to burst, one monotonic test was observed in open vessel configuration. The volume loss (leakage) profile for this tubular specimen ($[\pm 45^\circ]_S$ under pure hoop loading) is shown figure 4.6. The specimen was viewed through a clear polycarbonate sheet that was placed in front of the specimen test area to provide some protection in the event of an accidental failure. The vessel was closed when the applied stress reached 200 MPa (to ensure safety). As shown in figure 4.6, the compressibility effects are dominant in the correction.

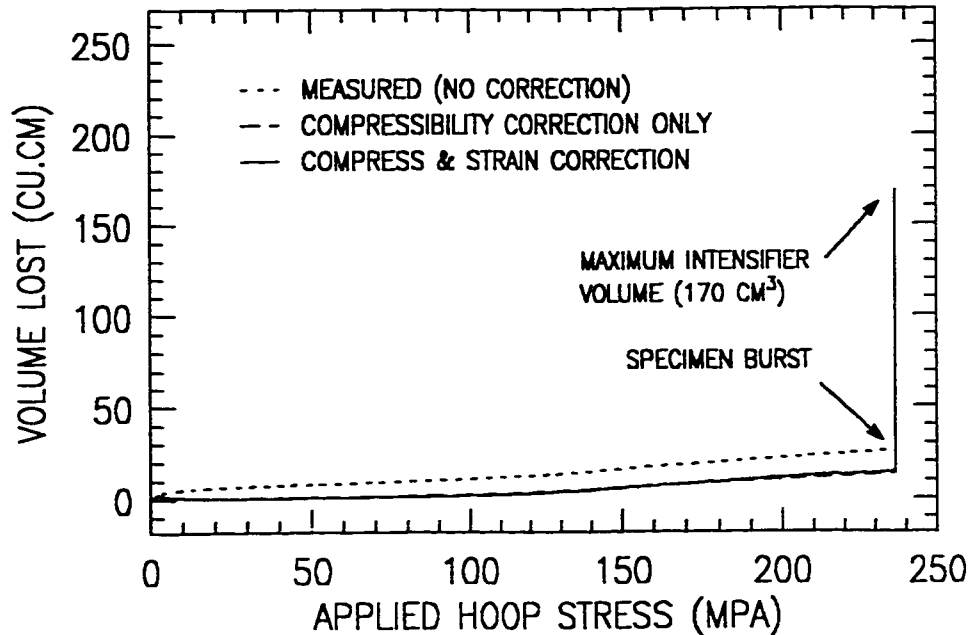


Figure 4.6: *Representative monotonic fluid loss (leakage) profile for a $[\pm 45^\circ]_S$ glass-fiber reinforced epoxy tubular specimen under pure hoop loading (1H:0A).*

From the figure, there appears to be an initiation of volume loss at approximately 80 MPa. However, for the portion of the test which was observed (0 to 200 MPa), there was no visible indication of weepage. Due to the relatively small loss noted in the figure, and the inability to get close to the specimen, it was not conclusive whether weepage had occurred or not.

If weepage had not occurred, one possible explanation for this apparent volume loss could be due to a difference in compressibility between that measured for the closed system (see figure 4.5) and that measured for the total system. When the compressibility of the intensifier (alone) was measured, the resulting compressibility function (especially for the first 10000 kPa), deviated from that determined from figure 4.5 (intensifier and connection hoses). Coincidentally, the point of leakage initiation in figure 4.6, corresponds to a pressure of approximately 6000 kPa. If the compressibility of the total system (with specimen and grips) is greater than that of the supply system alone, a drop in the apparent volume lost will occur. These differences in compressibility can be attributed to the differences in the volume of trapped air, and expansion effects in the hoses and seals.

Based on these considerations, the failure point for all monotonic tests in this study was assumed to be the point of abrupt leakage (burst) as shown in figure 4.6. For the cyclic tests, compressibility effects can be ignored since the maximum applied pressure is a constant (load control). As such, the volume lost due to compression can be eliminated by subtracting the apparent volume lost at the first cycle from the values of the remaining cycles.

CHAPTER 5

Biaxial Testing of $[\pm 71^\circ]_S$ Tubular Specimens

5.1 MONOTONIC BEHAVIOUR

5.1.1 *Experimental Method*

The biaxial monotonic behaviour of $[\pm 71^\circ]_S$ glass-fiber epoxy tubular specimens was investigated. Biaxial tests were performed for three biaxial stress ratios: pure hoop (1H:0A), pure axial (0H:1A), and the biaxial ratio defined by netting analysis (17H:2A). The monotonic tests were performed under load control at an equivalent stress rate of 0.7 MPa/s (100 psi/s). The definition of leakage failure was the loss of a fixed volume of fluid from the specimen. The tests were stopped by the control software when the volume lost by the internal pressure intensifier was approximately 150 cm^3 . For pure axial tests (0H:1A), a nominal pressure (approximately 20 to 30 psi) was applied to the tubes in order to measure the possibility of leakage, effectively making the actual loading ratio at failure approximately (1H:15A). This introduces a very small, but negligible, non-proportionality to the loading path. The fluid used for all $[\pm 71^\circ]_S$ tests was NUTO-H46 hydraulic oil, which has an absolute viscosity of 0.0656 $N.s/m^2$ (9.52×10^{-6} $lb.s/in^2$) at 30°C.

5.1.2 *Pure Hoop Loading*

The monotonic stress-strain response of a $[\pm 71^\circ]_S$ tubular specimen under pure hoop loading is shown in figure 5.1. In this figure, the experimental results are compared to the predicted linear response based on classical laminate theory (CLT). The predicted linear response shows excellent correlation for the axial direction, but under-

estimates the response in the hoop direction by approximately 20%. The experimental response exhibits slight non-linear behaviour for both hoop and axial directions. Considering experimental scatter due to variations in specimen and testing, the linear predictions show general agreement with the initial response of the specimen under load. The average applied hoop stress at failure was 260.1 MPa.

Since the applied load is uniaxial with respect to the hoop direction, the global laminate hoop modulus (E_H) and Poisson's ratio (ν_{HA}) can be determined experimentally from the slope of the hoop stress-strain curve (best fit), and predicted using CLT. The experimental and predicted laminate hoop modulus values (E_H) are 40.0 GPa and 32.5 GPa, respectively (see figure 5.1b). Under pure hoop loading, the laminate hoop Poisson's ratio (ν_{HA}) is the negative ratio of axial strain to hoop strain. This ratio can, therefore, be determined experimentally from the slope of axial strain to hoop strain, as shown in figure 5.2. The experimental and predicted Poisson's ratios (ν_{HA}) are 0.65 and 0.55, respectively.

Referring to figure 5.3, the macroscopic failure mode is highly localized matrix damage and fiber breakage located approximately 0.75 to 1.25 inches (20 to 30mm) from the end tab. This failure mode and location was consistent for all three specimens tested which indicates the presence of a stress/strain concentration effect at the specimen ends. The completion of the test was also marked by a noticeable audible indicator.

5.1.3 Pure Axial Loading

The monotonic stress-strain response of a $[\pm 71^\circ]_S$ tubular specimen under pure axial loading is shown in figure 5.4. In this figure, the predicted linear response shows excellent agreement with the experimental results. Compared to the pure hoop loading case, the predicted response shows better correlation in the direction perpendicular to the applied load, while slightly underestimating the response axially. The experimental response, again, exhibits some non-linearity to failure. The average applied axial stress at failure was 57.5 MPa.

Similar to the pure hoop tests, the laminate axial modulus (E_A) and Poisson's ratio (ν_{AH}) can be determined experimentally and analytically. The experimental and predicted laminate axial modulus values (E_A) are 14.0 GPa and 11.8 GPa, respectively

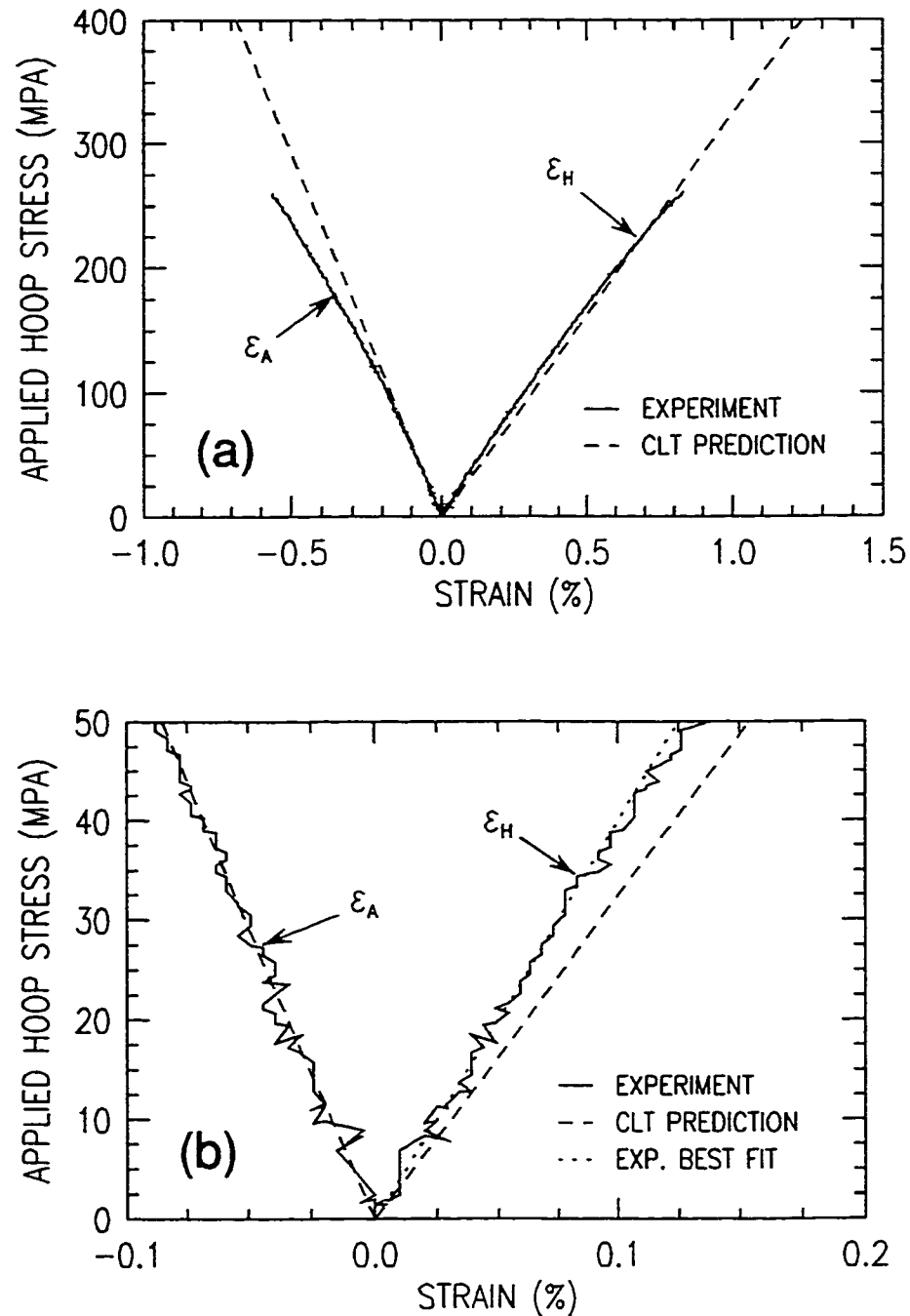


Figure 5.1: Monotonic stress-strain response of a $[\pm 71^\circ]_S$ glass-fiber reinforced epoxy tubular specimen under pure hoop loading (1H:0A); (a) stress-strain response to failure, (b) stress-strain response at the initial stages of loading.

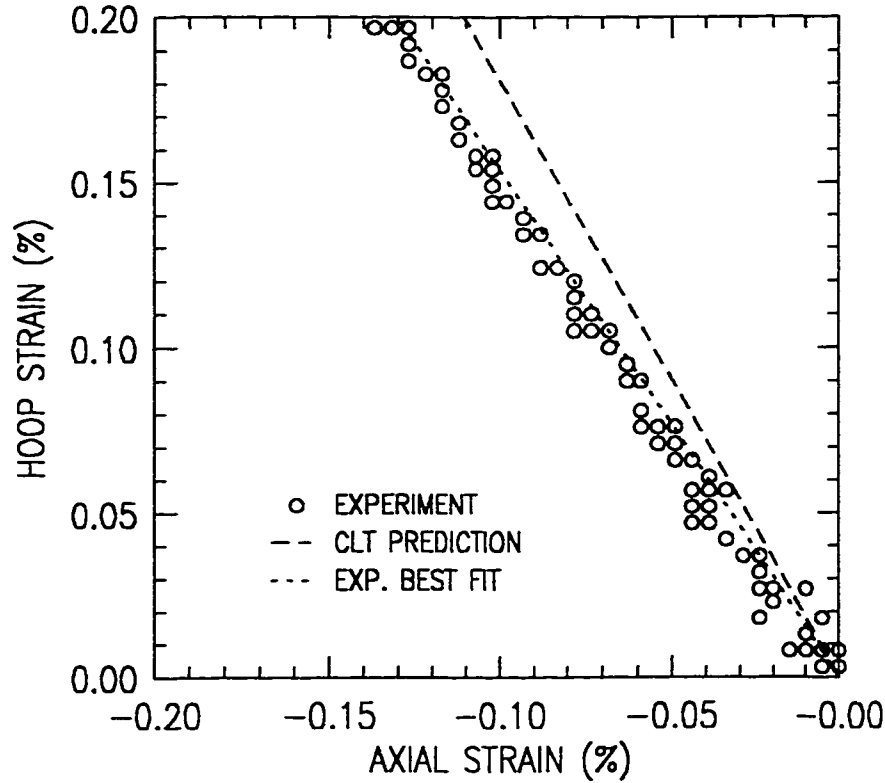


Figure 5.2: Hoop and axial strain response of a $[\pm 71^\circ]_S$ glass-fiber reinforced epoxy tubular specimen under pure hoop loading (1H:0A).

(see figure 5.4b). The predicted Poisson's ratio (ν_{AH}) of 0.20 coincides with the experimental data as shown in figure 5.5.

Assuming that the $[\pm 71^\circ]_S$ lay-up behaves as an orthotropic unit with respect to the specimen axis and that the material system behaves in a linear elastic manner, the hoop and axial laminate constants should be related by the expression [6],

$$\frac{\nu_{HA}}{E_H} = \frac{\nu_{AH}}{E_A} \quad (5.1)$$

To verify this assumption, the derived experimental and analytical elastic constants are substituted into the left and right sides of equation 5.1. The results are presented in table 5.1.3. It can be seen that this assumption is verified for the $[\pm 71^\circ]_S$ glass-fiber epoxy tubular specimens, implying that the material system can be modelled (at least initially) as linear elastic orthotropic units. This provides validation in the use of homogenized composite elements for modelling the elastic response of tubular specimens (see chapter 7).

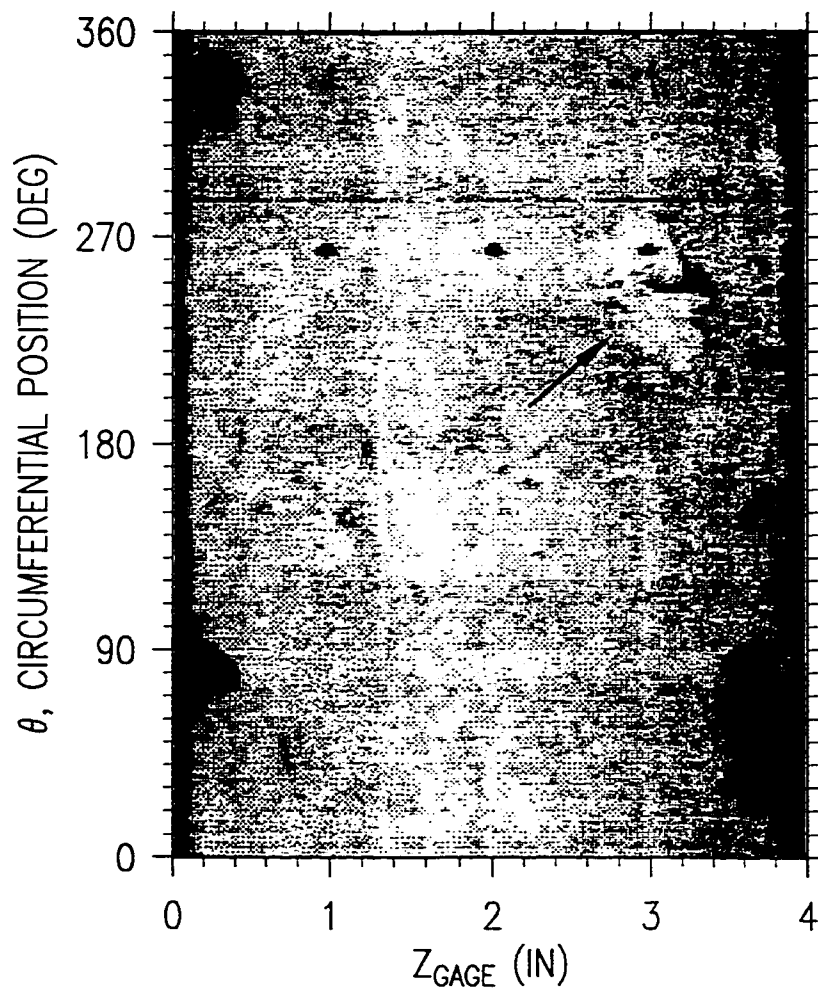


Figure 5.3: Macroscopic failure modes for $[\pm 71^\circ]_S$ glass-fiber reinforced epoxy tubular specimen under pure hoop (1H:0A) monotonic loading; (top) front view, (bottom) surface map.

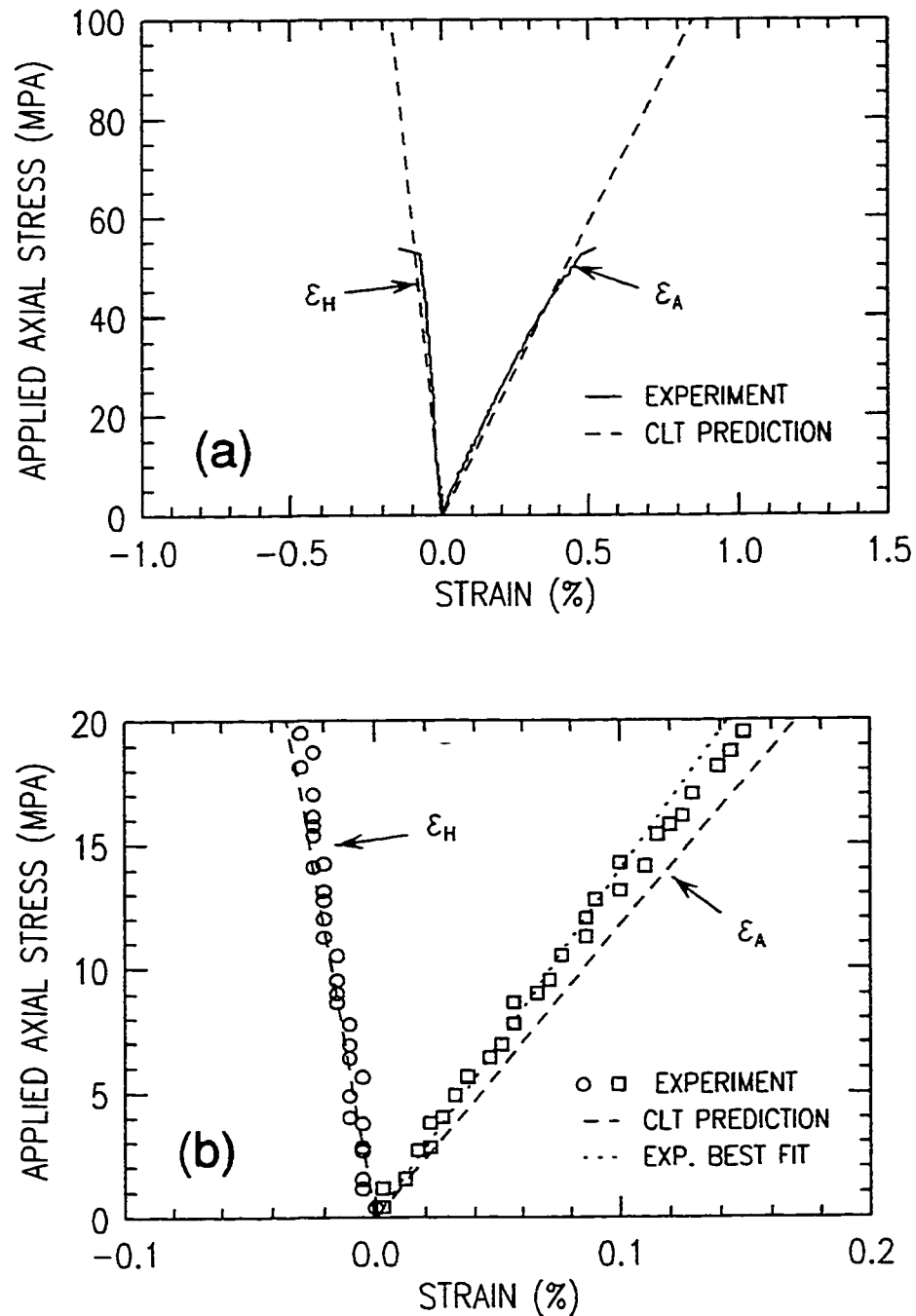


Figure 5.4: Monotonic stress-strain response of a $[\pm 71^\circ]_S$ glass-fiber reinforced epoxy tubular specimen under pure axial loading (0H:1A); (a) stress-strain response to failure, (b) stress-strain response at the initial stages of loading.

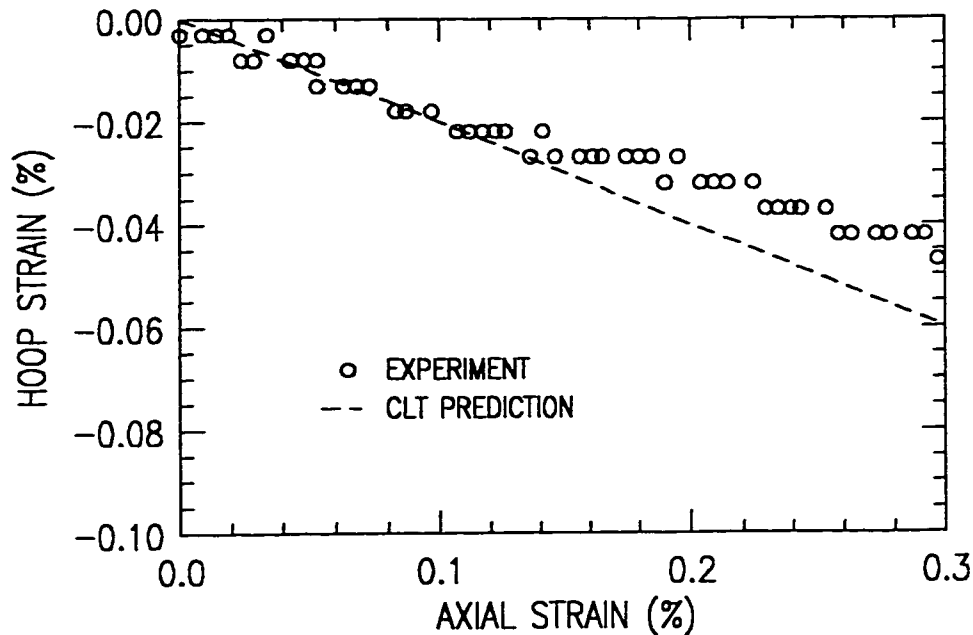


Figure 5.5: Hoop and axial strain response of a $[\pm 71^\circ]_S$ glass-fiber reinforced epoxy tubular specimen under pure axial loading (0H:1A).

As shown in figure 5.6, the macroscopic failure mode consists of multiple helical fractures resulting in total separation of the tubular specimen in the gage section. The fracture paths are parallel to the fiber angle orientations ($\pm\theta$), and are characterized by a combination of matrix cracking and fiber shearing. The end of the test was marked by a noticeable audible indicator. Since the internal fluid pressure was at a nominally low value (approximately 20 to 30 psi), the loss of fluid occurred only when sufficient damage to the specimen (ultimate failure) had occurred.

5.1.4 Loading Based on Netting Analysis

The monotonic stress-strain response of a $[\pm 71^\circ]_S$ tubular specimen under biaxial loading (17H:2A) is shown in figure 5.7. Similar to the pure hoop loading case, the predicted linear response shows excellent correlation with the experimental values in the axial direction but drastically underestimates experiments in the hoop direction. It should be noted, however, that even for this “fiber dominated” loading mode, some non-linear response is observed. This is most likely due to non-linear matrix shear effects and/or damage accumulation. The average applied hoop and axial stresses at

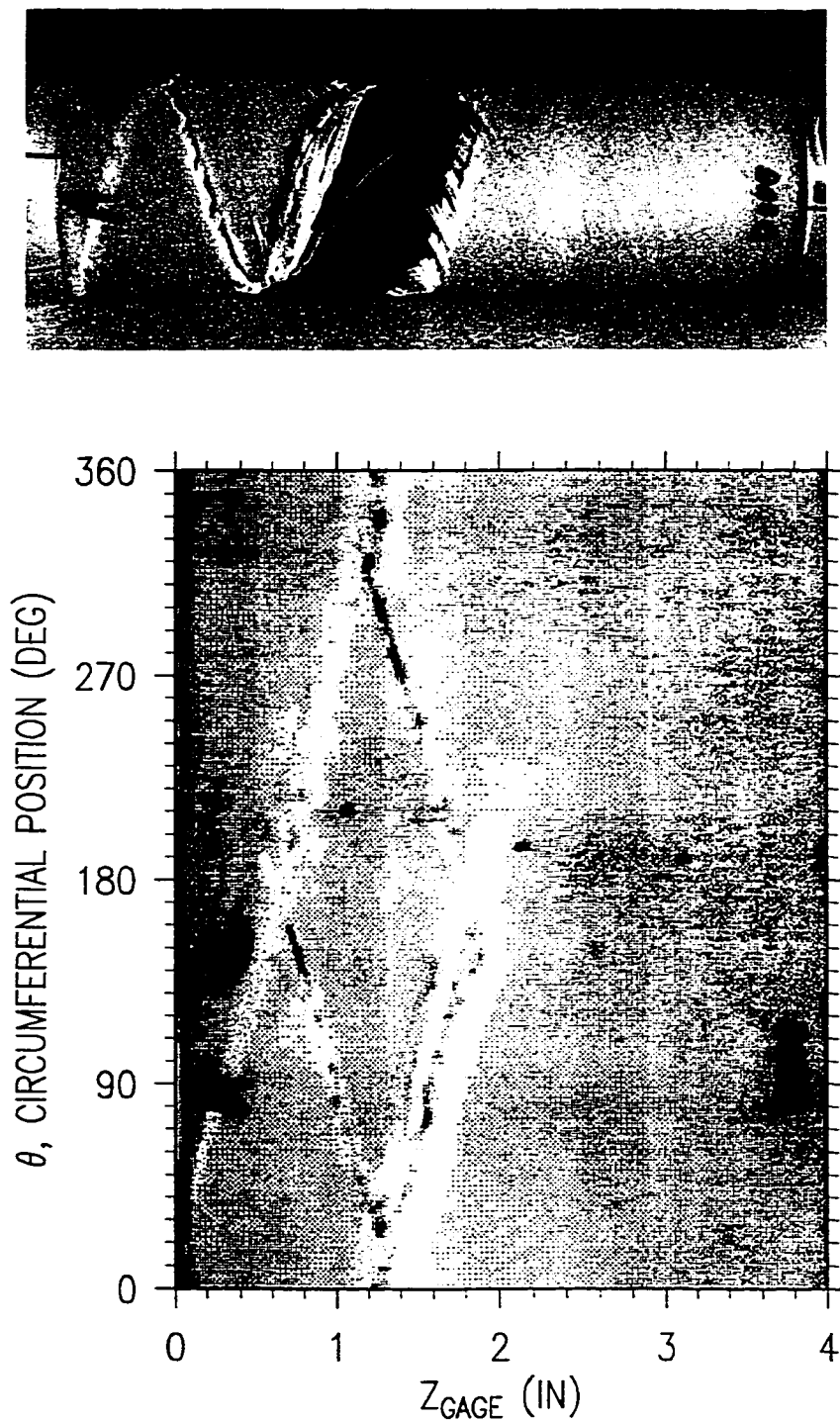


Figure 5.6: *Macroscopic failure modes for $[\pm 71^\circ]_S$ glass-fiber reinforced epoxy tubular specimen under pure axial (0H:1A) monotonic loading; (top) front view, (bottom) surface map.*

Table 5.1: *Experimentally and analytically derived elastic laminate constants for $[\pm 71^\circ]_S$ glass-fiber reinforced epoxy tubular specimens.*

	E_H (GPa)	E_A (GPa)	ν_{HA}	ν_{AH}	ν_{HA}/E_H (GPa) ⁻¹	ν_{AH}/E_A (GPa) ⁻¹
EXPERIMENT	40.0	14.0	0.65	0.20	0.0163	0.0143
PREDICTION (CLT)	32.5	11.8	0.55	0.20	0.0169	0.0169

failure were 291.4 MPa and 33.6 MPa, respectively.

From figure 5.8, it can be seen that the macroscopic failure mode for this loading case was similar to that observed for the pure hoop loading case. The failure mode was characterized by localized matrix cracking and fiber breakage located approximately 0.5 to 1.0 inches (13 to 25mm) from the end tab. As with the pure hoop case, this failure location indicates the presence of a stress/strain concentration near the ends.

5.2 CYCLIC BEHAVIOUR

5.2.1 Experimental Method

The behaviour of $[\pm 71^\circ]_S$ glass-fiber epoxy tubular specimens under cyclic loading was investigated for the biaxial stress ratios used in the preceding monotonic tests. The cyclic tests were performed under load control with a cyclic stress ratio of $R = 0.1$ ($R = \sigma_{min}/\sigma_{max}$). A sine waveform was used at a cyclic frequency of 1 Hz. The definition of failure was the loss of a fixed volume of fluid from the specimen (leakage). Leakage initiation* was assumed to occur when the volume of fluid lost was 1 cm^3 . The tests were stopped by the control software when the volume lost by the internal pressure intensifier was approximately 150 cm^3 . For some tests which exhibited moderate leakage rates, the intensifier was refilled and the test continued. For pure axial tests (0H:1A), a nominal internal pressure (approximately 20 to 30 psi) was applied to the tubes in order to measure the possibility of leakage.

*This represents a measurable value close to zero.

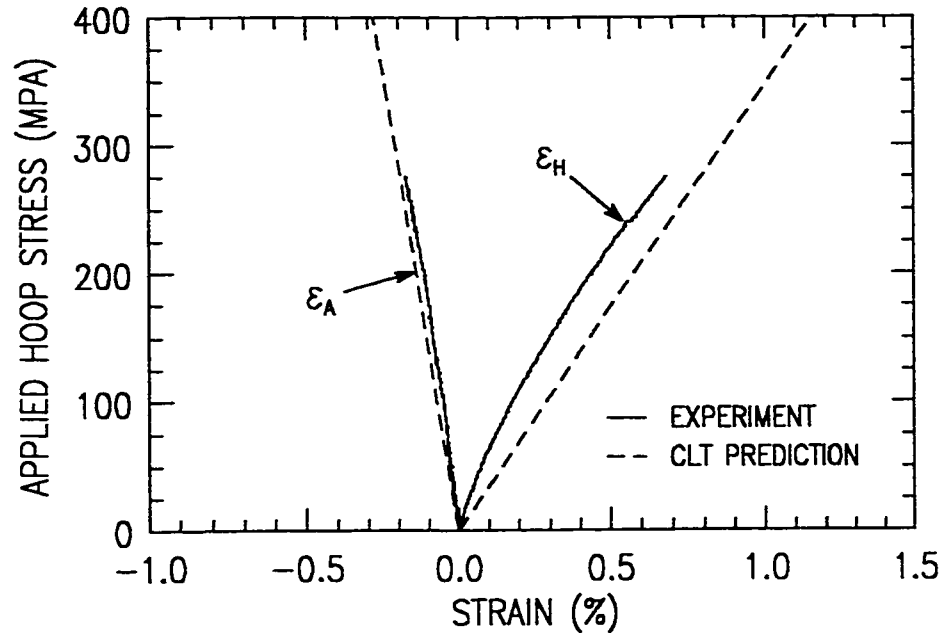


Figure 5.7: *Monotonic stress-strain response of a $[\pm 71^\circ]_S$ glass-fiber reinforced epoxy tubular specimen under biaxial loading (17H:2A).*

5.2.2 Pure Hoop Loading

The observed failure mode under pure hoop cyclic loading shows a marked difference from that found under monotonic loading. For all the maximum stress ranges investigated, the mode of failure was consistently found to be leakage at the end tabs as a result of grip induced matrix cracking.

Initially, it was assumed that the specimens had failed by distributed matrix cracking in the gage section. This was predicated by the observation that the entire surface of the specimen was wetted by hydraulic oil, indicating that distributed weepage failure had occurred. No other visible modes of damage were observed. Unfortunately, visual observations of the specimens during testing were not conducted due to safety concerns.

The failure locations were determined by re-testing the failed tubular specimens and visually observing the leakage. The tests were performed in open vessel configuration with the maximum stress values being reduced such that the applied pressure was not in excess of 500 psi (for safety considerations). A fluorescent penetrant tracer (20 ml of Magnaflux ZL-37 liquid penetrant) was mixed with hydraulic oil and in-

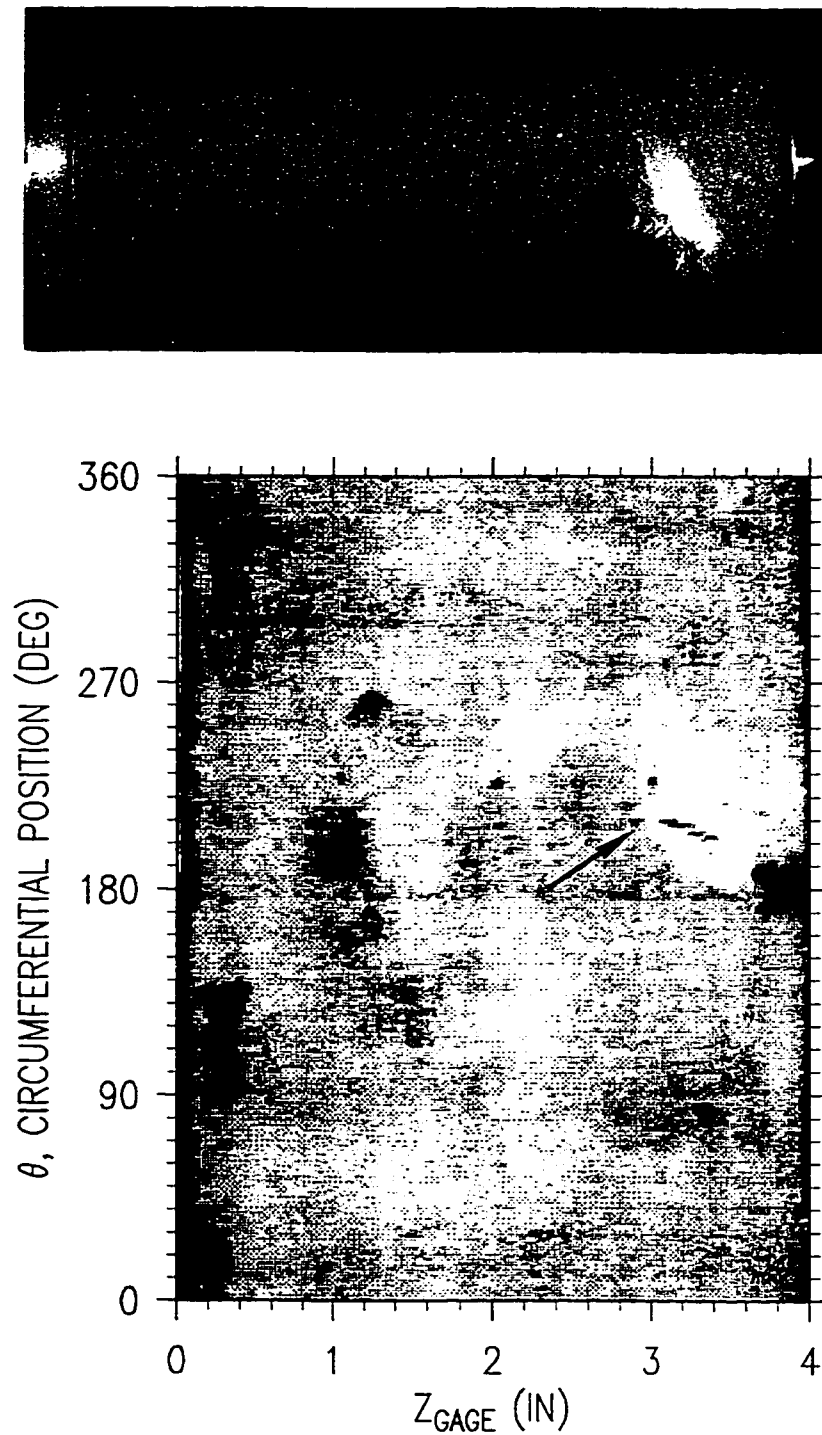


Figure 5.8: *Macroscopic failure modes for $[\pm 71^\circ]_S$ glass-fiber reinforced epoxy tubular specimen under biaxial (17H:2A) monotonic loading; (top) front view, (bottom) surface map.*

troduced into the specimen during the assembly of the grips. Under ultra-violet light, the leakage locations were readily observed at the tab/specimen interface (see figure 5.17). When attempting to section the specimen at the tabs for microscopic examination, the layers were found to separate quite easily, indicating the presence of extensive delamination failure at the ends.

In spite of the observed failure location, a limited series of cyclic tests were performed to determine whether the failure mode and location were consistent over a range of maximum applied stress values. It must be reminded that for each specimen tested, the cyclic stress-strain response cannot be directly correlated to the leakage profile since both results represent behaviour at two different locations in the specimen. As such, each will be treated separately in the following discussion.

Representative stress-strain curves for short-term ($\sigma_{h \max} = 230$ MPa) and long-term ($\sigma_{h \max} = 206.8$ MPa) cyclic tests under pure hoop loading (1H:0A) are presented in figure 5.9. The responses in the hoop direction are characterized by minimal cyclic creep and stiffness reduction, as expected for fiber-dominated loading. For the axial direction, some negative cyclic creep is observed for the short-term test, most likely due to the Poisson's effect and the matrix dominance in this direction. The negligible change in stiffness indicates a lack of damage accumulation in the gage section which was corroborated by micrographic observation.

Also in figure 5.9, experimental stress-strain curves are compared to the predicted linear response based on classical laminate theory (CLT). For the axial strain direction, the predicted response seems to correlate well with experiments. For the hoop direction, however, the linear prediction overestimates the experimental curves for all maximum stress values. This is contrary to the observation made under monotonic loading in which the predicted linear response underestimated the experimental results. This difference was initially attributed to experimental error and/or specimen variations, but an identical observation was made for the (17H:2A) loading case (see section 5.2.4). As such, this difference in behaviour can only be attributed to the effect of loading rate. For the monotonic tests, the loading rate was 0.7 MPa/s, while for the cyclic tests, the approximate loading rate based on a triangular waveform was 460 MPa/s (for $\sigma_{h \max} = 230$ MPa). From high strain rate hoop tests conducted by Al-Salehi et. al. [277] on $[\pm 65^\circ]$ and $[\pm 75^\circ]$ tubular specimens, it was observed that a moderate drop in secant modulus occurred with increasing strain rate. This could

explain the general position of the experimental curve with respect to the CLT prediction. This argument, however, cannot explain the stiffening effect observed within the cycle.

Representative fluid loss profiles for short-term ($\sigma_{h \max} = 230$ MPa) and long-term ($\sigma_{h \max} = 206.8$ MPa) cyclic tests are presented in figure 5.10. The gradual increase in slope (i.e. increase in volumetric flow rate) for both curves is the result of damage accumulation and propagation at the failure locations (specimen ends). For short-term tests (figure 5.10a), leakage begins to occur immediately from the start of test. It can be seen that a decrease in the applied maximum stress results in a delay in the start of leakage, and a decrease in the rate of fluid loss. Both are a result of the delayed initiation and coalescence of matrix cracks at the failure points.

Using the fluid loss profiles for all specimens tested, fatigue-life curves were constructed based on critical fluid loss levels of 1 and 10 cm^3 , as shown in figure 5.11. The results show a typical increase in initiation life with reduction in the maximum applied stress level. In order to quantify the fatigue-life behaviour, a linear (semi-log) equation was fit to the initiation data (1 cm^3). A reasonable fit is achieved for the lives between 10^2 and 10^5 cycles.

The scatter in the results, particularly the difference in cycles between the two fluid loss levels, can be attributed to a combination of manufacturing variation in these early specimens, and due to the complex nature of failure in the end tabs. Any variance in specimen quality at the end tab locations will be magnified due to the strain concentration effects at the tab.

5.2.3 Pure Axial Loading

Representative stress-strain curves for short-term and long-term cyclic tests are presented in figure 5.12. The cyclic stress-strain response for both regimes is characterized by very linear behaviour with minimal cyclic creep (approximately 0.05%) and negligible stiffness reduction. The predicted linear response based on CLT shows good correlation with observed experimental response.

The observed failure mode under cyclic loading is similar to that observed for monotonic loading. As shown in figure 5.13, the macroscopic failure mode consists of a helical fracture along the length of the gage section. The dominant fracture path

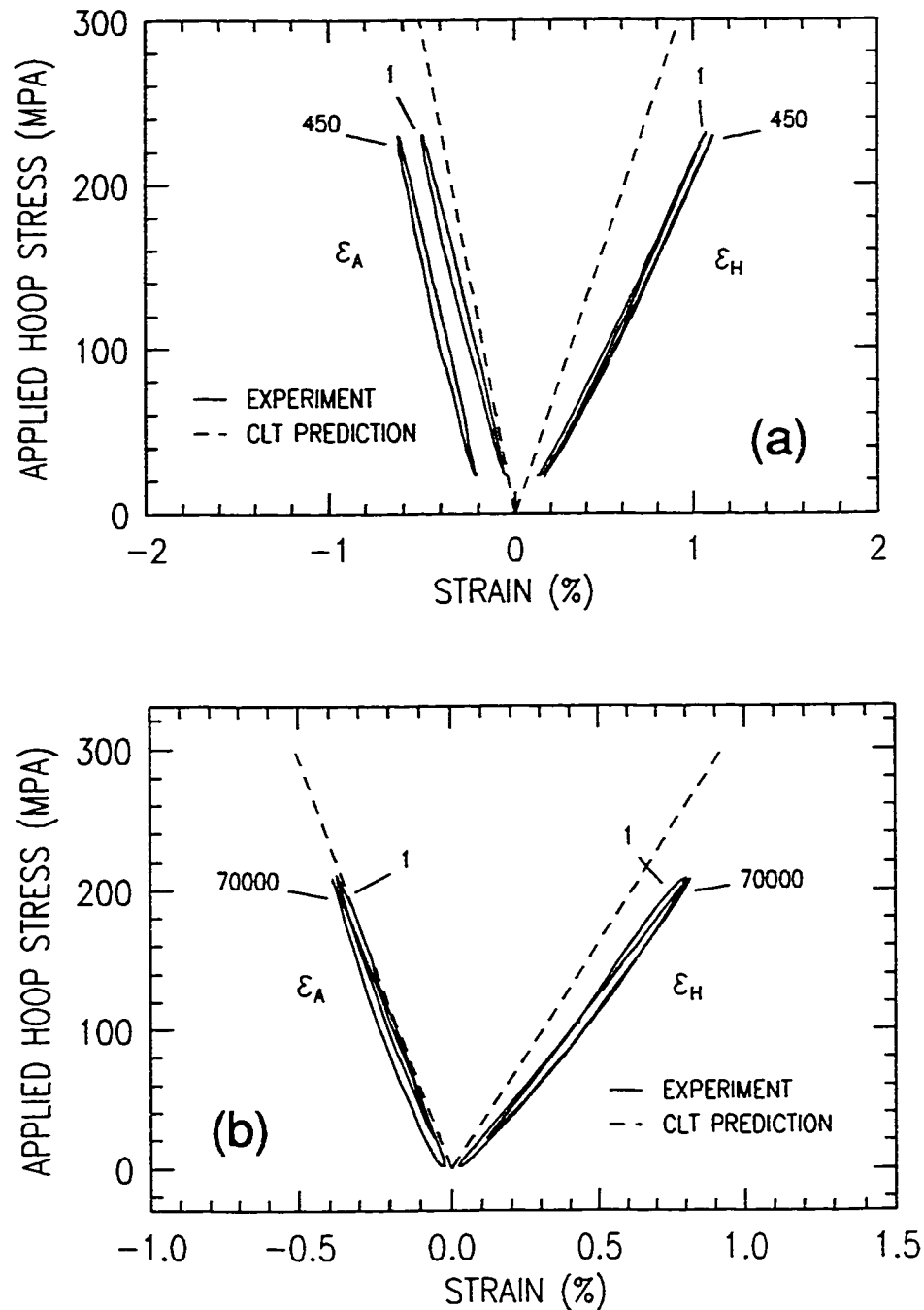


Figure 5.9: Representative cyclic stress-strain curves for $[\pm 71^\circ]_S$ glass-fiber reinforced epoxy tubular specimens under pure hoop loading (1H:0A); (a) short-term test ($\sigma_{h \max} = 230$ MPa), (b) long-term test ($\sigma_{h \max} = 206.8$ MPa).

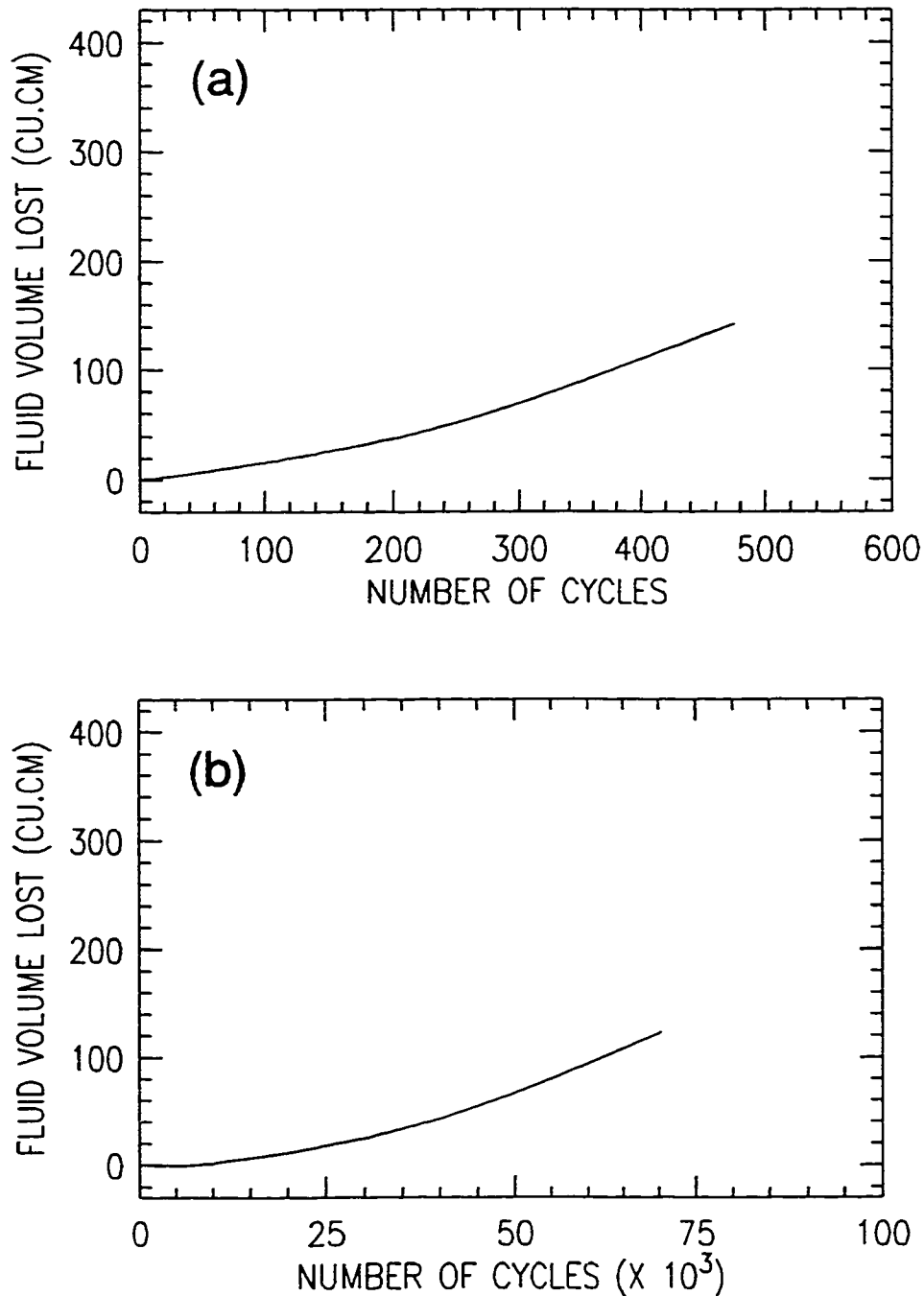


Figure 5.10: Representative cyclic fluid loss (leakage) profiles for $[\pm 71^\circ]_S$ glass-fiber reinforced epoxy tubular specimens under pure hoop loading (1H:0A); (a) short-term test ($\sigma_{h \max} = 230$ MPa), (b) long-term test ($\sigma_{h \max} = 206.8$ MPa).

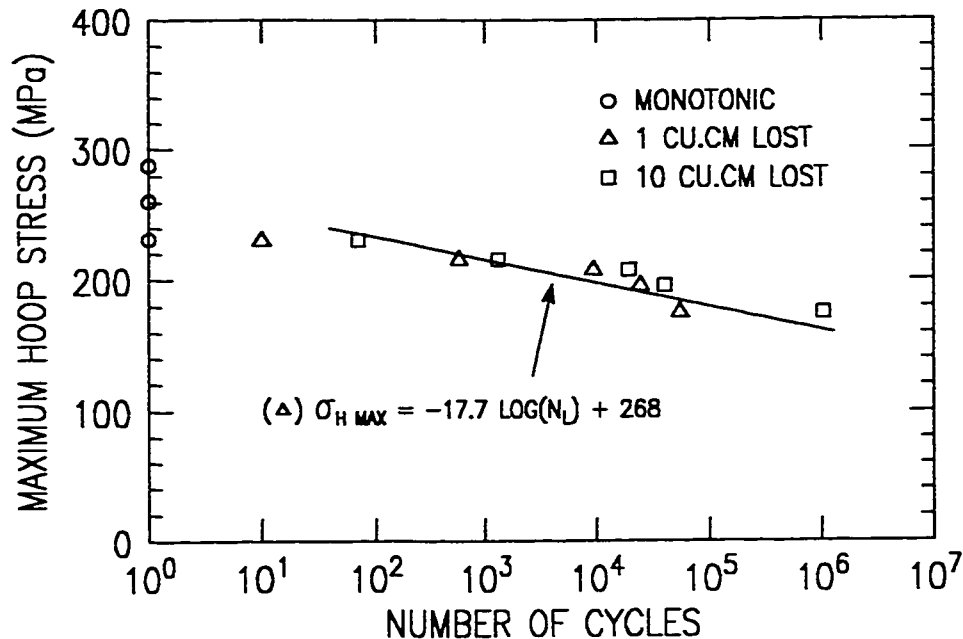


Figure 5.11: *Fatigue-life relationships based on critical volume loss for $[\pm 71^\circ]_S$ glass-fiber reinforced epoxy tubular specimens under pure hoop loading (1H:0A).*

is parallel to the fiber direction in the outer layer ($+71^\circ$), and is characterized by a combination of matrix cracking and fiber shearing through the wall thickness. A secondary crack, oriented at the opposite angle (-71°), can be observed intersecting the primary fracture. Similar to the monotonic test case, the end of the test was marked by a noticeable audible indicator.

In contrast to the gradual loss of fluid volume characterized by pressure dominated loadings, the volume loss for all cyclic axial tests was abrupt leakage, as shown in figure 5.14. For all pure axial tests, the leakage failure point was found to be coincident with the loss of load carrying capability in the axial direction (ultimate failure). This behaviour is attributed to the nominally low pressures used in these axial tests (approximately 20 to 30 psi). In order for fluid to flow through the specimen wall at a measureable rate, a substantial amount of damage would have to be present in the specimen (i.e. the wall must be highly permeable). Unfortunately, for thin-walled tubular specimens, the applied nominal pressure used in axial tests must be kept low in order to prevent substantial hoop loads from developing (and, thus, altering the biaxial loading ratio).

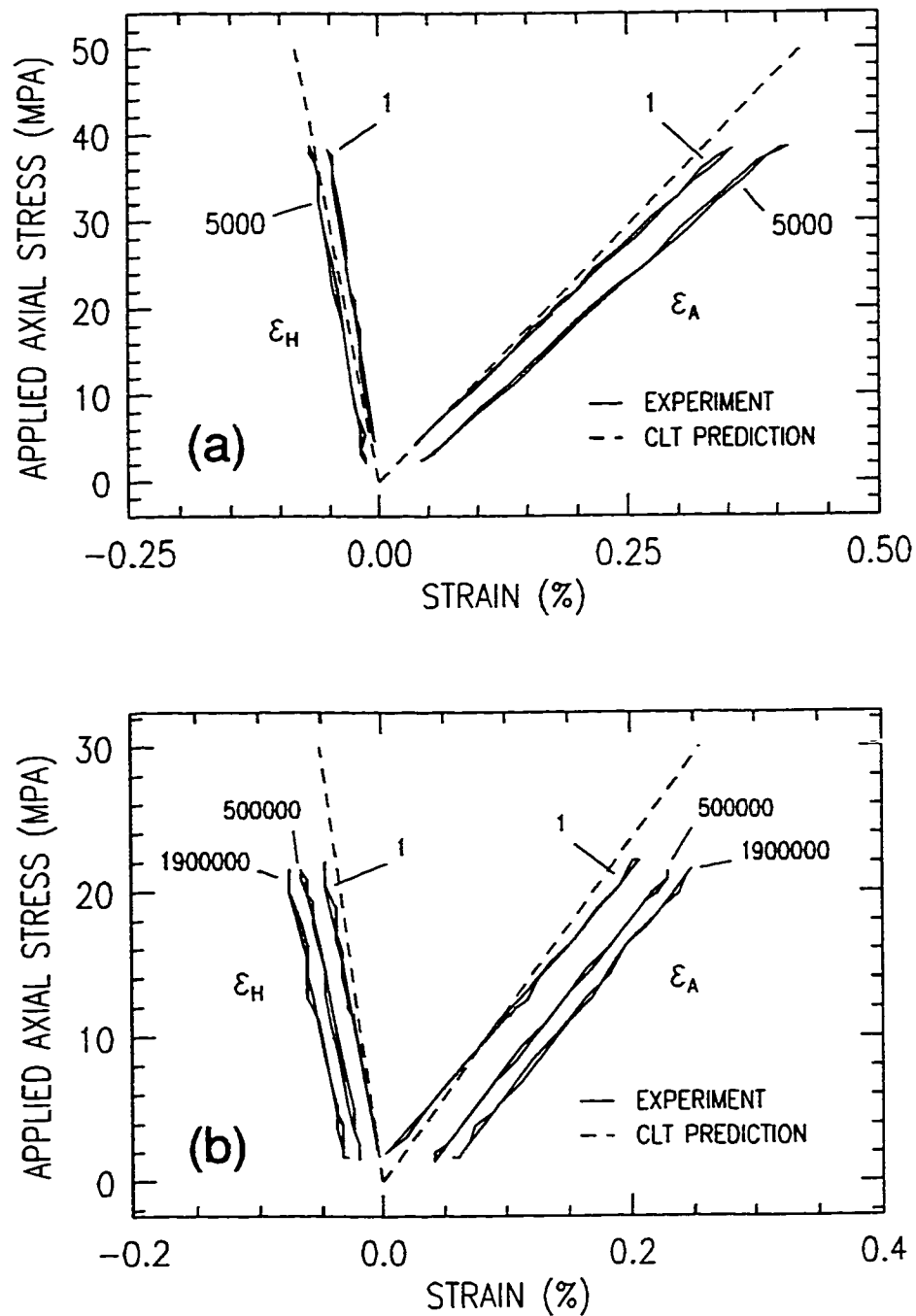


Figure 5.12: Representative cyclic stress-strain curves for $[\pm 71^\circ]_S$ glass-fiber reinforced epoxy tubular specimens under pure axial loading (0H:1A); (a) short-term test ($\sigma_{a \max} = 36$ MPa), (b) long-term test ($\sigma_{a \max} = 20$ MPa).

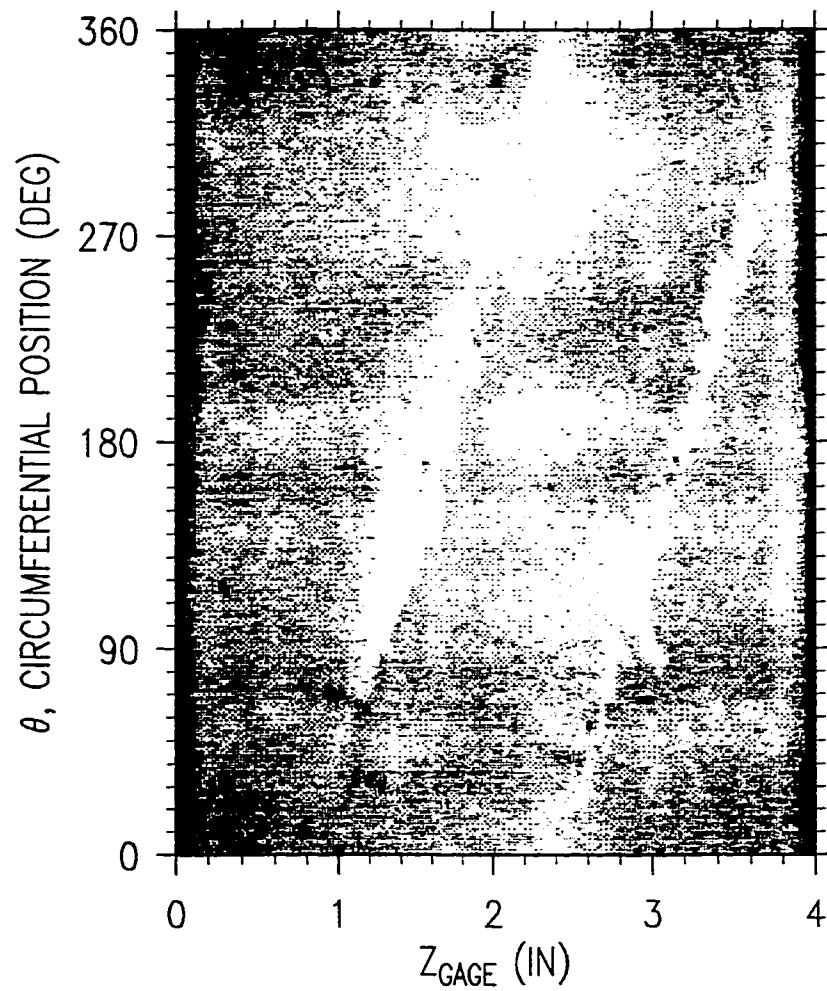
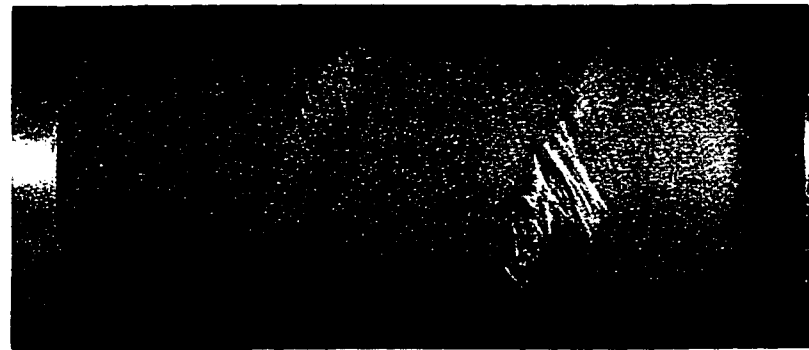


Figure 5.13: Macroscopic failure modes for $[\pm 71^\circ]_S$ glass-fiber reinforced epoxy tubular specimen under pure axial (0H:1A) cyclic loading; (top) front view, (bottom) surface map.

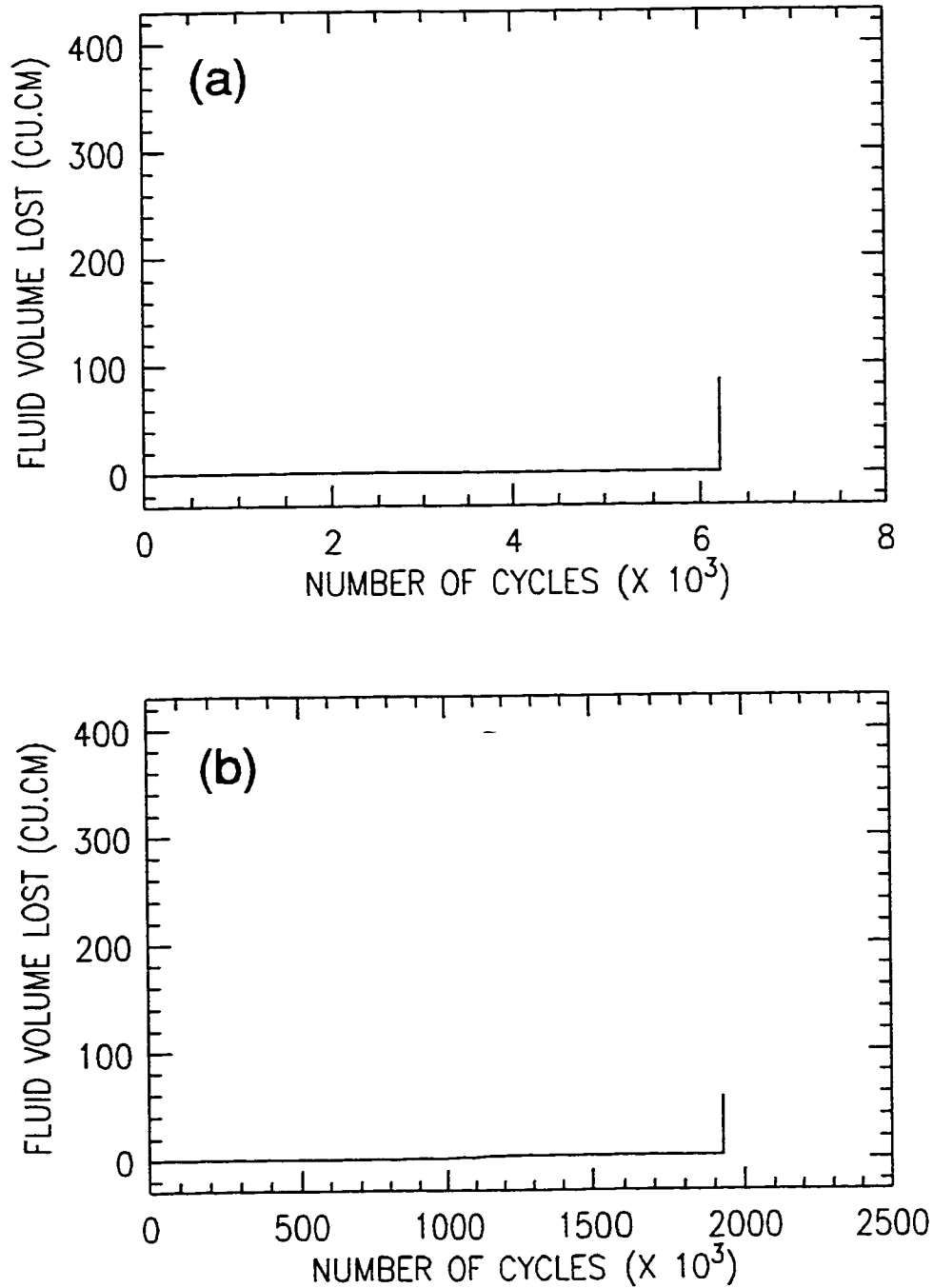


Figure 5.14: Representative cyclic fluid loss (leakage) profiles for $[\pm 71^\circ]_S$ glass-fiber reinforced epoxy tubular specimens under pure axial loading (0H:1A); (a) short-term test $\sigma_{a \max} = 36$ MPa, (b) long-term test $\sigma_{a \max} = 20$ MPa.

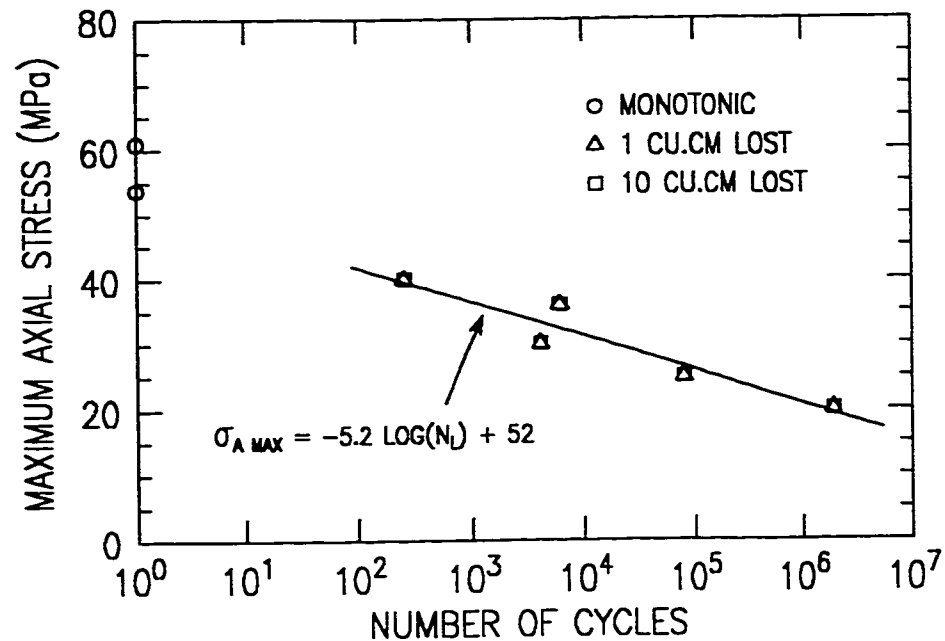


Figure 5.15: *Fatigue-life relationships based on critical volume loss for $[\pm 71^\circ]_S$ glass-fiber reinforced epoxy tubular specimens under pure axial loading (0H:1A)*

As shown in figure 5.15, fatigue-life curves were constructed based on critical fluid loss levels of 1 and 10 cm^3 . A linear (semi-log) equation was fit to the initiation data (1 cm^3), and was found to be a good representation. It can be seen that the fatigue lives based on a critical fluid loss of 1 and 10 cm^3 are coincident due to the abrupt nature of the failures.

5.2.4 Loading Based on Netting Analysis

Similar to the pure hoop cyclic loading case, the observed failure mode under (17H:2A) cyclic biaxial loading was also found to be localized leakage at the end tabs as a result of grip induced matrix cracking and delamination. In spite of the observed failure location, a limited series of cyclic tests was performed over a range of maximum applied stress values.

The cyclic stress-strain response of a $[\pm 71^\circ]_S$ tubular specimen under (17H:2A) biaxial loading is shown in figure 5.16. The characteristics exhibited by these tests are the same as those observed for the pure hoop loading case (refer to the discussion in section 5.2.2).

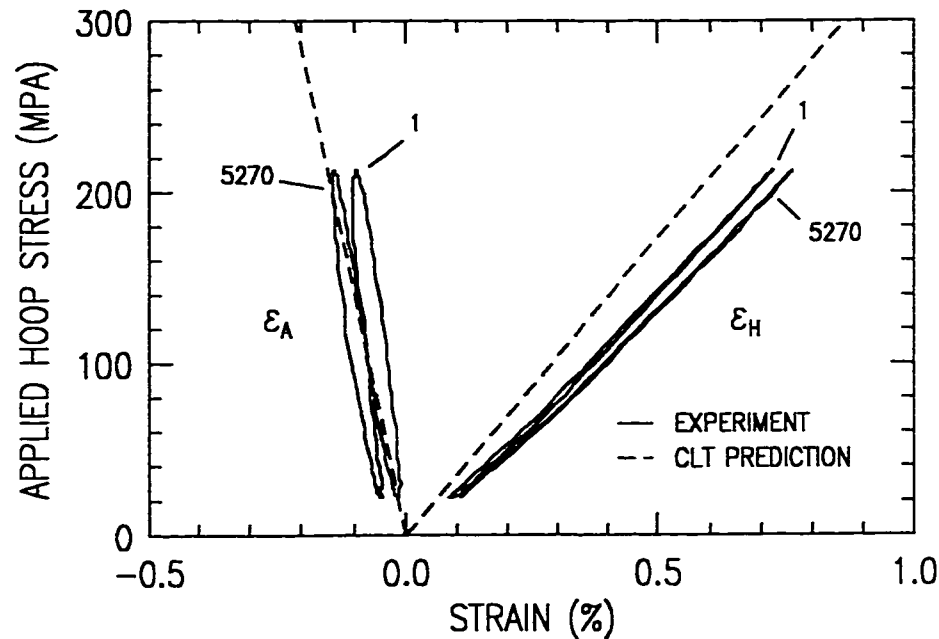


Figure 5.16: Representative cyclic stress-strain curve for $[\pm 71^\circ]_S$ glass-fiber reinforced epoxy tubular specimens under biaxial loading (17H:2A) - ($\sigma_{h \max} = 212.5 \text{ MPa}$).

The observed leakage locations for this loading ratio are shown in figure 5.17. As discussed in section 6.2.2, the failure locations were identified by re-testing the specimens with fluorescent tracers. A slight difference in failure location was noticed between the pure hoop (1H:0A) and netting analysis (17H:2A) loading cases. Both had prominent leakage site at the end tab locations, but only the specimens under (17H:2A) loading had a second leakage site at approximately 10 mm from the end tabs (see figure 5.17).

The fluid loss characteristics for these tests are also similar to those observed under pure hoop loading as shown in figure 5.18. A similar trend in the delay of leakage initiation and the decrease in fluid loss rate is observed with decreasing applied maximum stresses.

The fatigue-life curves based on critical fluid loss levels of 1 and 10 cm^3 were constructed as shown in figure 5.19. Similar to the other loading cases, a linear (semi-log) equation was fit to the initiation data (1 cm^3), and was found to be a reasonable representation.

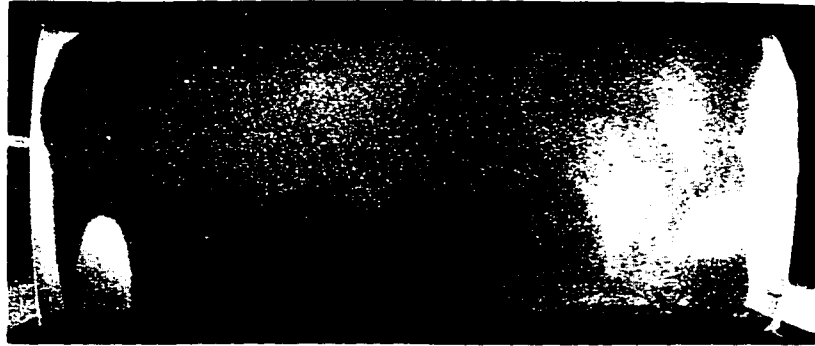


Figure 5.17: *Leakage failure mode for $[\pm 71^\circ]_S$ glass-fiber reinforced epoxy tubular specimen under biaxial (17H:2A) cyclic loading.*

5.3 BIAXIAL FAILURE ENVELOPES

Based on the monotonic and cyclic test results given in the previous sections, biaxial failure envelopes for the $[\pm 71^\circ]_S$ glass-fiber epoxy tubular specimens were constructed as shown in figure 5.20. The envelopes are plotted in the applied stress space (hoop and axial), and are based on the previously defined leakage initiation criteria (i.e. loss of 1 cm^3 of fluid). The applied monotonic stresses and strains at failure (leakage) are summarized in table 5.2. For the cyclic tests, the constant life contours are generated based on the best-fit equations given in figures 5.11, 5.15 and 5.19. In figure 5.20, the applied hoop and axial stresses correspond to that of the maximum applied stresses. The data points, for both monotonic and cyclic results, are fitted with spline curves in order to demonstrate the envelope trends.

The general shape of the envelope demonstrates the failure anisotropy of this lay-up. Under monotonic loading, the “fiber-dominated” hoop failure stresses are approximately 5 times higher than that of the “matrix-dominated” axial stresses. Specimens tested under pure axial loading were shown to fail in the gage section for both monotonic and cyclic tests. For the hoop dominated loading ratios (1H:0A and 17H:2A), however, all failures were located at or near the ends of the specimen, suggesting the presence of a stress/strain concentration. As such, the actual applied failure stresses should, in fact, be much larger than those measured. This can be seen when comparing the monotonic envelope to experiments conducted by Soden et al. [182] on thin-walled $[\pm 75^\circ]$ glass-fiber epoxy tubular specimens. Although the

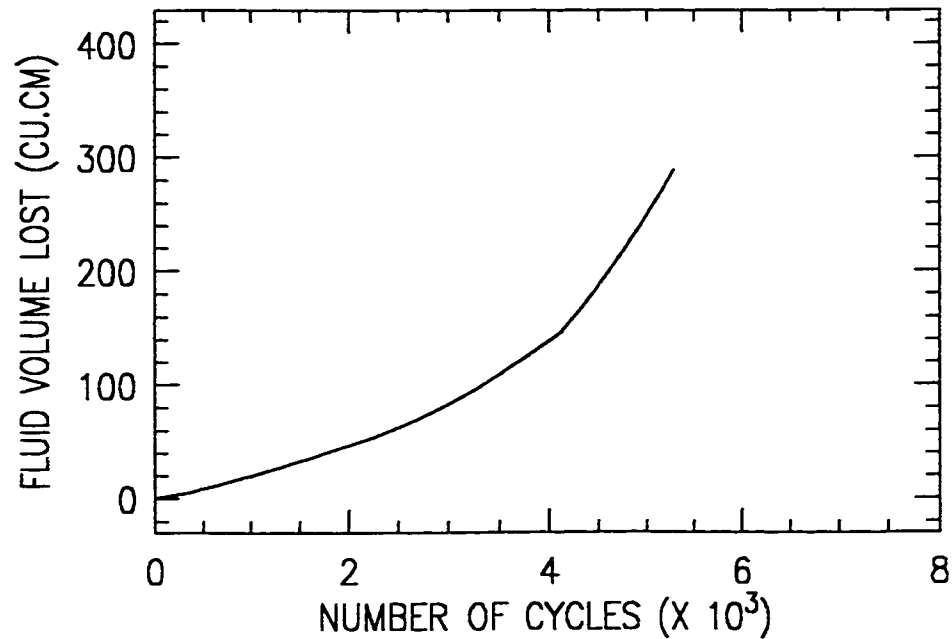


Figure 5.18: Representative cyclic fluid loss (leakage) profile for $[\pm 71^\circ]_S$ glass-fiber reinforced epoxy tubular specimens under biaxial loading (17H:2A) - ($\sigma_{h \max} = 212.5$ MPa).

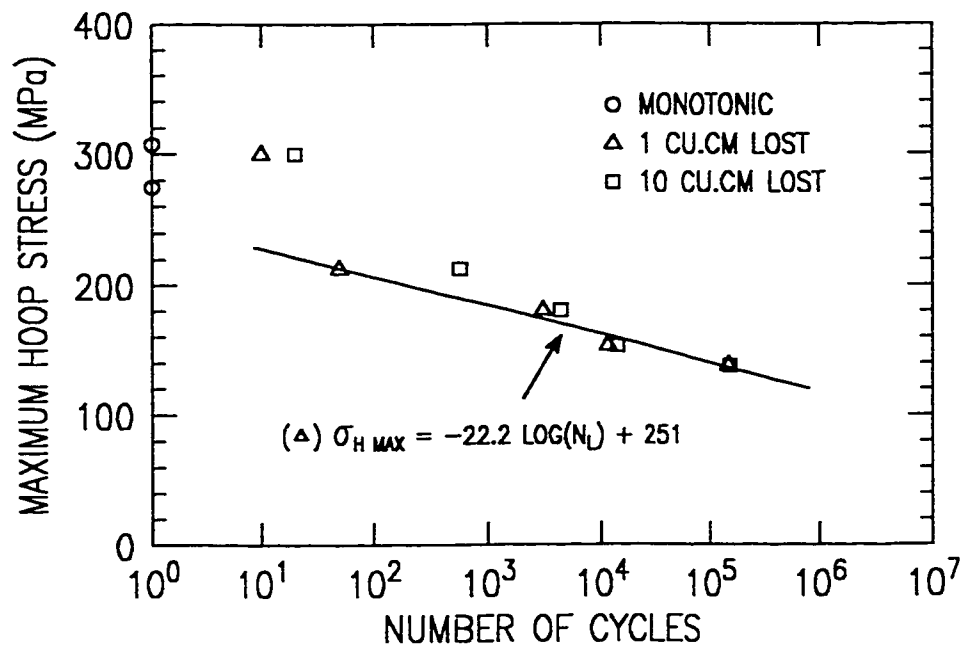


Figure 5.19: Fatigue-life relationships based on critical volume loss for $[\pm 71^\circ]_S$ glass-fiber reinforced epoxy tubular specimens under biaxial loading (17H:2A)

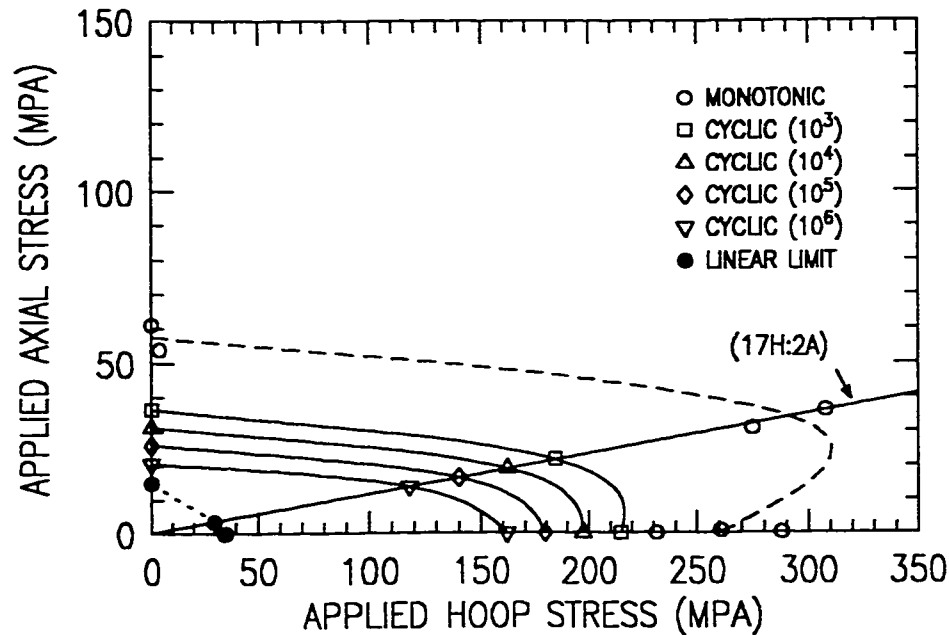


Figure 5.20: *Biaxial monotonic and cyclic failure (leakage) envelopes for $[\pm 71^\circ]_S$ glass-fiber reinforced epoxy tubular specimens in applied stress space.*

general shape of the envelopes are the same, the failure stresses found by Soden were 3 to 4 times higher in the hoop dominated loading directions. This large increase in apparent strength is likely due to the use of tapered end reinforcement in their specimen design. The axial failure stresses, however, were found to be identical to those observed in the current study.

A comparison between the monotonic and cyclic failure envelopes reveals that the long-term applied failure stress (10^6 cycles) is approximately 62%, 38% and 33% of the monotonic failure stress for the (1H:0A), (17H:2A) and (0H:1A) loading ratios, respectively. A direct comparison between the monotonic and cyclic envelopes, however, is deceptive without recognizing the differences in leakage failure modes and locations. For the pure axial loading ratio, the failure mode was a prominent fracture in the specimen gage section for both monotonic and cyclic loading. For the hoop dominated loading ratios (1H:0A and 17H:2A), however, the failures under monotonic and cyclic loading were vastly different. While monotonic loading produced a burst type failure (with fiber damage) away from the specimen ends, cyclic loading resulted in localized leakage at the end tabs. This clearly demonstrates the difficulty in using monotonic failure results to surmise the behaviour under cyclic loading.

Table 5.2: Average applied stresses and strains at failure (leakage) for $[\pm 71^\circ]_S$ glass-fiber reinforced epoxy tubular specimens under monotonic loading.

Biaxial Stress Ratio	Applied Hoop Stress (MPa)	Hoop Strain (%)	Applied Axial Stress (MPa)	Axial Strain (%)	Observed Failure Mode
(1H:0A)	260.1	0.88	0.4	-0.52	Helical separation along length of specimen
(0H:1A)	3.9	-0.21	57.5	0.57	Localized matrix damage and fiber breakage (20 to 30 mm from end tab)
(17H:2A)	291.4	0.68	33.6	-0.18	Localized matrix damage and fiber breakage (20 to 30 mm from end tab)

Predictions of the long-term failure envelope based on the linear elastic limit are also shown in figure 5.20. For this envelope, the stress values at the limit of linearity were estimated from the monotonic stress-strain curves for each of the loading ratios tested (see figures 5.1, 5.4 and 5.7). It can be seen that the predictions for the pure axial loading ratio is a good approximation of the long-term cyclic behaviour (corresponding to an extrapolated life of approximately 10^7 cycles). On the other hand, the predictions for the hoop dominated loading ratios are enormously conservative, considering that the plotted hoop failure stresses are probably under-valued (due to end effects).

Based on the observed results, the validity of the current $[\pm 71^\circ]_S$ specimen design depends on the required test objectives. For determining the elastic properties of the orthotropic material system, the current design is sufficient. For the determination of leakage failure, however, the current specimen design can only be considered valid for axial dominated loading ratios. The end failures observed in this study suggest that specimen end reinforcement may be necessary for this laminate geometry under hoop dominated loading conditions.

CHAPTER 6

Biaxial Testing of $[\pm 45^\circ]_S$ Tubular Specimens

6.1 MONOTONIC BEHAVIOUR

6.1.1 *Experimental Method*

The biaxial monotonic behaviour of $[\pm 45^\circ]_S$ glass-fiber epoxy tubular specimens was investigated. Biaxial tests were performed for three biaxial stress ratios: pure hoop (1H:0A), pure axial (0H:1A), and the biaxial ratio defined by netting analysis (1H:1A). The monotonic tests were performed under load control at an equivalent stress rate of 1.0 MPa/s (145 psi/s). The definition of failure was the point of abrupt leakage (burst). The tests were stopped by the control software when the volume lost by the internal pressure intensifier was approximately 150 cm^3 . For pure axial tests (0H:1A), a nominal pressure (approximately 20 to 30 psi) was applied to the tubes in order to measure the possibility of leakage, effectively making the actual loading ratio at failure approximately (1H:8A). This introduces a very small, but negligible, non-proportionality to the loading path. The fluid used for all $[\pm 45^\circ]_S$ tests was NUTO-H46 hydraulic oil, which has an absolute viscosity of 0.0656 $N.s/m^2$ ($9.52 \times 10^{-6} lb.s/in^2$) at 30°C.

6.1.2 *Pure Hoop Loading*

The monotonic stress-strain response of a $[\pm 45^\circ]_S$ tubular specimen under pure hoop loading is shown in figure 6.1. The experimental response is characterized by highly non-linear behaviour with large average strains at failure ($\sim 11\%$). This is indicative of the behaviour found by other studies for $[\pm 45^\circ]$ glass-fiber epoxy

coupon [103] and tubular specimens [182]. A stiffening in the stress-strain response can also be seen to occur starting at a hoop strain of approximately 5%. This effect is attributed to the rotation of the fibers towards the loading direction at high strain levels [278]. The average applied hoop stress at failure was 229.4 MPa.

A comparison of the experimental stress-strain curve and the predicted linear response based on classical laminate theory (CLT) is also shown in figure 6.1. The predicted linear response is seen to underestimate the experimental response in both the hoop and axial directions by approximately 20%.

Since this loading case is uniaxial with respect to the hoop direction, the global laminate hoop modulus (E_H) and Poisson's ratio (ν_{HA}) can be determined experimentally from the stress-strain curves (best fit), and predicted using CLT. Referring to figure 6.1b and 6.2, the experimental and predicted laminate hoop modulus values (E_H) are 14.3 GPa and 11.2 GPa, respectively, while the experimental and predicted hoop Poisson's ratio values (ν_{HA}) are 0.63 and 0.65, respectively. While the stiffness predictions both underestimated the experimental response, the predicted Poisson's ratio is very close to the experimental value.

As shown in figure 6.3, the macroscopic failure mode for this loading ratio was a highly destructive burst failure characterized by excessive matrix cracking and fiber breakage throughout the gage section. This is in contrast to the localized burst failure observed with the $[\pm 71^\circ]_S$ specimens under pure hoop loading. Because of the destructive nature of the failure, it was difficult to discern the failure initiation location or the effect of the ends. Not surprising, the end of the test was marked by a very loud audible indicator. As discussed in section 4.3.2, all monotonic tests (except one) were conducted in closed vessel mode which prevented any observation of the failure progression but ensured a safe testing environment. This failure demonstrates the advocacy of this decision.

6.1.3 Pure Axial Loading

The monotonic stress-strain response of a $[\pm 45^\circ]_S$ tubular specimen under pure axial loading is shown in figure 6.4. Similar to that of the pure hoop loading case, the stress-strain response is characterized by highly non-linear behaviour with relatively large average strains at failure ($\sim 9\%$). The predicted linear response, again, under-

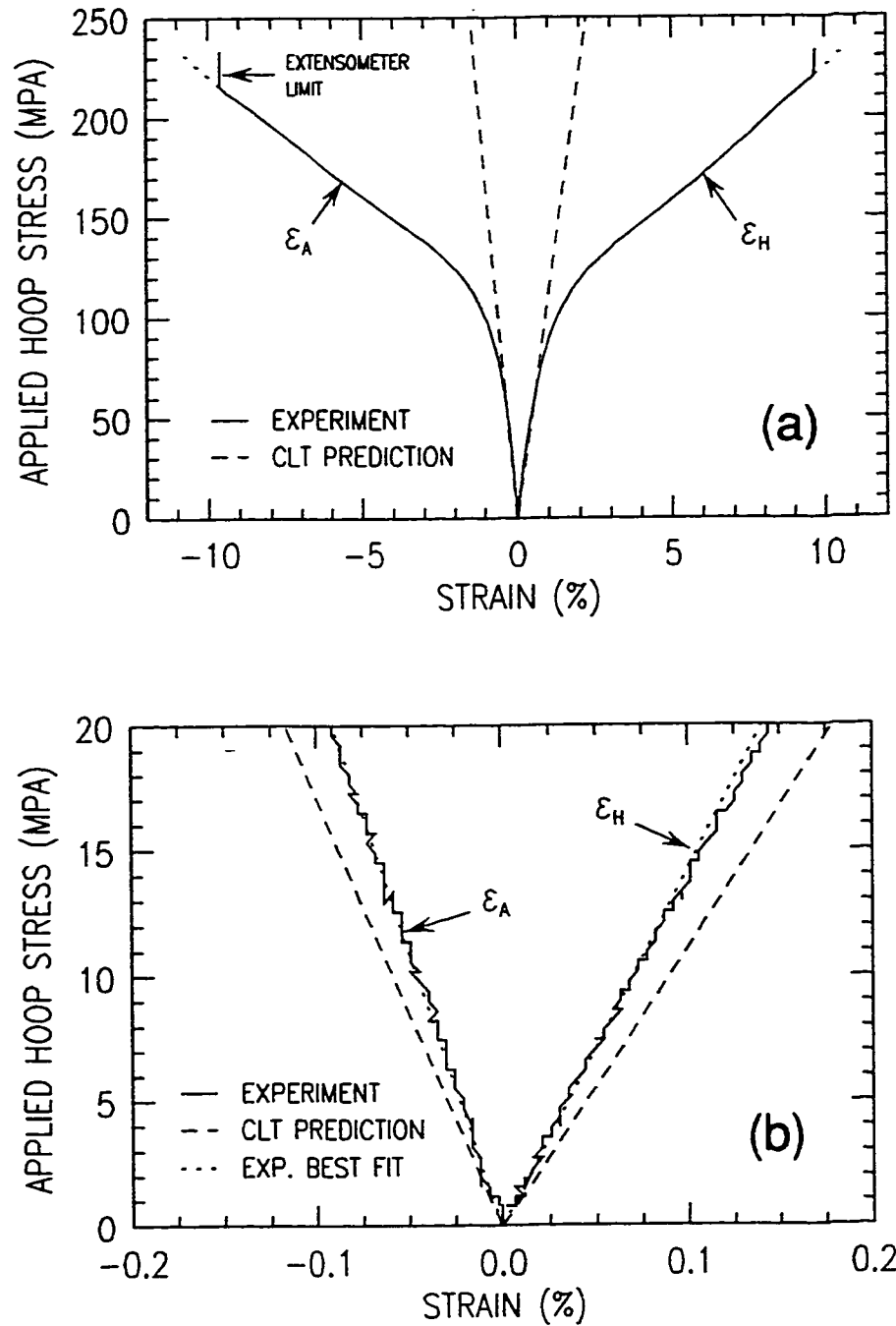


Figure 6.1: Monotonic stress-strain response of a $[\pm 45^\circ]_S$ glass-fiber reinforced epoxy tubular specimen under pure hoop loading (1H:0A); (a) stress-strain response to failure, (b) stress-strain response at the initial stages of loading.

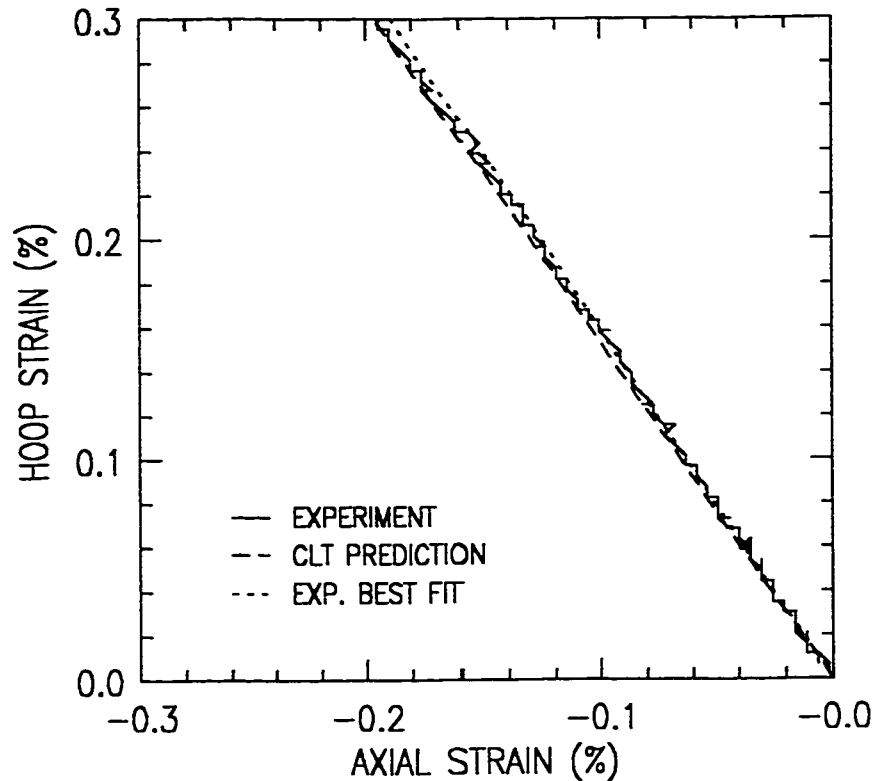


Figure 6.2: Hoop and axial strain response of a $[\pm 45^\circ]_S$ glass-fiber reinforced epoxy tubular specimen under pure hoop loading (1H:0A).

estimates the experimental results by approximately 25%. The average applied axial stress at failure was 159.0 MPa. Referring to figures 6.4b and 6.5, the experimental and predicted laminate axial modulus values (E_A) are 15.0 GPa and 11.2 GPa, respectively, while the experimental and predicted axial Poisson's ratio values (ν_{AH}) are 0.59 and 0.65, respectively. These values are in general agreement with the pure hoop loading case.

In order to check if the $[\pm 45^\circ]_S$ lay-up can be modeled as a linear elastic orthotropic unit, equation 5.1 can again be invoked. Calculation of the left and right hand sides of equation 5.1 are presented in table 6.1.3. As found for the $[\pm 71^\circ]_S$ geometry, the experimentally determined values of ν_{HA}/E_H and ν_{AH}/E_A are within 10% of each other, signifying verification of the assumption. The discrepancy with the predicted constants implies that the elastic properties used in the analysis may be underestimated.



Figure 6.3: *Burst failure mode for a $[\pm 45^\circ]_S$ glass-fiber reinforced epoxy tubular specimen under pure hoop (1H:0A) monotonic loading.*

Table 6.1: *Experimentally and analytically derived elastic laminate constants for $[\pm 45^\circ]_S$ glass-fiber reinforced epoxy tubular specimens.*

	E_H (GPa)	E_A (GPa)	ν_{HA}	ν_{AH}	ν_{HA}/E_H (GPa) ⁻¹	ν_{AH}/E_A (GPa) ⁻¹
EXPERIMENT	14.3	15.0	0.63	0.59	0.0441	0.0393
PREDICTION (CLT)	11.2	11.2	0.65	0.65	0.0580	0.0580

The observed macroscopic failure mode for the pure axial loading case is a single helical fracture resulting in total separation of the specimen in the gage section as shown in figure 6.6. The fracture path is parallel to the fiber angle orientation of the surface layer, and is characterized by a combination of matrix cracking and fiber breakage. Since the internal fluid pressure was at a nominally low value (approximately 20 to 30 psi), the loss of fluid occurred only when sufficient damage to the specimen (ultimate failure) had occurred.

6.1.4 Loading Based on Netting Analysis (Equi-biaxial)

The monotonic stress-strain response of a $[\pm 45^\circ]_S$ tubular specimen under equi-biaxial loading (1H:1A) is shown in figure 6.7. It can be seen that the behaviour

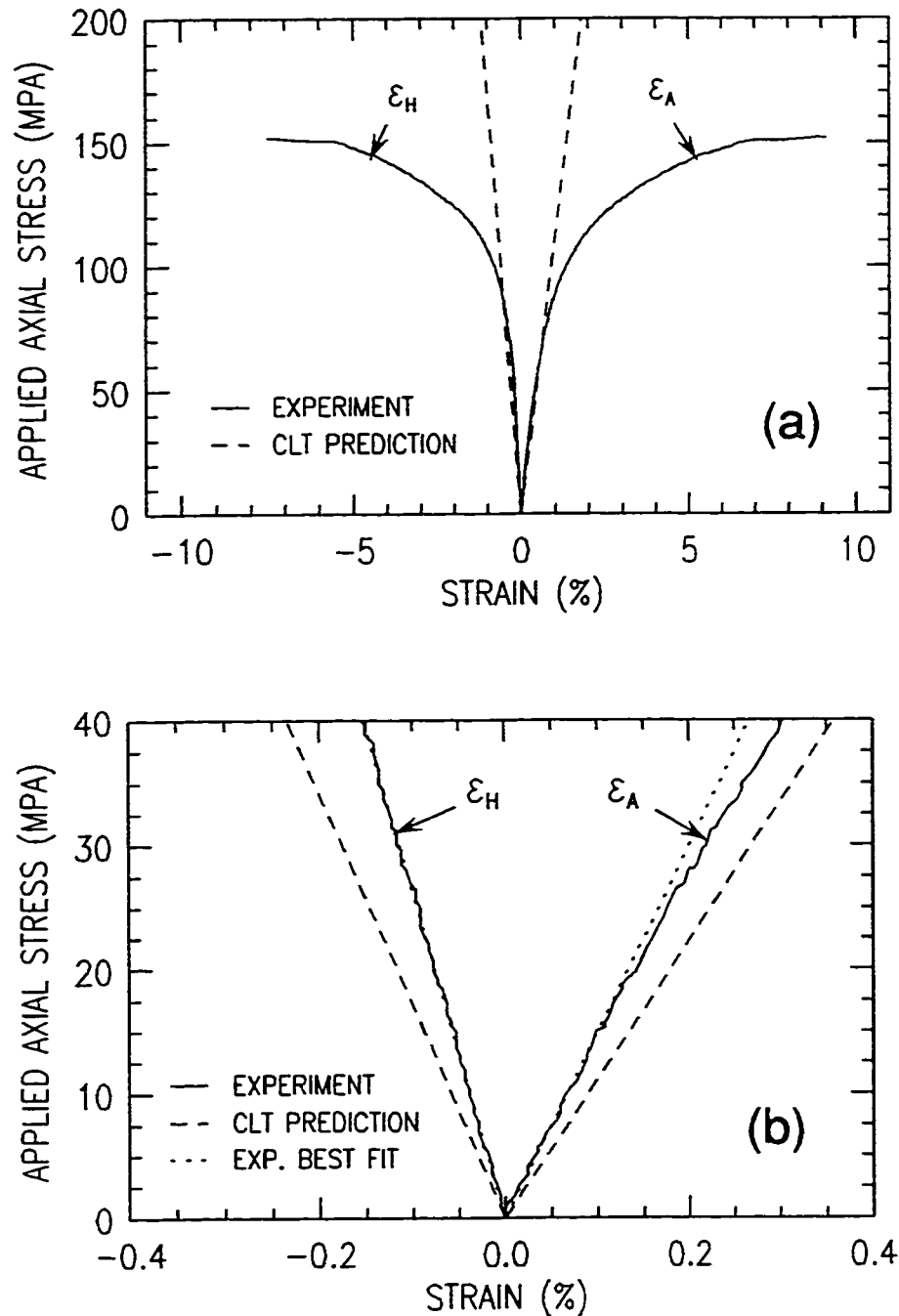


Figure 6.4: Monotonic stress-strain response of a $[\pm 45^\circ]_S$ glass-fiber reinforced epoxy tubular specimen under pure axial loading (0H:1A); (a) stress-strain response to failure, (b) stress-strain response at the initial stages of loading.

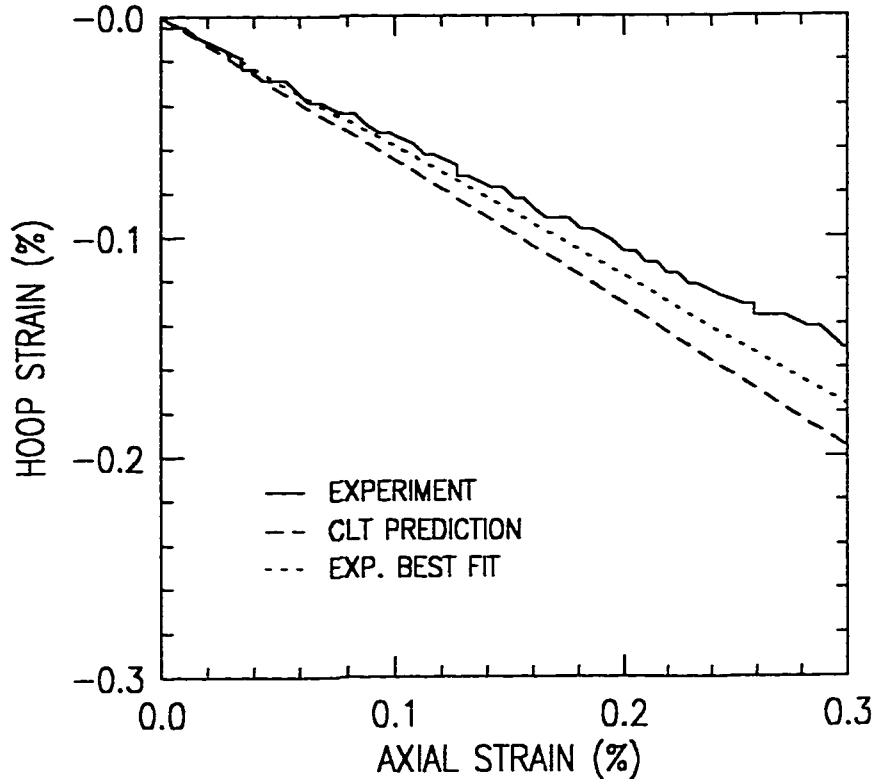


Figure 6.5: Hoop and axial strain response of a $[\pm 45^\circ]_S$ glass-fiber reinforced epoxy tubular specimen under pure axial loading (0H:1A).

exhibits only marginal non-linearity with strains at failure being approximately 1%, characteristic of fiber dominated loading conditions. This is in sharp contrast to the large strain, non-linear response for the same lay-up under pure hoop (1H:0A) and pure axial (0H:1A) loading. Contrary to the predicted equivalence under equibiaxial loading, a difference in the stress-strain response for the hoop and axial strain measurements was observed. The axial measurement is seen to exhibit more non-linearity and a higher strain at failure (see figure 6.7). The linear response predicted by CLT shows better correlation to the experimental results in the axial direction. The average applied stress at failure (hoop or axial) was 230.7 MPa, the highest for all three loading ratios considered.

The relationship between the hoop and axial strains for this loading ratio is shown in figure 6.8. Similar to the stress-strain response, the deviation from linearity is seen to occur almost from the start of the test. The predicted response seems to fit the initial trend.

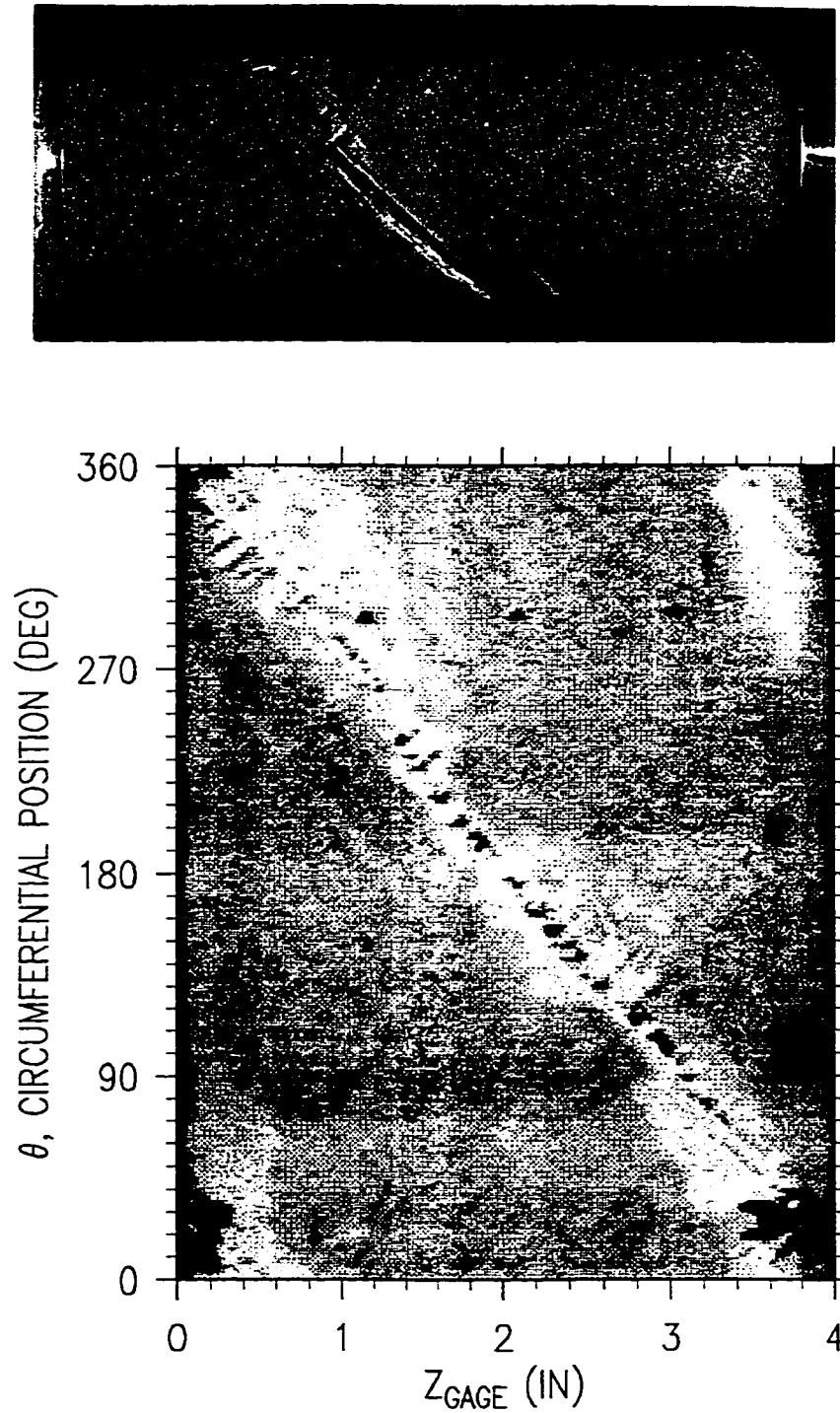


Figure 6.6: *Macroscopic failure modes for $[\pm 45^\circ]_S$ glass-fiber reinforced epoxy tubular specimen under pure axial (0H:1A) monotonic loading; (top) front view, (bottom) surface map.*

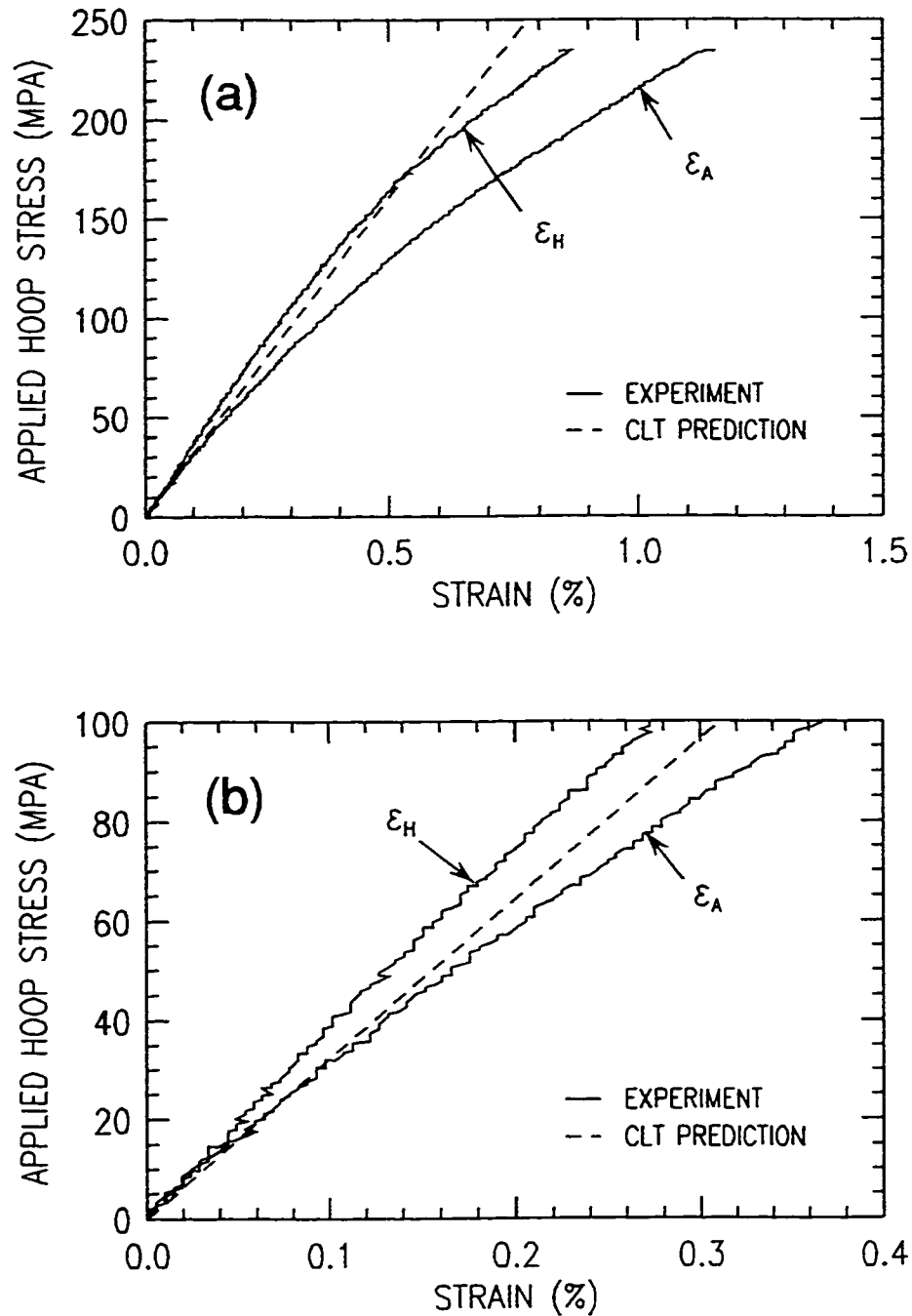


Figure 6.7: Monotonic stress-strain response of a $[\pm 45^\circ]_S$ glass-fiber reinforced epoxy tubular specimen under equi-biaxial loading (1H:1A); (a) stress-strain response to failure, (b) stress-strain response at the initial stages of loading.

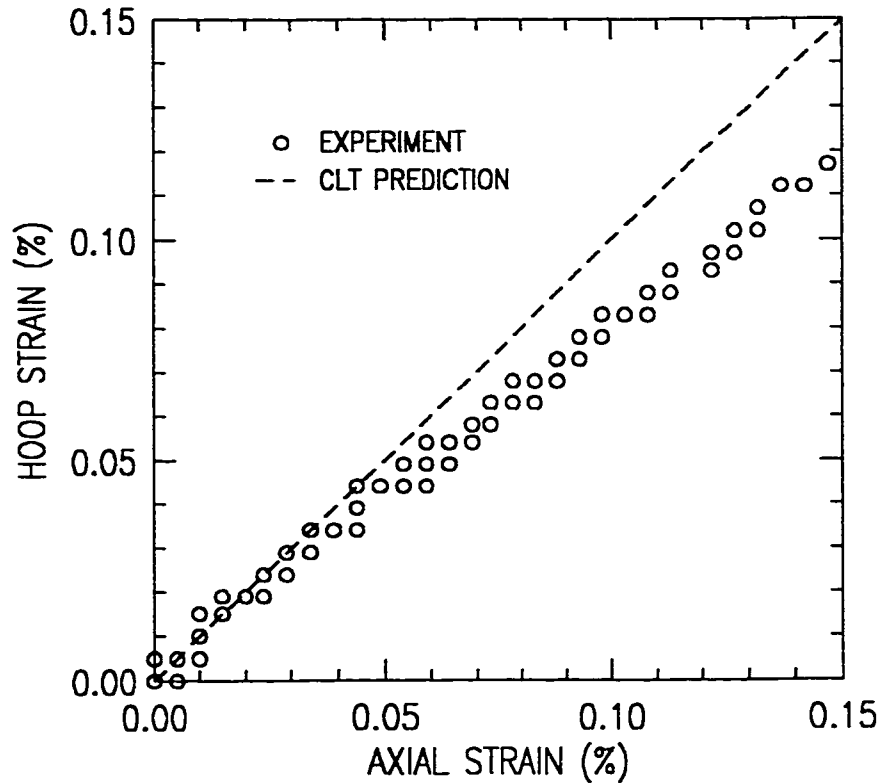


Figure 6.8: Hoop and axial strain response of a $[\pm 45^\circ]_S$ glass-fiber reinforced epoxy tubular specimen under equi-biaxial loading (1H:1A).

Referring to figure 6.9, it can be seen that the macroscopic failure mode observed for this loading case was identical to that observed for the pure axial loading case. This failure mode is characterized by a single helical fracture resulting in total separation of the specimen in the gage section.

6.2 CYCLIC BEHAVIOUR

6.2.1 Experimental Method

Biaxial cyclic tests were performed on $[\pm 45^\circ]_S$ glass-fiber epoxy tubular specimens for three biaxial loading ratios: pure hoop (1H:0A), axial dominated (1H:8A), and equi-biaxial (1H:1A). The (1H:8A) loading ratio was substituted for the pure axial (0H:1A) loading case (used in the monotonic tests) in order to maintain proper biaxial proportionality. The cyclic tests were performed under load control with a cyclic stress

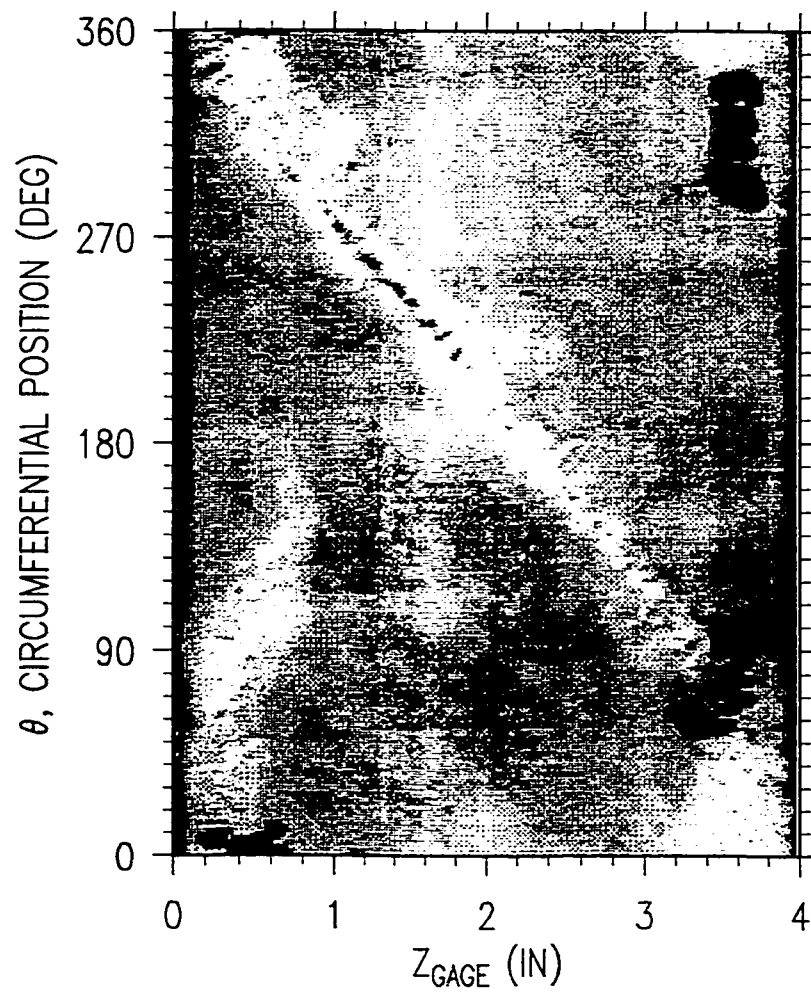


Figure 6.9: *Macroscopic failure modes for $[\pm 45^\circ]_S$ glass-fiber reinforced epoxy tubular specimen under equi-biaxial (1H:1A) monotonic loading; (top) front view, (bottom) surface map.*

ratio of $R = 0.1$ ($R = \sigma_{min}/\sigma_{max}$). A sine waveform was used with a cyclic frequency of 1 Hz. The tests were stopped by the control software when the volume lost by the internal pressure intensifier was approximately 150 cm^3 . For some tests which exhibited moderate leakage rates, the intensifier was refilled, and the test continued.

Since uniform weepage was encountered for this geometry under cyclic loading, critical permeability was used to define leakage failure (see section 4.2.1). Using equations 4.7 and 4.9, two critical values (0.1×10^{-12} and $10.0 \times 10^{-12} \text{ mm}^2$) were selected in order to quantify the initiation and post-initiation leakage behaviour. Both values were chosen based on the available range of measured permeabilities.

In an effort to determine the relationship between leakage and the physical damage state in the specimen, the following damage indicators were determined: a) cyclic creep strain evolution, and b) elastic stiffness reduction.

The maximum and minimum cyclic creep strains were determined from the measured stress-strain loops. For an angle-ply ($\pm\theta$) geometry under in-plane normal loading conditions, the average (in-plane) strain state in each layer is assumed to be equivalent due to strain compatibility throughout the laminate [6]. In order to better understand the relative contributions of each lamina strain component, the average strains in the material coordinate system (1, 2, 12) were derived from the measured principal strains (hoop and axial) using the following transformation (see figure 1.2):

$$\epsilon_1 = m^2 \epsilon_a + n^2 \epsilon_h$$

$$\epsilon_2 = n^2 \epsilon_a + m^2 \epsilon_h,$$

and

$$\gamma_{12} = 2 m n \epsilon_h - 2 m n \epsilon_a \tag{6.1}$$

where, $m = \cos \theta$, $n = \sin \theta$, and θ is the fiber angle orientation of the angle-ply (with respect to the axial direction).

For a $[\pm 45^\circ]$ angle-ply laminate, equations 6.1 become,

$$\epsilon_1 = \epsilon_2 = \frac{1}{2} (\epsilon_a + \epsilon_h),$$

and

$$\gamma_{12} = \epsilon_h - \epsilon_a \quad (6.2)$$

Damage accumulation under cyclic loading was characterized by measuring the global stiffness reduction in various loading directions. Three monotonic ramps (pure axial, torsion and pure hoop) were carried out at regular intervals during a cyclic test in order to quantify the axial, shear and hoop stiffness reduction*. For each loading ratio, stiffness reduction measurements were performed at two maximum applied stress levels (short-term and long-term). These applied stress levels were determined from the fatigue-life curves established by continuous cyclic tests (no stoppages). Before the start of each stiffness reduction test, a measurement was made to determine the initial stiffness values.

The monotonic ramps used to measure stiffness were performed at a loading rate of 0.1 MPa/s upto a maximum applied stress level of 10 MPa (unless otherwise noted). The maximum ramp limit was selected based on the long-term (10^6) stress levels taken from the baseline fatigue-life curves. From the resulting monotonic stress-strain curves, the elastic stiffness was calculated using linear regression based on all data points from 0 to 5 MPa. The volume lost during the monotonic ramps represented less than 1% of the total volume lost during the entire test. Before beginning each ramp, a hold period was issued (at zero load) until all measured strain rates fell below 10^{-6} s^{-1} . This was done to ensure that any visco-elastic relaxation effects at the end of the previous test did not influence the subsequent elastic stiffness measurements. This was the procedure used by Joseph and Perreux [201] for similar stiffness reduction tests on $[\pm 55^\circ]$ glass-fiber epoxy tubular specimens.

6.2.2 Pure Hoop Loading

A representative stress-strain response of a $[\pm 45^\circ]_S$ tubular specimen under pure hoop cyclic loading is shown in figure 6.10. The behaviour is characterized by significant cyclic creep and a progressively decreasing stiffness. The linear limit for each

*A second axial ramp was initially added to the sequence to verify if damage was introduced during the stiffness measurement procedure. The second axial stiffness values were subsequently found to be identical to the first, implying that the measurement procedure was, indeed, benign.

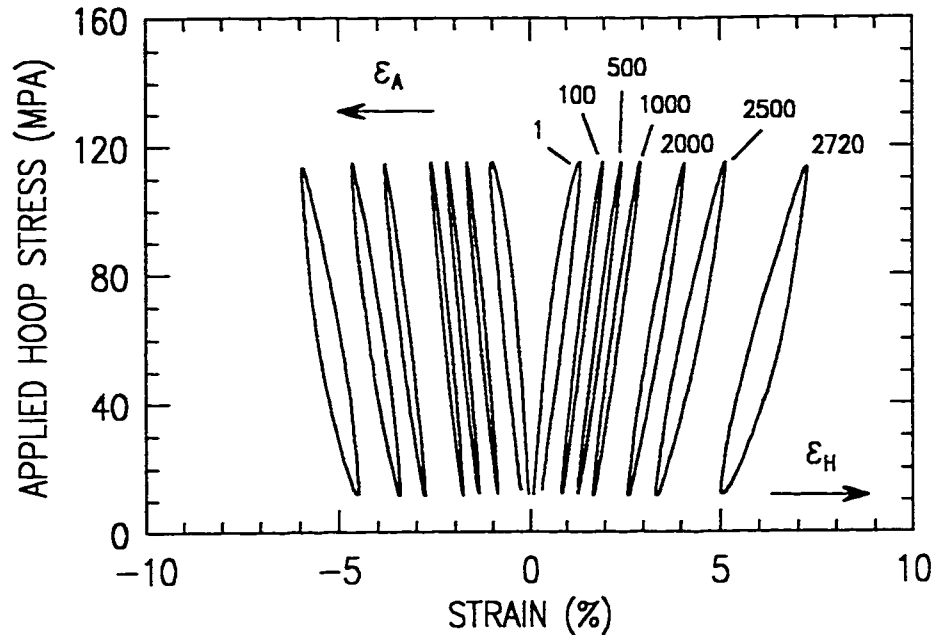


Figure 6.10: Representative cyclic stress-strain curve for $[\pm 45^\circ]_S$ glass-fiber reinforced epoxy tubular specimens under pure hoop loading (1H:0A) - ($\sigma_{h \max} = 115$ MPa).

successive loop is seen to drop with a noticeable increase in non-linear behaviour as the test progresses. The resulting enlargement of the hysteresis loops is representative of energy dissipation as a result of damage accumulation and heat generation. Referring to figure 6.11, it can be seen that the temperature rise is relatively moderate with two noticeable increases at the start and end of the test. The repeated temperature rises noted in this figure are the result of stoppages where monotonic stiffness measurements were made.

Macroscopic surface damage was seen to occur only for tests at the highest maximum stress levels, as shown in figure 6.12. This damage is characterized by a number of branching surface and sub-surface cracks with localized fiber breakage. Delamination (identified by the general whitened area) is also seen to occur at the center of the specimen. Although no visible surface damage was noted for the tests at lower maximum applied stresses, uniform weepage throughout the gage section was observed using penetrant tracers (see figure 6.13). The array of singular weepage points are the intersections of matrix cracks (along the fiber direction) in surface and sub-surface layers of the specimen.

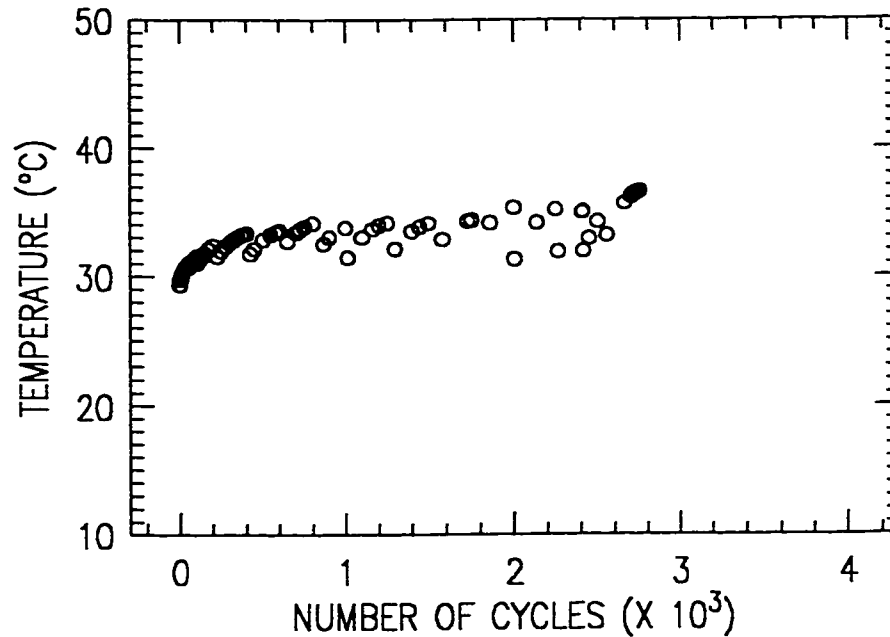


Figure 6.11: Measured surface temperature of a $[\pm 45^\circ]_S$ glass-fiber reinforced epoxy tubular specimens under pure hoop (1H:0A) cyclic loading - ($\sigma_{h \max} = 115 \text{ MPa}$).

The effect of applied maximum stress on the progressive nature of damage can be readily observed from the fluid volume loss (leakage) profiles, and the associated permeability curves. For tests conducted at a maximum hoop stress of 115 MPa, 100 MPa and 70 MPa, these curves are shown in figures 6.14, 6.15 and 6.16, respectively. From these figures, two phenomena are observed as the maximum applied stress level is decreased: a) the number of cycles to leakage initiation increases (i.e. initiation is delayed), and b) the subsequent fluid loss rate after initiation is seen to decrease. This second observation is reflected by a decreasing permeability value indicating significantly lower damage accumulation rates. For the highest applied stress level (figure 6.14), the leakage is seen to occur immediately from the start of the test with the resulting leakage rate (and permeability) being constant. This implies that matrix cracking is already saturated by the first few cycles. At the end of the test, abrupt fluid loss is noted, indicating the development of a dominant leakage path (confirmed by visible surface damage).

Using the permeability profiles, fatigue-life curves were constructed based on critical permeabilities of $0.1 \times 10^{-12} \text{ mm}^2$ (initiation) and $10 \times 10^{-12} \text{ mm}^2$ (post-initiation), as shown in figure 6.17. A linear (semi-log) equation was fit to both sets of data, and

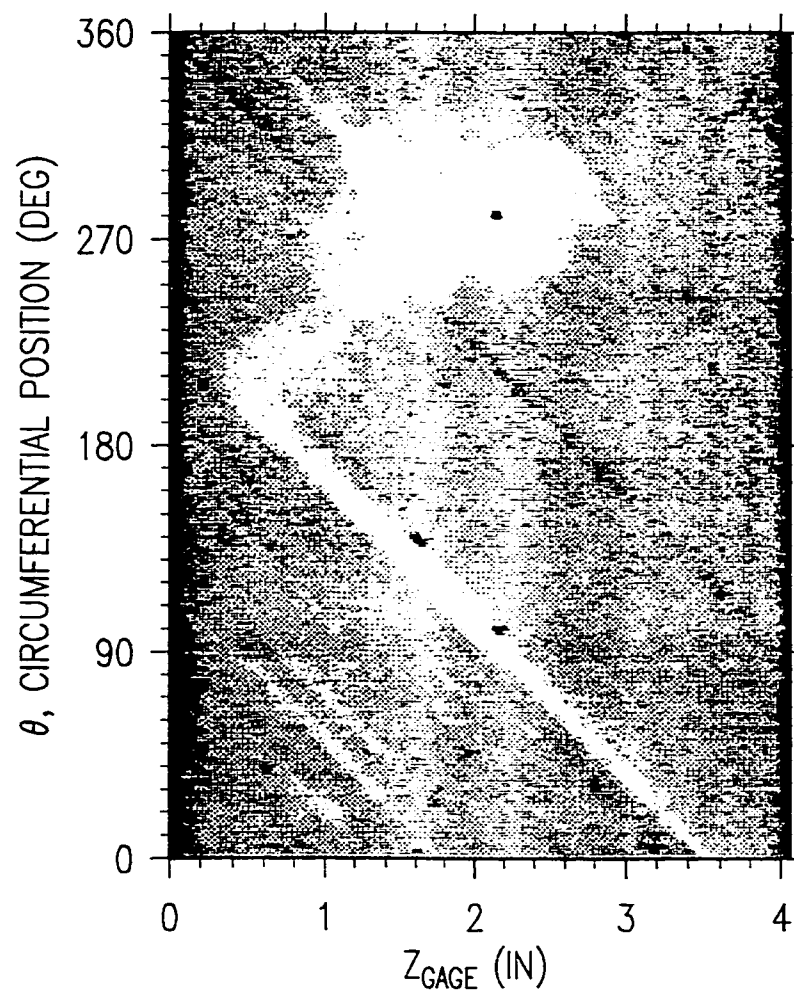


Figure 6.12: Macroscopic failure modes for $[\pm 45^\circ]_S$ glass-fiber reinforced epoxy tubular specimen under pure hoop (1H:0A) cyclic loading: (top) front view, (bottom) surface map.



Figure 6.13: *Weepage failure mode for $[\pm 45^\circ]_S$ glass-fiber reinforced epoxy tubular specimen under pure hoop (1H:0A) cyclic loading.*

was found to be a good representation in both cases. The results show a typical increase in leakage life with reduction in the maximum applied cyclic stress level. The difference in failure lives between the two critical values chosen is almost an order of magnitude. For applications where some loss of fluid is tolerable, these types of curves can significantly extend the expected design life.

Cyclic Creep Strain - (1H:0A)

The cyclic creep strain responses for short-term ($\sigma_{h \max} = 115$ MPa) and long-term ($\sigma_{h \max} = 70$ MPa) tests under pure hoop cyclic loading are presented in figures 6.18 and 6.19, respectively. In each figure, the measured creep strain in both the global (loading) and material coordinate systems is presented. The transformation between coordinate systems is made using equations 6.2. As shown in both figures, the creep response in the loading directions is due solely to the material's in-plane shear (γ_{12}) behaviour. It is interesting to note that this shear strain dominance is seen to occur for the entire duration of the tests. However, it is not known what portion of this response is recoverable (visco-elastic).

In comparing figures 6.18 and 6.19, it can be seen that a general increase in the creep rate occurs for the test with the higher applied maximum stress. The creep rate is seen to significantly increase at both the start and end of the test, with the middle period characterized by a slow and steady increase in cyclic creep. This three stage creep response is seen to correspond directly to the temperature profile shown in figure 6.11, and is consistent with observations made in other studies [25,279].

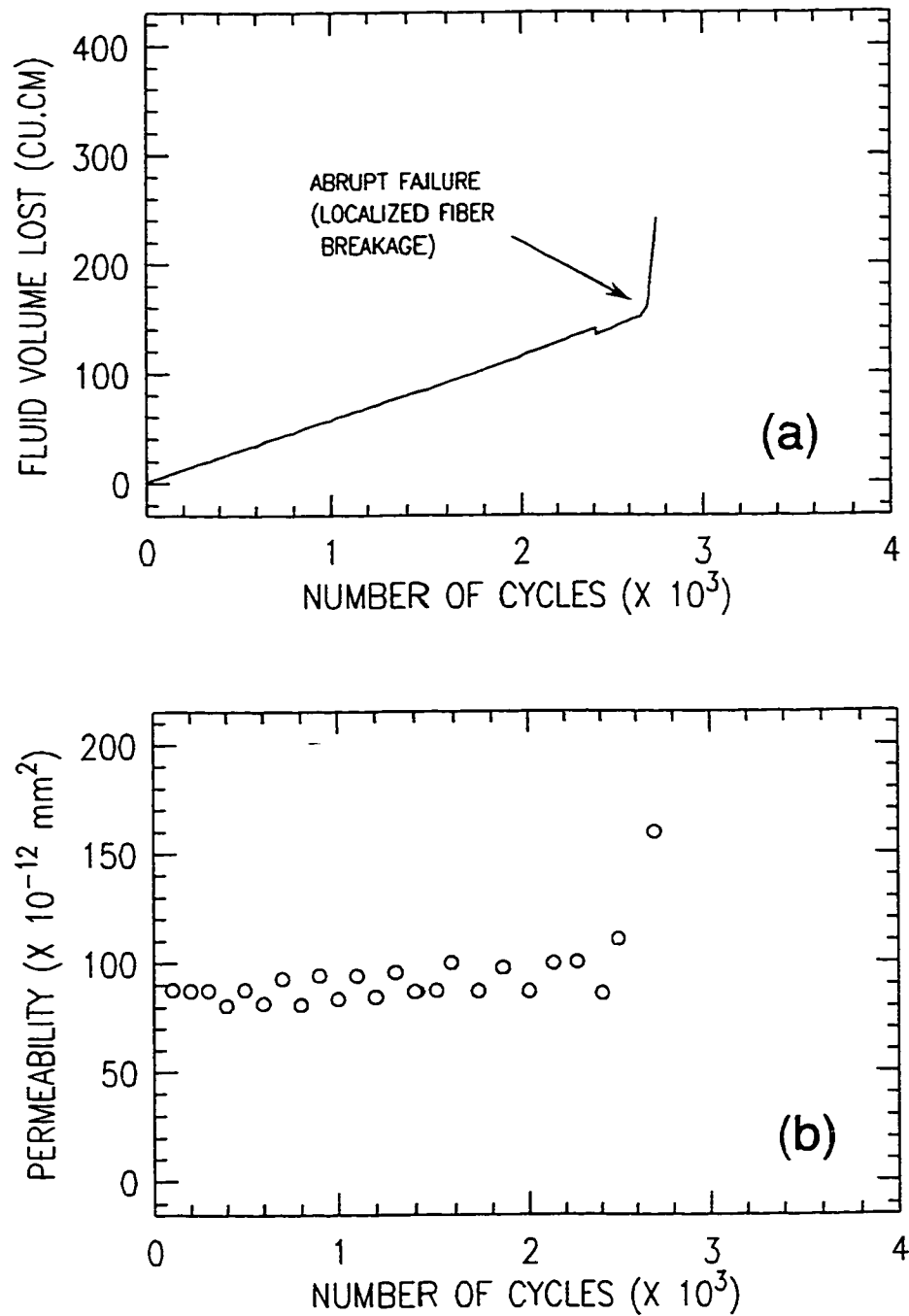


Figure 6.14: Fluid loss characteristics of a $[\pm 45^\circ]_S$ glass-fiber reinforced epoxy tubular specimen under pure hoop loading ($1H:0A$) - ($\sigma_{h \max} = 115$ MPa); (a) fluid volume loss (leakage) profile, (b) derived permeability curve.

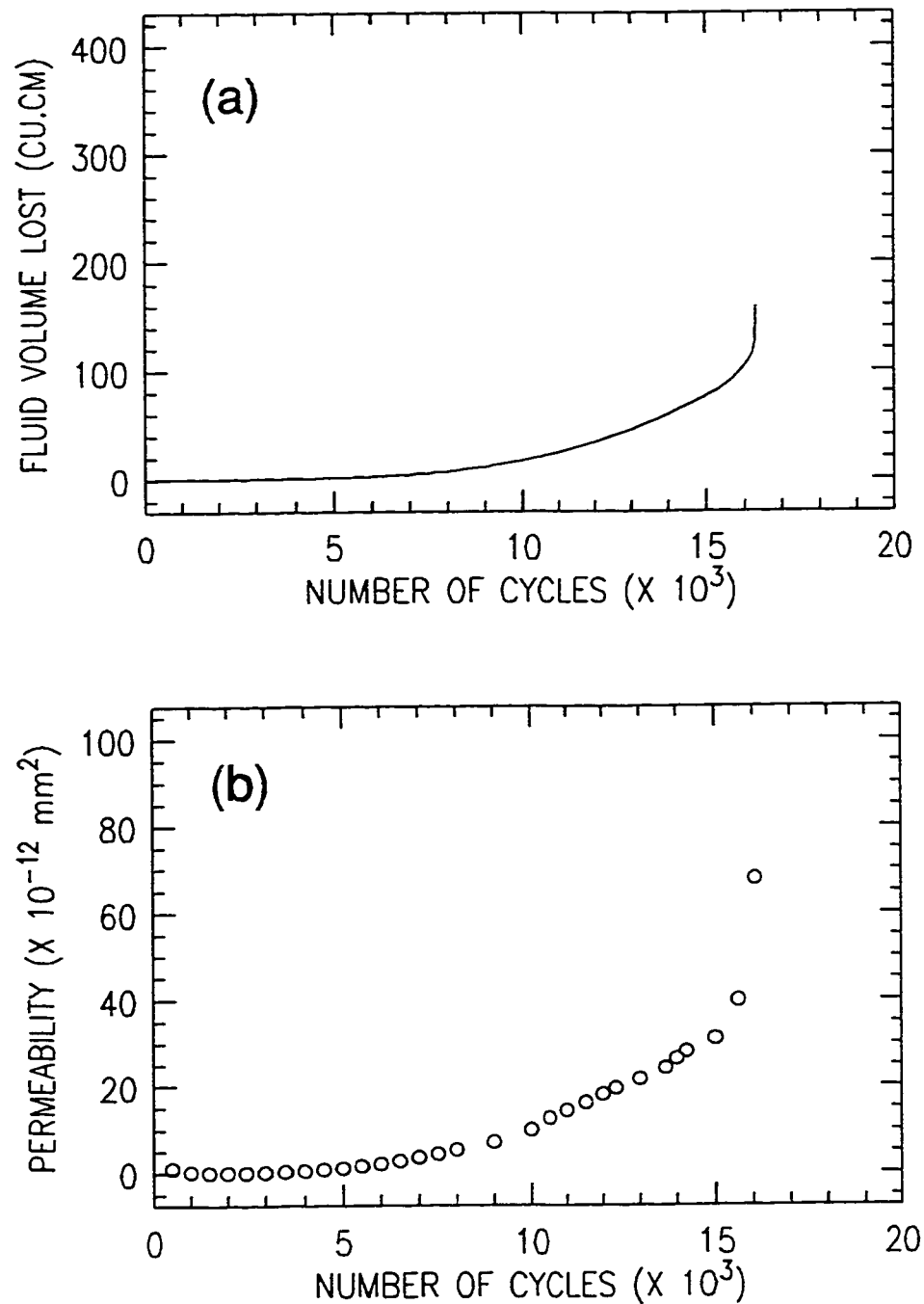


Figure 6.15: Fluid loss characteristics of a $[\pm 45^\circ]_S$ glass-fiber reinforced epoxy tubular specimen under pure hoop loading (1H:0A) - ($\sigma_{h \max} = 100$ MPa); (a) fluid volume loss (leakage) profile, (b) derived permeability curve.

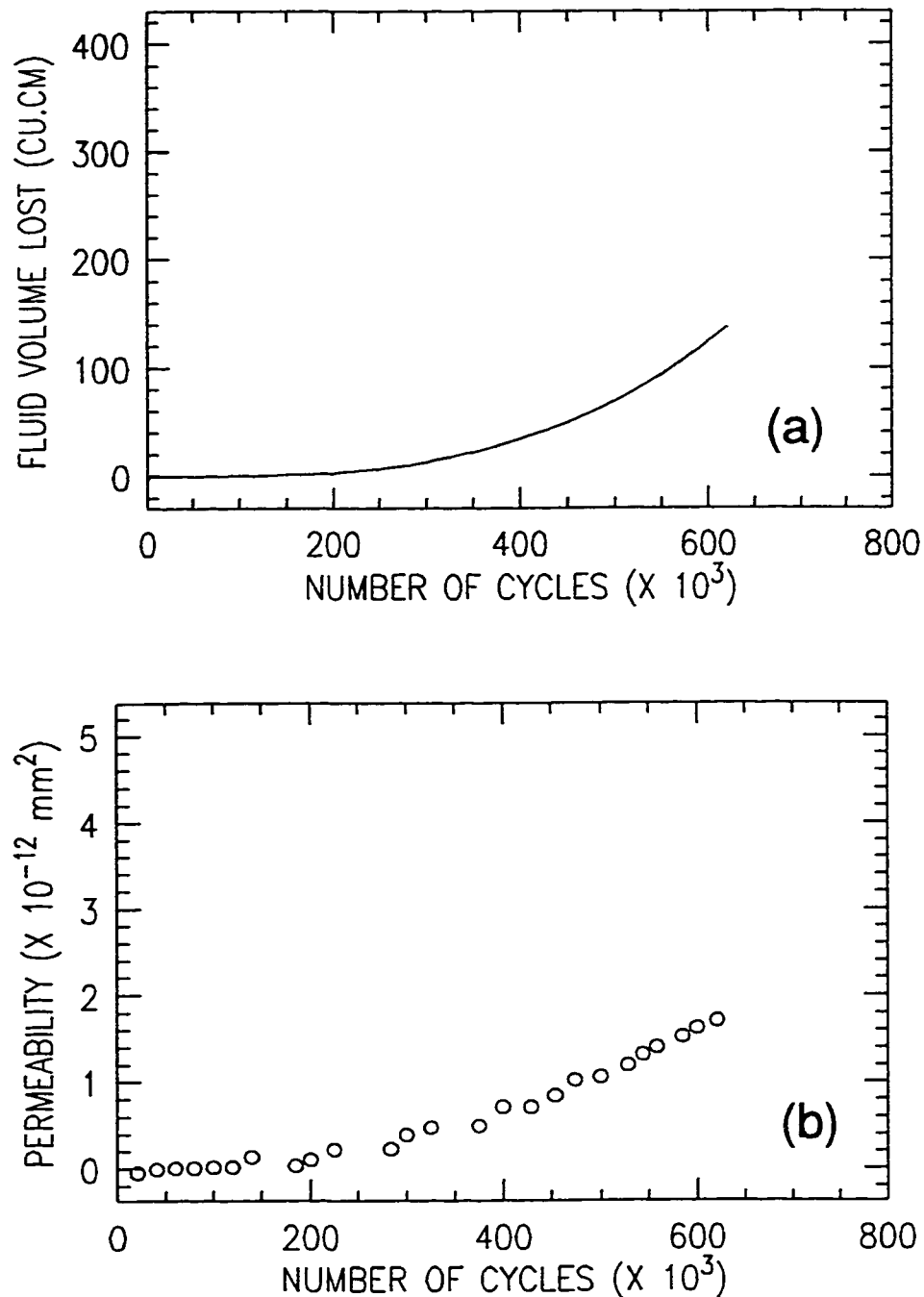


Figure 6.16: Fluid loss characteristics of a $[\pm 45^\circ]_S$ glass-fiber reinforced epoxy tubular specimen under pure hoop loading (1H:0A) - ($\sigma_{h \max} = 70$ MPa); (a) fluid volume loss (leakage) profile, (b) derived permeability curve.

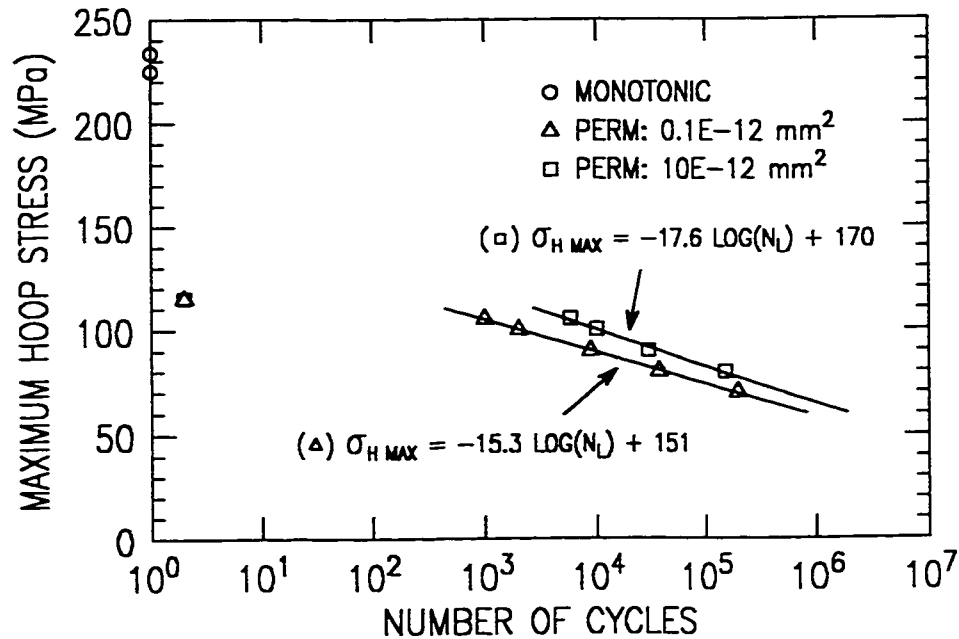


Figure 6.17: *Fatigue-life relationships for $[\pm 45^\circ]_S$ glass-fiber reinforced epoxy tubular specimens under pure hoop loading (1H:0A) based on critical permeability criterion.*

In an effort to define a possible threshold strain value at which leakage occurs, shear creep strain values were correlated with the calculated permeability, as shown in figure 6.20. The threshold for leakage initiation is seen to fall between a maximum shear strain of approximately 1.5% to 2.5% for the applied stress levels indicated. These threshold values are much smaller than the shear strains at burst observed under monotonic loading ($\sim 20\text{-}25\%$). Subsequent increases in permeability with increasing creep strain reflect the progressive formation and connectivity of matrix cracking. Since all tests were stopped after a fixed volume loss of approximately 170 cm^3 , it can be seen that the tests at a higher maximum stress level incurred more damage than that at the lower levels which is reflected by the differences in final permeabilities.

Stiffness Reduction - (1H:0A)

Stiffness reduction was measured for the pure hoop cyclic tests at maximum applied stress levels of 115 MPa (short-term) and 70 MPa (long-term). The resulting laminate axial, hoop and shear stiffness measurements for the *short-term test* ($\sigma_{h\text{ max}} = 115\text{ MPa}$) are shown in figures 6.21, 6.22 and 6.23, respectively. The stiffness values

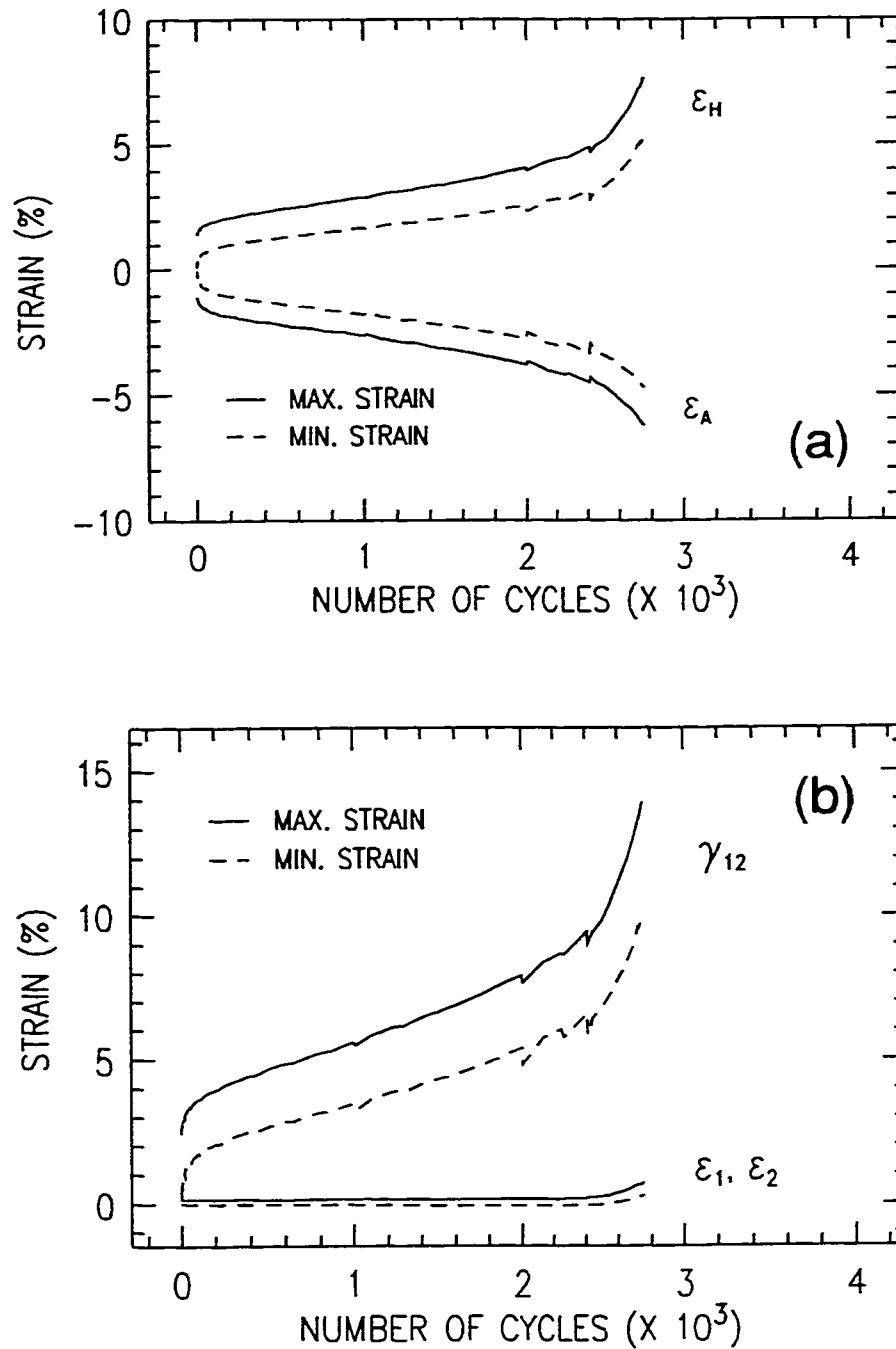


Figure 6.18: Measured cyclic creep strain curves for $[\pm 45^\circ]_S$ glass-fiber reinforced epoxy tubular specimens under pure hoop loading (1H:0A) - short-term test ($\sigma_{h \max} = 115$ MPa); (a) in global coordinates (loading directions), (b) in material coordinates.

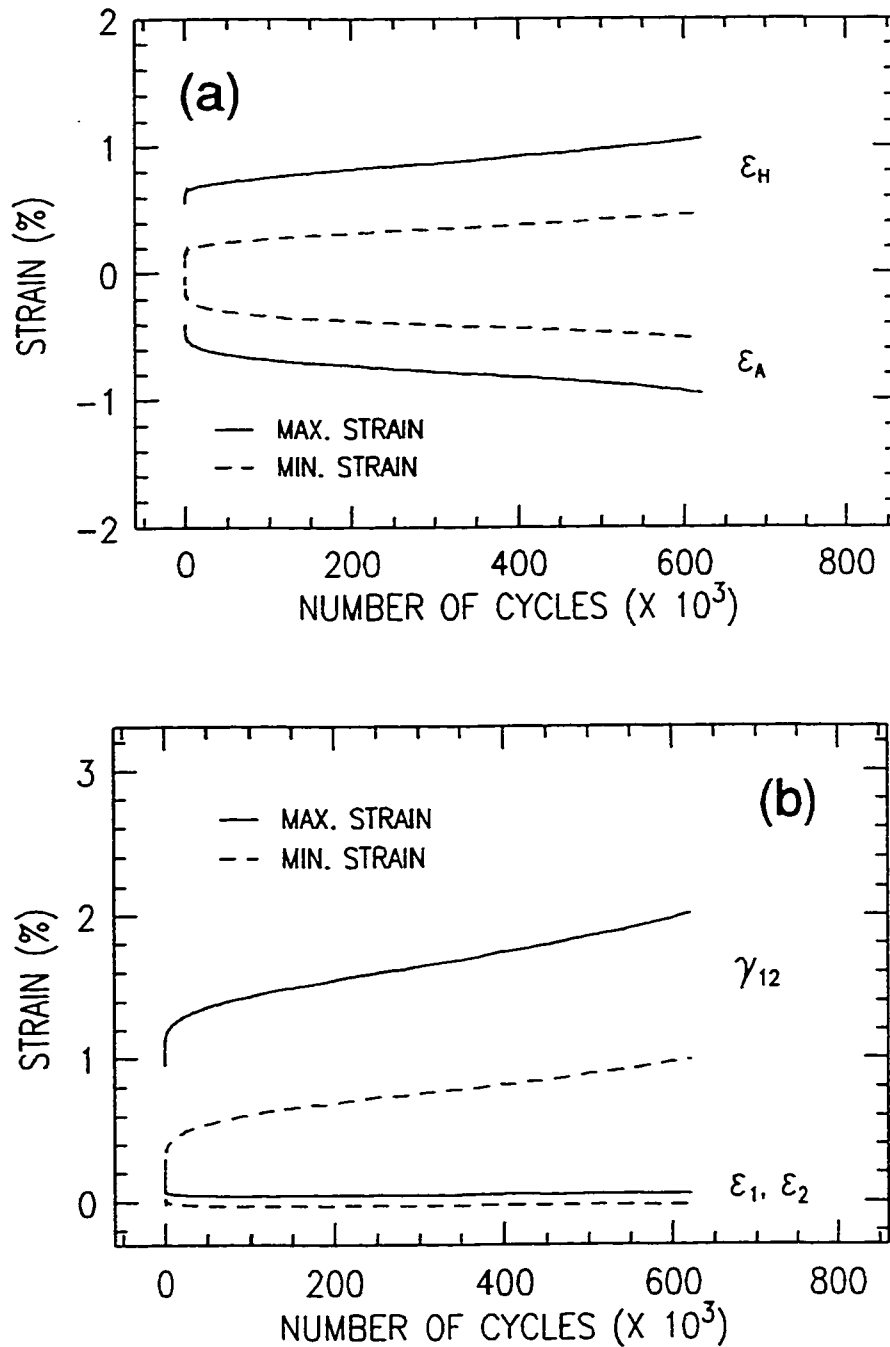


Figure 6.19: Measured cyclic creep strain curves for $[\pm 45^\circ]_S$ glass-fiber reinforced epoxy tubular specimens under pure hoop loading (1H:0A) - long-term test ($\sigma_{h \max} = 70$ MPa); (a) in global coordinates (loading directions), (b) in material coordinates.

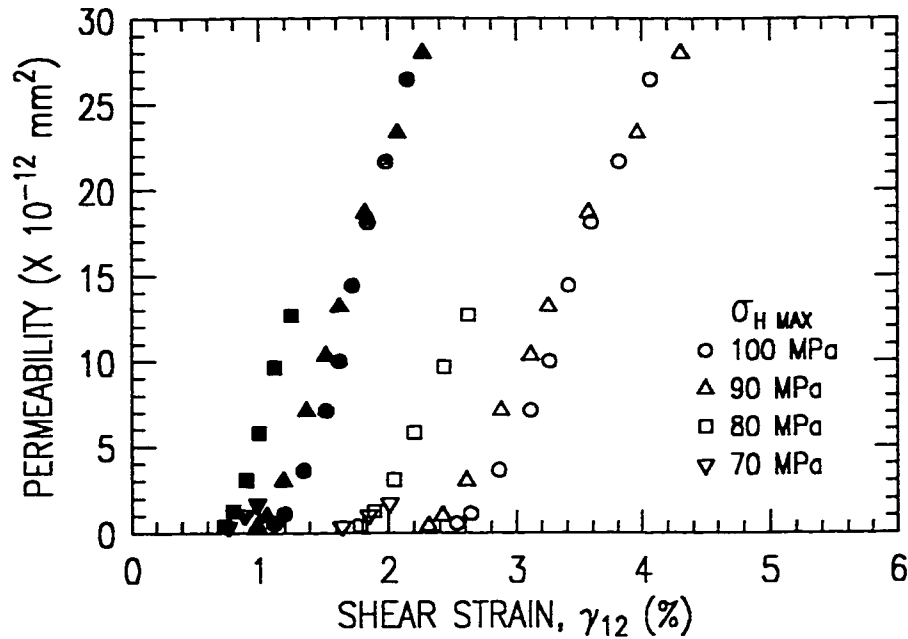


Figure 6.20: Relationship between the permeability and cyclic creep (shear) strain for $[\pm 45^\circ]_S$ glass-fiber reinforced epoxy tubular specimens under pure hoop loading (1H:0A); (open symbols) maximum cyclic shear strain value, and (closed symbols) minimum cyclic shear strain value.

are non-dimensionalized with respect to the initial value measured prior to the start of the cyclic test. The predicted initial and fully discounted[†] stiffness values based on classical laminate theory (CLT) are also presented.

From the axial and hoop stiffness measurements (figures 6.21 and 6.22), the progressive accumulation of damage is readily seen by decreases in the elastic modulus (reflected by the decreasing slope of the fitted lines) and stress at the linear elastic limit. This drop in linear elastic limit explains the enlarging hysteresis loops observed in the cyclic stress-strain response. The shift in the starting points of the monotonic curves reflects the presence of cyclic creep. Due to the symmetry of loading with respect to the laminate geometry, the stiffness reduction curves for both the axial and hoop measurements are practically identical[‡]. For these two loading conditions, the global response is clearly dominated by the behaviour of the matrix. This is

[†]The discounted predictions are determined using the classical assumption that the material's transverse modulus (E_2) and shear modulus (G_{12}) are both reduced to a nominally low value (a value of 0.69 MPa was used for each).

[‡]Since this equivalence was found for all stiffness measurements conducted in this study, only the axial stiffness reduction curves will be presented for the remainder of this chapter.

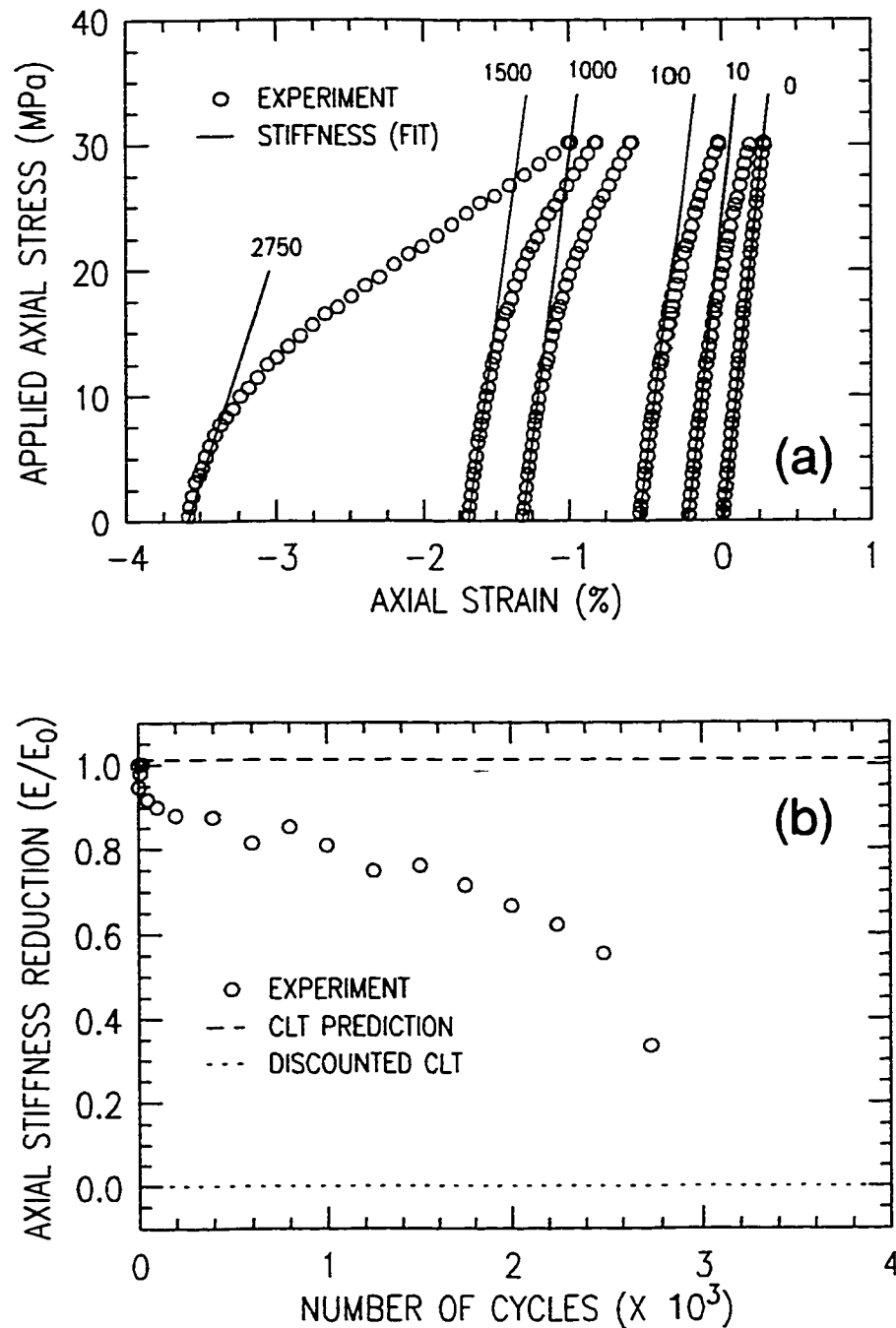


Figure 6.21: Measured axial laminate stiffness reduction of a $[\pm 45^\circ]_S$ glass-fiber reinforced epoxy tubular specimen under pure hoop (1H:0A) cyclic loading - ($\sigma_{h \max} = 115 \text{ MPa}$); (a) stiffness reduction evolution for selected monotonic ramps at indicated cycle numbers, (b) derived stiffness reduction curve.

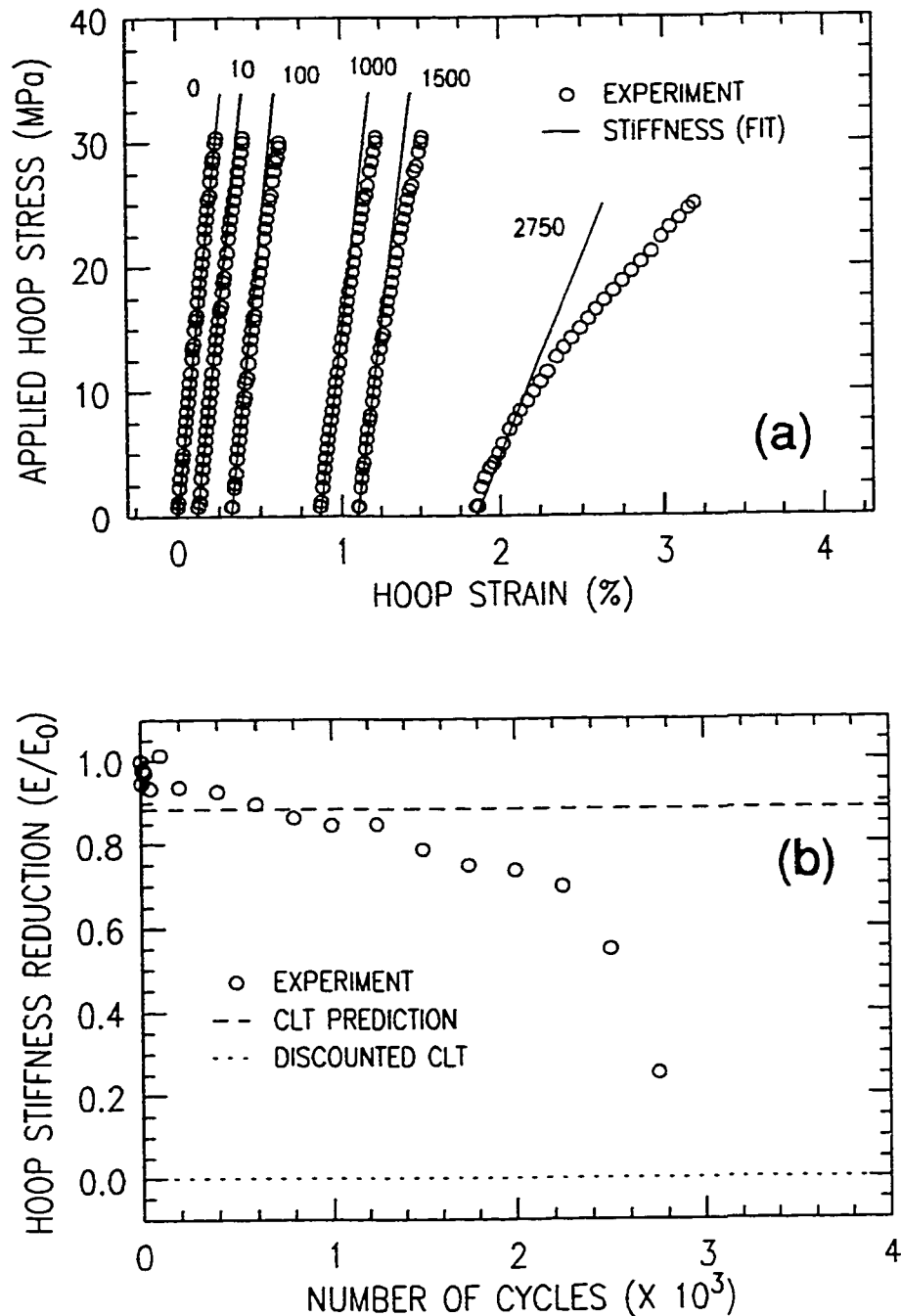


Figure 6.22: Measured hoop laminate stiffness reduction of a $[\pm 45^\circ]_S$ glass-fiber reinforced epoxy tubular specimen under pure hoop (1H:0A) cyclic loading - ($\sigma_{h \max} = 115$ MPa); (a) stiffness reduction evolution for selected monotonic ramps at indicated cycle numbers, (b) derived stiffness reduction curve.

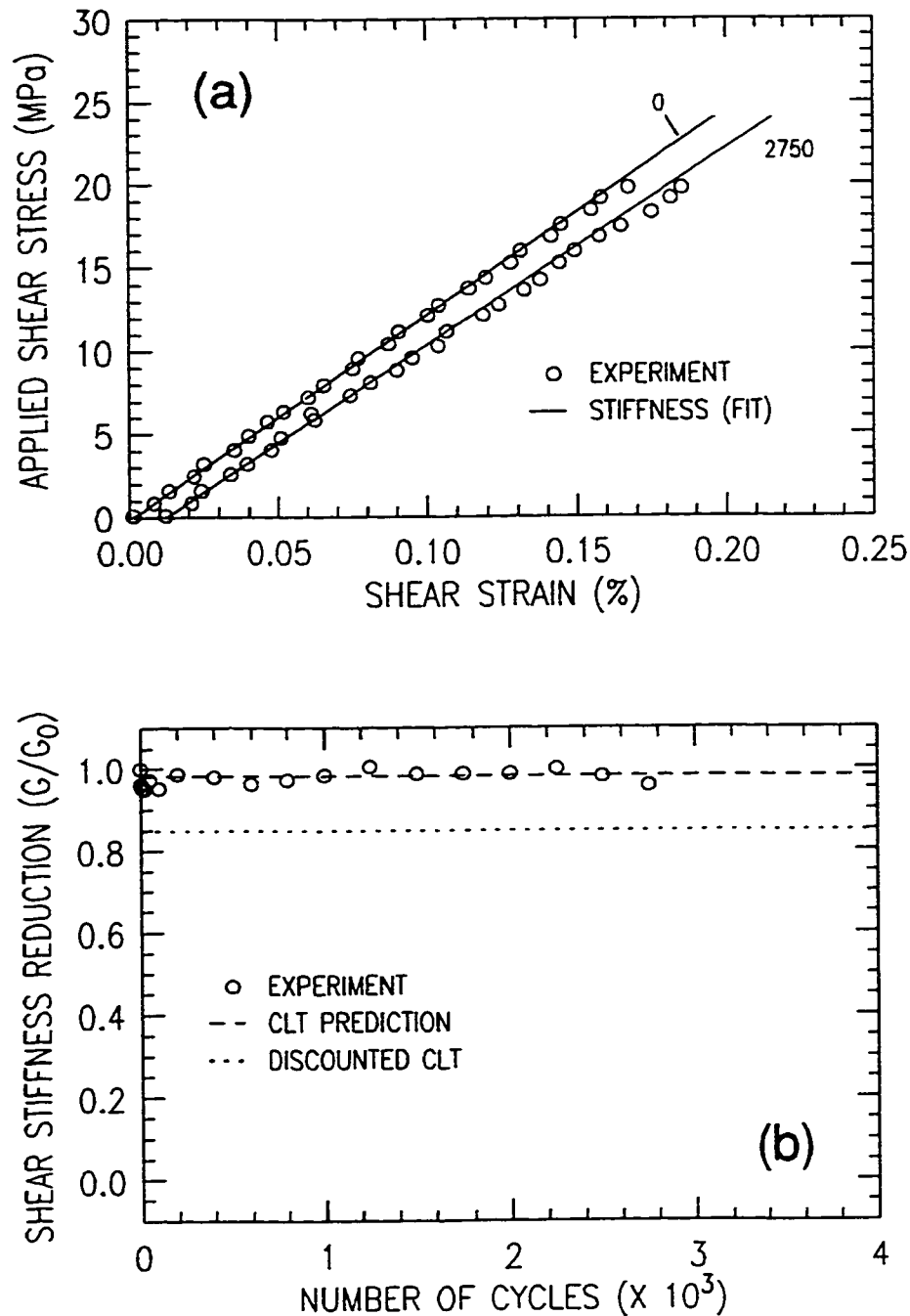


Figure 6.23: Measured shear laminate stiffness reduction of a $[\pm 45^\circ]_S$ glass-fiber reinforced epoxy tubular specimen under pure hoop (1H:0A) cyclic loading - ($\sigma_{h \max} = 115 \text{ MPa}$); (a) stiffness reduction evolution for selected monotonic ramps at indicated cycle numbers, (b) derived stiffness reduction curve.

reflected by the total loss in predicted stiffness values when the matrix properties are discounted.

From the stiffness reduction curves shown in figures 6.21b and 6.22b, the three stages of damage accumulation outlined in section 1.2.4 can be observed: 1) an initial drop in the elastic modulus due to the initiation and accumulation of matrix cracks, which occurs early in the life of the laminate, 2) a relatively long and linear region of moderate stiffness reduction during which crack coalescence, delamination and fiber micro-cracking begin to occur, and 3) a final drop in elastic modulus due to catastrophic failure events (i.e. fiber failure). These trends correspond to the observations made previously for the cyclic creep and surface temperature responses.

From the shear stiffness measurements (figure 6.23), the resulting matrix damage accumulation cannot be discerned due to the dominance of the fibers under this loading condition. This is reflected by the negligible drop in shear modulus, and the highly linear stress-strain response. The difference between the predicted initial and discounted shear stiffness values is only 15%. This highlights the sensitivity problems associated with measuring matrix damage for fiber dominated loading cases.

The resulting laminate axial stiffness reduction measurements for the *long-term* test ($\sigma_{h \max} = 70$ MPa) are shown in figure 6.24. When compared to the short-term stiffness reduction test (figure 6.21b), the long-term test exhibits the same general shape in the initial part of the curve. This corroborates the findings from other studies, which suggest that the same sequence of damage events occur for all applied stress levels (for a given laminate geometry and loading ratio) [67,274]. Since the long-term test was stopped before the occurrence of burst failure, no significant drop in modulus is observed at the end of the test. The initial drop in stiffness, however, is slightly larger than that of the short-term test ($\sim 10\%$). Similar to the short-term tests, the shear modulus reduction was also found to be negligible.

In order to correlate damage progression with observed leakage behaviour, a comparison is made between the leakage profiles and the stiffness reduction curves. For the short-term stiffness reduction test (see figures 6.14 and 6.21), leakage is seen to occur immediately from the start of the test, which coincides with an abrupt drop in stiffness within the first few cycles. After this point, the constant fluid loss rate and stabilized stiffness reduction curve both suggest that matrix crack saturation has occurred. The abrupt loss of fluid at the end of the test is also seen to coincide with

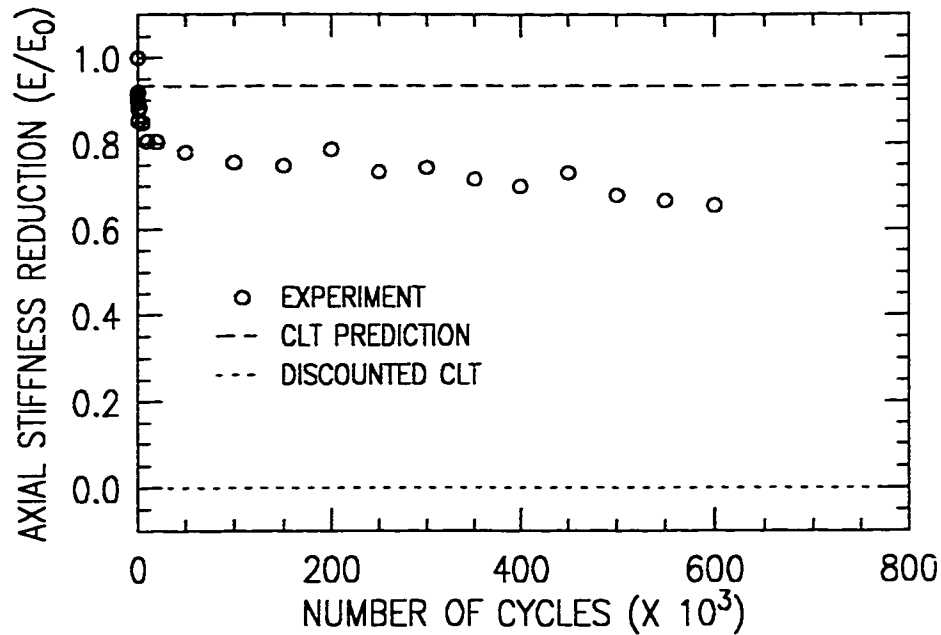


Figure 6.24: Measured axial laminate stiffness reduction of a $[\pm 45^\circ]_S$ glass-fiber reinforced epoxy tubular specimen under pure hoop (1H:0A) cyclic loading - ($\sigma_{h \max} = 70$ MPa).

the final drop in stiffness.

For the long-term test (see figures 6.16 and 6.24), however, no direct correlation between the point of leakage initiation and stiffness loss is observed. Based on the initial drop in stiffness, matrix cracking is seen to saturate quite early in the test (<10,000 cycles). Leakage initiation, however, does not occur until approximately 200,000 cycles.

6.2.3 Axial Dominated Loading

A representative stress-strain curve of a $[\pm 45^\circ]_S$ tubular specimen under axial dominated (1H:8A) cyclic loading is presented in figure 6.25. Due to material symmetry and loading equivalence, this stress-strain response is similar to that found for the pure hoop (1H:0A) loading ratio. It is characterized by significant cyclic creep, a progressively decreasing stiffness and enlargement of the hysteresis loops. These events are reflected by the associated surface temperature profile shown in figure 6.26.

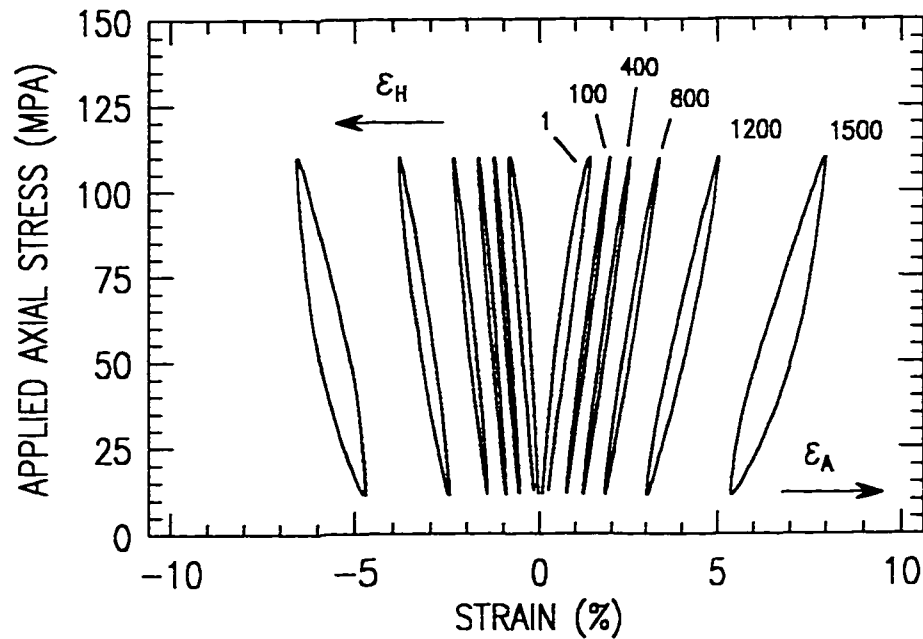


Figure 6.25: Representative cyclic stress-strain curve for $[\pm 45^\circ]_S$ glass-fiber reinforced epoxy tubular specimens under axial dominated loading (1H:8A) - ($\sigma_{h \max} = 110$ MPa).

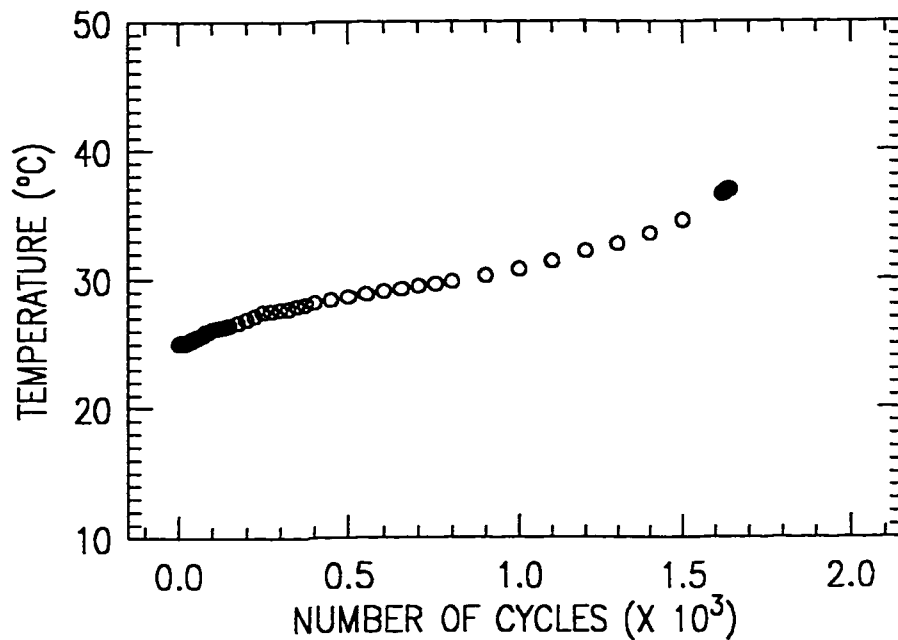


Figure 6.26: Measured surface temperature of a $[\pm 45^\circ]_S$ glass-fiber reinforced epoxy tubular specimens under axial dominated (1H:8A) cyclic loading - ($\sigma_{h \max} = 110$ MPa).

While the general stress-strain behaviour was similar to the pure hoop case, the observed macroscopic (ultimate) failure mode for the axial dominated tests (1H:8A) was different. Referring to figure 6.27, the failure is characterized by the obliteration of the matrix phase (with relatively little fiber breakage) resulting in a “brush type” fracture through the wall thickness. The fracture surface is uniformly distributed around the tubular specimen but is always located to one side of the gage section. Due to the loss of matrix integrity, the fibers are seen to contract on the inside of the tube, as shown in figure 6.28. It should be noted that this cyclic failure mode is also different from that observed under axial monotonic loading (see figure 6.6).

The fluid loss (leakage) profiles and the associated permeability curves are presented in figures 6.29, 6.30 and 6.31, for tests conducted with a maximum applied stress of 100 MPa, 75 MPa and 60 MPa, respectively. The negative permeability values in figure 6.29b are due to the sensitivity of the numerical differentiation to small errors in volume loss over a small number of cycles. Based on the lack of observable leakage, the permeability value for this curve was assumed to be zero up to burst.

Referring to figures 6.30 and 6.31, the long-term fluid loss characteristics of the axial dominated (1H:8A) loading case is seen to be similar to that of the pure hoop loading case (i.e. weepage followed by abrupt fluid loss). The short-term behaviour, however, is quite different (see figure 6.29). Whereas weepage is observed under pure hoop loading, the short-term leakage mode under axial dominated loading is seen to be abrupt fluid loss. This abrupt leakage behaviour is identical to that observed for the $[\pm 71^\circ]_S$ tubular specimens under pure axial cyclic loading (see section 5.2.3).

Due to the nominally low fluid pressures applied during the axial dominated tests, a measurable loss of fluid will only occur when: a) an extensive amount of damage through the wall thickness is present (i.e. short-term behaviour), or b) enough time is available for fluid to slowly permeate (i.e. long-term behaviour). This loading case clearly demonstrates how the observed leakage modes are governed by both the damage accumulation rates, and applied pressure conditions (i.e. fluid driving force).

Referring to figure 6.32, fatigue-life curves were constructed from the permeability profiles based on critical values of $0.1 \times 10^{-12} \text{ mm}^2$ (initiation) and $10 \times 10^{-12} \text{ mm}^2$ (post-initiation). A linear (semi-log) equation was fit to the initiation data, and was found to be a reasonable fit. The difference between the initiation and post-initiation data is quite small, particularly, for the short-term tests ($\sim 10^3$). These points overlap

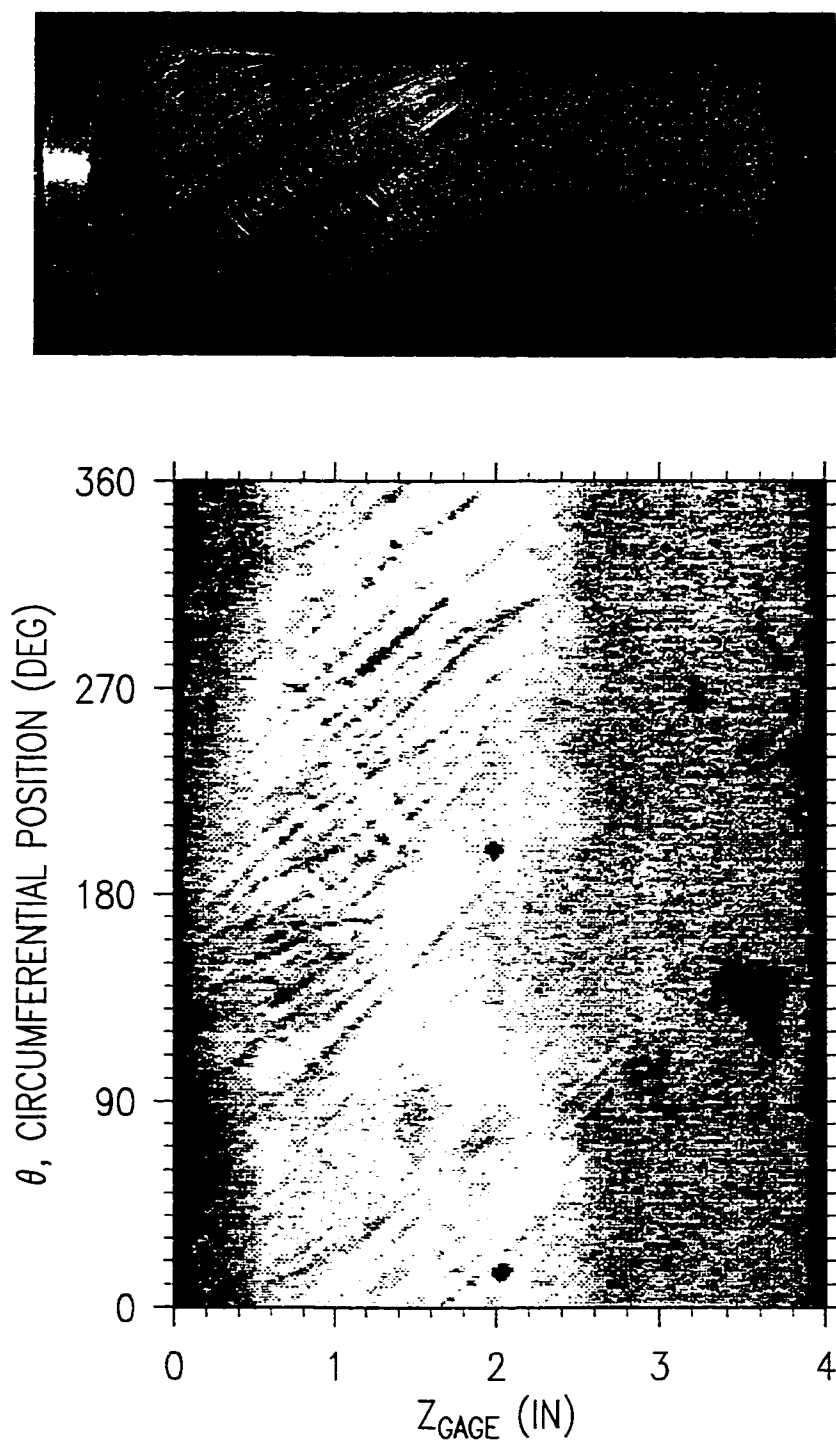


Figure 6.27: Macroscopic failure modes for $[\pm 45^\circ]_S$ glass-fiber reinforced epoxy tubular specimen under axial dominant (1H:8A) cyclic loading; (top) front view, (bottom) surface map.

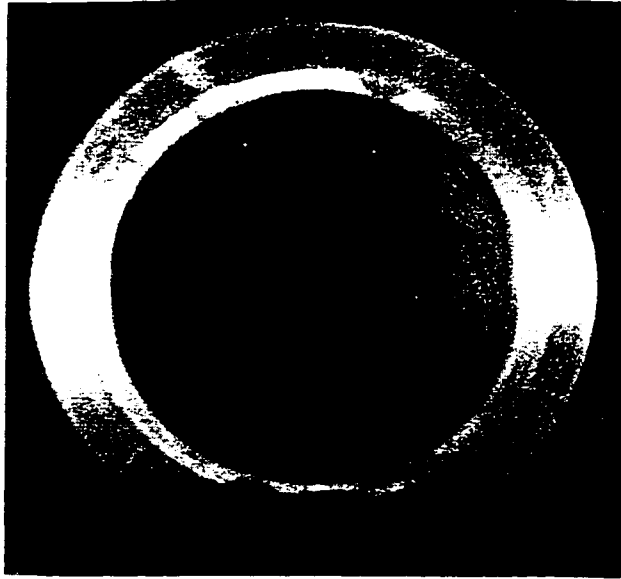


Figure 6.28: *Contraction of fibers on the inside of a $[\pm 45^\circ]_S$ glass-fiber reinforced epoxy tubular specimen under axial dominated (1H:8A) cyclic loading at failure.*

due to the abrupt leakage observed for these tests. When compared to the pure hoop loading case (see figure 6.17), the fitted initiation curves are seen to be quite similar.

Cyclic Creep Strain - (1H:8A)

A representative cyclic creep strain curve for the axial dominated loading ratio is shown in figure 6.33. This curve, presented in the material coordinate system, was derived from the measured strains using the transformation given in equation 6.2. When compared to the response under pure hoop (1H:0A) loading, the same general shape and trends are observed. For an equivalent applied stress level, however, the total creep strain and its accumulation rate is much higher for the axial dominated loading case. This is seen to occur over the entire range of maximum applied stresses. This result is surprising due to assumed equivalence between these tests. The slight biaxiality of the (1H:8A) loading ratio is not a factor since the additional applied hoop stress should, in fact, act to retard the creep strain.

The relationship between permeability and shear creep strain is shown in figure 6.34. For the applied stress levels indicated, the threshold values for leakage initiation occur between maximum shear strain levels of approximately 1.2% to 2.2%.

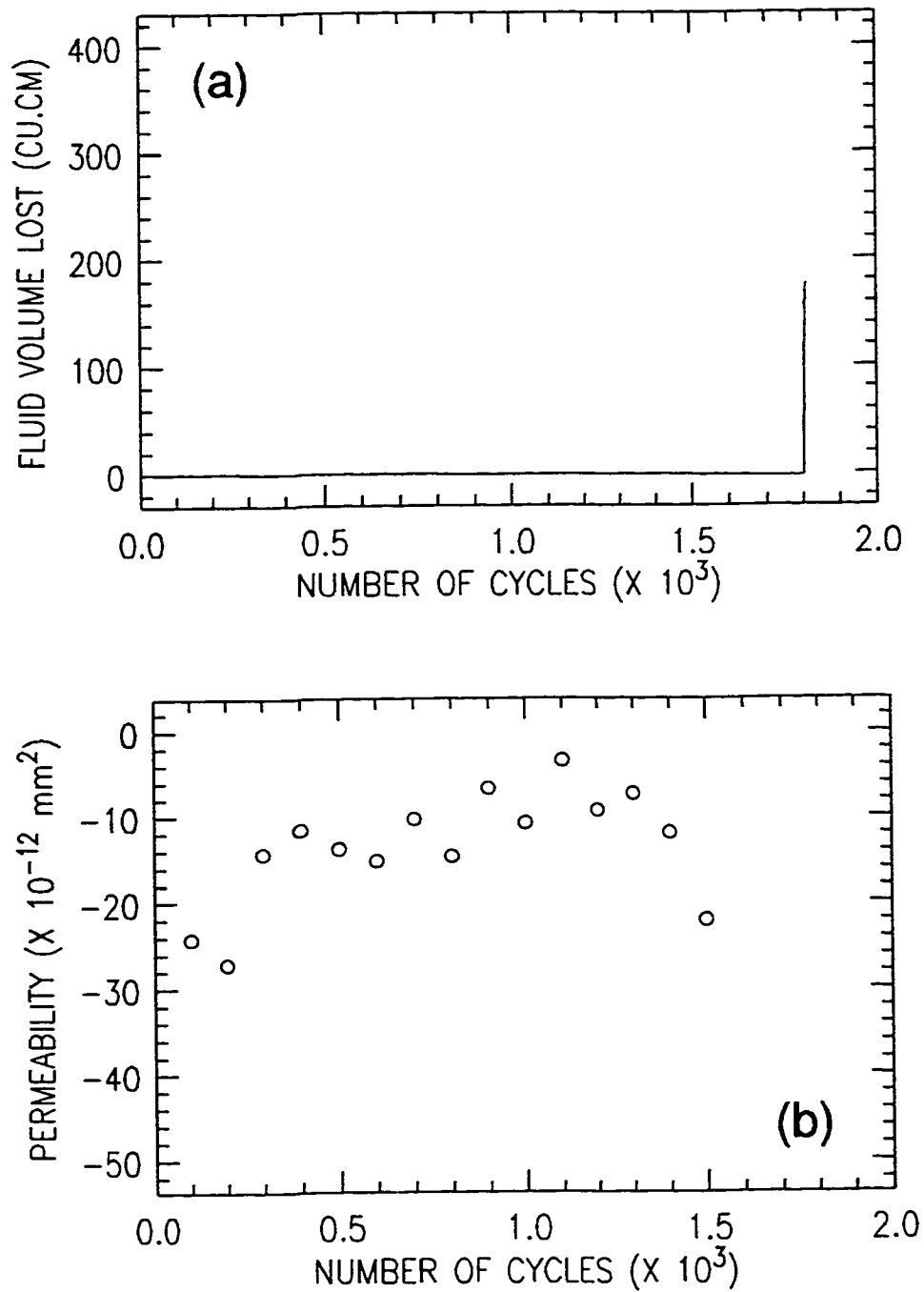


Figure 6.29: Fluid loss characteristics of a $[\pm 45^\circ]_S$ glass-fiber reinforced epoxy tubular specimen under axial dominated loading (1H:8A) - ($\sigma_{a \max} = 100$ MPa); (a) fluid volume loss (leakage) profile, (b) derived permeability curve.

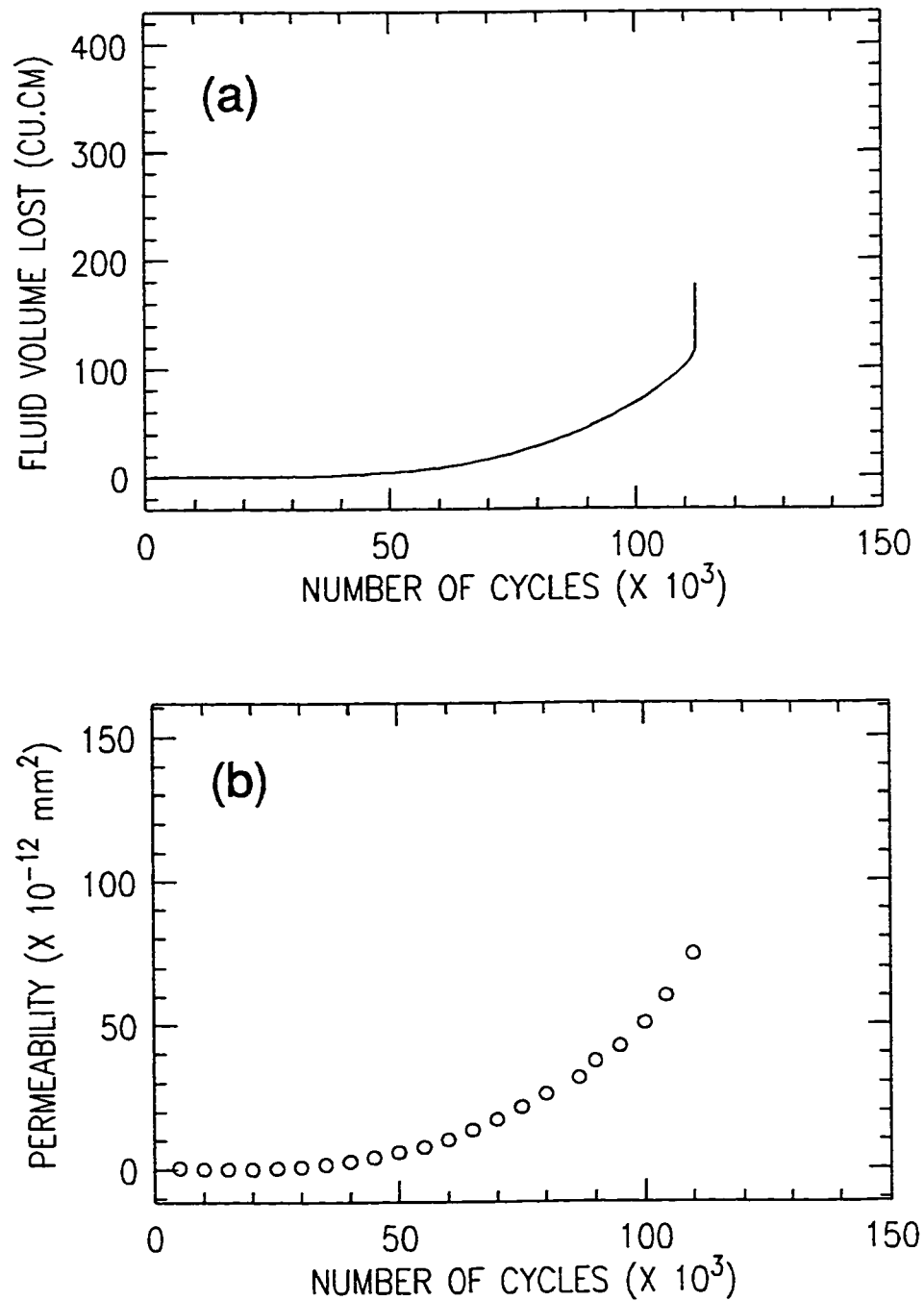


Figure 6.30: Fluid loss characteristics of a $[\pm 45^\circ]_S$ glass-fiber reinforced epoxy tubular specimen under axial dominated loading (1H:8A) - ($\sigma_{a \max} = 75$ MPa); (a) fluid volume loss (leakage) profile, (b) derived permeability curve.

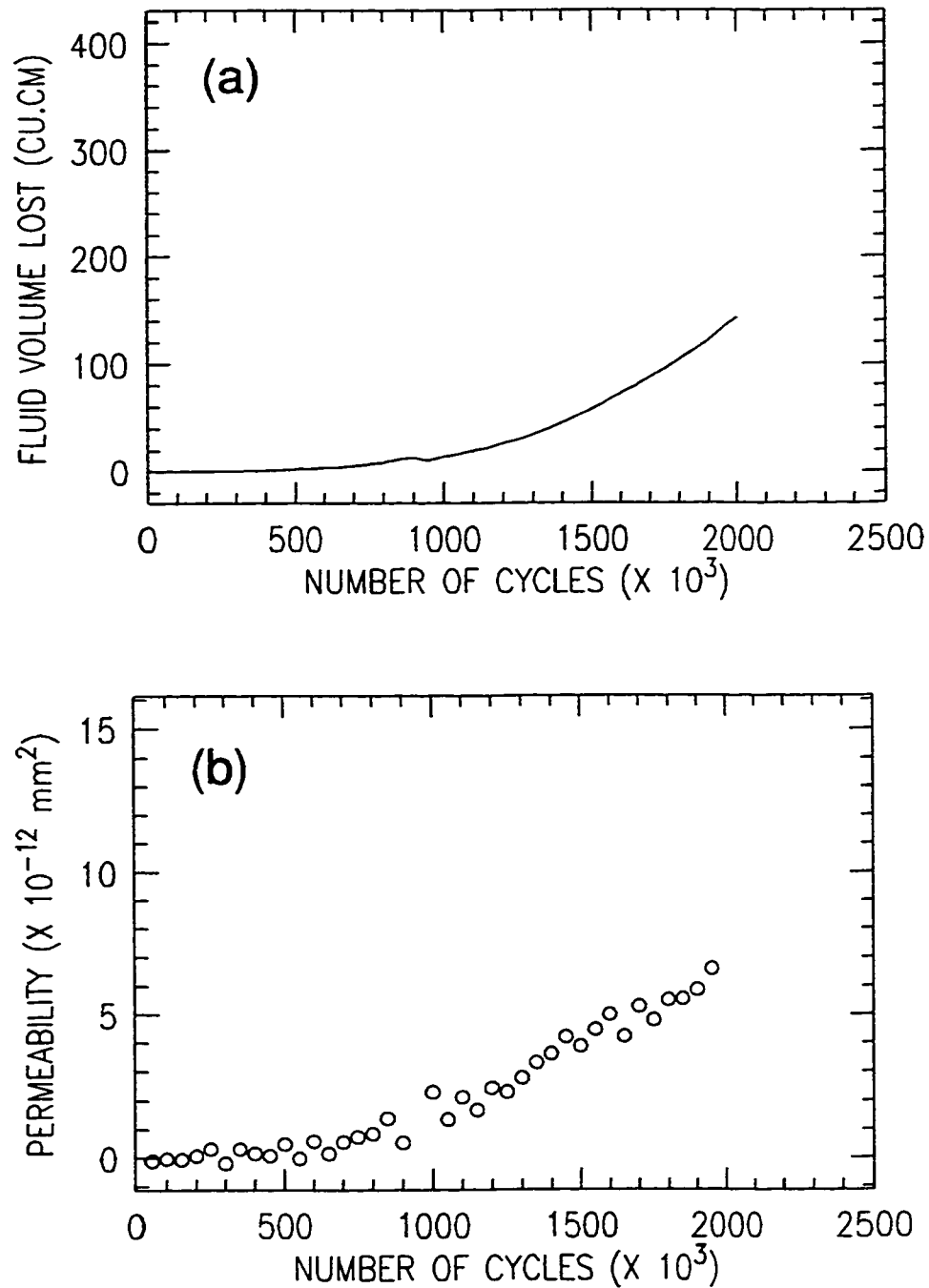


Figure 6.31: Fluid loss characteristics of a $[\pm 45^\circ]_S$ glass-fiber reinforced epoxy tubular specimen under axial dominated loading (1H:8A) - ($\sigma_{a \max} = 60$ MPa); (a) fluid volume loss (leakage) profile, (b) derived permeability curve.

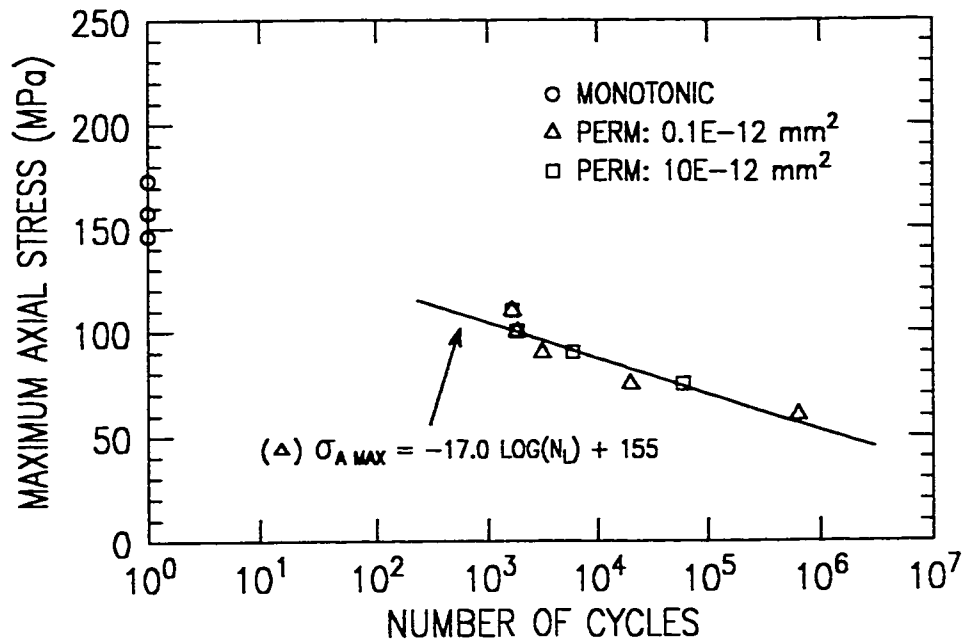


Figure 6.32: Fatigue-life relationships for $[\pm 45^\circ]_S$ glass-fiber reinforced epoxy tubular specimens under axial dominated loading (1H:8A) based on critical permeability criterion.

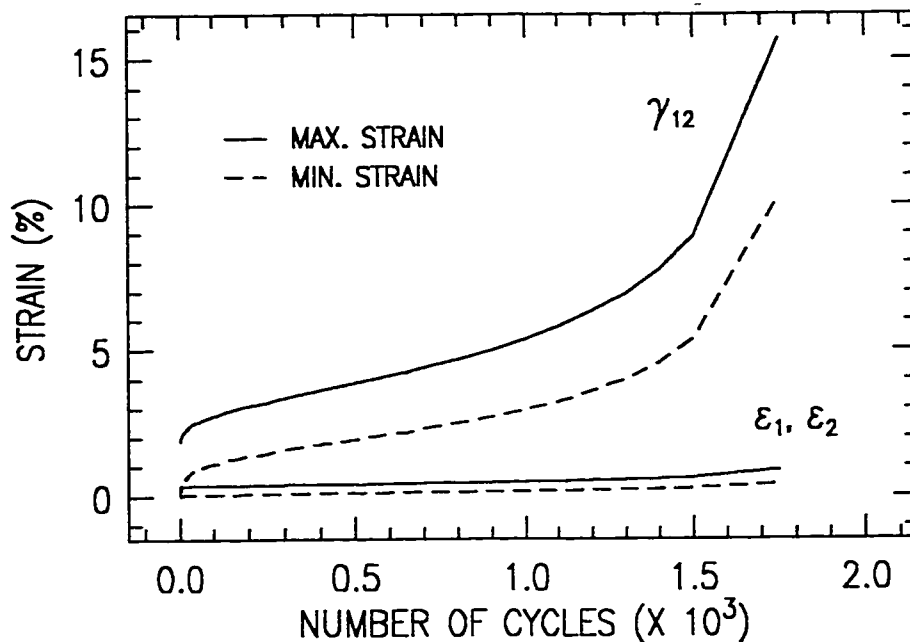


Figure 6.33: Measured cyclic creep strain curves in the material coordinate system for $[\pm 45^\circ]_S$ glass-fiber reinforced epoxy tubular specimens under axial dominated loading (1H:8A).

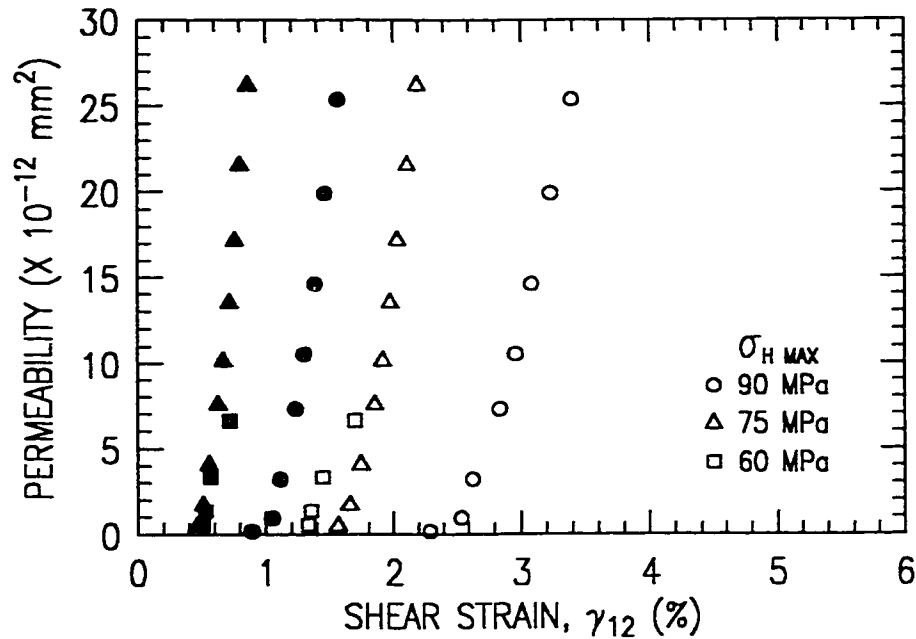


Figure 6.34: Relationship between the permeability and cyclic creep (shear) strain for $[\pm 45^\circ]_S$ glass-fiber reinforced epoxy tubular specimens under axial dominated loading (1H:8A).

When the results for the pure hoop loading ratio (see figure 6.20) are superimposed, it can be seen that leakage initiation occurs at the same strain values (for an equivalent applied maximum stress).

Stiffness Reduction - (1H:8A)

Stiffness reduction was measured for the axial dominated (1H:8A) cyclic tests at maximum applied stress levels of 100 MPa (short-term) and 60 MPa (long-term). For the short-term test ($\sigma_{a \text{ max}} = 100$ MPa), the axial and shear stiffness reduction measurements are shown in figures 6.35 and 6.36, respectively. It can be seen that both curves have the same general shape and characteristics compared to that of the short-term, pure hoop loading case (see figures 6.21 and 6.23). The shear stiffness reduction curve, however, shows slightly more sensitivity to matrix damage accumulation.

For the long-term test ($\sigma_{a \text{ max}} = 60$ MPa), the axial stiffness reduction measurement is shown in figure 6.37. This curve is also seen to exhibit the same characteristics as that found for the pure hoop loading case. Compared to the short-term test, however, the behaviour is characterized by a higher initial drop in stiffness, followed by

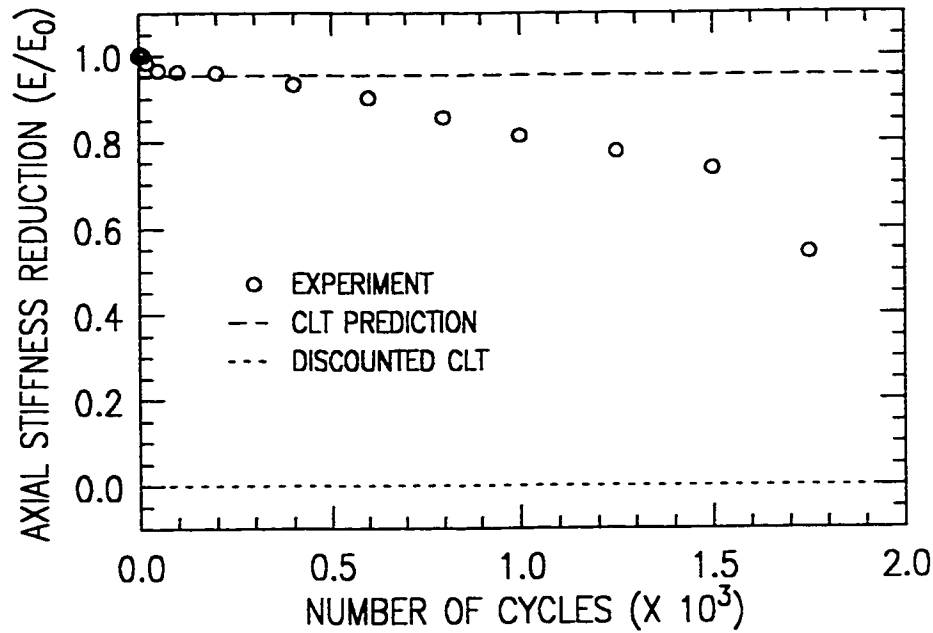


Figure 6.35: Measured axial laminate stiffness reduction of a $[\pm 45^\circ]_S$ glass-fiber reinforced epoxy tubular specimen under axial dominated (1H:8A) cyclic loading - ($\sigma_{a \max} = 100 \text{ MPa}$).

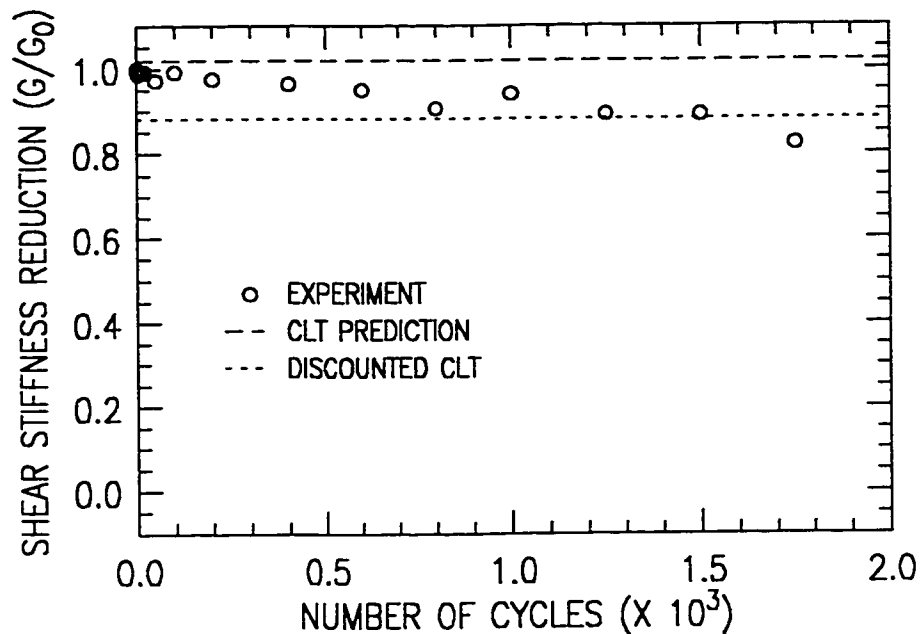


Figure 6.36: Measured shear laminate stiffness reduction of a $[\pm 45^\circ]_S$ glass-fiber reinforced epoxy tubular specimen under axial dominated (1H:8A) cyclic loading - ($\sigma_{a \max} = 100 \text{ MPa}$).

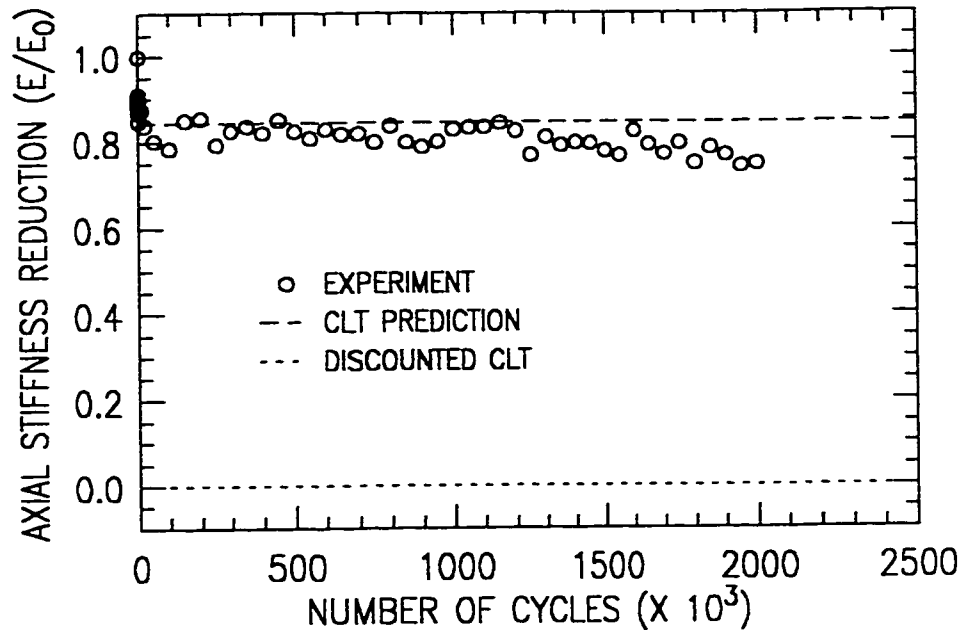


Figure 6.37: Measured axial laminate stiffness reduction of a $[\pm 45^\circ]_S$ glass-fiber reinforced epoxy tubular specimen under axial dominated (1H:8A) cyclic loading - ($\sigma_{a \max} = 60 \text{ MPa}$).

a very flat response in the measured stiffness values. The shear stiffness reduction curve, however, was found to be similar to that of the short-term profile.

The relationship between leakage and measured damage accumulation is determined by comparing the fluid loss profiles to the stiffness reduction curves. For the short-term leakage profile and stiffness reduction (see figures 6.29 and 6.35), the point of abrupt leakage is seen to correspond to the final drop in stiffness at approximately 1,700 cycles. No leakage is detected prior to this point. For the long-term test (see figures 6.31 and 6.37), however, there is no observable correlation between the leakage initiation point and stiffness reduction. Whereas matrix cracking is seen to saturate quite early in the test ($<10,000$ cycles), leakage initiation does not occur until approximately 400,000 cycles.

6.2.4 Loading Based on Netting Analysis (Equi-biaxial)

The cyclic stress-strain response of a $[\pm 45^\circ]_S$ tubular specimen under equi-biaxial (1H:1A) loading is shown in figure 6.38. The response is characterized by minimal

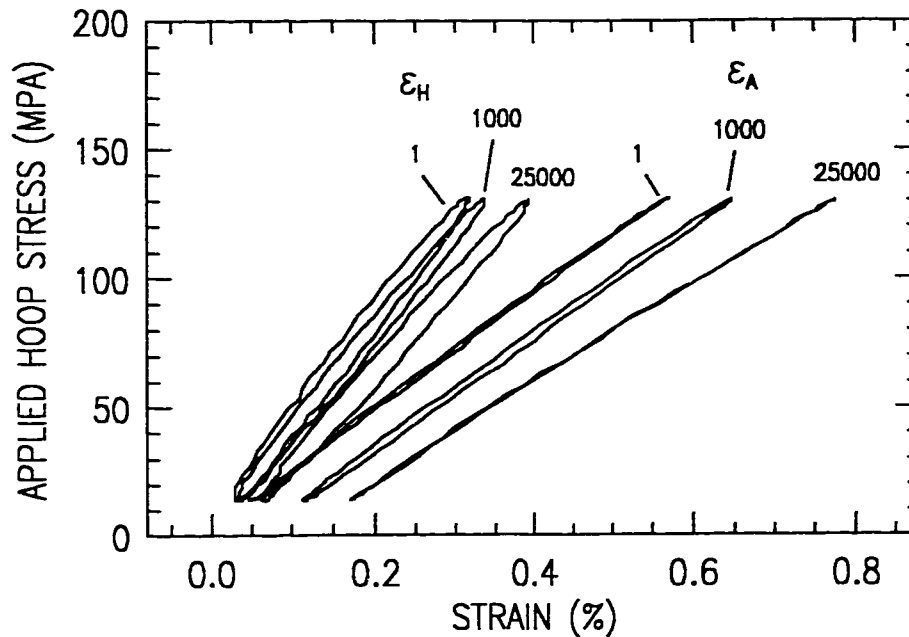


Figure 6.38: Representative cyclic stress-strain curve for $[\pm 45^\circ]_S$ glass-fiber reinforced epoxy tubular specimens under equi-biaxial loading (1H:1A) - ($\sigma_{h \max} = 130$ MPa).

cyclic creep and stiffness reduction, as expected for this fiber-dominated loading case (note the strain scale in the figure). This is in contrast to the observed large-strain, matrix dominated behaviour for the pure hoop (1H:0A) and axial dominated (1H:8A) loading ratios. Although the stress-strain curves from the hoop and axial measurements should be identical for this loading case, the hoop response is shown to be much stiffer. This surprising phenomenon was seen repeatedly for all monotonic and cyclic tests.

For the equi-biaxial (1H:1A) loading case, no visible macroscopic damage was observed for any of the tests conducted. However, using the penetrant tracing method described in section 5.2.2, uniform weepage throughout the entire gage section of the specimen was observed (see figure 6.39). In order to verify the existence of matrix cracks, scanning electron micrographs of the specimen wall were taken. Referring to figure 6.40 (top), characteristic transverse matrix cracking[§] can be seen throughout the wall thickness. These transverse cracks span the thickness of each ply, and are perpendicular to the direction of applied load. Since this sample was sectioned along

[§]Since the SEM samples were extracted from an oil saturated specimen, the cracks show up in white due to the inability of the required carbon coating to adhere to the surface.

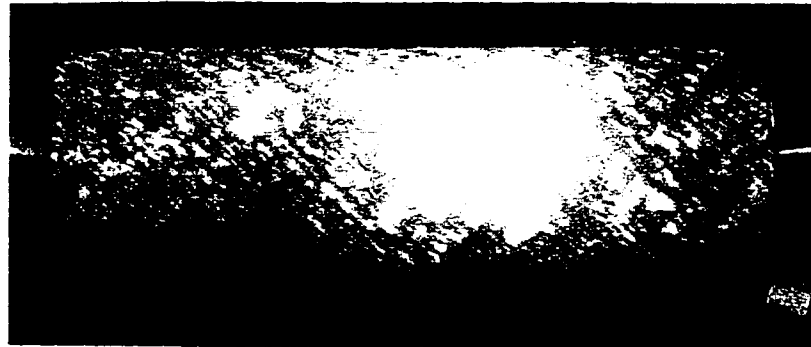


Figure 6.39: *Weepage failure mode for a $[\pm 45^\circ]_S$ glass-fiber reinforced epoxy tubular specimen under equi-biaxial (1H:1A) cyclic loading.*

one of the fiber directions, the matrix cracks in the odd layers are not visible. A contiguous path is formed by the intersection of cracks at neighbouring layers, and by growth of delaminations from existing transverse cracks (see bottom of figure 6.40).

A typical fluid volume loss (leakage) profile and derived permeability curve for the equi-biaxial cyclic tests are shown in figure 6.41. While the initial part of the curve is characteristic of weepage behaviour previously encountered, the response towards the end is different. Contrary to previously examined profiles where the fluid loss rate is seen to exponentially increase, the fluid loss rate for the equi-biaxial case is shown to approach a constant value (i.e. linear response). This effect is more prominent for lower maximum applied stress levels (see figure 6.42). The constant fluid loss rate is reflected by a plateau at the end of the permeability curve. This suggests that the multiplication and growth of matrix cracks has reached a limiting state (saturation). Compared to the matrix dominated loading cases, however, further crack opening and coalescence is restricted by the fiber dominated constraining layers (as reflected by the minimal creep strains).

Applying the same critical values used for the other loading ratios, the fatigue-life curves for the equi-biaxial (1H:1A) cyclic tests are shown in figure 6.43. A linear (semi-log) equation was fit to both sets of data, and was found to be a reasonable representation. The slopes of both fatigue-life curves are seen to be higher than those of the pure hoop (1H:0A) and axial dominated (1H:8A) loading ratios. In terms of leakage failure, this indicates that cyclic loading is more detrimental for this applied loading condition.

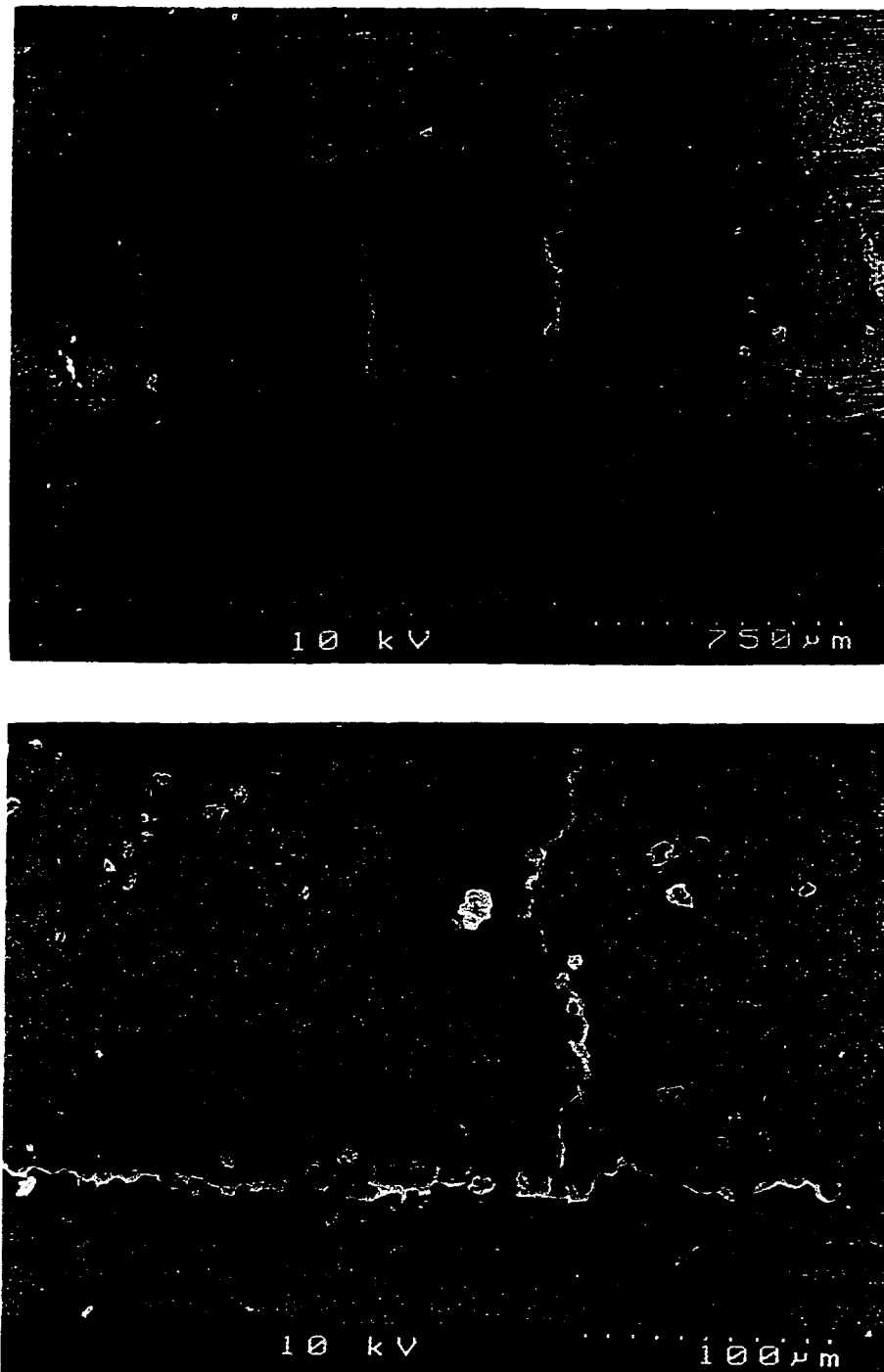


Figure 6.40: Scanning electron micrographs of matrix damage for a $[\pm 45^\circ]_S$ glass-fiber reinforced epoxy tubular specimen under equi-biaxial (1H:1A) cyclic loading (sectioned at 45° with respect to the tube axis); (top) through width section, (bottom) local transverse cracking and delamination failure.

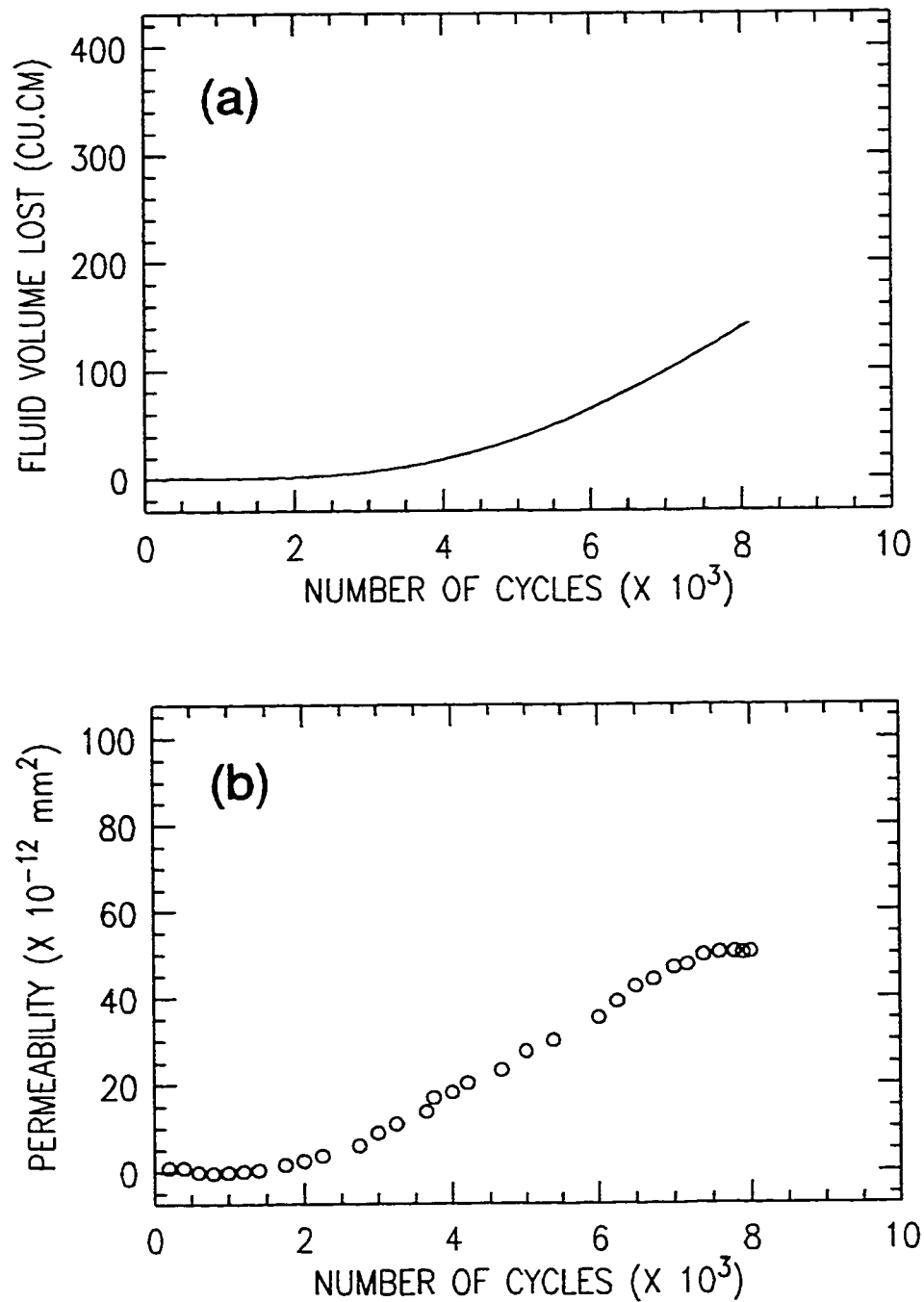


Figure 6.41: Fluid loss characteristics of a $[\pm 45^\circ]_S$ glass-fiber reinforced epoxy tubular specimen under equi-biaxial loading ($1H:1A$) - ($\sigma_{h \max} = 145$ MPa); (a) fluid volume loss (leakage) profile, (b) derived permeability curve.

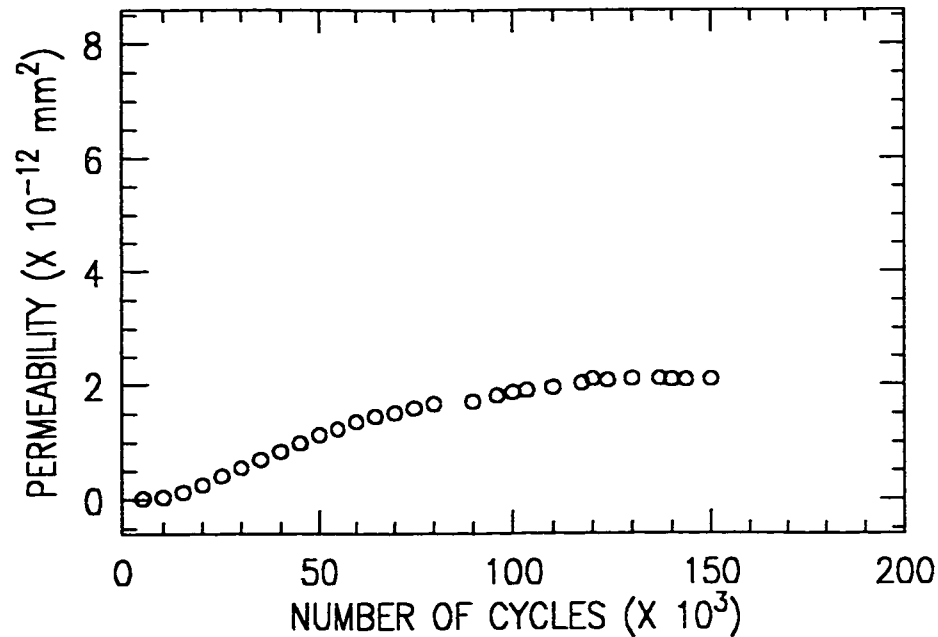


Figure 6.42: *Permeability profile for $[\pm 45^\circ]_S$ glass-fiber reinforced epoxy tubular specimens under equi-biaxial loading (1H:1A) - ($\sigma_{h \max} = 110 \text{ MPa}$).*

Stiffness Reduction - (1H:1A)

The axial and shear stiffness measurements for the short-term, equi-biaxial cyclic test ($\sigma_{h \max} = 145 \text{ MPa}$) are shown in figures 6.44 and 6.45, respectively. When compared to the other loading ratios, the equi-biaxial stiffness reduction exhibits the same general shape in the initial part of the curve. For the later part of the curves, however, the stiffness values seem to be stabilizing to a constant value. This corroborates the limiting behaviour observed in the permeability curves. There is no noticeable correlation, however, between the leakage initiation point and stiffness reduction. The long-term stiffness responses were found to be very similar to those of the short-term tests, and, therefore, are not included.

6.3 BIAXIAL FAILURE ENVELOPES

From the monotonic and cyclic test results given in the previous sections, biaxial failure envelopes for the $[\pm 45^\circ]_S$ glass-fiber epoxy tubular specimens were constructed. Referring to figure 6.46, the envelopes are plotted in the applied stress space (hoop

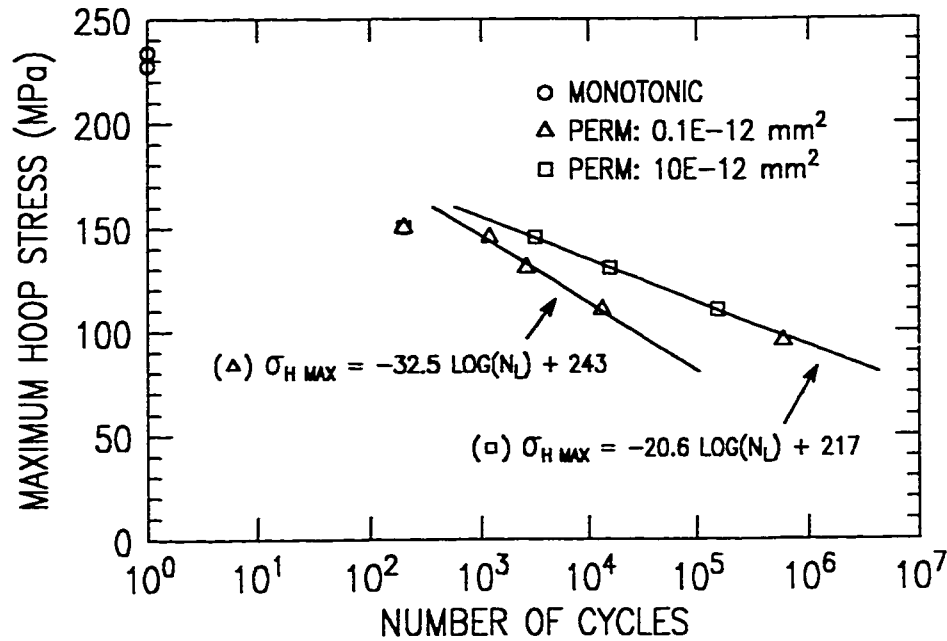


Figure 6.43: *Fatigue-life relationships for $[\pm 45^\circ]_S$ glass-fiber reinforced epoxy tubular specimens under equi-biaxial loading (1H:1A) based on critical permeability criterion.*

and axial), and are based on leakage initiation (i.e. critical permeability of $0.1 \times 10^{-12} \text{ mm}^2$). The applied monotonic stresses and strains at failure (leakage) are summarized in table 6.2. For the cyclic tests, the constant life contours are generated based on the fitted equations given in figures 6.17, 6.32 and 6.43. The data points, for both monotonic and cyclic results, are fitted with spline curves in order to demonstrate the envelope trends.

It can be seen from figure 6.46 that the monotonic failure envelope is slightly asymmetric with respect to the 1H:1A loading ratio. Since the laminate geometry is symmetric with respect to the loading axis, this is contrary to what was expected. The applied hoop stress at failure was approximately 50% higher than that of the applied axial failure stress. This is identical to observations made by Soden et al. [182] for monotonic tests on $[\pm 45^\circ]$ filament-wound glass-fiber epoxy tubulars. In their study, Soden [182] considered two effects to account for this observed asymmetry: a) the development of an additional axial force on the specimen due to pressure (as a result of specimen barrelling), and b) the generation of a triaxial state of stress in the specimen wall due to the applied pressure (i.e. addition of a radial stress component). Both effects, however, were reported to be quite small, and the authors were unable to

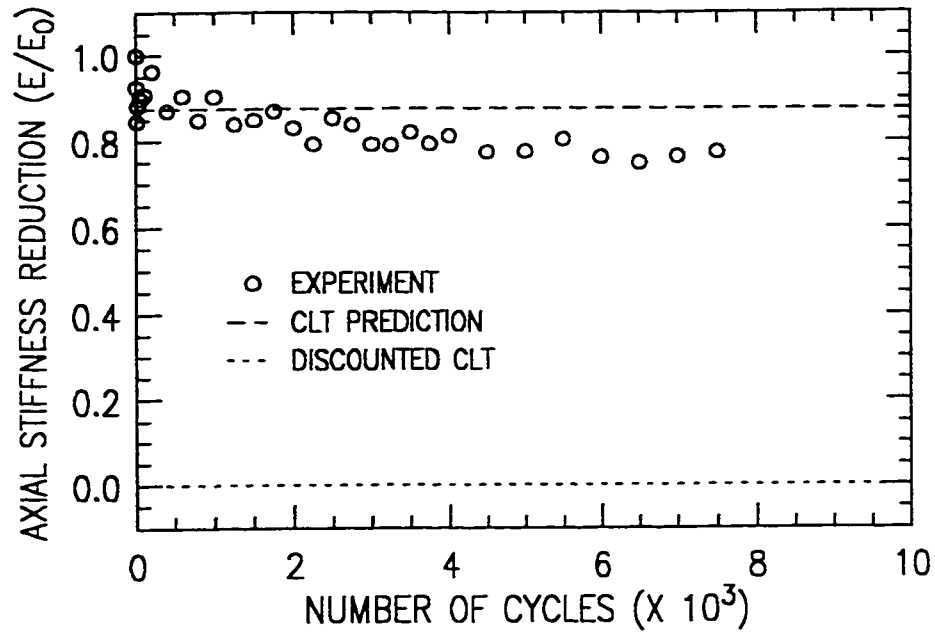


Figure 6.44: Measured axial laminate stiffness reduction of a $[\pm 45^\circ]_S$ glass-fiber reinforced epoxy tubular specimen under equi-biaxial (1H:1A) cyclic loading - ($\sigma_{h \max} = 145 \text{ MPa}$).

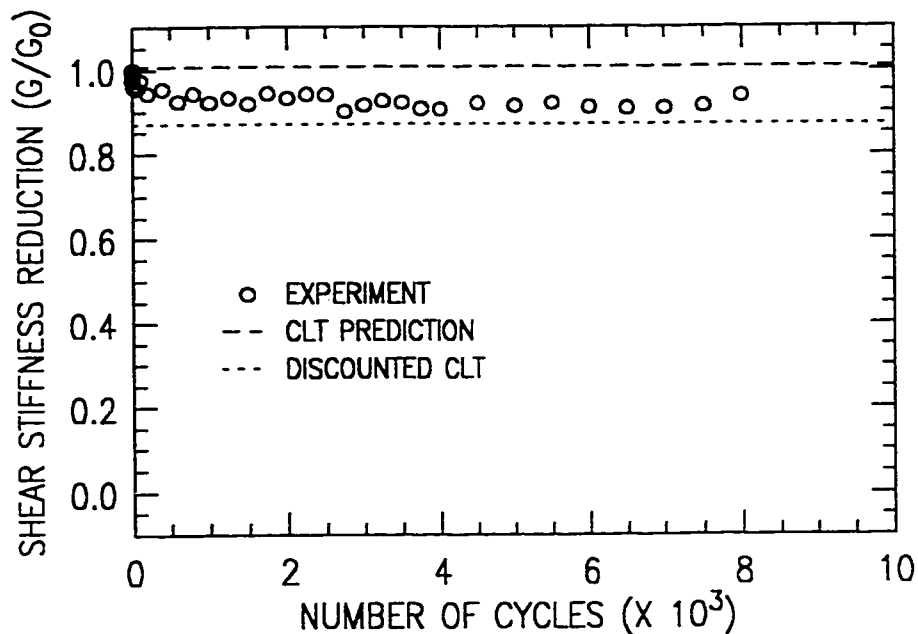


Figure 6.45: Measured shear laminate stiffness reduction of a $[\pm 45^\circ]_S$ glass-fiber reinforced epoxy tubular specimen under equi-biaxial (1H:1A) cyclic loading - ($\sigma_{h \max} = 145 \text{ MPa}$).

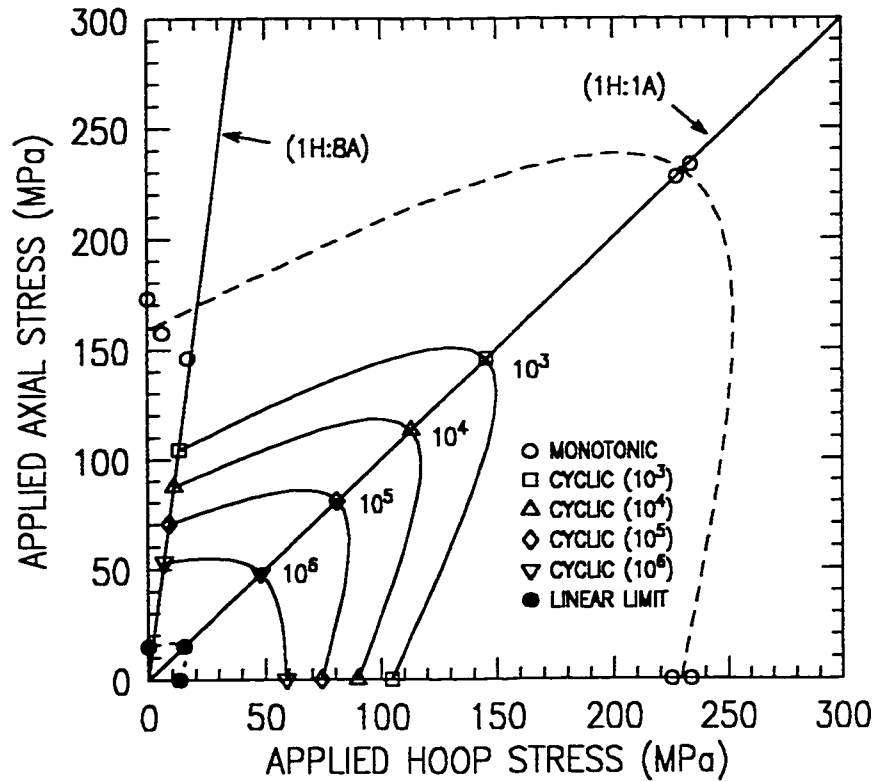


Figure 6.46: Biaxial monotonic and cyclic failure (leakage) envelopes for $[\pm 45^\circ]_S$ glass-fiber reinforced epoxy tubular specimens in applied stress space.

explain this behaviour.

The stress-strain response prior to ultimate failure also shows this asymmetric behaviour. For equivalent stress levels, all axial dominated loading cases were seen to exhibit higher strains compared to the hoop dominated cases under both monotonic and cyclic loading. For the equi-biaxial (1H:1A) loading case, this difference between hoop and axial response is clearly demonstrated (see figure 6.7). This would suggest that the observed behaviour is most likely due to non-linear barrelling effects imposed by the constrained ends and applied loading conditions. The non-linear material behaviour (time dependent) and anisotropy may, in fact, add to this effect. Unfortunately, this is extremely difficult to verify.

Contrary to the observations made for the monotonic failure envelope, the cyclic failure envelopes are seen to be fairly symmetrical with respect to the applied loading directions. These constant-life failure envelopes are based on leakage initiation, which is seen to occur long before the non-linear effects predominate (i.e. $< 2.5\%$ strain for

Table 6.2: Average applied stresses and strains at failure (leakage) for $[\pm 45^\circ]_S$ glass-fiber reinforced epoxy tubular specimens under monotonic loading.

Biaxial Stress Ratio	Applied Hoop Stress (MPa)	Hoop Strain (%)	Applied Axial Stress (MPa)	Axial Strain (%)	Observed Failure Mode
(1H:0A)	229.4	10.6	0.0	-10.9	Burst failure - extensive matrix cracking and fiber breakage
(0H:1A)	16.8	-7.26	159.0	9.67	Helical separation along length of specimen
(1H:1A)	230.7	0.83	230.7	1.16	Helical separation along length of specimen

all specimens). The observed symmetry is a manifestation of the similarity between the fitted fatigue-life curves for the pure hoop (1H:0A) and axial dominated (1H:8A) loading ratios (see figures 6.17 and 6.32). This suggests that the initial progression of damage leading to leakage initiation is very similar for these loading cases.

A comparison between the monotonic and cyclic failure envelopes reveals that the long-term applied failure stress (10^6 cycles) is approximately 25%, 20% and 33% of the monotonic failure stress for the (1H:0A), (1H:1A) and (1H:8A) loading ratios, respectively. Although all specimens were seen to fail in the gage section, the mode of failure was different for monotonic and cyclic loading conditions. For the monotonic tests, all specimens failed by abrupt fluid loss (burst) which coincided with the ultimate failure point (excessive fiber failure). For the cyclic tests, however, all specimens were seen to initially fail by weepage due to uniformly distributed matrix cracking[¶]. Under pure hoop (1H:0A) and axial dominated loading (1H:8A), abrupt leakage failure was observed to follow this weepage behaviour.

The stages of damage progression, as measured by creep strain and elastic modulus, were seen to be quite similar for all tests conducted. Although matrix crack

[¶]with the exception of the short-term (low cycle) axial dominated cyclic tests which were also seen to fail by abrupt leakage (see section 6.2.3 for details)

saturation (defined by the initial drop in stiffness) was seen to precede leakage initiation, no direct correlation between these two was found to exist. Particularly for long-term tests, the life at matrix saturation was seen to be significantly less than that of leakage initiation. This discrepancy demonstrates that leakage behaviour is governed not only by the formation of cracks, but also by their inter-connectivity through the wall thickness. The opening of existing transverse cracks, and the formation of interlaminar cracks does not significantly influence the measured stiffness reduction.

The predicted long-term failure envelope based on the linear elastic limit is also shown in figure 6.46. The limiting stress values used in this envelope were estimated from the monotonic stress-strain curves for each of the loading ratios tested (see figures 6.1, 6.4 and 6.7). Similar to the tests conducted on $[\pm 71^\circ]_S$ specimens, the linear limit envelope is seen to be quite conservative, corresponding to an extrapolated life of approximately 10^9 .

In summary, the current $[\pm 45^\circ]_S$ specimen design seems to be valid for evaluating the response and leakage characteristics for all tensile biaxial loading ratios under cyclic loading. No significant end effects were observed for leakage initiation. If the barrelling effect is, in fact, responsible for the observed differences in hoop and axial behaviour, modifications to the specimen ends may be required to accurately determine the monotonic failure envelope.

CHAPTER 7

Stress-Strain Distributions and Failure Analysis of Tubular Specimens

7.1 METHODOLOGY

In this chapter, the stress and strain distributions in $[\pm 71^\circ]_S$ and $[\pm 45^\circ]_S$ glass-fiber epoxy tubular specimens are determined using finite element analysis. The purpose of this exercise is to determine the validity of the current specimen design for studying matrix dominated (leakage) failure modes in fiber reinforced composite tubular specimens. This analysis will be used to clarify the effects of the end condition on the observed failure modes and locations. By invoking the maximum strain failure criterion, prediction of the applied failure stresses at leakage will also be considered.

7.1.1 Description of the Finite Element Model

Linear elastic finite element methods have been used in a number of studies to investigate the stress and strain distributions in composite tubular specimen designs [150, 262–264, 266, 280–282]. In these studies, however, no attempt was made to predict specific failure modes and locations. For specimens used to determine ultimate failure properties, the use of linear elastic methods may not be suitable in cases where the observed stress-strain behaviour is highly non-linear. However, if the analysis is restricted to the prediction of damage initiation events (such as matrix cracking), the use of linear methods may provide valuable insight.

In this study, the $[\pm 71^\circ]_S$ and $[\pm 45^\circ]_S$ glass-fiber epoxy tubular specimens under various applied loading ratios were modeled using the general purpose finite element

package ANSYS. From the available element library, a 2D homogenized shell formulation was selected (ANSYS SHELL99) for two reasons: 1) the leakage behaviour of interest (weepage) is predominantly due to the initiation and accumulation of transverse matrix cracks which is governed by the in-plane stress/strain state, and 2) the accurate determination of out-of-plane stress/strain components, particularly at the interlaminar interface, requires the use of 3D elements which tend to necessitate very large computational resources.

The SHELL99 element is an 8 node isoparametric shell element which can be used to model multi-layered (anisotropic) laminated structures. In this element, shear deformation is included in the derivation by assuming that straight lines normal to the mid-surface remain straight but not necessarily perpendicular after deformation. In the construction of the solution, the composite layer properties are homogenized prior to solving for the global degrees of freedom. The layer strains are determined using conventional shell strain-displacement relations. A complete derivation of this element can be found in reference [283].

The finite element mesh used in this analysis is shown in figure 7.1. Since the laminate properties (orthotropic and homogenized) and boundary conditions (applied loads and displacements) are symmetric with respect to the cylindrical geometry, the required number of elements was reduced by modeling only 1/8 of the tubular specimen. Since most of the specimen tab is effectively clamped in the grips, only the tapered section was included in the model. The taper in the tab geometry was created by using successively thicker shell elements at the ends. Due to the high strain gradients observed, the mesh was refined at the specimen ends in order to improve the accuracy of the solution. Two mesh sizes (290 and 1056 elements) were tested to investigate solution convergence. For the case of the $[\pm 71^\circ]_S$ specimen under (17H:2A) loading, the difference in maximum transverse strain (at the specimen ends) between these two mesh sizes was found to be only 1.5%. The larger mesh was deemed acceptable and was used in subsequent analysis.

Two separate analyses were performed for each $[\pm 71^\circ]_S$ and $[\pm 45^\circ]_S$ tubular specimen to determine the mechanical and thermal stress/strain distributions. These analyses were performed separately due to differences in the fixed boundary conditions at the end of the tube. Since the analysis is linear, the overall stress/strain distribution was found by superposition. The elastic properties used in this analysis

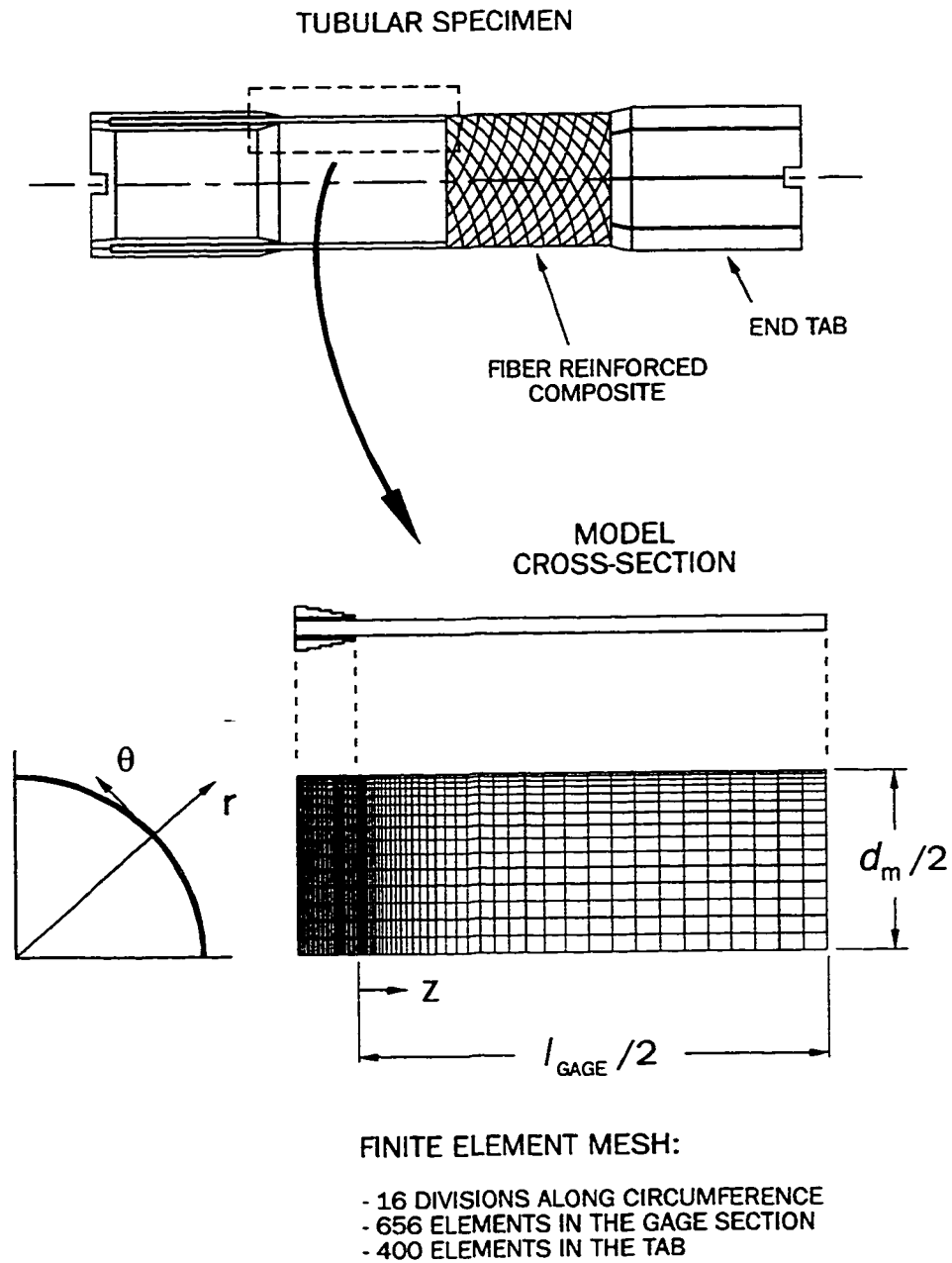


Figure 7.1: *Finite element mesh of glass-fiber reinforced epoxy tubular specimens.*

Table 7.1: *Elastic properties for tubular specimen components.*

Property	E-Gl/Ep Composite (3M-1003)	Aluminum (6061-T6)	Epoxy Adhesive
E_1 (GPa)	41.7	71.0	4.8
E_2, E_3 (GPa)	13.0	—	—
ν_{12}, ν_{13}	0.3	0.33	0.34
ν_{23}	0.4	—	—
G_{12}, G_{13} (GPa)	3.4	26.2	1.8
G_{23} (GPa)	4.6	—	—
α_1 ($\times 10^{-6}/^\circ C$)	8.6	—	—
α_2 ($\times 10^{-6}/^\circ C$)	21.9	—	—
Reference	[64]*	[284]	[285]

*confirmed by in-house tests

are given in table 7.1.

For the mechanical analysis, the specimen is modeled with fully clamped end conditions (at the back of the tab section) which emulates the fixed grip system used in the experimental procedure. The mechanical loads are introduced to the specimen by the proportional application of hoop and axial tractions (stresses). The hoop stress (σ_h) is produced by an applied pressure load (P) on the inside surface of the tubular specimen, while the axial stress (σ_a) is generated by applied axial stress resultants (N_z in force per unit length) at the end of the specimen. For a given biaxial stress ratio (i.e. $\sigma_h:\sigma_a$), the load boundary conditions can be determined using the following relations:

$$\text{for pressure, } P = \frac{\sigma_h w}{r_m}$$

$$\text{for axial stress resultant, } N_z = \sigma_a w$$

where, r_m and w are the mean radius and wall thickness of the specimen, respectively.

Referring to figure 7.1, the symmetry (displacement) boundary conditions used in the analysis are as follows:

$$\begin{aligned} \text{along the boundary } z = \frac{l_g}{2}, \quad u_\theta = \beta_r = \beta_\theta = \beta_z = 0 \\ \text{and along the boundaries } \theta = 0 \text{ and } \frac{\pi}{2} \quad u_\theta = \beta_r = \beta_z = 0 \end{aligned} \quad (7.1)$$

where, u and β are the prescribed nodal displacements and rotations, respectively.

In addition to the symmetry boundary conditions specified by equation 7.1, a fully clamped condition is imposed at the tab by:

$$\text{along the boundary } z = -l_t, \quad u_r = u_\theta = u_z = \beta_r = \beta_\theta = \beta_z = 0$$

The thermal analysis is performed to determine the residual stress/strain distribution as a result of elevated temperature curing. In contrast to the boundary conditions for the mechanical loading case (i.e. clamped ends), the tube is assumed to be unconstrained throughout its length during the molding procedure. As such, only a simple composite cylinder (1/8 model) *without tabs* is required in the analysis. A temperature drop of -139°C (-250°F) is imposed to simulate the post-cure condition. In order to prevent any rigid body displacements or rotations, the same symmetry conditions as defined by equation 7.1 are used along with the following free end boundary conditions:

$$\text{along the boundary } z = 0, \quad u_\theta = u_z = \beta_r = \beta_z = 0$$

In the following sections, the strain distributions determined by the mechanical analysis were found to be uniform along the the circumference (due to symmetry) but varied along the length and through the thickness of the specimen. These distributions are, therefore, presented along the length of the specimen for the inner and outer layers only. Conversely, the strain distributions determined by the thermal analysis were only found to vary linearly through the wall thickness. These linear distributions are, therefore, summarized by the strain values at the inner and outer surface of the tubular specimen, as shown in table 7.2.

The associated ANSYS batch files used for both the mechanical and thermal analysis are provided in Appendix F.

Table 7.2: *In-plane residual thermal strains for the $[\pm 71^\circ]_S$ and $[\pm 45^\circ]_S$ glass-fiber reinforced epoxy tubular specimens as determined at the inner and outer layer ($\Delta T = -139^\circ C$ or $-250^\circ F$).*

Location	ϵ_{1t} (%)	ϵ_{2t} (%)	γ_{12t} (%)
$[\pm 71^\circ]_S$ (inner layer)	-0.015	0.025	0.113
$[\pm 71^\circ]_S$ (outer layer)	-0.005	0.026	0.120
$[\pm 45^\circ]_S$ (inner layer)	-0.054	0.131	0.007
$[\pm 45^\circ]_S$ (outer layer)	-0.046	0.138	0.007

7.1.2 Description of the Failure Analysis

Once the strain distributions have been determined by finite element analysis, the maximum strain failure criterion can be invoked to predict the failure mode, failure location and the applied failure stresses in the tubular specimen. The advantages of this failure criterion are its relative simplicity and ability to differentiate between failure modes. In addition, there is a growing body of evidence suggesting that matrix failure in composite laminates is, in fact, governed by limiting strains.

Mieras [160] found that the strains at leakage were similar for various applied stress levels during static fatigue (creep) testing of glass-fiber epoxy pipes. Hoover et al. [66] investigated the effect of stress and strain controlled loading on matrix crack formation in $[\pm\theta, 90^\circ]_S$ glass/epoxy coupons. This study showed that under constant stress, crack multiplication occurred as a result of creep. The resulting development of each transverse crack (with time), however, was found to correlate to a unique strain level for different applied stresses.

Lending further support, the independent and non-interacting characteristics of the maximum strain failure criterion has also been experimentally demonstrated by a number of different studies. Francis et al. [171] performed experiments on $[0^\circ, 90^\circ]_S$ and $[\pm 45^\circ]_S$ thin-walled graphite/epoxy tubular specimens under quasi-static loading

in order to determine the effects of combined hoop and shear loading on the matrix crack initiation (first ply failure). In their study, the transverse and shear matrix failure modes were found to be independent. The resulting shape of the experimental failure envelope (crack initiation) was the same as that generated using the maximum strain failure criterion. Wang and Socie [102] found similar results for biaxial compression tests on glass-fiber epoxy cross-ply and unidirectional cruciform specimens. This study found that the ultimate compressive failure strains in the principal loading directions were independent of one another.

Swanson and co-workers successfully used the maximum strain failure criterion to predict the biaxial failure envelopes for a variety of carbon/epoxy quasi-isotropic tubular specimens [183, 185, 188]. As pointed out by Hart-Smith [286], these "well designed" lay-ups exhibit relatively linear behaviour to failure for all biaxial ratios due to the multi-directional placement of the fibers, and relatively high modulus (and lower strain to failure) in the fiber direction.

For the maximum strain criterion, failure in a layer is assumed to have occurred when one of the following conditions in the material coordinate system is satisfied (only in-plane loading is considered):

$$\text{for tensile fiber failure, } \frac{\epsilon_1^+}{\epsilon_{1f}^+} = 1,$$

$$\text{for compressive fiber failure, } \frac{\epsilon_1^-}{\epsilon_{1f}^-} = 1,$$

$$\text{for tensile transverse matrix failure, } \frac{\epsilon_2^+}{\epsilon_{2f}^+} = 1,$$

$$\text{for compressive transverse matrix failure, } \frac{\epsilon_2^-}{\epsilon_{2f}^-} = 1,$$

and

$$\text{for in-plane shear failure, } \frac{\gamma_{12}}{\gamma_{12f}} = 1 \quad (7.2)$$

where, ϵ_i is the total (in-situ) strain due to mechanical and thermal loading, and ϵ_{if} is the critical failure strain as determined by characterization tests (+ and - denote tensile and compressive loading, respectively).

Table 7.3: *Critical failure strains for use with maximum strain failure criterion (3M-1003 Scotchply Glass-fiber Epoxy).*

	Critical Strain (%)	Characterization Specimen
ϵ_{1f}^+	= 2.3	Unidirectional Tubular (measured in-house)
ϵ_{1f}^-	= -1.5	Unidirectional Cruciform (reference [102])
ϵ_{2f}^+	= 0.5	Unidirectional Coupon (measured in-house)
ϵ_{2f}^-	= -1.8	Unidirectional Cruciform (reference [102])
γ_{12f}	= 1.3	Cross-ply Iosipescu (measured in-house)

For each of these loading cases ($i = 1, 2, 12$), the total (in-situ) strain represents the combination of applied mechanical strain (ϵ_m) and thermal residual strain (ϵ_t), as follows:

$$\epsilon_i = \epsilon_{im} + \epsilon_{it} \quad (\text{for } i = 1, 2, 12) \quad (7.3)$$

The critical strain values used in this study are summarized in table 7.3. These values were selected based on available data from in-house tests and sources in the literature. Fiber and transverse failure strain values were all determined from tests conducted using unidirectional specimens. Since no criteria currently exists for specifying the shear failure strain at initiation, it was taken as the point of non-linearity on the shear stress-strain curve, defined by the intersection of an approximate bi-linear fit. The assumption made is that the point of non-linearity represents the onset of damage initiation.

In examining the leakage behaviour of tubular specimens, two definitions of failure are considered in the following analysis: 1) initiation failure, and 2) through wall failure. Initiation failure* is assumed to occur when the failure criterion is first satisfied at any point in the structure. Conversely, through wall failure is assumed to occur

*also referred to as first ply failure in other references

only when the failure criterion is satisfied in *all layers at a given point*. Whereas the initiation failure is representative of the onset of damage, the through wall definition is assumed to be more representative of leakage failure.

7.2 ANALYSIS OF $[\pm 71^\circ]_S$ TUBULAR SPECIMENS

Thermal and mechanical finite element analysis was performed on the $[\pm 71^\circ]_S$ tubular specimens. Mechanical strain distributions (as determined at the integration points) for the tubular specimens were calculated for the following biaxial stress ratios: (1H:0A), (17H:2A), (1H:1A) and (0H:1A). Results from the thermal analysis are presented in table 7.2. The total (in-situ) strain distributions were found by superposition of the mechanical and thermal solutions as given by equation 7.3. By invoking the maximum strain failure criterion (equations 7.2), the failure location, failure mode and applied failure stress (for initiation and through wall failure) were determined. These predictions were compared to the experimental results and observations presented in chapter 5.

7.2.1 Pure Hoop Loading

The in-plane mechanical stress and strain distributions for the $[\pm 71^\circ]_S$ tubular specimen under pure hoop (1H:0A) loading are shown in figure 7.2. Results are presented for the top (outer) and bottom (inner) layers of the tubular specimen. The stress and strain values are normalized with respect to applied hoop stress (with the strain being made non-dimensional by using the calculated laminate hoop stiffness). Although the absolute value of shear strain is used in the failure analysis, negative shear stress and strain results (as calculated) are presented in the figure for clarity.

It can be seen in both figures that high gradients exist at the ends of the specimen due to the clamping effect of the grips. Inside the tabs ($z/l_g < 0$), the in-plane response is reduced significantly. The boundary effect is limited to approximately 1/2 a specimen diameter from the tab (~ 19 mm or 0.75 in). The distributions throughout most of the gage section is seen to be very uniform, converging to the values predicted by classical laminate theory (CLT). Since curvature effects are not incorporated into the CLT analysis, the values predicted by CLT are equivalent to those of the FEA at

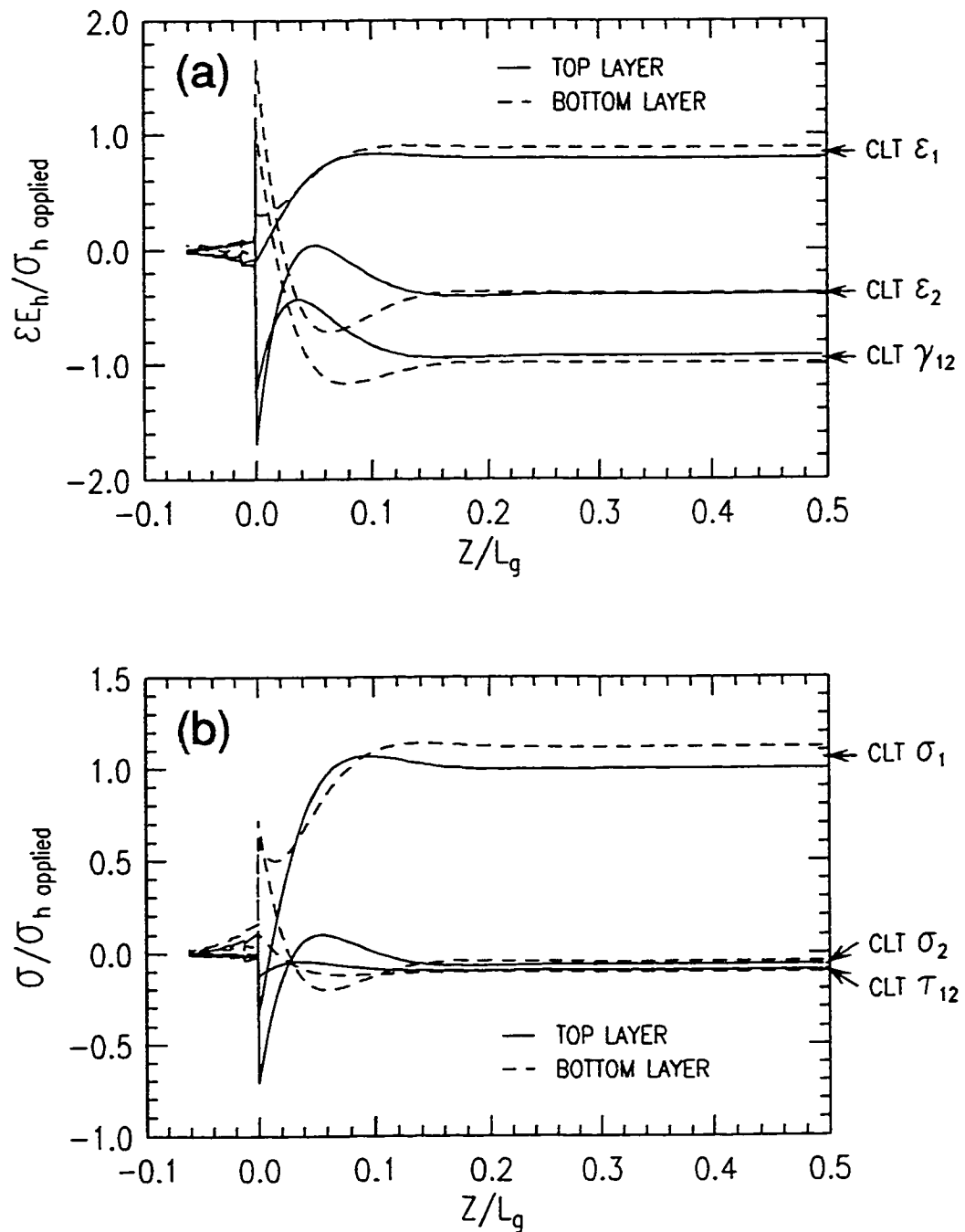


Figure 7.2: Non-dimensional stress (a) and strain (b) distributions along the half gage length of a $[\pm 71^\circ]_S$ glass-fiber reinforced epoxy tubular specimen under pure hoop loading (1H:0A).

the mid-surface. In the gage section, the applied load is taken mainly by the fibers, with the transverse strain being compressive.

The effect of the various failure modes (as defined by the maximum strain failure criterion) is best expressed by the distributions of failure strain ratios as shown in figure 7.3. The predicted location for both initiation and through wall failure is at the end of the specimen, as a result of combined matrix cracking (transverse tension and shear failure). This is representative of the observed behaviour under cyclic loading, but is not representative of the localized burst failure mode seen for monotonic loading (see figure 5.3). Although fiber failure is not predicted by this analysis, the location of the observed monotonic burst point is seen to correspond with that of the highest fiber stress and strain values along the length of the specimen (see figure 7.2).

The predicted initiation and through wall (hoop) failure stresses were 93.2 MPa and 310.1 MPa, respectively. Compared to the experimental monotonic (260.1 MPa) and cyclic hoop stress at 10^3 (214.9 MPa), the predicted through wall hoop stress is 19% and 44% higher, respectively. The predicted initiation hoop stress is seen to be very conservative.

7.2.2 *Pure Axial Loading*

For the pure axial (0H:1A) loading ratio, the mechanical stress and strain distributions are presented in figure 7.4. When compared to the pure hoop (1H:0A) loading case, the gradients at the end of the specimen are not as severe. The load is taken predominantly by the transverse matrix and shear components. The boundary effect due to the clamped ends is, again, seen to be limited to a length of approximately $1/2$ a specimen diameter from the tab.

The strain ratio distribution, shown in figure 7.5, demonstrates that the failure throughout the specimen is governed by the tensile transverse failure strain. All distributions are relatively uniform over the entire gage section. The predicted through wall axial stress at failure (64.0 MPa) was found to correlate quite well with the experimental monotonic result (57.5 MPa). As predicted, the actual failure mode is seen to be (helical) transverse matrix cracking along the length of the gage section (see figure 5.6).

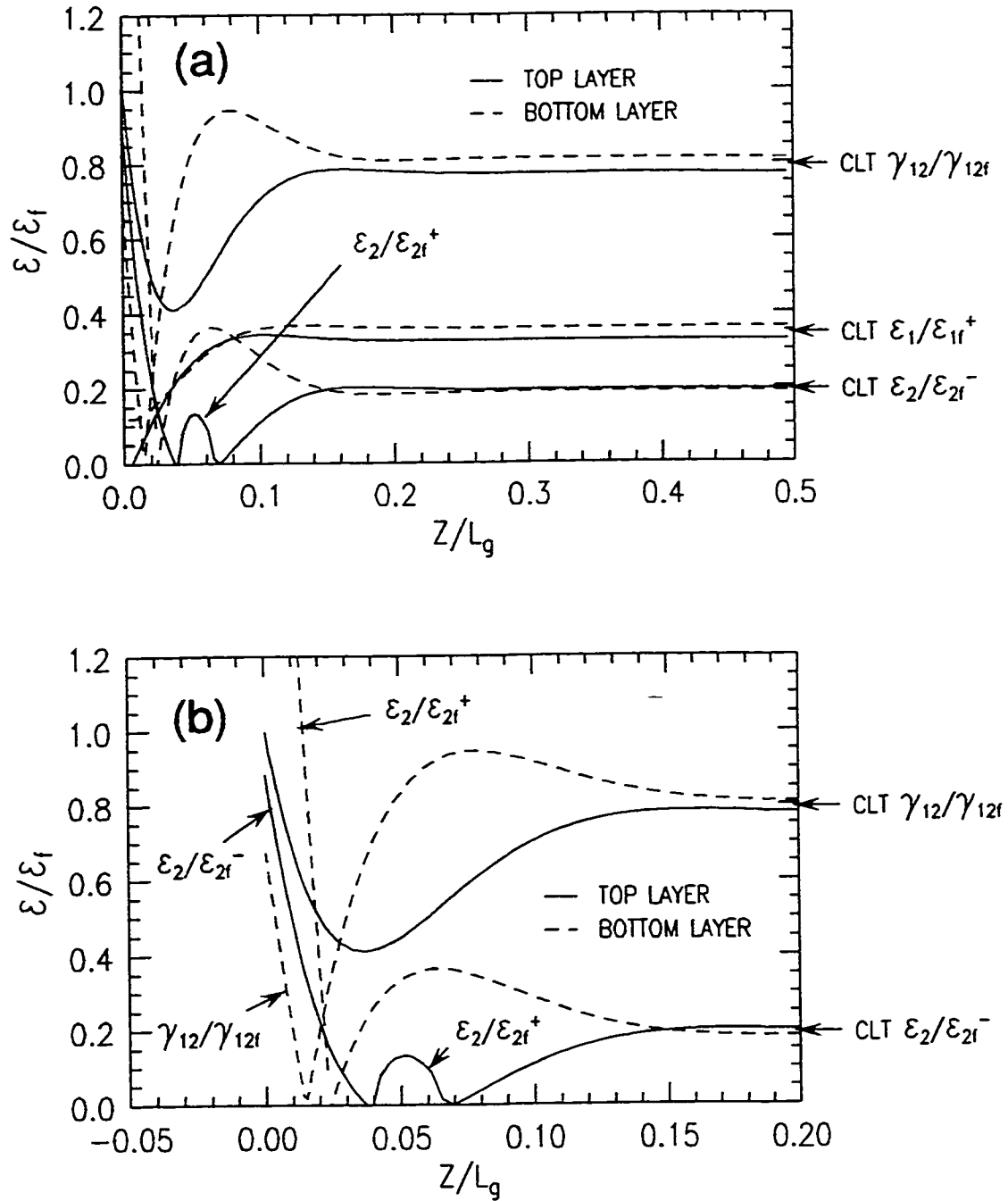


Figure 7.3: In-plane failure strain ratios based on through wall failure for a $[\pm 71^\circ]_s$ glass-fiber reinforced epoxy tubular specimen under pure hoop loading ($1H:0A$) - (σ_h applied = 310.1 MPa); (a) along half gage length, (b) concentration effects at the tab ($\epsilon_1/\epsilon_{1f}^+$ was omitted for clarity).

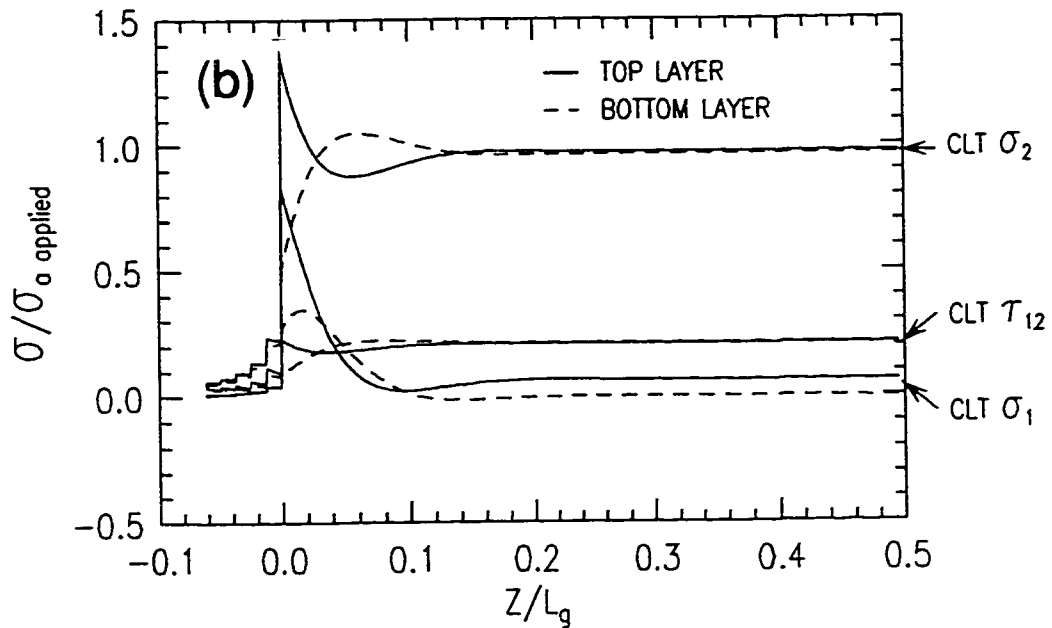
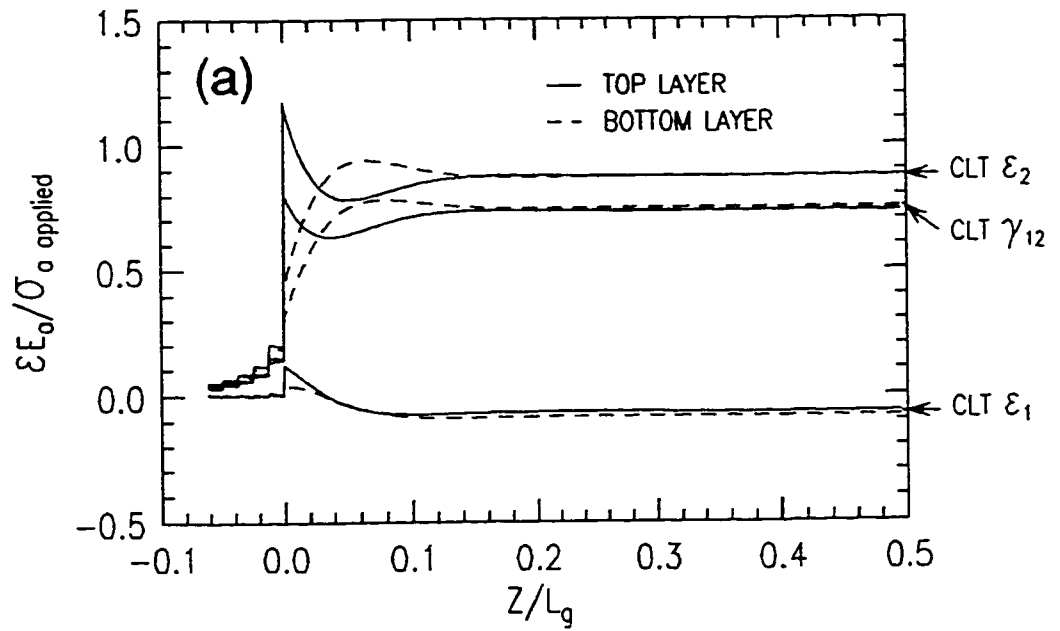


Figure 7.4: Non-dimensional stress (a) and strain (b) distributions along the half gage length of a $[\pm 71^\circ]_S$ glass-fiber reinforced epoxy tubular specimen under pure axial loading (0H:1A).

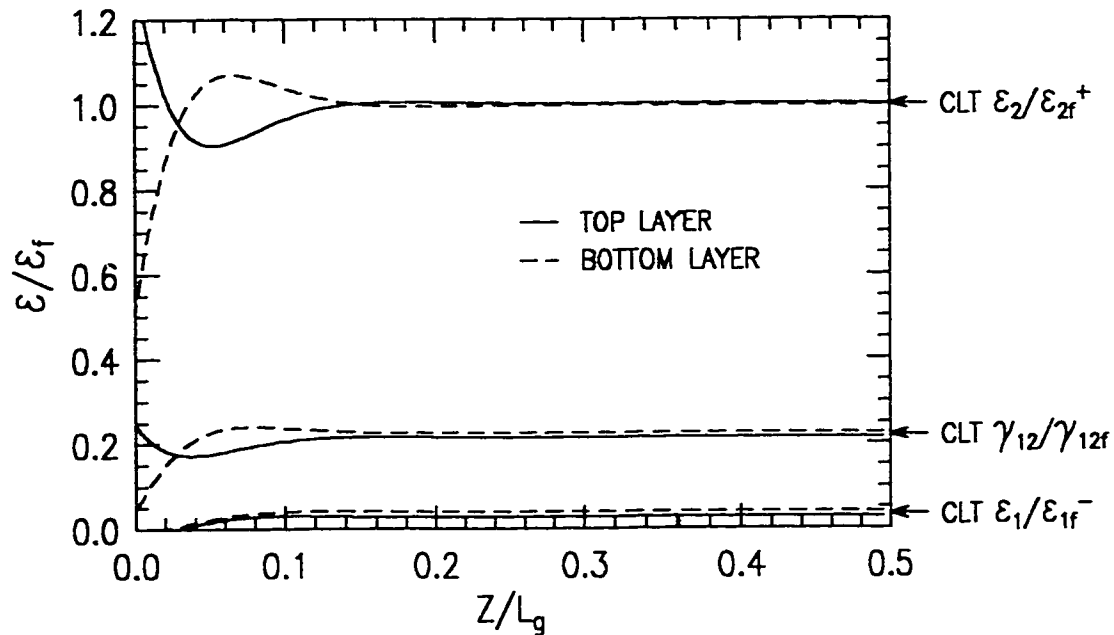


Figure 7.5: *In-plane failure strain ratios based on through wall failure for a $[\pm 71^\circ]_s$ glass-fiber reinforced epoxy tubular specimen under pure axial loading (0H:1A) - (σ_a applied = 64.0 MPa).*

The predicted initiation failure stress (48.2 MPa) was also found to be similar to the experimental results but the location of failure was shown to be at the end of the specimen (at the top layer). Even though damage initiation is predicted at the specimen ends (at the outer layer only), through wall failure is suppressed at this point due to the much lower strains at the inner layer.

The axial stress at failure predicted by classical laminate theory (64.0 MPa) was shown to be identical to that predicted by FEA. This is not surprising since the stress and strain distributions were found to be uniform over the gage section of the specimen.

7.2.3 Loading Based on Netting Analysis

The mechanical stress and strain distributions for the $[\pm 71^\circ]_s$ tubular specimen under (17H:2A) biaxial loading are shown in figure 7.6. These distributions are similar to those of the pure hoop loading case (figure 7.2) with a slight reduction in the transverse (less compressive) and shear strains values throughout the specimen. The

distribution is again characterized by high stress/strain gradients at the end of the specimen converging to uniform values in the gage section.

As shown in figure 7.7, the failure strain ratio distribution is also similar to that found for the pure hoop loading case. One significant difference, however, is the substantial increase in the tensile transverse strain ratio between $z/l_g = 0.02$ and $z/l_g = 0.1$ (parabolic shaped concentration). Although leakage was shown to occur predominantly at the end of the specimens, the maximum point of this concentration ($z/l_g \sim 0.06$) is seen to correspond to the location of a second observed leakage point (see figure 5.17).

The predicted initiation and through wall failure stresses were 85.8 MPa and 393.3 MPa, respectively. Compared to the experimental monotonic (260.1 MPa) and cyclic hoop stress at 10^3 (214.9 MPa), the predicted through wall hoop stress is seen to be 16% and 30% higher, respectively. Similar to the pure hoop loading case, the predicted location for both initiation and through wall failure is at the specimen ends. This, again, is only representative of the observed behaviour under cyclic loading conditions.

7.3 ANALYSIS OF $[\pm 45^\circ]_S$ TUBULAR SPECIMENS

Thermal and mechanical finite element analysis was also performed on the $[\pm 45^\circ]_S$ tubular specimens. The same methodology used in the analysis of the $[\pm 71^\circ]_S$ tubular specimens was invoked here (see introduction to section 7.2). Mechanical strain distributions, however, were calculated for the following biaxial stress ratios: (1H:0A), (2H:1A), (1H:1A), (1H:2A), (1H:8A) and (0H:1A). Predictions were compared to the experimental results and observations from chapter 6.

7.3.1 *Pure Hoop Loading*

The in-plane mechanical stress and strain distributions for the $[\pm 45^\circ]_S$ tubular specimen under pure hoop (1H:0A) loading are shown in figure 7.8. It can be seen in these figures that only moderate stress/strain gradients exist at the ends of the specimen due to the clamping effect of the grips. Similar to the $[\pm 71^\circ]_S$ tubular specimen, the boundary effect for the $[\pm 45^\circ]_S$ specimen is limited to approximately 1/2 a specimen diameter from the tab (~ 19 mm or 0.75 in). The distributions throughout

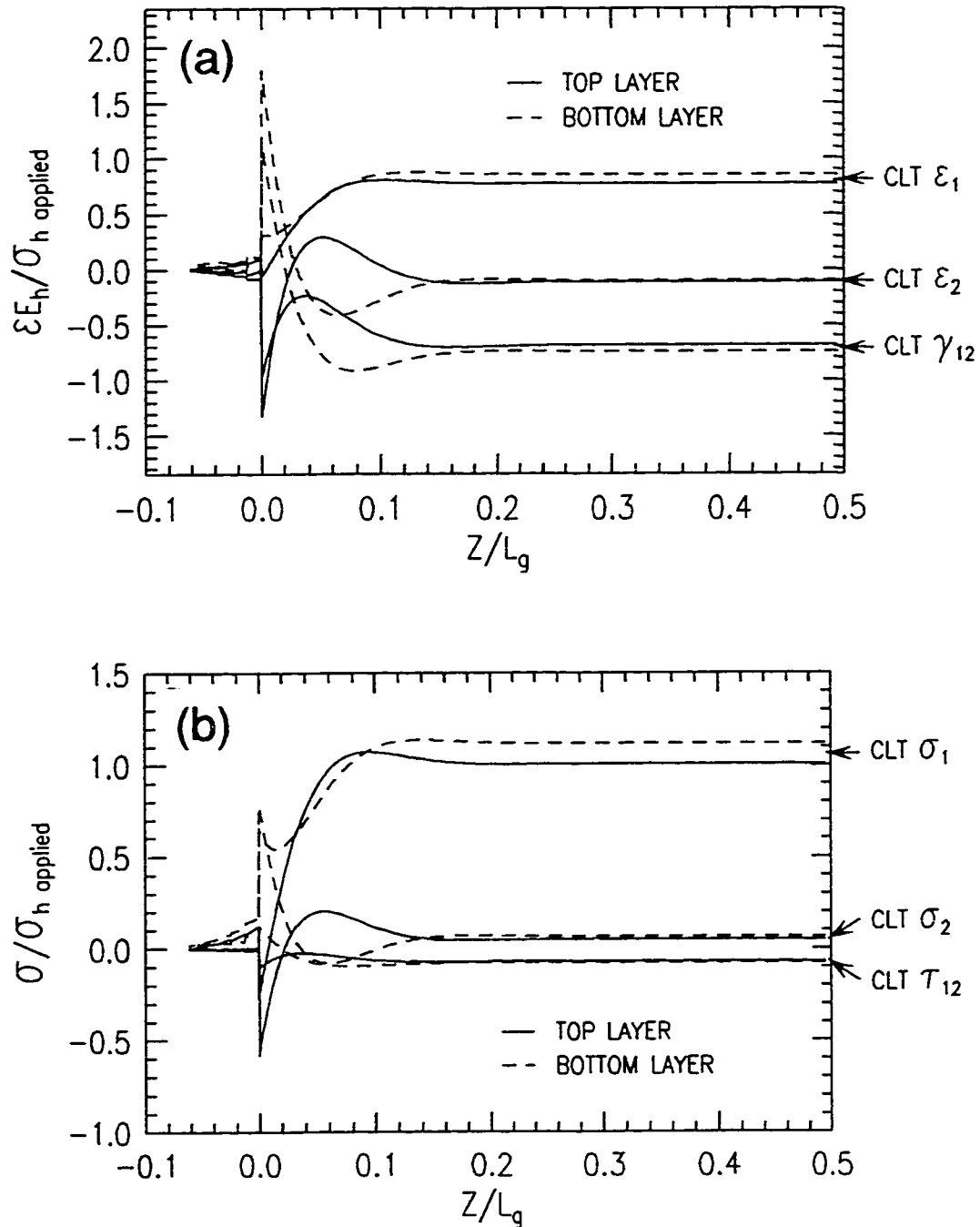


Figure 7.6: Non-dimensional stress (a) and strain (b) distributions along the half gage length of a $[\pm 71^\circ]_s$ glass-fiber reinforced epoxy tubular specimen under (17H:2A) biaxial loading.

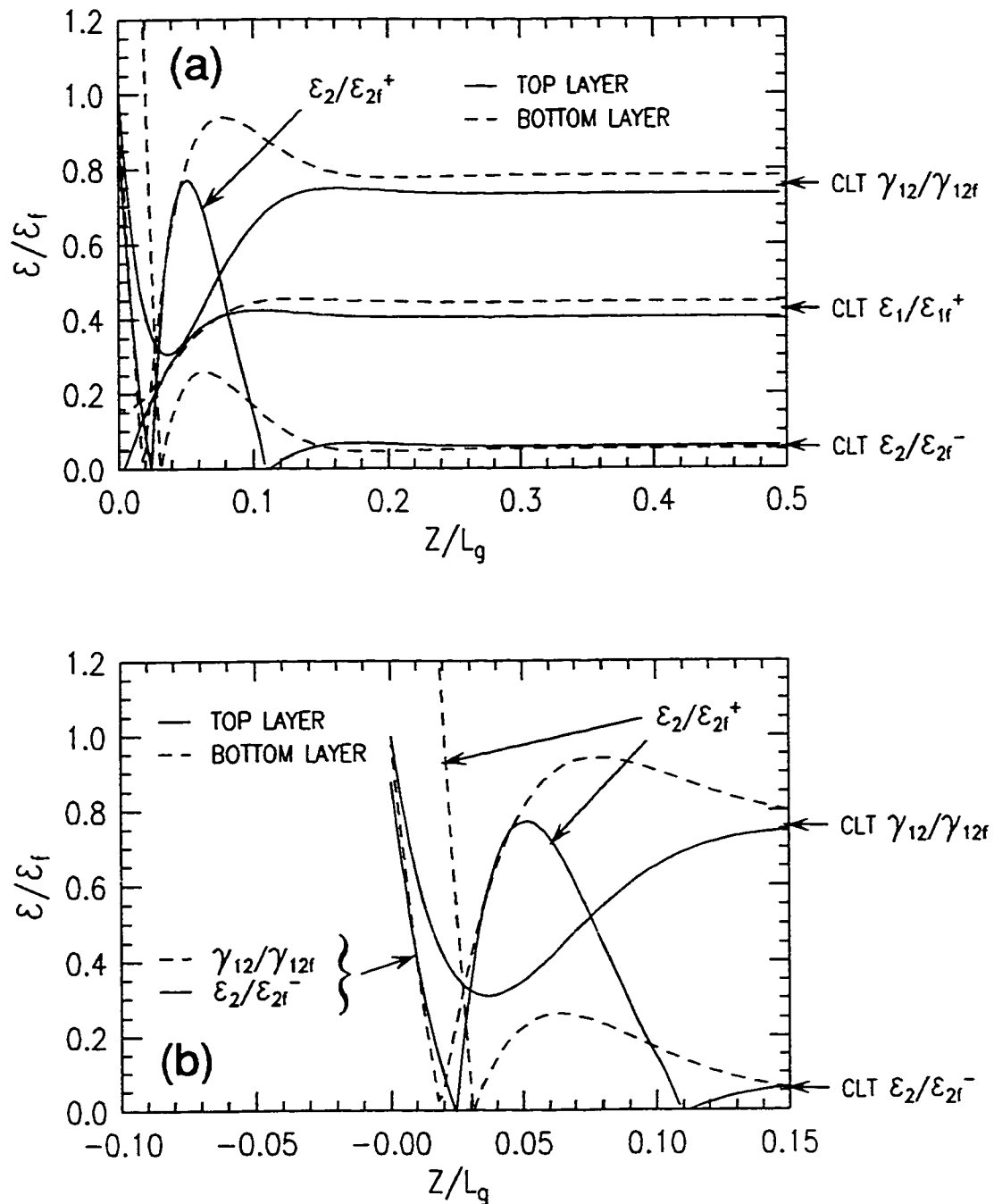


Figure 7.7: In-plane failure strain ratios based on through wall failure for a $[\pm 71^\circ]_s$ glass-fiber reinforced epoxy tubular specimen under (17H:2A) biaxial loading - ($\sigma_{h \text{ applied}} = 393.3 \text{ MPa}$); (a) along half gage length, (b) concentration effects at the tab ($\epsilon_1/\epsilon_{1f}^+$ was omitted for clarity).

the gage section is seen to be dominated by a uniform in-plane shear response, with results converging to the values predicted by classical laminate theory (CLT).

The matrix shear component is also seen to dominate the failure behaviour, as shown by the failure strain distribution in figure 7.9. Although the through wall matrix failure (due to shear) is uniform over most of the gage section (85%), it is seen to be suppressed over a small area at the specimen ends (~ 6 mm in length). This failure distribution is confirmed by the actual weepage pattern observed under cyclic loading (see figure 6.13). The predicted initiation and through wall failure stresses were 67.9 MPa and 88.3 MPa, respectively. The through wall value is seen to correlate, quite well, with the cyclic hoop stress at 10^3 (104.7 MPa) but was significantly smaller than the monotonic stress at failure (229.4 MPa).

7.3.2 Axial Dominated Loading

For the axial dominated (1H:8A) loading ratio, the mechanical stress and strain distributions are presented in figure 7.10. When compared to the pure hoop loading case, the distributions are seen to be very similar over the entire length of the specimen (including the gradients at the end). The distribution is, again, dominated by a uniform in-plane shear response.

The failure strain ratio distribution for the axial dominated (1H:8A) loading case is shown in figure 7.11. It can be seen that the through wall failure mode is predicted to be matrix cracking in the gage section due to the uniformly distributed in-plane shear strains. The predicted initial and through wall axial failure stresses are 69.3 MPa and 100.7 MPa, respectively. The through wall value is seen to correlate with the cyclic stress at 10^3 cycles (104.4 MPa).

7.3.3 Loading Based on Netting Analysis (Equi-biaxial)

The mechanical stress and strain distributions under equi-biaxial (1H:1A) loading are shown in figure 7.12. Once again, moderate stress/strain gradients are present at the specimen ends due to the clamping effect of the grips. Similar to the other loading cases, this effect stabilizes at approximately $1/2$ a specimen diameter from the tab. Compared to the pure hoop (1H:0A) and axial dominated loading cases (1H:8A), however, the distributions throughout the gage section are now dominated

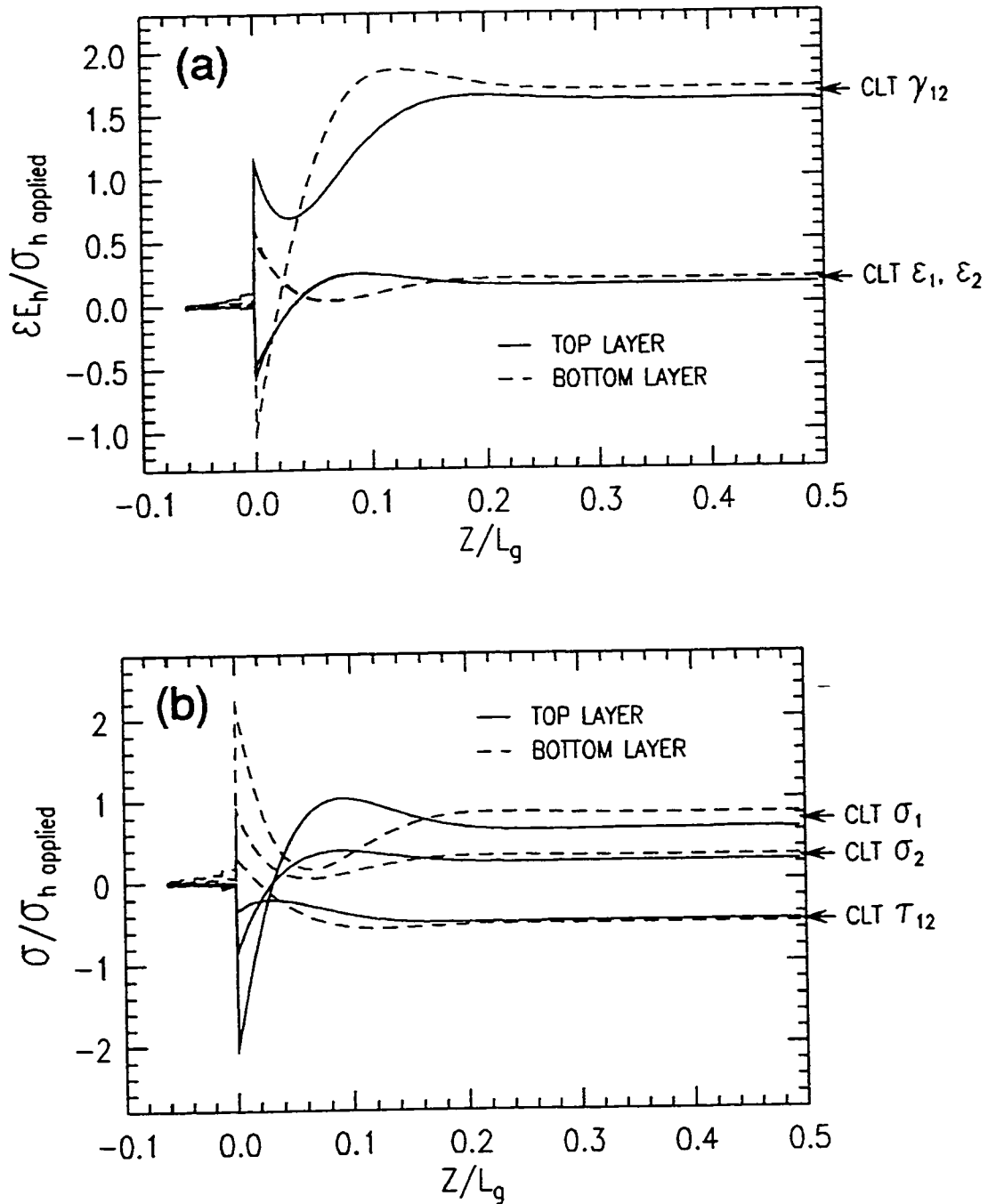


Figure 7.8: Non-dimensional stress (a) and strain (b) distributions along the half gage length of a $[\pm 45^\circ]_S$ glass-fiber reinforced epoxy tubular specimen under pure hoop loading (1H:0A).

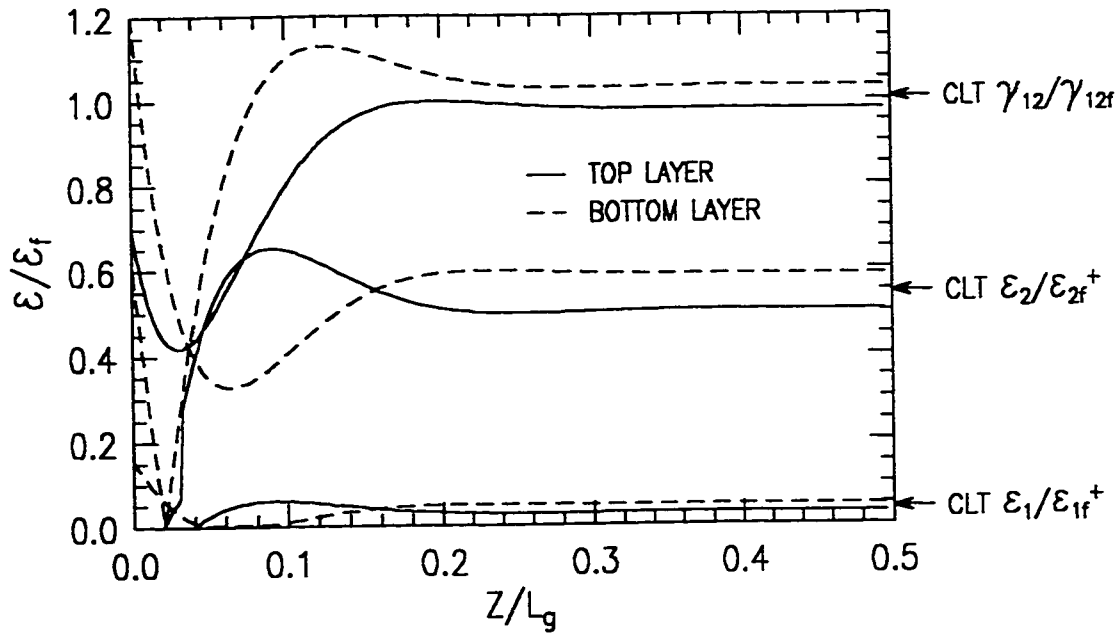


Figure 7.9: In-plane failure strain ratios based on through wall failure for a $[\pm 45^\circ]_S$ glass-fiber reinforced epoxy tubular specimen under pure hoop loading (1H:0A) - (σ_h applied = 88.3 MPa).

by the fiber (ϵ_1) and transverse (ϵ_2) strains.

The relative influence of these strain components on the predicted failure behaviour is demonstrated in figure 7.13. Due to the lower strain to failure in the transverse direction (ϵ_{2f}), matrix cracking is seen to dominate. The predicted through wall failure due to transverse matrix cracking is uniform over most of the gage section (90%). This is again confirmed by the observed weepage pattern under cyclic loading (see figure 6.39). The predicted initiation and through wall failure stresses are 83.2 MPa and 117.1 MPa, respectively. In contrast to observations made for the other loading ratios, the through wall failure stress is seen to be quite conservative compared to both the experimental monotonic (230.7 MPa) and cyclic stress at a life of 10^3 (145.7 MPa).

7.4 PREDICTION OF BIAXIAL FAILURE ENVELOPES

The predicted and experimental biaxial failure envelopes for the $[\pm 71^\circ]_S$ and $[\pm 45^\circ]_S$ tubular specimens are shown in figures 7.14 and 7.15, respectively. Pre-

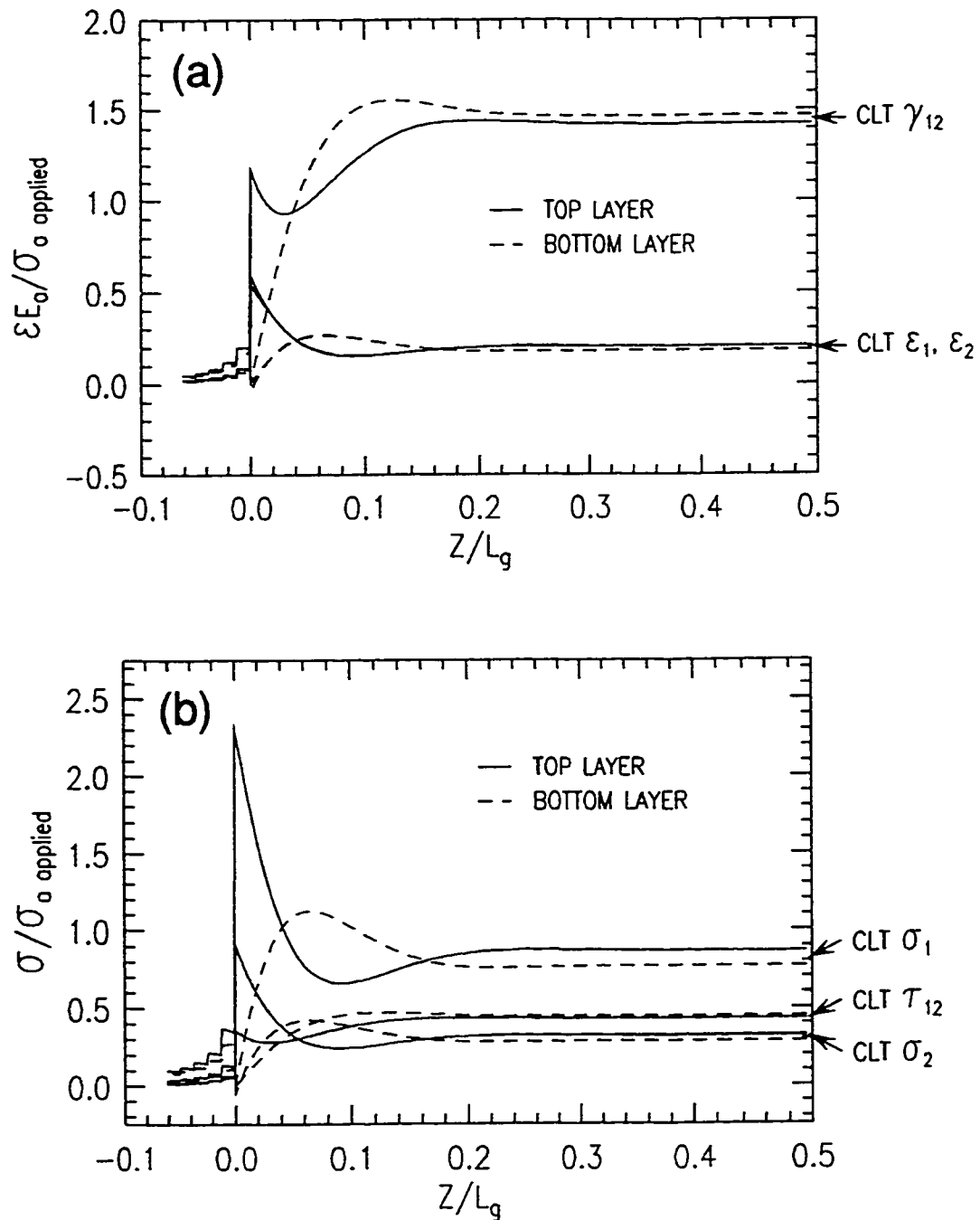


Figure 7.10: Non-dimensional stress (a) and strain (b) distributions along the half gage length of a $[\pm 45^\circ]_s$ glass-fiber reinforced epoxy tubular specimen under axial dominated loading (1H:8A).

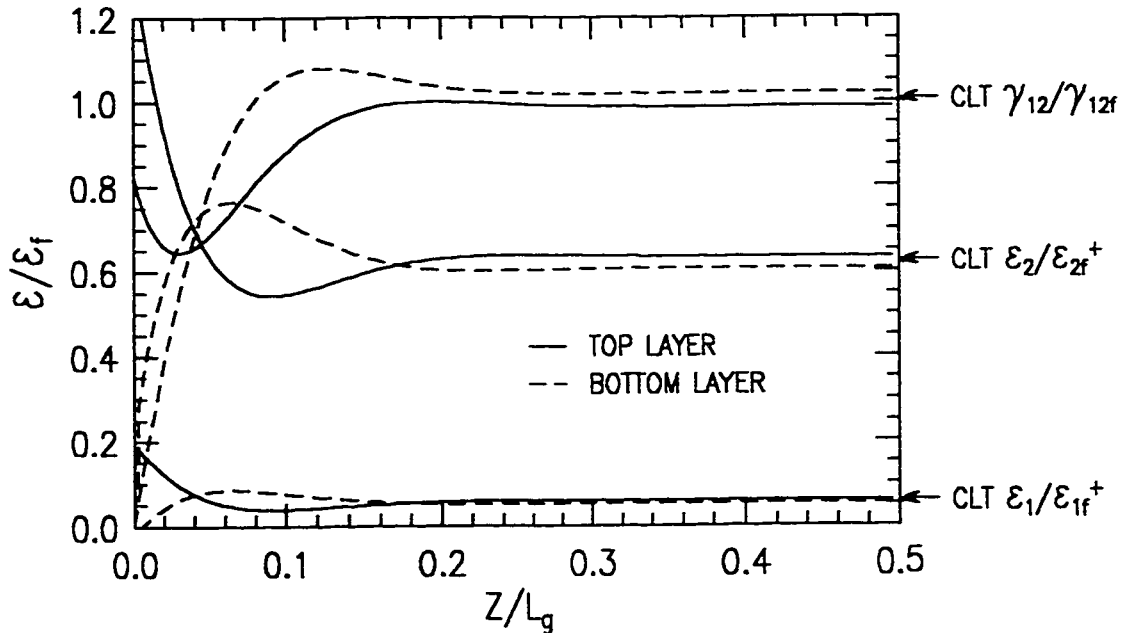


Figure 7.11: *In-plane failure strain ratios based on through wall failure for a $[\pm 45^\circ]_S$ glass-fiber reinforced epoxy tubular specimen under axial dominated biaxial loading (1H:8A) - (σ_h applied = 100.7 MPa).*

dictions based on initiation and through wall failure definitions are provided. The predicted failure points are joined by linear segments to demonstrate the general shape of the envelopes. The predicted and experimental failure results, including failure mode and location, are summarized in tables 7.4 and 7.5.

For both specimen geometries, the through wall assumption is seen to accurately predict the failure mode and location under cyclic loading conditions. This is not surprising since the observed weepage behaviour under cyclic loading was found to be representative of the matrix cracking failures predicted by the analysis. This also explains the symmetry in the cyclic failure envelopes for the $[\pm 45^\circ]_S$ specimens (see figure 6.46). From figures 7.8 and 7.10, it can be seen that there is little difference between the elastic strain distributions for the $[\pm 45^\circ]_S$ hoop and axial dominated loading cases. Although non-linear effects manifest themselves in the monotonic failure envelope, the cyclic (leakage) envelopes are dictated by low strain, matrix damage events. While the $[\pm 71^\circ]_S$ geometry was seen to be affected by specimen end conditions, the elastic stress/strain distributions in the $[\pm 45^\circ]_S$ specimens were very uniform for all loading ratios.

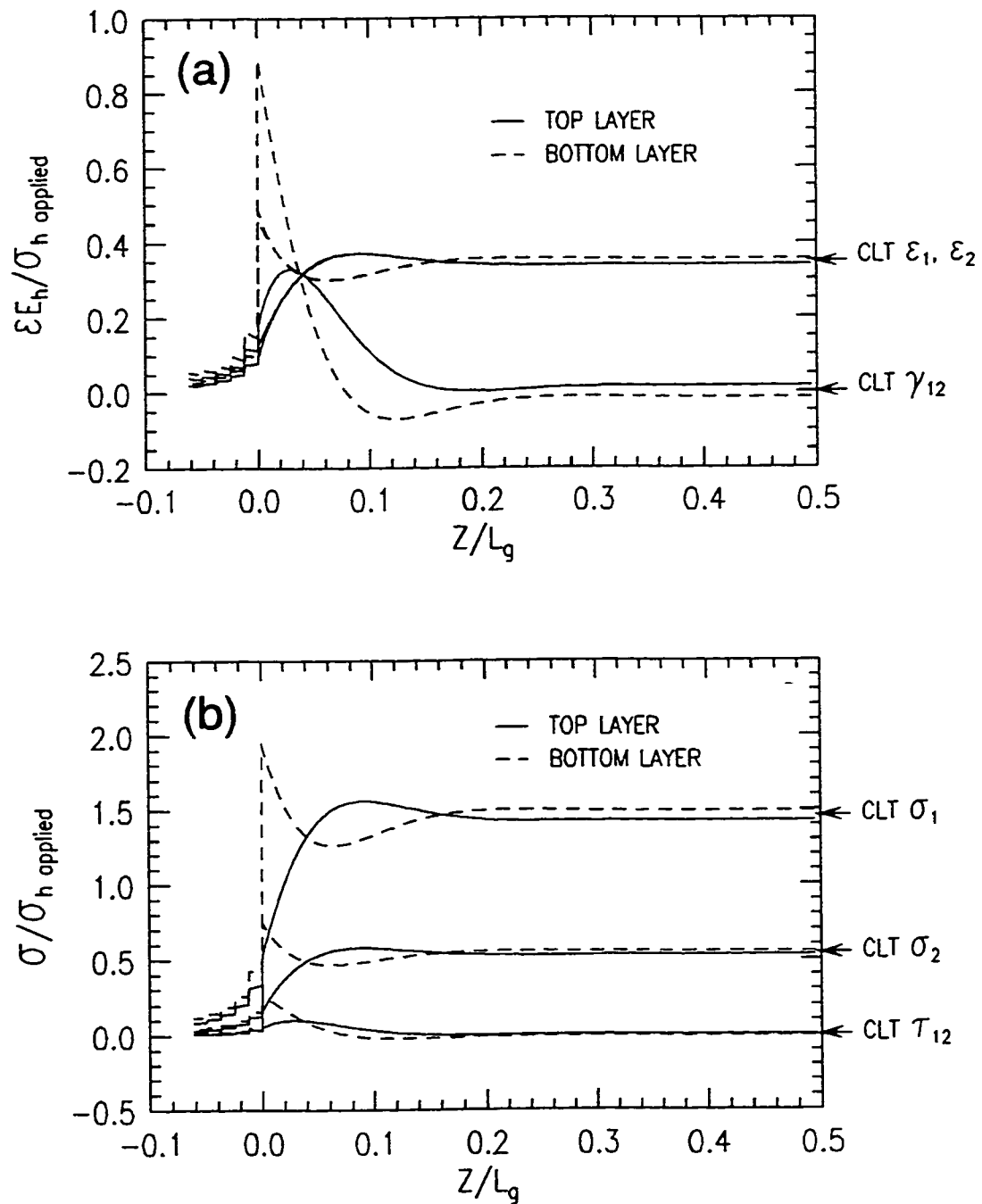


Figure 7.12: Non-dimensional stress (a) and strain (b) distributions along the half gage length of a $[\pm 45^\circ]_s$ glass-fiber reinforced epoxy tubular specimen under equibiaxial loading (1H:1A).

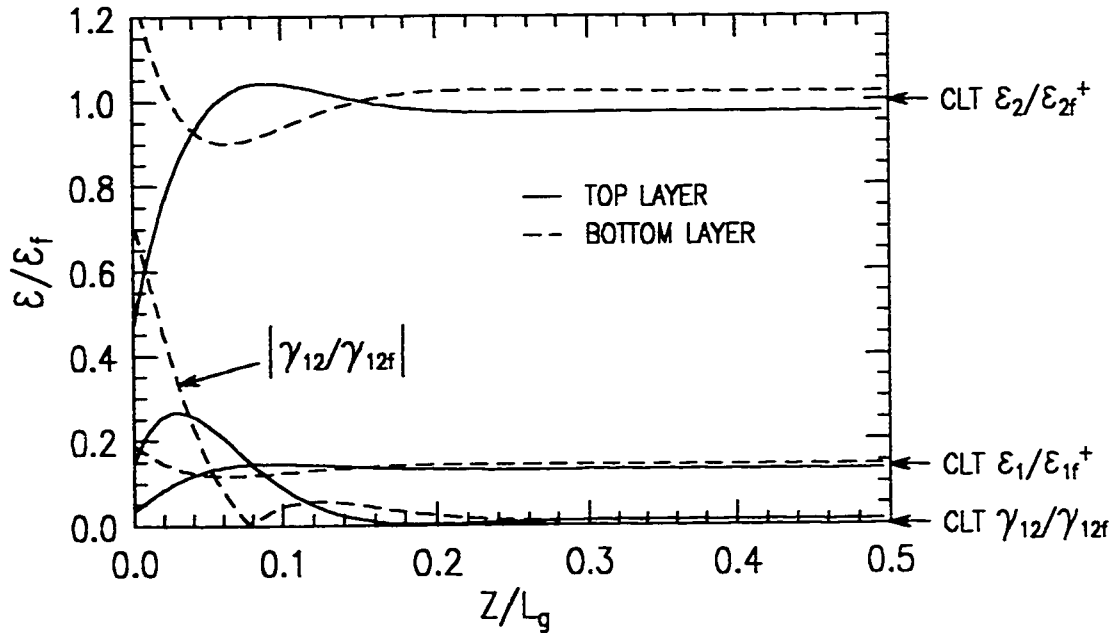


Figure 7.13: In-plane failure strain ratios based on through wall failure for a $[\pm 45^\circ]_S$ glass-fiber reinforced epoxy tubular specimen under equi-biaxial loading (1H:1A) - (σ_h applied = 117.1 MPa).

When compared to the monotonic test results, the observed discrepancies in predicted failure mode and location can be attributed to the competing effects of damage accumulation rate and fluid flow rate (see permeability relation in equation 4.6). Although matrix cracking is typically the first mode of failure observed under monotonic loading, a measurable leakage rate cannot be detected unless sufficient time is provided for fluid to permeate (the initial flow rates are very small). This explains the matrix dominated weepage behaviour observed in other studies for tests conducted for slow monotonic rates [204] and under long-term static loading [160]. Since the monotonic ramp rates used in this study were relatively fast (< 30 minutes to failure), ultimate (fiber) failure was achieved before there was a significant loss in fluid volume. Due to progressive damage and load re-distribution effects, the monotonic failure modes and locations could not be predicted by the current analysis.

In general, the accuracy of the predicted failure stresses is seen to depend upon the specimen geometry, biaxial loading ratio and critical strain values selected. For the $[\pm 71^\circ]_S$ geometry, the initiation and through wall predictions show good correlation to the experimental results for the pure axial (0H:1A) loading case. Under

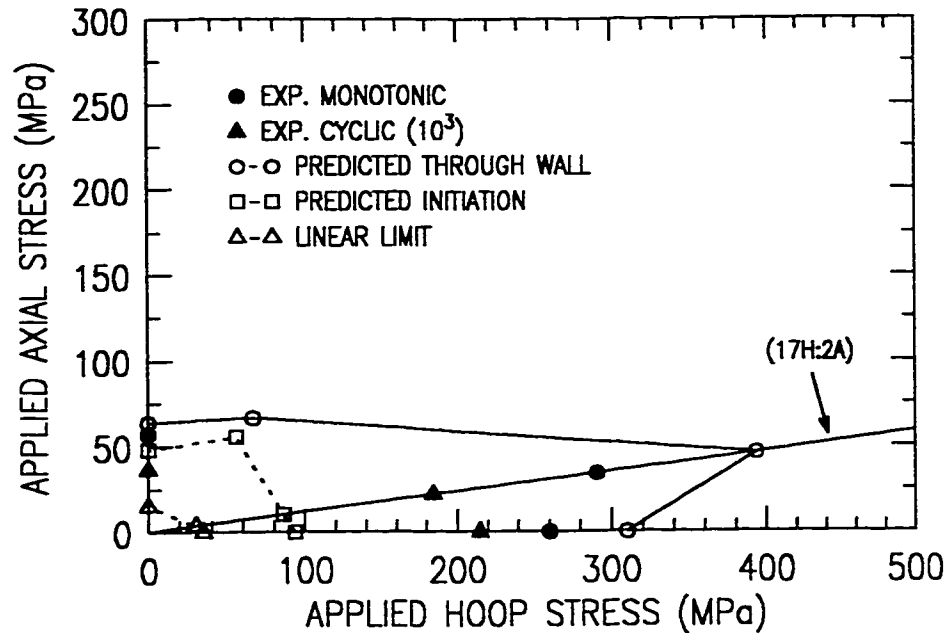


Figure 7.14: Predicted and experimental biaxial failure (leakage) envelopes for $[\pm 71^\circ]_S$ glass-fiber reinforced epoxy tubular specimens in applied stress space.

hoop dominated loading (1H:0A and 17H:2A), however, the predicted through wall failure stresses are seen to be significantly higher than the experimental results. This difference could be due to the delamination failure mode observed at the specimen ends (see section 5.2.2). Since this analysis is restricted to in-plane behaviour, this failure mode is not taken into account. The results imply that the in-plane analysis may be too approximate for the multiaxial stress field at the tab. Although the failure values for this loading case are not exact, the predicted leakage location is seen to correspond to that observed under cyclic loading conditions.

For the $[\pm 45^\circ]_S$ tubular specimens, the predicted through wall failure stresses are seen to best represent low cycle fatigue failure. The predicted stresses for the shear dominated loading ratios (1H:0A and 1H:8A) were seen to correlate to the applied stress level at approximately 10^3 cycles. This is not unexpected since the critical shear strain value used in this analysis ($\gamma_{12f} = 1.3\%$) was similar to the range of cyclic shear strains observed at leakage initiation (see figures 6.20 and 6.34). For the equi-biaxial (1H:1A) loading case, however, the predicted failure stress is lower than the short-term cyclic envelope. Since the behaviour under this loading ratio is dominated by the transverse strain (ϵ_2), the difference between predicted and experimental results

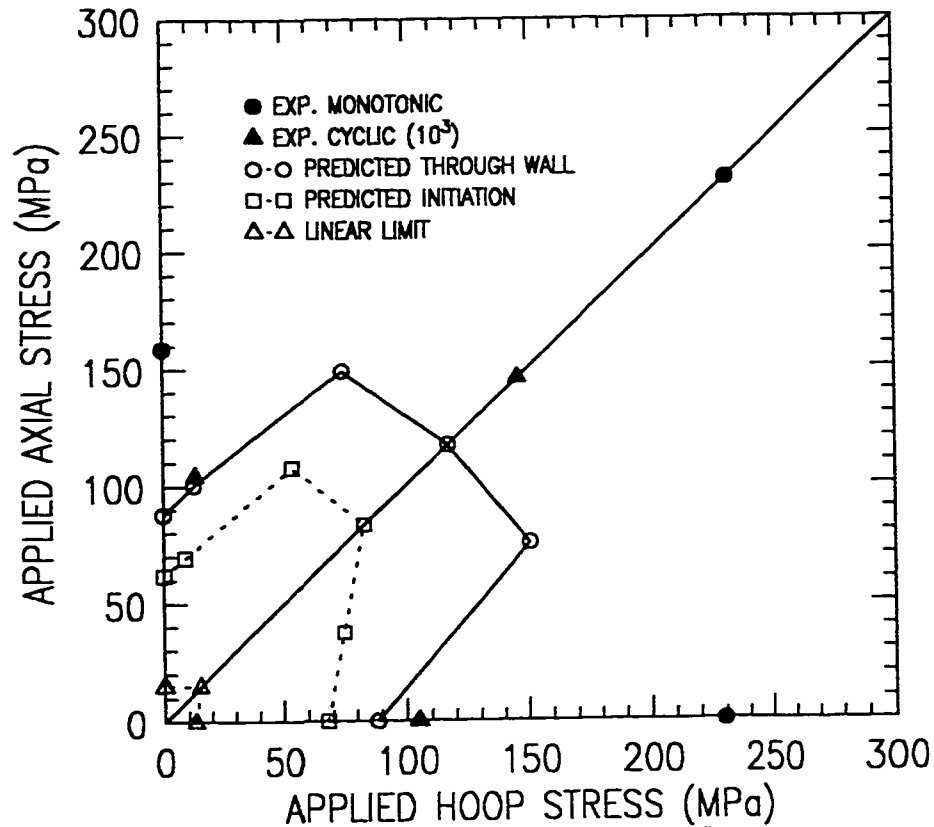


Figure 7.15: Predicted and experimental biaxial failure (leakage) envelopes for $[\pm 45^\circ]_s$ glass-fiber reinforced epoxy tubular specimens in applied stress space.

indicate that the critical transverse strain value (ϵ_{2f}), used in this study, may be low.

The critical failure values (and how they are determined) are seen to have an enormous impact on the predicted failure stresses. Transverse failure strains (ϵ_{2f}), traditionally, have been derived from characterization tests on unidirectional lamina[†]. It has been demonstrated in a number of studies, however, that the in-situ transverse failure strain of a ply within a laminate is affected by the constraint of its neighbouring plies. For tests conducted on $[0^\circ, 90^\circ]_n$ cross-ply coupons, the in-situ transverse strain to failure of the 90° ply has been shown to increase as the thickness of this layer decreases (i.e. as $n \rightarrow 0$) [71, 72]. Critical values derived from unidirectional characterization tests are, therefore, only representative of laminates with very thick layers or negligible constraint.

[†]This was also done in the current study.

Table 7.4: Summary of experimental and predicted failure results for $[\pm 71^\circ]_s$ glass-fiber reinforced epoxy tubular specimens under biaxial loading.

Biaxial Stress Ratio	EXP Mono Failure Stress (MPa)	EXP Cyclic Failure Stress [†] (MPa)	FEA Init Failure Stress (MPa)	FEA Init Failure Mode	FEA Init Failure Location	FEA Wall Failure Stress (MPa)	FEA Wall Failure Modes	FEA Wall Failure Location	CLT Wall Failure Stress (MPa)	CLT Wall Failure Mode
(1H:0A)	260.1(h)	214.9(h)	93.2(h)	$\epsilon_2^+(I)$	END	310.1(h)	$\epsilon_2^+(I)/\gamma_{12}(O)$	END	401.8(h)	γ_{12}
(17H:2A)	291.4(h)	184.4(h)	85.8(h)	$\epsilon_2^+(I)$	END	393.3(h)	$\epsilon_2^+(I)/\gamma_{12}(O)$	END	536.2(h)	γ_{12}
(1H:1A)	N/A	N/A	55.6(a)	$\epsilon_2^+(O)$	END	66.6(a)	$\epsilon_2^+(I/O)$	GAGE	66.7(a)	ϵ_2^+
(0H:1A)	57.5(a)	36.4(a)	48.2(a)	$\epsilon_2^+(O)$	END	64.0(a)	$\epsilon_2^+(I/O)$	GAGE	64.0(a)	ϵ_2^+

* Abbreviations: EXP (Experimental), FEA (Finite Element Analysis), CLT (Classical Laminate Theory), Init (Initiation), Wall (Through Wall), h (Applied Hoop Stress), a (Applied Axial Stress), N/A (Not Available), I (Failure at Inner Surface), O (Failure at Outer Surface).

[†]At 10^3 cycles.

Table 7.5: Summary of experimental and predicted failure results for $[\pm 45^\circ]_s$ glass-fiber reinforced epoxy tubular specimens under biaxial loading.

Biaxial Stress Ratio	EXP Mono Failure Stress (MPa)	EXP Cyclic Failure Stress [†] (MPa)	FEA Init Failure Stress (MPa)	FEA Init Failure Mode	FEA Init Failure Location	FEA Wall Failure Stress (MPa)	FEA Wall Failure Modes	FEA Wall Failure Location	CLT Wall Failure Stress (MPa)	CLT Wall Failure Mode
(1H:0A)	229.4(h)	104.7(h)	67.9(h)	$\epsilon_2^+(I)$	END	88.3(h)	$\gamma_{12}(I/O)$	GAGE	87.8(h)	γ_{12}
(2H:1A)	N/A	N/A	74.8(h)	$\epsilon_2^+(I)$	END	150.7(h)	$\gamma_{12}(I)/\epsilon_2^+(O)$	GAGE	156.8(h)	ϵ_2^+
(1H:1A)	230.7(h)	145.7(h)	83.2(h)	$\epsilon_2^+(I)$	END	117.1(h)	$\epsilon_2^+(I/O)$	GAGE	117.6(h)	ϵ_2^+
(1H:2A)	N/A	N/A	107.7(a)	$\epsilon_2^+(O)$	END	149.0(a)	$\epsilon_2^+(I/O)$	GAGE	156.8(a)	ϵ_2^+
(1H:8A)	N/A	104.4(a)	69.3(a)	$\epsilon_2^+(O)$	END	100.7(a)	$\gamma_{12}(I/O)$	GAGE	100.4(a)	γ_{12}
(0H:1A)	159.0(a)	N/A	62.0(a)	$\epsilon_2^+(O)$	END	88.1(a)	$\gamma_{12}(I/O)$	GAGE	87.8(a)	γ_{12}

* Abbreviations: EXP (Experimental), FEA (Finite Element Analysis), CLT (Classical Laminate Theory), Init (Initiation), Wall (Through Wall), h (Applied Hoop Stress), a (Applied Axial Stress), N/A (Not Available), I (Failure at Inner Surface), O (Failure at Outer Surface).

[†] At 10^3 cycles.

This would explain the relatively low predicted failure stress for the $[\pm 45^\circ]_S$ specimens under equi-biaxial loading (1H:1A). For this loading ratio, the $[\pm 45^\circ]_S$ geometry acts like a cross-ply under biaxial tension. The resulting in-situ transverse strength will be much higher due to ply constraint. Conversely, this also explains the good correlation found between predicted and experimental results for the $[\pm 71^\circ]_S$ specimen under pure axial loading (0H:1A). For this laminate geometry, there is relatively little ply constraint in the axial direction, and, thus, failure strains derived from unidirectional specimens are appropriate.

Even though this constraint phenomenon has been known for some time, no methodologies have been developed to quantify the transverse in-situ failure strength in laminates. It is also not known whether this constraint effect applies to failure under in-plane shear loading. One problem encountered in determining this is that shear failures (at least under monotonic loading) do not produce the same visible crack formations that are found for transverse matrix cracking. Instead, discoloration or whitening of the failure area is observed. Shear failure values, as measured by the various conventional characterization procedures [287–290], often show wide discrepancies. Thus, an appropriate definition of shear failure is also unresolved.

The predicted failure stresses based on the damage initiation definition were found to be quite conservative. This is expected since leakage is predicated by the accumulation of multiple inter-connected cracks, not by their initiation. In addition, the predicted initiation and experimentally observed failure locations were not necessarily the same. This demonstrates the potential error associated with defining the leakage failure based on the initiation definition. When compared to the monotonic limit of linear elastic behaviour, the initiation failure values are seen to be much larger. This suggests that the initial non-linearity observed in the monotonic stress-strain curves may be due to non-linear visco-elastic effects or micro-scale damage accumulation (rather than macroscopic matrix cracking).

CHAPTER 8

Conclusions

From the preceding chapters, it can be seen that the leakage behaviour of fiber reinforced composite tubes can be quite complex. Through careful experimental characterization and numerical modeling, a better understanding of the leakage process under monotonic and cyclic loading conditions has been achieved.

A new biaxial testing machine was developed to conduct the experimental study. This machine is capable of imposing a biaxial state of stress or strain in a tubular specimen through the application of independent differential pressure, axial force and torsion servo-hydraulic control. Stress/strain controlled, monotonic/cyclic, and in-phase/out-of-phase (non-proportional) tests can be performed with this system. Specialized transducer systems to measure load, torque, hoop strain and axial strain have been developed. The associated computer control hardware and software allows for a number of complex user-defined loading and acquisition schemes. The software is a key element in the system since it provides supervisory control tasks (i.e. test initialization, waveform generation, system alarm handling, and automatic waveform adjustment), and allows for efficient management/extraction of the large output datafiles. The ability to measure fluid volume loss and elastic modulus (during cyclic testing) are essential features for characterizing leakage behaviour in fiber reinforced composite specimens.

Specimens were fabricated from pre-impregnated composite tapes (prepregs) using a tube rolling method, in conjunction with an inflatable mandrel molding process. Compared to other fabrication methods which use external pressure for consolidation, the inflatable mandrel technique was found to produce composite tubes without overt defects. The new specimen fabrication methodology is versatile and relatively

inexpensive to implement, and produces high quality laboratory specimens with repeatable material and geometrical characteristics. The specimen design consists of a straight composite tube with bonded aluminum end tabs. This configuration allows for a wide range of specimen geometries and sizes. The tabs provide a precise surface for specimen installation and high pressure seals, and allow for the application of large clamping forces without damage to the composite tube.

Leakage failure in composite tubular specimens can be categorized by two distinct modes: a) abrupt leakage (burst), and b) weepage (slow progressive loss of fluid). By using Darcy's Law for flow through a permeable medium, a relation which defines the fluid flow characteristics in a damaged composite tube is developed (see equation 4.6). From this relation, the leakage rate is shown to be a function of the damage state (permeability), applied pressure, specimen geometry (wall thickness and surface area) and fluid characteristics (viscosity). A new damage parameter, based on the permeability, can be used to define functional failure for weepage type behaviour. For a given laminate geometry and loading condition, the permeability profile can be calculated from the experimentally determined fluid volume loss curves (after appropriate volume corrections are made). By defining a critical damage value for a particular application, the permeability profile can be used to generate the fatigue-life curves.

Biaxial monotonic and cyclic tests were performed on $[\pm 71^\circ]_S$ and $[\pm 45^\circ]_S$ glass-fiber epoxy tubular specimens in the tensile-tensile regime. Failure location, macroscopic failure mode, and leakage failure stress were found to be dependent upon the lay-up geometry, applied biaxial loading ratio and loading type (monotonic versus cyclic). In general, specimens under monotonic loading were seen to fail by abrupt leakage (burst), while those subjected to cyclic loading failed by weepage. This difference in failure mode can be attributed to the competing effects of damage accumulation rate and fluid loss rate (i.e. an observable leakage rate can only be detected if sufficient damage or time is available for fluid to flow). In addition to this difference in failure mode, the shapes of monotonic and cyclic leakage envelopes were not the same. This would suggest that models used to predict the cyclic envelope based on the monotonic envelope [198, 291, 292], may be inappropriate for the leakage failure definition.

For the $[\pm 71^\circ]_S$ tubular specimens, general anisotropy with respect to the applied loading directions (hoop and axial) was demonstrated for both monotonic and

cyclic failure envelopes. The mode of failure under pure axial loading was found to be similar for both monotonic and cyclic loading (single predominant helical fracture through gage section). For hoop dominated loading, however, monotonic failure occurred by localized burst failure (fiber breakage) close to the specimen ends. For the cyclic tests, leakage was observed to originate from the end tabs due to intra- and inter-laminar matrix cracking. The observed end failures suggest that specimen end reinforcement may be necessary for this laminate geometry under hoop dominated loading conditions.

For the $[\pm 45^\circ]_S$ geometry, all specimens were seen to fail in the gage section for both monotonic and cyclic loading conditions. While the failure under monotonic loading was catastrophic (abrupt leakage), the cyclic failure mode was characterized by uniformly distributed matrix cracking throughout the specimen. The cyclic creep strain and elastic stiffness reduction were measured in an attempt to correlate physical damage parameters to leakage failure. From these measurements, the saturation of transverse matrix cracks was quite distinguishable. Although leakage was seen to occur after this initial crack saturation, no distinct correlation was found between leakage initiation life and the damage parameters. This is explained by the fact that leakage is governed not only by the formation of cracks, but also by their coalescence and inter-connectivity through the wall thickness. The use of stiffness reduction as a criterion for leakage failure, therefore, may result in unnecessarily conservative designs.

Based on the experimentally determined damage parameters, and micrographic examination, three distinct stages of damage progression occur under cyclic loading. The first stage is characterized by the rapid accumulation of transverse matrix cracks until a saturation point is reached. These cracks are seen to span the layer thickness and propagate along the fiber direction. The total number of cracks in a particular layer is governed by the ply thickness, the location of the ply within the laminate, and the fiber angle orientation of the layer with respect to the applied loads. For this first stage, no measurable leakage is observed.

The second stage of damage progression begins at the point of transverse crack saturation, and is characterized by a significantly slower damage accumulation rate. During this stage, fluid loss begins to occur. The transfer of fluid between plies takes place at the intersection sites of transverse cracks in adjacent layers (verified by the

formation of uniformly distributed oil droplets on the surface). The rate of fluid loss is seen to gradually increase due to the formation of interlaminar cracks originating from the existing transverse crack field.

The last stage of damage progression is characterized by the development of significant macroscopic damage (i.e. fiber breakage). This results in abrupt fluid loss due to the formation of a dominant leakage path.

The prediction of long-term behaviour, based on the monotonic linear elastic limit, was investigated. In general, these predictive envelopes were seen to be very conservative (based on the extrapolated estimates from the fatigue-life relations). No consistent relationship between the linear limit and long-term cyclic envelopes was found to exist. The deficiency of this approximation may lie in the fact that the non-linearity observed in the monotonic stress-strain curves may not necessarily be due to the initiation of macroscopic damage, but may be a result of visco-elastic effects or microstructural damage accumulation. In addition, the monotonic loading rate has been shown to affect this linear elastic limit [204]. The determination of the linear limit may also be too subjective, particularly when examining data at different stress-strain scales.

The finite element method, used in conjunction with the maximum strain failure criterion and through wall failure definition, was seen to accurately predict failure modes and locations for all specimens exhibiting weepage type failures (i.e. cyclic loading). The prediction of applied failure stresses, however, was inconsistent. The accuracy of the predicted failure stresses is seen to depend upon the specimen geometry, biaxial loading ratio and critical strain values selected. While classical laminate theory (CLT) was shown to reasonably predict the initial elastic behaviour of all stress-strain responses, its use in predicting failure in the tubular specimens was accurate only when the distribution of stresses and strains (which contribute to failure) were uniform along the gage section.

REFERENCES

- [1] F Ellyin, J Wolodko, G Murphy, and J Graham. *Advanced Composite Materials with Application to Bridges*, chapter 5 - Material Processing and Manufacturing Technology, pages 126–178. Canadian Society for Civil Engineering, 1991.
- [2] M Munro. Review of manufacturing of fiber composite components by filament winding. *Polymer Composites*, 9(5):352–359, 1988.
- [3] R A Simonds, W Stinchcomb, and R M Jones. Mechanical behavior of braided composite materials. In J D Whitcomb, editor, *Composite Materials: Testing and Design (Eighth Conference)*, ASTM STP 972, pages 438–453, Philadelphia, 1988. American Society for Testing and Materials.
- [4] J H Campbell and J L Kittelson. The tape winding process and applications. *Composite Polymers*, 4(6):423–437, 1991.
- [5] R M Jones. *Mechanics of Composite Materials*. Scripta Book Company, 1975.
- [6] I M Daniel and O Ishai. *Engineering Mechanics of Composite Materials*. Oxford University Press, 1994.
- [7] S W Tsai. A survey of macroscopic failure criteria for composite materials. *Journal of Reinforced Plastics and Composites*, 3:40–62, January 1984.
- [8] M N Nahas. Survey of failure and post-failure theories of laminated fiber-reinforced composites. *Journal of Composites Technology and Research*, 8(4):138–153, 1986.
- [9] P Labossiere and K W Neale. Macroscopic failure criteria for fibre-reinforced composite materials. *Solid Mechanics Archives*, 12(2):439–450, 1987.
- [10] M J Owen and D J Rice. Biaxial strength behaviour of glass fabric-reinforced polyester resins. *Composites*, 12(1):13–25, 1981.
- [11] M A Zocher, D H Allen, S E Groves, and W W Feng. Evaluation of first ply failure in a three-dimensional load space. *Journal of Composite Materials*, 29(12):1649–1678, 1995.

-
- [12] M J Hinton, P D Soden, and A S Kaddour. Strength of composite laminates under biaxial loads. *Applied Composite Materials*, 3:151–162, 1996.
- [13] I Shahid and F-K Chang. An accumulative damage model for tensile and shear failures of laminated composite plates. *Journal of Composite Materials*, 29(7):926–981, 1995.
- [14] C C Chamis, P L N Murthy, and L Minnetyan. Progressive fracture of polymer matrix composite structures. *Theoretical and Applied Fracture Mechanics*, 25:1–15, 1996.
- [15] C E Harris, T W Coats, D H Allen, and D C Lo. A progressive damage model and analysis methodology for predicting the residual strength of composite laminates. *Journal of Composites Technology and Research*, 19(1):3–9, 1997.
- [16] C K H Dharan. Fatigue failure mechanisms in a unidirectionally reinforced composite material. In *Fatigue of Composite Materials, ASTM STP 569*, pages 171–188, Philadelphia, 1975. American Society for Testing and Materials.
- [17] H T Hahn and J G Williams. Compression failure mechanisms in unidirectional composites. In J M Whitney, editor, *Composite Materials: Testing and Design (Seventh Conference), ASTM STP 893*, pages 115–139, Philadelphia, 1986. American Society for Testing and Materials.
- [18] P M Jelf and N A Fleck. Compression failure mechanisms in unidirectional composites. *Journal of Composite Materials*, 26(18):2706–2726, 1992.
- [19] D Hull. *An Introduction to Composite Materials*. Cambridge University Press, 1981.
- [20] C Wood and W Bradley. A new technique to study the interfacial strength and transverse cracking scenario in composite materials. In C J Spragg and L T Drzal, editors, *Fiber, Matrix, and Interface Properties, ASTM STP 1290*, pages 132–151, Philadelphia, 1996. American Society for Testing and Materials.
- [21] D J Nicholls. Effect of stress biaxiality on the transverse tensile strain-to-failure of composites. In J M Whitney, editor, *Composite Materials: Testing and Design (Seventh Conference), ASTM STP 893*, pages 109–114, Philadelphia, 1986. American Society for Testing and Materials.
- [22] L E Asp, L A Berglund, and P Gudmundson. Effects of a composite-like stress state on the fracture of epoxies. *Composites Science and Technology*, 53:27–37, 1995.

-
- [23] R S Kody and A J Lesser. Deformation and yield of epoxy networks in constrained states of stress. *Journal of Materials Science*, 32:5637–5643, 1997.
- [24] J B Koeneman and T P Kicher. Creep behavior of elastic fiber/epoxy matrix composite materials. In *Composite Materials: Testing and Design (Second Conference)*, ASTM STP 497, pages 503–515, Philadelphia, 1972. American Society for Testing and Materials.
- [25] D Kujawski and F Ellyin. Rate/frequency-dependent behaviour of fiber-glass/epoxy laminates in tensile and cyclic loading. *Composites*, 26:719–723, 1995.
- [26] D W Scott, J S Lai, and A-H Zureick. Creep behavior of fiber-reinforced polymeric composites: A review of the technical literature. *Journal of Reinforced Plastics and Composites*, 14:588–617, 1995.
- [27] T J Lu, X Ji, and X R Gu. The effect of resin properties on the strength of filamentary structures. *Journal of Strain Analysis*, 24(2):107–113, 1989.
- [28] D Cohen and K A Lowe. The influence of epoxy matrix properties on delivered fiber strength in filament wound composite pressure vessels. *Journal of Reinforced Plastics and Composites*, 10:112–131, 1991.
- [29] S Liu and J A Nairn. The formation and propagation of matrix microcracks in cross-ply laminates during static loading. *Journal of Reinforced Plastics and Composites*, 11:158–178, February 1992.
- [30] P W M Peters and G S Springer. Effects of cure and sizing on fiber-matrix bond strength. *Journal of Composite Materials*, 21:157–171, 1987.
- [31] M F Horstemeyer and G H Staab. Interface debonding in fatigue cycling of glass reinforced plastics. *Journal of Reinforced Plastics and Composites*, 9:446–455, September 1990.
- [32] S Subramanian, J S Elmore, W W Stinchcomb, and K L Reifsnider. Influence of fiber-matrix interphase on the long-term behavior of graphite/epoxy composites. In R B Deo and C R Saff, editors, *Composite Materials: Testing and Design (Twelfth Volume)*, ASTM STP 1274, pages 69–87, Philadelphia, 1996. American Society for Testing and Materials.
- [33] R Pyrz. Disorder and fracture model for transversely loaded composite materials. In *Proceedings of the 4th International Conference on Computer Aided Assessment and Control (Fukuoka, Japan)*, 1996.

-
- [34] M J Owen, J R Griffiths, and M S Found. Biaxial stress fatigue testing of thin-walled GRP cylinders. In *Proceedings of the 1975 International Conference on Composite Materials. Geneva, Switzerland (April 7-11)/Boston, USA (April 14-18)*, pages 917-941, 1975.
- [35] J P Faivre and R Muller. Fatigue strength of a glass/epoxy composite. *Composite Polymers*, 4(6):375-385, 1991.
- [36] S R Swanson, D S Cairns, M E Gyll, and D Johnson. Compression fatigue response for carbon fiber with conventional and toughened epoxy matrices with damage. *Journal of Engineering Materials and Technology*, 115:116-121, January 1993.
- [37] S M Spearing, P A Lagace, and H L N McManus. On the role of lengthscale in the prediction of failure of composite structures: Assessment and needs. *Applied Composite Materials*, 5:139-149, 1998.
- [38] H T Hahn and R Y Kim. Fatigue behavior of composite laminate. *Journal of Composite Materials*, 10:156-180, April 1976.
- [39] S Kellas and J Morton. Strength scaling in fiber composites. *AIAA Journal*, 30(4):1074-1080, 1992.
- [40] K E Jackson, S Kellas, and J Morton. Scale effects in the response and failure of fiber reinforced composite laminates loaded in tension and in flexure. *Journal of Composite Materials*, 26(18):2674-2705, 1992.
- [41] T K O'Brien and S Salpekar. Scale effects on the transverse tensile strength of graphite/epoxy composites. In E T Camponeschi, Jr., editor, *Composite Materials: Testing and Design (Eleventh Volume)*, ASTM STP 1206, pages 23-52, Philadelphia, 1993. American Society for Testing and Materials.
- [42] B D Harper, G H Staab, and R S Chen. A note on the effects of voids upon the hygral and mechanical properties of as4/3502 graphite/epoxy. *Journal of Composite Materials*, 21:280-289, 1987.
- [43] J R Wood and M G Bader. Void control for polymer-matrix composites (1): Theoretical and experimental methods for determining the growth and collapse of gas bubbles. *Composites Manufacturing*, 5(3):139-147, 1994.
- [44] C W Dill, S M Tipton, E H Glaessgen, and K D Branscum. Fatigue strength reduction imposed by porosity in a fiberglass composite. In *Damage Detection in Composite Materials*, ASTM STP 1128, pages 152-162, Philadelphia, 1992. American Society for Testing and Materials.

- [45] J Bai, P Seeleuthner, and P Bompard. Mechanical behaviour of $\pm 55^\circ$ filament-wound glass-fibre/epoxy-resin tubes: I. microstructural analysis, mechanical behaviour and damage mechanisms of composite tubes under pure tensile loading, pure internal pressure, and combined loading. *Composites Science and Technology*, 57:141–153, 1997.
- [46] F Ellyin, D Kujawski, and T Gorr. The effect of void content on the monotonic and fatigue properties of fiberglass/epoxy laminates. In *CANCOM93. Second Canadian International Composites Conference and Exhibition*, pages 615–622, Montreal, Canada, 1993. Canadian Association for Composite Structures and Materials.
- [47] S F M Almeida and Z S N Neto. Effect of void content on the strength of composite laminates. *Composite Structures*, 28(2):139–148, 1994.
- [48] P Olivier, J P Cottu, and B Ferret. Effects of cure cycle pressure and voids on some mechanical properties of carbon/epoxy laminates. *Composites*, 26:509–515, 1995.
- [49] A L Highsmith, J J Davis, and K L E Helms. The influence of fiber waviness on the compressive behavior of unidirectional continuous fiber composites. In G C Grimes, editor, *Composite Materials: Testing and Design (Tenth Volume)*, ASTM STP 1120, pages 20–36, Philadelphia, 1992. American Society for Testing and Materials.
- [50] H M Hsiao and I M Daniel. Effect of fiber waviness on stiffness and strength reduction of unidirectional composites under compressive loading. *Composites Science and Technology*, 56:581–593, 1996.
- [51] D J Bradley, D O Adams, and H E Gascoigne. Interlaminar strains and compressive reductions due to nested layer waviness in composite laminates. *Journal of Reinforced Plastics and Composites*, 17(11):989–1011, 1998.
- [52] M R Piggott. The effect of fibre waviness on the mechanical properties of unidirectional fibre composites: A review. *Composites Science and Technology*, 53:201–205, 1995.
- [53] H K Telegadas and M W Hyer. The influence of layer waviness on the stress state in hydrostatically loaded cylinders: Failure and predictions. *Journal of Reinforced Plastics and Composites*, 11:127–145, 1992.
- [54] T Stecenko and M R Piggott. Fiber waviness and other mesostructures in filament wound materials. *Journal of Reinforced Plastics and Composites*, 16(18):1659–1674, 1997.

-
- [55] V B Antokhonov, A S Struchkov, V N Bulmanis, and Y I Gusev. Effect of design and technological factors on the strain capacity and strength of cross-reinforced wound composites. *Mechanics of Composite Materials*, 24(4):467–475, 1988.
- [56] A M Zakrzhevskii and V V Khitrov. Effect of interweaving on the load-carrying capacity of wound thick-walled rods of composites in torsion. *Mechanics of Composite Materials*, 24(4):516–523, 1988.
- [57] D W Radford. Cure shrinkage induced warpage in flat uni-axial composites. *Journal of Composites Technology and Research*, 15(4):290–296, 1993.
- [58] K S Olofsson. Stress development in wet filament wound pipes. *Journal of Reinforced Plastics and Composites*, 16(4):372–390, 1997.
- [59] B S Kim and T F Lehnhoff. Stresses induced in fiber-reinforced tubes due to changes in temperature and moisture. *Journal of Engineering Materials and Technology*, 117:228–234, April 1995.
- [60] M A Stone, I F Schwartz, and H D Chandler. Residual stresses associated with post-cure shrinkage in GRP tubes. *Composites Science and Technology*, 57:47–54, 1997.
- [61] L K Jain and Y W Mai. Stresses and deformations induced during manufacturing. part i: Theoretical analysis of composite shells and cylinders. *Journal of Composite Materials*, 31(7):672–695, 1997.
- [62] R Y Kim and H T Hahn. Effect of curing stresses on the first ply failure in composite laminates. *Journal of Composite Materials*, 13:2–16, January 1979.
- [63] K W Garrett and J E Bailey. Multiple transverse fracture in 90° cross-ply laminates of a glass fibre-reinforced polyester. *Journal of Materials Science*, 12:157–168, 1977.
- [64] A L Highsmith and K L Reifsnider. Stiffness-reduction mechanisms in composite laminates. In K L Reifsnider, editor, *Damage in Composite Materials*, ASTM STP 775, pages 103–117, Philadelphia, 1982. American Society for Testing and Materials.
- [65] M D Kistner, J M Whitney, and C E Browning. First-ply failure of graphite/epoxy laminates. In J R Vinson and M Taya, editors, *Recent Advances in Composites in the United States and Japan*, ASTM STP 864, pages 44–61, Philadelphia, 1985. American Society for Testing and Materials.

-
- [66] J W Hoover, D Kujawski, and F Ellyin. Transverse cracking of symmetric and unsymmetric glass-fibre/epoxy-resin laminates. *Composites Science and Technology*, 57:1513–1526, 1997.
- [67] S L Ogin, P A Smith, and P W R Beaumont. Matrix cracking and stiffness reduction during fatigue of a (0/90)_s GFRP laminate. *Composites Science and Technology*, 22:23–31, 1985.
- [68] M C Lafarie-Frenot and C Henaff-Gardin. Formation and growth of 90° ply fatigue cracks in carbon/epoxy laminates. *Composites Science and Technology*, 40:307–324, 1991.
- [69] R H Moore and D A Dillard. Time-dependent matrix cracking in cross-ply laminates. *Composites Science and Technology*, 39:1–12, 1990.
- [70] R D Jamison, K Shulte, K L Reifsnider, and W W Stinchcomb. Characterization and analysis of damage mechanisms in tension-tension fatigue of graphite/epoxy laminates. In *Effects of Defects in Composite Materials, ASTM STP 836*, pages 21–55, Philadelphia, 1984. American Society for Testing and Materials.
- [71] A Parvizi, K W Garrett, and J E Bailey. Constrained cracking in glass fibre-reinforced epoxy cross-ply laminates. *Journal of Materials Science*, 13:195–201, 1978.
- [72] D L Flagg and M H Kural. Experimental determination of the in situ transverse lamina strength in graphite/epoxy laminates. *Journal of Composite Materials*, 16:103–116, 1982.
- [73] C T Herakovich. Influence of layer thickness on the strength of angle-ply laminates. *Journal of Composite Materials*, 16:216–227, May 1982.
- [74] R B Pipes, B E Kaminski, and N J Pagano. Influence of the free edge upon the strength of angle-ply laminates. In *Analysis of Test Methods for High Modulus Fibers and Composites, ASTM STP 521*, pages 218–228, Philadelphia, 1973. American Society for Testing and Materials.
- [75] C T Herakovich. Failure modes and damage accumulation in laminated composites with free edges. *Composites Science and Technology*, 36:105–119, 1989.
- [76] W Becker and G Kress. Stiffness reduction in laminate coupons due to the free-edge effect. *Composites Science and Technology*, 52:109–115, 1994.
- [77] M Caslini, C Zanotti, and T K O'Brien. Study of matrix cracking and delamination in glass/epoxy laminates. *Journal of Composites Technology and Research*, 9(4):121–130, 1987.

-
- [78] J Zhang, C Soutis, and J Fan. Strain energy release rate associated with local delamination in cracked composite laminates. *Composites*, 25(9):851–862, 1994.
- [79] S A Salpekar, T K O'Brien, and K N Shivakumar. Analysis of local delamination caused by angle ply matrix cracks. *Journal of Composite Materials*, 30(4):418–440, 1996.
- [80] J G Williams and M D Rhodes. Effect of resin on impact damage tolerance of graphite/epoxy laminates. In I M Daniel, editor, *Composite Materials: Testing and Design (Sixth Conference)*, ASTM STP 787, pages 450–480, Philadelphia, 1982. American Society for Testing and Materials.
- [81] D S Cairns and P A Lagace. A consistent engineering methodology for the treatment of impact in composite materials. *Journal of Reinforced Plastics and Composites*, 11:395–412, April 1992.
- [82] S A Salpekar. Analysis of delamination in cross-ply laminates initiating from impact induced matrix cracking. *Journal of Composites Technology and Research*, 15(2):88–94, 1993.
- [83] D Kujawski. Width effects on the tensile strength and fatigue behavior of angle-ply laminates. *International Journal of Fatigue*, 20(8):575–580, 1998.
- [84] R Prinz. Growth of delaminations under fatigue loading. In *Characterization, Analysis and Significance of Defects in Composite Materials*, AGARD Conference Proceedings No. 355, pages 5–1 to 5–27, 1983.
- [85] A D Reddy, L W Rehfield, F Weinstein, and E A Armanios. Interlaminar fracture processes in resin matrix composites under static and fatigue loading. In J D Whitcomb, editor, *Composite Materials: Testing and Design (Eighth Conference)*, ASTM STP 972, pages 340–355, Philadelphia, 1988. American Society for Testing and Materials.
- [86] T K O'Brien. Mixed-mode strain-energy-release rate effects on edge delamination of composites. In *Effects of Defects in Composite Materials*, ASTM STP 836, pages 125–142, Philadelphia, 1984. American Society for Testing and Materials.
- [87] A S D Wang, M Slomiana, and R B Bucinell. Delamination crack growth in composite laminates. In W S Johnson, editor, *Delamination and Debonding of Materials*, ASTM STP 876, pages 135–167, Philadelphia, 1985. American Society for Testing and Materials.

-
- [88] P L N Murthy and C C Chamis. Composite interlaminar fracture toughness: Three-dimensional finite-element modeling for mixed mode I, II, and fracture. In J D Whitcomb, editor, *Composite Materials: Testing and Design (Eighth Conference)*, ASTM STP 972, pages 23–40, Philadelphia, 1988. American Society for Testing and Materials.
- [89] P Davies and F Rannou. The effect of defects in tubes: Part 1. mode I delamination resistance. *Applied Composite Materials*, 1:333–349, 1995.
- [90] M J Salkind. Fatigue of composites. In *Composite Materials: Testing and Design (Second Conference)*, ASTM STP 497, pages 143–169, Philadelphia, 1972. American Society for Testing and Materials.
- [91] R Talreja. Conceptual framework for the interpretation of fatigue damage mechanisms in composite materials. *Journal of Composites Technology and Research*, 7(1):25–29, 1985.
- [92] P T Curtis. The fatigue behaviour of fibrous composite materials. *Journal of Strain Analysis*, 24(4):235–244, 1989.
- [93] M J Owen, T R Smith, and R Dukes. Failure of glass-reinforced plastics with special reference to fatigue. *Plastics and Polymers*, 37:227–233, June 1969.
- [94] H C Kim and L J Ebert. Axial fatigue failure sequence and mechanisms in unidirectional fiberglass composites. *Journal of Composite Materials*, 12:139–152, April 1978.
- [95] L Lorenzo and H T Hahn. Fatigue failure mechanisms in unidirectional composites. In H T Hahn, editor, *Composite Materials: Fatigue and Fracture*, ASTM STP 907, pages 210–232, Philadelphia, 1986. American Society for Testing and Materials.
- [96] H El Kadi and F Ellyin. Effect of stress ratio on the fatigue of unidirectional glass fibre/epoxy composite laminae. *Composites*, 25(10):917–924, 1994.
- [97] M J Owen and R J Howe. The accumulation of damage in a glass-reinforced plastic under tensile and fatigue loading. *Journal of Physics D: Applied Physics*, 5:1637–1649, 1972.
- [98] L J Broutman and S Sahu. A new theory to predict cumulative fatigue damage in fiberglass reinforced plastics. In *Composite Materials: Testing and Design (Second Conference)*, ASTM STP 497, pages 170–188, Philadelphia, 1972. American Society for Testing and Materials.

-
- [99] K L Reifsnider, K Shulte, and J C Duke. Long-term fatigue behavior of composite materials. In T K O'Brien, editor, *Long-Term Behavior of Composites, ASTM STP 813*, pages 136–159, Philadelphia, 1983. American Society for Testing and Materials.
- [100] A Haque, J Krishnagopalan, and S Jeelani. Fatigue damage in laminated composites. *Journal of Reinforced Plastics and Composites*, 12:1058–1069, October 1993.
- [101] B Harris. Fatigue and accumulation of damage in reinforced plastics. *Composites*, pages 214–220, October 1977.
- [102] J Z Wang and D F Socie. Failure strength and damage mechanisms of E-glass/epoxy laminates under in-plane biaxial compressive deformation. *Journal of Composite Materials*, 27(1):40–58, 1993.
- [103] F Ellyin and D Kujawski. Tensile and fatigue behaviour of glassfibre/epoxy laminates. *Construction and Building Materials*, 9(6):425–430, 1995.
- [104] V L Tahiri, C Henaff-Gardin, and M C Lafarie-Frenot. Damage and in-plane shear behaviour of a ($\pm 45^\circ$) carbon/epoxy laminate under quasi-static and fatigue tensile loadings. In G Lütjering and H Nowack, editors, *Proceedings of the 6th International Fatigue Congress (Fatigue 96) - Berlin, Germany*, pages 1561–1566, May 6–10, 1996.
- [105] M M Shokrieh, O P Eilers, and L B Lessard. Characterization of a graphite/epoxy composite under in-plane shear fatigue loading. In T S Gates and A H Zureick, editors, *High Temperature and Environmental Effects on Polymeric Composites (Second Volume), ASTM STP 1302*, pages 133–148, Philadelphia, 1997. American Society for Testing and Materials.
- [106] A Conle and J P Ingall. Effects of mean stress on the fatigue of composite materials. *Journal of Composites Technology and Research*, 7(1):3–11, 1985.
- [107] A Rotem. Tensile and compressive failure modes of laminated composites loaded by fatigue with different mean stress. *Journal of Composites Technology and Research*, 12(4):201–208, 1990.
- [108] A Rotem. The fatigue behavior of composite laminates under various mean stresses. *Composite Structures*, 17:113–126, 1991.
- [109] D Kujawski and F Ellyin. An effective stress parameter for long-term fatigue strength of fiber-reinforced plastic pipes. *Journal of Composite Technology and Research*, 18(3):215–220, 1996.

- [110] A Rotem and H G Nelson. Failure of a laminated composite under tension-compression fatigue loading. *Composites Science and Technology*, 36:45–62, 1989.
- [111] C T Sun and W S Chan. Frequency effect on the fatigue life of laminated composites. In S W Tsai, editor, *Composite Materials: Testing and Design (Fifth Conference)*, ASTM STP 674, pages 418–430, Philadelphia, 1979. American Society for Testing and Materials.
- [112] J F Mandell and U Meier. Effect of load frequency and lay-up on fatigue life of composites. In T K O'Brien, editor, *Long-Term Behavior of Composites*, ASTM STP 813, pages 55–77, Philadelphia, 1983. American Society for Testing and Materials.
- [113] J W Dally and L J Broutman. Frequency effects on the fatigue of glass reinforced plastics. *Journal of Composite Materials*, 1:424–442, 1967.
- [114] A Rotem. Load frequency effect on the fatigue strength of isotropic laminates. *Composites Science and Technology*, 46:129–138, 1993.
- [115] W W Stinchcomb, K L Reifsnider, L A Marcus, and R S Williams. Effects of frequency on the mechanical response of two composite materials to fatigue loads. In *Fatigue of Composite Materials*, ASTM STP 569, pages 115–129, Philadelphia, 1975. American Society for Testing and Materials.
- [116] C R Saff. Effect of load frequency and lay-up on fatigue life of composites. In T K O'Brien, editor, *Long-Term Behavior of Composites*, ASTM STP 813, pages 78–91, Philadelphia, 1983. American Society for Testing and Materials.
- [117] L C Bank, T R Gentry, and A Barkatt. Accelerated test methods to determine the long-term behavior of FRP composite structures: Environmental effects. *Journal of Reinforced Plastics and Composites*, 14:559–587, 1995.
- [118] H T Sumsion and D P Williams. Effects of environment on the fatigue of graphite-epoxy composites. In *Fatigue of Composite Materials*, ASTM STP 569, pages 226–247, Philadelphia, 1975. American Society for Testing and Materials.
- [119] G S Springer. Environmental effects on epoxy matrix composites. In S W Tsai, editor, *Composite Materials: Testing and Design (Fifth Conference)*, ASTM STP 674, pages 291–312, Philadelphia, 1979. American Society for Testing and Materials.
- [120] J M Hale, A G Gibson, and S D Speake. Tensile strength testing of GRP pipes at elevated temperatures in aggressive offshore environments. *Journal of Composite Materials*, 32(10):969–986, 1998.

- [121] D Choqueuse, P Davies, F Mazeas, and R Baizeau. Aging of composites in water: Comparison of five materials in terms of absorption kinetics and evolution of mechanical properties. In T S Gates and A H Zureick, editors, *High Temperature and Environmental Effects on Polymeric Composites (Second Volume)*, ASTM STP 1302, pages 73–96, Philadelphia, 1997. American Society for Testing and Materials.
- [122] T K Tsotsis and S M Lee. Long-term durability of carbon- and glass-epoxy composite materials in wet environments. *Journal of Reinforced Plastics and Composites*, 16(17):1609–1621, 1997.
- [123] E Vauthier, J C Abry, T Bailliez, and A Chateauminis. Interactions between hygrothermal ageing and fatigue damage in unidirectional glass/epoxy composites. *Composites Science and Technology*, 58:687–692, 1998.
- [124] F R Jones, J W Rock, and A R Wheatley. Stress corrosion cracking and its implications for the long-term durability of E-glass fibre composites. *Composites*, 14(3):262–269, 1983.
- [125] A Bledzki, R Spaude, and G W Ehrenstein. Corrosion phenomena in glass fibers and glass reinforced thermosetting resins. *Composites Science and Technology*, 23:263–285, 1985.
- [126] A Chateauminis, B Chabert, J P Soulier, and L Vincent. Hygrothermal ageing effects on the static fatigue of glass/epoxy composites. *Composites*, 24(7):547–555, 1993.
- [127] M Watanabe. Effect of water environment on fatigue behavior of fiberglass reinforced plastics. In S W Tsai, editor, *Composite Materials: Testing and Design (Fifth Conference)*, ASTM STP 674, pages 345–367, Philadelphia, 1979. American Society for Testing and Materials.
- [128] A Chateauminis, L Vincent, B Chabert, and J P Soulier. Study of the interfacial degradation of a glass-epoxy composite during hygrothermal ageing using water diffusion measurements and dynamic mechanical thermal analysis. *Polymer*, 35(22):4766–4774, 1994.
- [129] F R Jones. The role of moisture diffusion and matrix plasticisation on the environmental stress corrosion of GRP. *Journal of Strain Analysis*, 24(4):35–45, 1989.
- [130] M Watanabe. Prediction of leakage life and deterioration in water for fiberglass reinforced plastic vessels. In S W Tsai, editor, *Composite Materials: Testing and Design (Fifth Conference)*, ASTM STP 674, pages 324–344, Philadelphia, 1979. American Society for Testing and Materials.

-
- [131] C Suri and D Perreux. The effects of mechanical damage in a glass fibre/epoxy composite on the absorption rate. *Composites Engineering*, 5(4):415–424, 1995.
- [132] I Ghorbel and P Spiteri. Durability of closed-end pressurized GRP pipes under hygrothermal conditions. part 1: Monotonic tests. *Journal of Composite Materials*, 30(14):1562–1580, 1996.
- [133] D Perreux and C Suri. A study of the coupling between the phenomena of water absorption and damage in glass/epoxy composite pipes. *Composites Science and Technology*, 57:1403–1413, 1997.
- [134] Y Youssef, S Labonte, C Roy, and D Lefebvre. An effective flat cruciform-shaped specimen for biaxial testing of CFRP laminates. *Science and Engineering of Composite Materials*, 3(4):259–267, 1994.
- [135] Z Fawaz and K W Neale. A cruciform specimen for the evaluation of biaxial properties of advanced composites. *Transactions of the Canadian Society of Mechanical Engineers (CSME)*, 19(1):25–36, 1995.
- [136] A Makinde, L Thibodeau, and K W Neale. Development of an apparatus for biaxial testing using cruciform specimens. *Experimental Mechanics*, 32:138–144, 1992.
- [137] J. P. Boehler, S. Demmerle, and S. Koss. A new direct biaxial testing machine for anisotropic materials. *Experimental Mechanics*, 34:1–9, 1994.
- [138] D L Jones, P K Poulouse, and H Liebowitz. Effect of biaxial loads on the static and fatigue properties of composite materials. In K J Miller and M W Brown, editors, *Multiaxial Fatigue, ASTM STP 853*, pages 413–427, Philadelphia, 1985. American Society for Testing and Materials.
- [139] I M Daniel. Biaxial testing of graphite/epoxy laminates with cracks. In C C Chamis, editor, *Test Methods and Design Allowables for Fibrous Composites, ASTM STP 734*, pages 109–128, Philadelphia, 1981. American Society for Testing and Materials.
- [140] J C Radon and C R Wachnicki. Biaxial fatigue of glass fiber reinforced polyester resin. In K J Miller and M W Brown, editors, *Multiaxial Fatigue, ASTM STP 853*, pages 396–412, Philadelphia, 1985. American Society for Testing and Materials.
- [141] E W Smith and K J Pascoe. The role of shear deformation in the fatigue failure of a glass fibre-reinforced composite. *Composites*, pages 237–243, October 1977.

- [142] E W Smith and K J Pascoe. Biaxial fatigue of a glass-fibre reinforced composite. part 1: fatigue and fracture behaviour. In M W Brown and K J Miller, editors, *Biaxial and Multiaxial Fatigue, EGF 3*, pages 367–396, London, 1989. Mechanical Engineering Publications.
- [143] G T Mase. Biaxial characterization of carbon/epoxy unidirectional and quasi-isotropic composites. *Journal of Energy Resources Technology*, 113:189–192, September 1991.
- [144] W Knappe and W Schneider. The role of failure criteria in the fracture analysis of fiber/matrix composites. In H H Kausch, J A Hassell, and R I Jaffee, editors, *Deformation and Fracture of High Polymers*, pages 543–555, 1973.
- [145] U Hütter, H Schelling, and H Krauss. An experimental study to determine failure envelope of composite materials with tubular specimens under combined loads and comparison between several classical criteria. *AGARD-CP-163*, 1975.
- [146] S R Swanson, M J Messick, and Z Tian. Failure of carbon/epoxy lamina under combined stress. *Journal of Composite Materials*, 21:619–630, 1987.
- [147] G E Foley, M E Roylance, and W W Houghton. Use of torsion tubes to measure in-plane shear properties of filament-wound composites. In C C Chamis, editor, *Test Methods for Design Allowables for Fibrous Composites (Second Volume), ASTM STP 1003*, pages 208–223, Philadelphia, 1989. American Society for Testing and Materials.
- [148] S E Groves. Failure characterization of composite materials. Technical Report UCRL-100133, Lawrence Livermore National Laboratories, January 1989.
- [149] R E Lyon, D L Schumann, and S J DeTeresa. Matrix-dominated mechanical properties of a fiber composite lamina. In E T Camponeschi, Jr., editor, *Composite Materials: Testing and Design (Eleventh Volume), ASTM STP 1206*, pages 7–22, Philadelphia, 1993. American Society for Testing and Materials.
- [150] R R Rizzo and A A Vicario. A finite element analysis of laminated anisotropic tubes. *Journal of Composite Materials*, 4:344–359, 1970.
- [151] N J Pagano and J M Whitney. Geometric design of composite cylindrical characterization specimens. *Journal of Composite Materials*, 4:360–378, 1970.
- [152] J M Whitney, N J Pagano, and R B Pipes. Design and fabrication of tubular specimens for composite characterization. In *Composite Materials: Testing and Design, 2nd Conference, ASTM STP 497*, pages 52–67, Philadelphia, 1972. American Society for Testing and Materials.

- [153] F Foral and W D Humphrey. Biaxial stress testing of intraply hybrid composites. *Journal of Composites Technology and Research (ASTM)*, 7(1):19–25, 1985.
- [154] E Krempl, D M Elzey, B Z Hong, T Ayar, and R G Loewy. Uniaxial and biaxial fatigue properties of thin-walled composite tubes. *Journal of the American Helicopter Society*, pages 3–10, July 1988.
- [155] M S Derstine, M J Pindera, and D E Bowles. Experimental/analytical characterization of composite tubes under combined loading. *Experimental Mechanics*, pages 336–344, December 1990.
- [156] T Fujii and F Lin. Fatigue behavior of a plain-woven glass fabric laminate under tension/torsion biaxial loading. *Journal of Composite Materials*, 29(5):573–590, 1995.
- [157] H Kawakami, T Fujii, and Y Morita. Fatigue degradation and life prediction of glass fabric polymer composite under tension/torsion biaxial loadings. *Journal of Reinforced Plastics and Composites*, 15:183–195, 1996.
- [158] C Gargiulo, M Marchetti, and A Rizzo. Prediction of failure envelopes of composite tubes subjected to biaxial loadings. *Acta Astronautica*, 39(5):355–368, 1996.
- [159] J Bax. Deformation behaviour and failure of glassfibre-reinforced resin material. *Plastics and Polymers*, 38:27–30, 1970.
- [160] H J M A Mieras. Irreversible creep of filament-wound glass-reinforced resin pipes. *Plastics and Polymers*, 41:84–89, 1973.
- [161] M J Owen and J R Griffiths. Evaluation of biaxial stress failure surfaces for a glass fabric reinforced polyester resin under static and fatigue loading. *Journal of Materials Science*, 13:1521–1537, 1978.
- [162] M J Owen and D J Rice. Biaxial strength behavior of glass-reinforced polyester resins. In I M Daniel, editor, *Composite Materials: Testing and Design (Sixth Conference)*, ASTM STP 787, pages 124–144, Philadelphia, 1982. American Society for Testing and Materials.
- [163] T R Guess and F P Gerstle, Jr. Deformation and fracture of resin matrix composites in combined stress states. *Journal of Composite Materials*, 11:146–163, 1977.
- [164] T R Guess. Biaxial testing of composite cylinders: Experimental-theoretical comparison. *Composites*, 11(3):139–148, 1980.

- [165] D Hull, M J Legg, and B Spencer. Failure of glass/polyester filament wound pipe. *Composites*, 9(1):17-24, 1978.
- [166] B Spencer and D Hull. Effect of winding angle on the failure of filament wound pipe. *Composites*, 9(4):263-271, 1978.
- [167] M L C Jones and D Hull. Microscopy of failure mechanisms in filament-wound pipe. *Journal of Materials Science*, 14:165-174, 1979.
- [168] P D Soden, D Leadbetter, P R Griggs, and G C Eckold. The strength of a filament wound composite under biaxial loading. *Composites*, 9(4):247-250, 1978.
- [169] G C Eckold, D Leadbetter, P D Soden, and P R Griggs. Lamination theory in the prediction of failure envelopes for filament wound materials subjected to biaxial loading. *Composites*, 9(4):243-246, 1978.
- [170] J C Lenain and A R Busnell. The behaviour of GRP tubes under cyclic pressurisation. *Composites*, pages 77-82, April 1978.
- [171] P H Francis, D E Walrath, and D N Weed. First ply failure of G/E laminates under biaxial loadings. *Fibre Science and Technology*, 12:97-110, 1979.
- [172] E Krempl and T M Niu. Graphite/epoxy [± 45]_s tubes: Their static axial and shear properties and their fatigue behavior under completely reversed load controlled loading. *Journal of Composite Materials*, 16:172-187, 1982.
- [173] E Krempl and D An. Effect of interlaminar normal stresses on the uniaxial zero-to-tension fatigue behavior of graphite/epoxy tubes. In T K O'Brien, editor, *Composite Materials: Fatigue and Fracture (Third Volume)*, ASTM STP 1110, pages 659-666, Philadelphia, 1991. American Society for Testing and Materials.
- [174] V K S Choo and D Hull. Influence of radial compressive stress owing to pressure on the failure modes of composite tube specimens. *Journal of Composite Materials*, 17:344-356, 1983.
- [175] V K S Choo. Effect of loading path on the failure of fibre reinforced composite tubes. *Journal of Composite Materials*, 19:525-532, 1985.
- [176] R F Floral and W D Humphrey. Biaxial stress behavior of graphite and kevlar 49/epoxy composites and hybrids. *AIAA Journal*, 22(1):111-116, 1984.
- [177] R F Floral and D R Gilbreath. Delamination failure modes in filament-wound composite tubes. In P A Lagace, editor, *Composite Materials: Fatigue and Fracture (Second Volume)*, ASTM STP 1012, pages 313-325, Philadelphia, 1989. American Society for Testing and Materials.

- [178] M W K Rosenow. Wind angle effects in glass fibre-reinforced polyester filament wound pipes. *Composites*, 15(2):144–152, 1984.
- [179] J Highton, A B Adeoye, and P D Soden. Fracture stresses for ± 75 degree filament wound GRP tubes under biaxial loads. *Journal of Strain Analysis*, 20(3):139–150, 1985.
- [180] P D Soden, R Kitching, and P C Tse. Experimental failure stresses for $\pm 55^\circ$ filament wound glass fibre reinforced plastic tubes under biaxial loads. *Composites*, 20(2):125–135, 1989.
- [181] J Lee, P D Soden, R Kitching, and P C Tse. Strength of filament wound GRP tubes with axisymmetric steps. *Composites*, 20(3):234–243, 1989.
- [182] P D Soden, R Kitching, P C Tse, and Y Tsavalas. Influence of winding angle on the strength and deformation of filament-wound composite tubes subjected to uniaxial and biaxial loads. *Composites Science and Technology*, 46:363–378, 1993.
- [183] S R Swanson and A P Christoforou. Response of quasi-isotropic carbon/epoxy laminates to biaxial stress. *Journal of Composite Materials*, 20:457–471, 1986.
- [184] S R Swanson and B C Trask. An examination of failure strength in $[0/\pm 60]$ laminates under biaxial stress. *Composites*, 19(5):400–406, 1988.
- [185] S R Swanson and B C Trask. Strength of quasi-isotropic laminates under off-axis loading. *Composites Science and Technology*, 34:19–34, 1989.
- [186] S R Swanson and G R Toombes. Characterization of prepreg tow carbon/epoxy laminates. *Journal of Engineering Materials and Technology (ASME)*, 111:150–153, 1989.
- [187] G E Colvin, Jr. and S R Swanson. Mechanical characterization of IM7/8551-7 carbon/epoxy under biaxial stress. *Journal of Engineering Materials and Technology (ASME)*, 112:61–67, 1990.
- [188] S R Swanson and Y Qian. Multiaxial characterization of T800/3900-2 carbon/epoxy composites. *Composites Science and Technology*, 43:197–203, 1992.
- [189] G E Colvin, Jr. and S R Swanson. In-situ compressive strength of carbon/epoxy AS4/3501-6 laminates. *Journal of Engineering Materials and Technology (ASME)*, 115:122–128, 1993.
- [190] S Amijima, T Fujii, and T Sagami. Nonlinear behavior of plain woven G.F.R.P. under repeated biaxial tension/torsion loading. *Journal of Energy Resources Technology (ASME)*, 113:235–240, 1991.

-
- [191] T Fujii, S Amijima, and F Lin. Study on strength and nonlinear stress-strain response of plain woven glass fiber laminates under biaxial loading. *Journal of Composite Materials*, 26(17):2493–2510, 1992.
- [192] T Tanaka, T Akagawa, and T Fujii. Nonlinear behavior of glass fabric composites under biaxial tension-torsion loading. In *Proceedings of the ASM Materials Congress*, October 1993.
- [193] T Tanaka, T Fujii, and M Kamada. Effect of loading path on the stress-strain relation and progressive damage of a polymer-matrix composite under tension/torsion biaxial loading. *Journal of Thermoplastic Composite Materials*, 9:329–341, 1996.
- [194] C Cazeneuve, P Joguet, J C Maile, and C Oytana. Predicting the mechanical behaviour of kevlar/epoxy and carbon/epoxy filament-wound tubes. *Composites*, 23(6):415–424, 1992.
- [195] J Mistry. Theoretical investigation into the effect of the winding angle of the fibres on the strength of filament wound GRP pipes subjected to combined external pressure and axial compression. *Composite Structures*, 20:83–90, 1992.
- [196] J Mistry, A G Gibson, and Y S Wu. Failure of composite cylinders under combined external pressure and axial load. *Composite Structures*, 22:193–200, 1992.
- [197] T L Norman, T S Civelek, and J Prucz. Fatigue of quasi-isotropic composite cylinders under tension-tension loading. *Journal of Reinforced Plastics and Composites*, 11:1286–1301, November 1992.
- [198] S R Frost and A Cervenka. Glass fibre-reinforced epoxy matrix filament-wound pipes for use in the oil industry. *Composites Manufacturing*, 5:73–82, 1994.
- [199] S R Frost. Predicting the long term fatigue behaviour of filament wound glass fibre/epoxy matrix pipes. In *Proceedings of the 10th International Conference on Composite Materials (ICCM-10)*, Whistler B.C., Canada, Vol.1, pages 649–656, August 1995.
- [200] D Perreux, J-F Maire, C Siqueira, D Varchon, and C Oytana. Multiaxial testing of composite materials. *Materiaux et Techniques*, 82(6-7):37–40, 1994.
- [201] E Joseph and D Perreux. Fatigue behaviour of glass-fibre/epoxy matrix filament-wound pipes: Tension loading tests and results. *Composites Science and Technology*, 52:469–480, 1994.

-
- [202] D Perreux and E Joseph. The effect of frequency on the fatigue performance of filament-wound pipes under biaxial loading: Experimental results and damage model. *Composites Science and Technology*, 57:353–364, 1997.
- [203] L Ferry, D Perreux, D Varchon, and J LeBras. Tensile failure of filament-wound pipes under long-term creep loading: A probabilistic analysis. *Composites Science and Technology*, 57:1281–1288, 1997.
- [204] M Carroll, F Ellyin, D Kujawski, and A S Chiu. The rate-dependent behaviour of $\pm 55^\circ$ filament-wound glass-fibre/epoxy tubes under biaxial loading. *Composites Science and Technology*, 55:391–403, 1995.
- [205] D Kujawski, F Ellyin, and M S Culen. The fatigue behaviour of filament-wound fiberglass/epoxy tubes under cyclic pressure. *Journal of Reinforced Plastics and Composites*, 17(3):268–281, 1998.
- [206] H Levi, O Ishai, E Altus, and I Sheinman. Mechanical performance of thin-walled tubular composite elements under uniaxial loading, part 1: Tensile behavior. *Composite Structures*, 31:163–170, 1995.
- [207] O Ishai, H Levi, E Altus, and I Sheinman. Mechanical performance of thin-walled tubular composite elements under uniaxial loading, part 2: Compressive behavior. *Composite Structures*, 31:171–175, 1995.
- [208] L V Smith and S R Swanson. Failure of braided composite cylinders under biaxial tension. *Journal of Composite Materials*, 29(6):766–784, 1995.
- [209] S R Swanson and L V Smith. Comparison of the biaxial strength properties of braided and laminated carbon fiber composites. *Composites Part B*, 27B(1):71–77, 1996.
- [210] I Ghorbel. Durability of closed-end pressurized GRP pipes under hygrothermal conditions. part 2: Creep tests. *Journal of Composite Materials*, 30(14):1581, 1996.
- [211] J Bai, G Hu, and P Bompard. Mechanical behaviour of $\pm 55^\circ$ filament-wound glass-fibre/epoxy resin tubes: II. micromechanical model of damage initiation and the competition between different mechanisms. *Composites Science and Technology*, 57:155–164, 1997.
- [212] G Hu, J Bai, E Demianouchko, and P Bompard. Mechanical behaviour of $\pm 55^\circ$ filament-wound glass-fibre/epoxy resin tubes: III. macromechanical model of the macroscopic behaviour of tubular structures with damage and failure envelope prediction. *Composites Science and Technology*, 58:19–29, 1998.

- [213] E Demianouchko and J Bai. Stress state analyses of a $\pm 55^\circ$ filament-wound composite tube with damage effect. *Composite Structures*, 37:233–239, 1997.
- [214] S S Wang, S Srinivasan, and B Cole. Long-term leakage failure and life prediction of fiber composite laminate tubing under combined internal pressure and axial loading: Theory and experiments. In *2nd International Conference on Composite Materials for Offshore Operations*, 1997.
- [215] A P Christoforou and S R Swanson. Strength loss in composite cylinders under impact. *Journal of Engineering Materials and Technology*, 110:180–184, April 1988.
- [216] A P Christoforou, S R Swanson, and S W Beckwith. Lateral impact of composite cylinders. In P A Lagace, editor, *Composite Materials: Fatigue and Fracture (Second Volume)*, ASTM STP 1012, pages 373–386, Philadelphia, 1989. American Society for Testing and Materials.
- [217] B Mustafa, S Li, P D Soden, S R Reid, C M Leech, and M J Hinton. Lateral indentation of filament wound GRP tubes. *Int. J. Mech. Sci.*, 34(6):443–457, 1992.
- [218] K L Alderson and K E Evans. Failure mechanisms during the transverse loading of filament-wound pipes under static and low velocity impact conditions. *Composites*, 23(3):167–173, 1992.
- [219] R C Tennyson and S K Kumar. Delamination damage and its effect on buckling of laminated cylindrical shells. *AGARD-CP-530*, pages 9–1 to 9–6, 1992.
- [220] S Li, P D Soden, S R Reid, and M J Hinton. Indentation of laminated filament-wound composite tubes. *Composites*, 24(5):407–421, 1993.
- [221] S Ramakrishna and D Hull. Energy absorption capability of epoxy composite tubes with knitted carbon fibre fabric reinforcement. *Composites Science and Technology*, 49:349–356, 1993.
- [222] H Hamada and S Ramakrishna. Comparison of static and impact energy absorption of carbon fiber/PEEK. In R B Deo and C R Saff, editors, *Composite Materials: Testing and Design (Twelfth Volume)*, ASTM STP 1274, pages 182–197, Philadelphia, 1996. American Society for Testing and Materials.
- [223] N K Gupta, R Velmurugan, and S K Gupta. An analysis of axial crushing of composite tubes. *Journal of Composite Materials*, 31(13):1262, 1997.
- [224] D D Dubey and A J Vizzini. Energy absorption of composite plates and tubes. *Journal of Composite Materials*, 32(2):158–176, 1998.

- [225] P Arnaud and P Hamelin. Dynamic characterization of structures: A study of energy absorption in composite tubes. *Composites Science and Technology*, 58:709–715, 1998.
- [226] P H Francis, D E Walrath, D F Sims, and D N Weed. Biaxial fatigue loading of notched composites. *Journal of Composite Materials*, 11:488–501, October 1977.
- [227] W S Carswell, S Singh, and E H Chandler. The effects of circular cut-outs on anisotropic GRP tubes. In *Third International Conference on Composite Materials*, pages 276–290, 1980.
- [228] M J Graves and P A Lagace. Damage tolerance of composite cylinders. *Composite Structures*, 4:75–91, 1985.
- [229] O O Ochoa, P Roschke, and R Bafrali. Damage tolerance of composite tubes under compressive loading. *Composite Structures*, 19:1–14, 1991.
- [230] K Takemura and T Fujii. Fatigue strength and damage progression in a circular-hole-notched GRP composite under combined tension/torsion loading. *Composites Science and Technology*, 52:519–526, 1994.
- [231] C U Ranniger, P A Lagace, and M J Graves. Damage tolerance and arrest characteristics of pressurized graphite/epoxy tape cylinders. In R H Martin, editor, *Composite Materials: Fatigue and Fracture (Fifth Volume)*, ASTM STP 1230, pages 407–426, Philadelphia, 1995. American Society for Testing and Materials.
- [232] J H Starnes, Jr. and C A Rose. Nonlinear response of thin cylindrical shells with longitudinal cracks and subjected to internal pressure and axial compression loads. In *38th AIAA/ASME/ASCE/AHS/ASC Structures, Structural Dynamics and Materials Conference, Kissimmee, Florida, AIAA Paper No.97-1144*, April 7-10, 1997.
- [233] J Pabiot, M Herbeaux, M Benteyn, H Fliervoet, A Leroy, and J P Faivre. Influence of the fibre/matrix interface on the long-term behaviour of filament wound epoxy/glass tubing systems. *Composite Polymers*, 4(5):299–315, 1991.
- [234] P H Petit. A simplified method of determining the in-plane shear stress-strain response of unidirectional composites. In *Composite Materials: Testing and Design (First Conference)*, ASTM STP 460, Philadelphia, 1969. American Society for Testing and Materials.
- [235] A Rotem and Z Hashin. Failure modes of angle ply laminates. *Journal of Composite Materials*, 9:191–206, April 1975.

-
- [236] D F Sims and V H Brogdon. Fatigue behavior of composites under different loading modes. In K L Reifsnider and K N Lauraitis, editors, *Fatigue of Filamentary Composite Materials, ASTM STP 636*, pages 185–205, Philadelphia, 1977. American Society for Testing and Materials.
- [237] J J Lucas. Effect of specimen geometry on fatigue strength of boron and glass epoxy composites. *Journal of Materials*, 7(4):586–589, 1972.
- [238] D P Kendall. Crack growth resistance in laminated, glass-epoxy sheet. *Journal of Materials*, 7(3):430–434, 1972.
- [239] A Voloshin and M Arcan. Failure of unidirectional fiber-reinforced materials - new methodology and results. *Experimental Mechanics*, pages 280–284. August 1980.
- [240] S Parhizgar, L W Zachary, and C T Sun. Application of the principles of linear fracture mechanics to the composite materials. *International Journal of Fracture*, 20:3–15, 1982.
- [241] W Hwang and K S Han. Fatigue of composite materials - damage model and life prediction. In P A Lagace, editor, *Composite Materials: Fatigue and Fracture (Second Volume), ASTM STP 1012*, pages 87–102, Philadelphia, 1989. American Society for Testing and Materials.
- [242] G H Staab and A Gilat. High strain rate response of angle-ply glass/epoxy laminates. *Journal of Composite Materials*, 29(10):1308–1320, 1995.
- [243] R O Ritchie, F A McClintock, E K Tschegg, and H Nayeb-Hashemi. Mode iii fatigue crack growth under combined torsional and axial loading. In K J Miller and M W Brown, editors, *Multiaxial Fatigue, ASTM STP 853*, pages 203–227, Philadelphia, 1985. American Society for Testing and Materials.
- [244] J Y Bérard, D L McDowell, and S D Antolovich. Damage observation of a low-carbon steel under tension-torsion low-cycle fatigue. In D L McDowell and R Ellis, editors, *Advances in Multiaxial Fatigue, ASTM STP 1191*, pages 326–344, Philadelphia, 1993. American Society for Testing and Materials.
- [245] E H Jordan and C T Chan. A unique elevated-temperature tension-torsion fatigue test rig. *Experimental Mechanics*, 27:172–178, 1987.
- [246] R M Andrews and M W Brown. Elevated temperature out-of-phase fatigue behaviour of a stainless steel. In M W Brown and K J Miller, editors, *Biaxial and Multiaxial Fatigue, EGF 3*, pages 641–658, London, 1989. Mechanical Engineering Publications.

- [247] A Nitta, T Ogata, and K Kuwabara. Fracture mechanisms and life assessment under high strain biaxial cyclic loading of type 304 stainless steel. *Fatigue and Fracture of Engineering Materials and Structures*, 12(2):77–92, 1989.
- [248] S Kalluri and P J Bonacuse. In-phase and out-of-phase axial-torsional fatigue behavior of haynes 188 superalloy at 760°C. In D L McDowell and R Ellis, editors, *Advances in Multiaxial Fatigue, ASTM STP 1191*, pages 133–150. Philadelphia, 1993. American Society for Testing and Materials.
- [249] S R Swanson, A P Christoforou, and G E Colvin, Jr. Biaxial testing of fiber composites using tubular specimens. *Experimental Mechanics*, 28:283–243, 1988.
- [250] J Rotvel. Biaxial fatigue tests with zero mean stresses using tubular specimens. *Int. J. of Mech. Sci.*, 12:597–613, 1970.
- [251] F Ellyin and B Valaire. High-strain biaxial fatigue test facility. In *Proceedings of the 1982 Joint Conference on Experimental Mechanics, (SESA and JSME) Society for Experimental Stress Analysis and Japan Society of Mechanical Engineers*, pages 136–143, Hawaii, May 1992.
- [252] F Ellyin, K Golos, and Z Xia. In-phase and out-of-phase multiaxial fatigue. *Journal of Engineering Materials and Technology*, 113:112–118, 1991.
- [253] J M H Andrews and E G Ellison. A testing rig for cycling at high biaxial strains. *Journal of Strain Analysis*, 8(3):168–175, 1973.
- [254] B W Cole and R B Pipes. Filamentary composite laminates subjected to biaxial stress fields. *AFFDL-TR-73-115*, 1973.
- [255] U S Lindholm, A Nagy, L M Yeakley, and W L Ko. Design of a test machine for biaxial testing of composite laminate cylinders. *AFFDL-TR-75-83*, 1975.
- [256] F Ellyin and J P Grass. Détermination expérimentale de surface d'écoulement plastique du titane 50a - première partie: Instrumentation. *Transactions CSME*, 3(3):156–162, 1975.
- [257] D Lefebvre, C Chebl, L Thibodeau, and E Khazzari. A high-strain biaxial-testing rig for thin-walled tubes under axial load and pressure. *Experimental Mechanics*, 23:384–392, 1983.
- [258] C C Lawrence. Multiaxial fatigue testing machine for polymers. In K J Miller and M W Brown, editors, *Multiaxial Fatigue, ASTM STP 853*, pages 33–46, Philadelphia, 1985. American Society for Testing and Materials.

-
- [259] R J H Baten et al. Requirements for the permitted size of the alignment errors of load frames for fatigue testing and a proposal for a relevant measuring method. In R Papirno and H C Weiss, editors, *Factors That Affect the Precision of Mechanical Tests, ASTM STP 1025*, pages 117–135, Philadelphia, 1989. American Society for Testing and Materials.
- [260] D F Lefebvre, H Ameziane-Hassani, and K W Neale. Accuracy of multiaxial fatigue testing with thin-walled tubular specimens. In R Papirno and H C Weiss, editors, *Factors That Affect the Precision of Mechanical Tests, ASTM STP 1025*, pages 103–114, Philadelphia, 1989. American Society for Testing and Materials.
- [261] J Highton and P D Soden. End reinforcement and grips for anisotropic tubes. *Journal of Strain Analysis*, 17(1):31–43, 1982.
- [262] S Groves, R Sanchez, R Lyon, and F Magness. Evaluation of cylindrical shear joints for composite materials. *Journal of Composite Materials*, 26(8):1134–1150, 1992.
- [263] G R Toombes, S R Swanson, and D S Cairns. Biaxial testing of composite tubes. *Experimental Mechanics*, 25(2):186–192, 1985.
- [264] L V Smith and S R Swanson. Design of a cylindrical specimen for biaxial testing of composite materials. *Journal of Reinforced Plastics and Composites*, 16(6):550–565, 1997.
- [265] J M Whitney, G C Grimes, and P H Francis. Effect of end attachment on the strength of fiber-reinforced composite cylinders. *Experimental Mechanics*, pages 185–192, May 1973.
- [266] T R Guess and C B Haizlip, Jr. End-grip configurations for axial loading of composite tubes. *Experimental Mechanics*, pages 31–36, 1980.
- [267] M Carroll. Lay-up and rate effects on fiberglass/epoxy laminates and tubulars. Master's thesis, Department of Mechanical Engineering, University of Alberta, Spring 1994.
- [268] H El Kadi. *Analysis and Failure of Laminated Fiber Reinforced Composites*. PhD thesis, Department of Mechanical Engineering, University of Alberta, Fall 1993.
- [269] D N Weed and P H Francis. Process development for the fabrication of high-quality composite tubes. *Fibre Science and Technology*, 10:89–100, 1977.

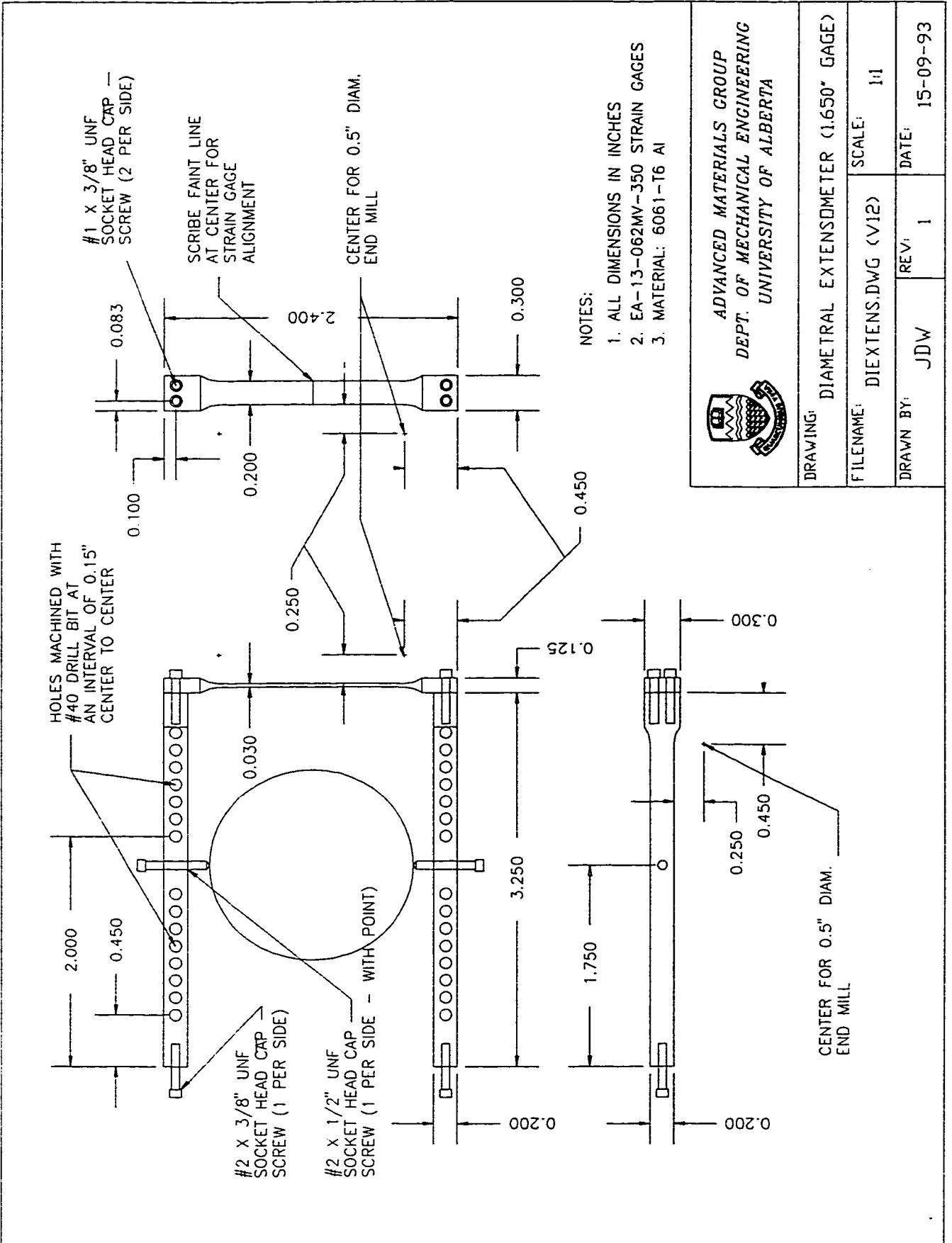
- [270] B S Kim and T F Lehnhoff. Polymeric composite tube fabrication. *Journal of Engineering Materials and Technology*, 117:235–237, 1995.
- [271] H Darcy. *Les Fontaines Publiques de la Ville de Dijon*. Victor Dalmont, Paris, 1856.
- [272] T K O'Brien. Stiffness change as a nondestructive damage measurement. In W W Stinchcomb, editor, *Proceedings of the Conference on the Mechanics of Nondestructive Testing, Virginia Polytechnic Institute and State University, Blacksburg, VA*, pages 101–121, September 10–12, 1980.
- [273] E T Camponeschi and W W Stinchcomb. Stiffness reduction as an indicator of damage in graphite/epoxy laminates. In I M Daniel, editor, *Composite Materials: Testing and Design (Sixth Conference), ASTM STP 787*, pages 225–246, Philadelphia, 1982. American Society for Testing and Materials.
- [274] A Poursatip, M F Ashby, and P W R Beaumont. Damage accumulation during fatigue of composites. In T Hayashi, K Kawata, and S Umekawa, editors, *4th International Conference on Composite Materials (ICCM-IV), Tokyo*, pages 693–700, 1982.
- [275] J N Yang, L J Lee, and D Y Sheu. Modulus reduction and fatigue damage of matrix dominated composite laminates. *Composite Structures*, 21:91–100, 1992.
- [276] Whitworth H A. A stiffness degradation model for composite laminates under fatigue loading. *Composite Structures*, 40(2):95–101, 1998.
- [277] F A R Al-Salehi, S T S Al-Hassani, and M J Hinton. An experimental investigation into the strength of angle ply GRP tubes under high rate of loading. *Journal of Composite Materials*, 23:288–305, March 1989.
- [278] M R Wisnom. The effect of fibre rotation in $\pm 45^\circ$ tension tests on measured shear properties. *Composites*, 26(1):25–32, 1995.
- [279] Y Kanagawa, T Ishida, S Murakami, and K Tanaka. Observation of internal damage and inelastic deformation of graphite/epoxy tubes $[\pm 45]_4$ under cyclic axial loading. *Science and Engineering of Composite Materials*, 3(2):111–121, 1994.
- [280] R R Rizzo and A A Vicario. A finite element analysis for stress distribution in gripped tubular specimens. In *Composite Materials: Testing and Design, 2nd Conference, ASTM STP 497*, pages 68–88, Philadelphia, 1972. American Society for Testing and Materials.

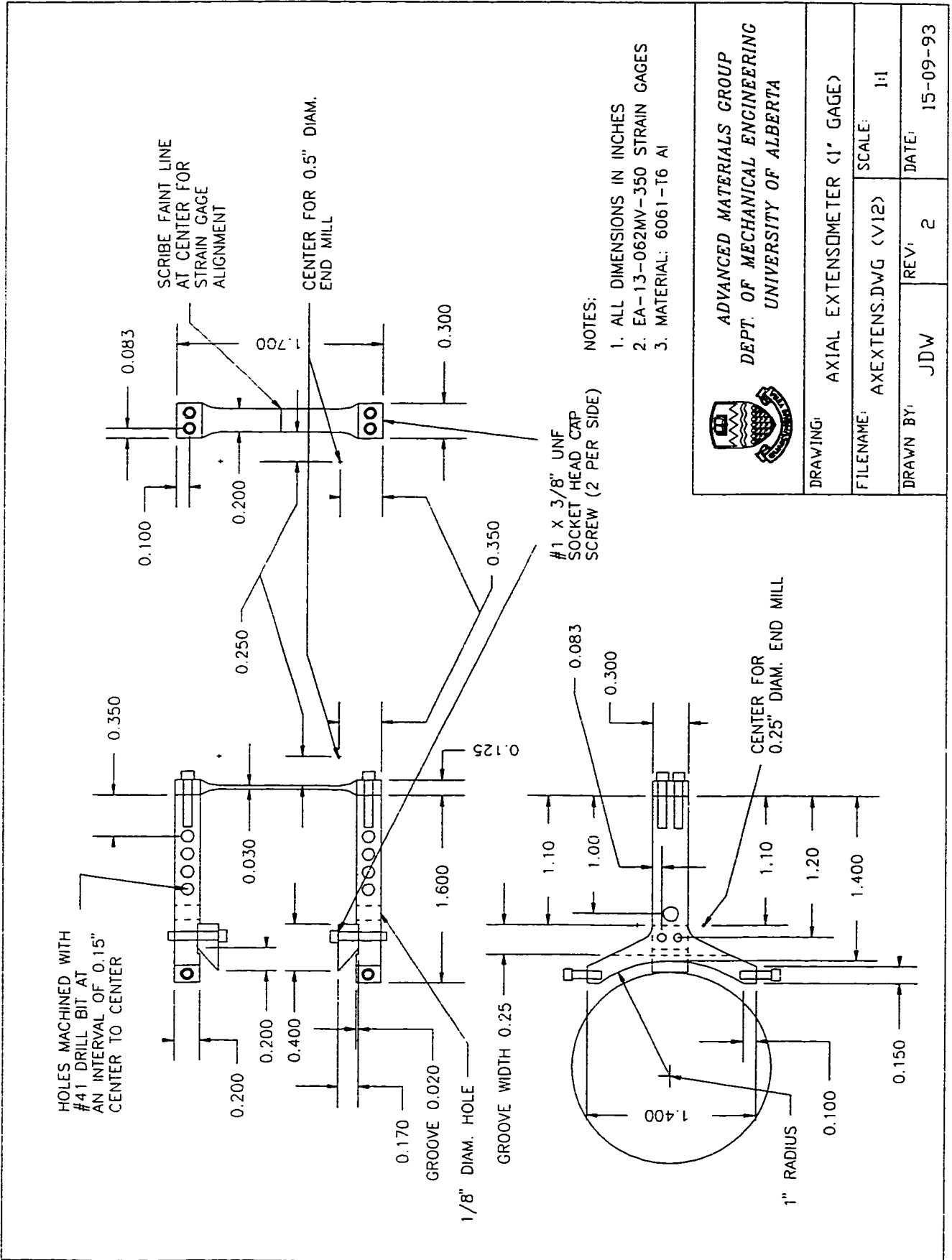
- [281] R C Reuter, Jr. and T R Guess. Analysis, testing and design of filament wound, carbon-carbon burst tubes. In *Composite Materials: Testing and Design, 3rd Conference, ASTM STP 546*, pages 67–83, Philadelphia, 1974. American Society for Testing and Materials.
- [282] I M Daniel, T Liber, R Vanderby, and G M Koller. Analysis of tubular specimen for biaxial testing of composite laminates. In *Proceedings of the Third International Conference on Composite Materials (ICCM-3), Paris*, pages 840–855, August 26–29, 1980.
- [283] S M Yunus, P C Kohnke, and S Saigal. An efficient through-thickness integration scheme in an unlimited layer doubly curved isoparametric composite shell element. *International Journal for Numerical Methods in Engineering*, 28:2777–2793, 1989.
- [284] J E Shigley and L D Mitchell. *Mechanical Engineering Design*. McGraw-Hill, 4th edition, 1983.
- [285] T R King, D M Blacketter, D E Walrath, and D F Adams. Micromechanics prediction of the shear strength of carbon fiber/epoxy matrix composites: The influence of the matrix and interface strengths. *Journal of Composite Materials*, 4:558–573, 1992.
- [286] L J Hart-Smith. A re-examination of the analysis of in-plane matrix failures in fibrous composite laminates. *Composites Science and Technology*, 56:107–121, 1996.
- [287] S R Swanson, M Messick, and G R Toombes. Comparison of torsion tube and iosipescu in-plane shear test results for a carbon fibre-reinforced epoxy composite. *Composites*, 16(3):220–224, 1985.
- [288] F Pierron and A Vautrin. Accurate comparative determination of the in-plane shear modulus of t300/914 by the iosipescu and 45° off-axis tests. *Composites Science and Technology*, 52:61–72, 1994.
- [289] T Dickson and M Munro. Selection of an in-plane shear test method based on the shear sensitivity of laminate tensile modulus. *Composites*, 26(1):17–24, 1995.
- [290] D F Adams and E Q Lewis. Experimental assessment of four composite material shear test methods. *Journal of Testing and Evaluation*, 25(2):174–181, 1997.
- [291] G P Sendekyj. *Life Prediction for Resin-Matrix Composite Materials*, chapter 10, pages 431–483. Elsevier Science Publishers, 1991.

-
- [292] Z Fawaz and F Ellyin. Fatigue failure model for fibre-reinforced materials under general loading conditions. *Journal of Composite Materials*, 28(15):1432–1451, 1994.

APPENDIX A

Diametral and Axial Extensometer Drawings





ADVANCED MATERIALS GROUP
DEPT. OF MECHANICAL ENGINEERING
UNIVERSITY OF ALBERTA

DRAWING:	AXIAL EXTENSOMETER (1" GAGE)
FILENAME:	AXEXTENS.DWG (V12)
SCALE:	1:1
DRAWN BY:	JDW
REV:	2
DATE:	15-09-93

APPENDIX B

Datafiles for Testing Machine Data-Acquisition and Control Software

1. Test Datafile (MTM30.EXE)
2. Cyclic Sequence File (MTM30.EXE)
3. Monotonic Sequence File (MTM30.EXE)
4. Calibration Datafile (MTM30.EXE)
5. Graphics Datafile (MTM30.EXE)
6. Configuration Datafile (EXTRA30.EXE)

INDEXES:

1. Output File Headers
2. Output Columns
3. Valid Units

TEST DATAFILE FOR MTM30.EXE - PAGE 1 OF 1

START SPECIMEN

description = "Sample Datafile Specification"
 material = "3M-1003 E-Gl/Ep - {+/-45}s 8 layer"
 specimen type (T-TUBE or C-COUPON) = T
 specimen outside diameter = 1.6679 in
 specimen inside diameter = 1.5284 in
 specimen gage length = 4.000 in
 wall thickness (K-THICK or N-THIN) = N
 END SPECIMEN

START TEST

compensation type (S-SOFTWARE, H-HARDWARE, or N-NONE) = S
 ramping time (to start and to zero) = 5 s
 ramp (and hold) step frequency (Hz) = 10
 ramp sampling frequency (Hz) = 2
 hold minimum stress rate = 0 psi/s
 hold minimum strain rate = 1e-6 strain/s
 hold percent sample trigger = 10
 internal pressure intensifier stop alarm level = 1 cu.in
 internal pressure intensifier percent sample trigger = 10
 external trigger counter initial value (1-255) = 1
 END TEST

START CONTROL

1.a. int. pressure control type (L-LOAD, D-DISP, or N-NONE) = L
 b. int. pressure span setting (0 to 10 V) = 10
 2.a. axial control type (L-LOAD, D-DISP, or N-NONE) = L
 b. axial span setting (0 to 10 V) = 10
 3.a. torsional control type (L-LOAD, D-DISP, or N-NONE) = L
 b. torsional span setting (0 to 10 V) = 10
 4.a. ext. pressure control type (L-LOAD or N-NONE) = N
 b. ext. pressure span setting (0 to 10 V) = 10
 END CONTROL

START CYCLIC

cyclic sequence file = "CYCSEQ.DAT"
 cyclic waveform (S-SINE or T-TRIANGULAR) = S -
 cyclic frequency (Hz) = 1.0
 number of samples per cycle = 100
 sequential data buffer size (# of cycles) = 100
 circular data buffer size - end of test data saved (# of cycles) = 10
 sample hold period following test (Y-YES or N-NO) = N
 cycle starting point (N-MIN, M-MEAN, or X-MAX) = N
 allow automatic set point adjustment (Y-YES or N-NO) = Y
 automatic set point adjustment cycle increment = 500
 automatic set point adjustment starting cycle = -50
 1.a. mean differential pressure/stress/strain = 1500 psi
 b. differential pressure/stress/strain amplitude = 1490 psi
 c. differential pressure signal phase offset = 0 deg
 2.a. mean axial load/stress/strain/voltage = 1500 psi
 b. axial load/stress/strain/voltage amplitude = 1490 psi
 c. axial signal phase offset = 0 deg
 3.a. mean torsional load/stress/strain/voltage = 0 psi
 b. torsional load/stress/strain/voltage amplitude = 0 psi
 c. torsional signal phase offset = 0 deg
 END CYCLIC

START MONOTONIC 1

monotonic sequence file = "MONOSEQ.DAT "
 step frequency (Hz) = 5
 sampling frequency (Hz) = 1
 circular data buffer size - end of test data saved (# of steps) = 10
 sample hold period following test (Y-YES or N-NO) = Y
 1.a. differential pressure/stress/strain/voltage rate = 0 psi/s
 b. differential pressure/stress/strain limit = 0 psi
 2.a. axial load/stress/strain/voltage rate = 150 psi/s
 b. axial load/stress/strain/voltage limit = 1500 psi
 3.a. torsional load/stress/strain/voltage rate = 90 psi/s
 b. torsional load/stress/strain/voltage limit = 950 psi
 END MONOTONIC

* MORE MONOTONIC RAMPS CAN BE ADDED, DESIGNATED AS "START MONOTONIC 2", ETC.

CYCLIC SEQUENCE FILE FOR MTM30.EXE - PAGE 1 OF 1

```
*
* Format: <Cycle Number> <Code> <Option>
*       where: <Code> is
*
*       A - Initiate Automatic Waveform Adjustment
*       M - Initiate Monotonic Test Sequence (for Stiffness Measurements)
*       P - Purge Sequential Buffers to Disk
*       S - Stop Test
*       T - Trigger External Event   OPTIONS: (+) Increment Counter Value
*                                       (nnn) Explicit Counter Value
*
*       W - Write Current Cycle to Sequential Buffer
*
1 W
5 A
9 T 005
10 W
20 W
30 W
40 W
49 T +
50 M
60 W
70 W
80 W
90 W
99 T +
100 M
150 W
200 W
250 W
300 W
350 W
400 W
450 W
499 T +
500 M
600 W
700 W
800 W
900 P
1000 S
```

MONOTONIC SEQUENCE FILE FOR MTM30.EXE - PAGE 1 OF 1

```
*  
* Format: <Time (seconds)> <Code> <Option>  
*       where: <Code> is  
*  
*       S - Stop Test  
*       T - Trigger External Event   OPTIONS: (+) Increment Counter Value  
*                                     (nnn) Explicit Counter Value  
*  
2.0 T 001  
4.0 T +  
6.0 T +  
8.0 T +  
10.0 T +  
20.0 T +  
30.0 T +  
40.0 T +  
50.0 S
```

CALIBRATION DATAFILE FOR MTM30.EXE - PAGE 1 OF 1

START CALIBRATION

calibration constant (internal pressure) = 1000.0 psi(p)/V
calibration constant (external pressure) = 10 psi(p)/V
calibration constant (axial force) = 6000.0 lbf/V
calibration constant (torque) = 1000 in.lbf/V
calibration constant (diametral extensometer displacement) = .016079 in/V
calibration constant (axial extensometer displacement) = .01001 in/V
calibration constant (torsional extensometer rotation) = 10 deg/V
calibration constant (int. pressure intensifier volume) = 1.0679 cu.in/V
calibration constant (ext. pressure intensifier volume) = 10 cu.in/V
calibration constant (axial LVDT displacement) = 0.19913 in/V
calibration constant (torsional RVIT rotation) = 1.00 deg/V
calibration constant (thermocouple) = 10 C/V
calibration constant (strain gage #1) = 0.01 strain/V
calibration constant (strain gage #2) = 0.03 strain/V
calibration constant (strain gage #3) = 0.04 strain/V
calibration constant (strain gage #4) = 0.10 strain/V

END CALIBRATION

START GAGE LENGTH

sample actual gage lengths = Y
diametral extensometer calibration gage length = 1.665 in
axial extensometer calibration gage length = 1.0 in
torsional extensometer calibration gage length = 4 in

END GAGE LENGTH

START LOAD TRAIN COMPLIANCE

axial compliance (extension/force) = 0.0023 in/lbf
torsional compliance (rotation/torque) = 0.05 deg/in.lbf
END LOAD TRAIN COMPLIANCE

START FLUID SYSTEM

fluid viscosity (specimen) = 100 N.s/sq.m
fluid compressibility = 100 1/psi(p)
int. pressure system supply tubing volume = 2.0 cu.in
ext. pressure system supply tubing volume = 3.0 cu.in
END FLUID SYSTEM

GRAPHICS DATAFILE FOR MTM30.EXE - PAGE 1 OF 1

```
*
* NOTE: Axis type is based on output column index.
*
START GRAPH
Graph #1, X Axis Type = 16
      X Axis Maximum = 0.05 STRAIN
      X Axis Minimum = 0.00 STRAIN
      X Axis - Allow Auto Scaling (Y-YES or N-NO) = Y
Graph #1, Y Axis Type = 7
      Y Axis Maximum = 300.0 MPA
      Y Axis Minimum = 0.0 MPA
      Y Axis - Allow Auto Scaling (Y-YES or N-NO) = Y
      Plot Monotonic Data (Y-YES or N-NO) = Y
Graph #2, X Axis Type = 19
      X Axis Maximum = 0.00 STRAIN
      X Axis Minimum = -0.05 STRAIN
      X Axis - Allow Auto Scaling (Y-YES or N-NO) = Y
Graph #2, Y Axis Type = 10
      Y Axis Maximum = 300.0 MPA
      Y Axis Minimum = 0.0 MPA
      Y Axis - Allow Auto Scaling (Y-YES or N-NO) = Y
      Plot Monotonic Data (Y-YES or N-NO) = Y
Graph #3, X Axis Type = 1
      X Axis Maximum = 3600 S
      X Axis Minimum = 0 S
      X Axis - Allow Auto Scaling (Y-YES or N-NO) = Y
Graph #3, Y Axis Type = 24
      Y Axis Maximum = 11 CU.IN
      Y Axis Minimum = 0 CU.IN
      Y Axis - Allow Auto Scaling (Y-YES or N-NO) = Y
      Plot Monotonic Data (Y-YES or N-NO) = N
END GRAPH
```

CONFIGURATION DATAFILE FOR EXTRA30.EXE - PAGE 1 OF 3

```

*
* NOTE: COMMENTS ARE STARTED WITH '*'
*
* Descriptions are copied to the start of the output file for
* reference purposes (all empty strings are ignored).
DESCRIPTION 1 = "Sample Cyclic Test - Hysteresis Loops"
DESCRIPTION 2 = ""
DESCRIPTION 3 = ""
DESCRIPTION 4 = ""

* Define Input and Output filenames
* (Note: This definition can be over-riden by filenames defined
*       on the command line).
INPUT FILE = "test1.tmp"
OUTPUT FILE = "test1.out"

* Define Processing Buffer Size (in # of points)
PROCESS BUFFER COUNT = 1000

* Define Output Formatting
* Use: ASCII (default) or VOSSPLOT
FORMAT = VOSSPLOT

* Define Output Units Type
* Use: ENGLISH (default) or METRIC
UNITS = ENGLISH

* Define Output Columns (see OUTPUT COLUMN LIST for reference numbers)
* (Note: At least ONE column is required)
* Format: COLUMN = <column number 1>, <column number 2>, ...
*       where <column number> is ALL or any valid column numbers (delimited by comma)
COLUMN = 1, 2, 4, 8, 11, 14, 17, 20, 23, 25, 27, 30, 33, 35, 37, 39, 41

* Cumulative Value Flags
* Defines whether column values are to be cumulative after transducer
* constants have been changed within an input file (e.g. due to
* specimen re-installation)
* Format: CUMULATIVE = <column number 1>, <column number 2>, ...
*       where <column number> is ALL or any valid column numbers (delimited by comma)
CUMULATIVE = ALL

* Columns Titles
* Format: COL TITLE = <title format>
*       where <format> is (0) - No column titles
*                       (1) - Column titles at start of listing only
*                       (2) - Column titles at each header section
COL TITLE = 1

* Define Header Filter (see HEADER LIST for reference numbers)
* Format: HEADER = <header number 1>, <header number 2>, ...
*       where <header number> is ALL or header numbers 5 thru 9 (delimited by comma)
* Format: HEADER = ALL, 0, ... , n
HEADER = ALL

* Header Titles
* Format: HEAD TITLE = <title format>
*       where <format> is (0) - No header titles
*                       (1) - Header titles at each header section
*                       (2) - Header descriptors (text) in separate column
*                       (3) - Header descriptors (numbers) in separate
*                           column (e.g. 9.1)
HEAD TITLE = 2

* Space Between Header Sections
* Format: HEAD SPACE
HEAD SPACE

```


CONFIGURATION DATAFILE FOR EXTRA30.EXE - PAGE 2 OF 3

* Define Monotonic Test Sequence
 * (Note: If TEST MONOTONIC test header is specified, then at least ONE
 * sequence is required)
 * Format: = ALL, 0, ... , n
 * Format: MONOTONIC TEST = <test number 1>, <test number 2>, ...
 * where <test number> is ALL or any valid sequence numbers (delimited by comma)
 MONOTONIC TEST = ALL

* Define Cycle Filter
 * This defines whether the list is ACTIVE, and whether the list
 * is cycles which are to be PROCESSED or REJECTED.
 * Format: CYCLE FILTER = <option>
 * where <option> is NONE - list is ignored.
 * KEEP - cycles in list are PROCESSED while remaining
 * cycles are ignored.
 * REJECT - cycles in list are IGNORED while remaining
 * cycles are processed.
 CYCLE FILTER = NONE

* Cycle Filter List (cycle number)
 START CYCLE FILTER:
 10
 20
 100
 END CYCLE FILTER:

* Data Reduction
 * Reduces the number of output data points by a given percentage but
 * keeps the first number of given points as requested (note: for all types,
 * the first data point is always kept! ... for ramp types only, the last data
 * point is kept!)
 * Format: REDUCE = <percent reduction>, <consecutive starting points>
 REDUCE = 50, 10

* Ramp Data Limit (non-cyclic data only)
 * Format: RAMP LIMIT = <column>, <max. limit>, <min. limit>
 * where <limit> is a value, NONE (no limit), or MAX/MIN
 * (Note: no unit checking is provided ... it is up to the user to ensure
 * that valid units are maintained)
 RAMP LIMIT = 3, MAX, NONE

* Basic Algebraic Processes
 * Format: <action> = <column>, <quantity>
 * Actions include MULTIPLY and ADD
 * (Note: no unit checking is provided ... it is up to the user to ensure
 * that valid units are maintained)
 * e.g. MULTIPLY = 6, 2
 MULTIPLY = 6, 2
 ADD = 6, 1.1

* Graph Hysteresis Loops
 * (Note: This switch is only valid when NO COMMANDS are specified!)
 * Format: CLOSE LOOPS = <x column>, <y column>, <label switch>
 * where <x column> and <y column> are the column numbers to be specified
 * in the output graphics command (VOSSPLOT ONLY)
 * <label switch> = LABEL (include loop number labels)
 * or NONE (do not include loop number labels)
 *
 CLOSE LOOPS = 1, 16, NONE

* Triggered Events Filter
 * Parses out data for triggered event list only.
 * Format: TRIGGERS ONLY
 TRIGGERS ONLY

* Processing Summary Switch
 * Outputs a copy of the processing parameters
 PROCESSING SUMMARY

CONFIGURATION DATAFILE FOR EXTRA30.EXE - PAGE 3 OF 3

* Warning Stoppage Switch
 * Stops processing and waits for user verification after warning is
 * encountered
 WARNING STOP

* Pressure Compensation Switch
 * Instructs program to take axial force due to pressurization into account
 PRESSURE COMPENSATION

* Load Train Compliance Switch
 * Instructs program to take load train compliance into account for
 * displacement/rotation and strain calculations for stroke type
 * transducers
 LOAD TRAIN COMPLIANCE

* Volume Correction Switch
 * Instructs program to correct volume lost data for specimen expansion
 * and compressibility effects
 * Format: VOLUME CORRECTION = <diametral strain column>, <axial strain column>
 *
 VOLUME CORRECTION = 16, 19

* COMMANDS: (Only ONE of the following commands is performed - that being
 * the last command given in the file)
 *

* No Commands Switch
 * Turns OFF all subsequently listed commands (used for easy switching)
 NO COMMANDS

* Group Summary
 * Determines Max., Min. and Ave. values for specified data set.
 * Format: GROUP = <grouped quantity #1>, <grouped quantity #2>, ...
 GROUP = AVE, MIN, MAX, RANGE, MID, AMP

* Linear Regression
 * Format: LINEAR FIT = <column x>, <column y>, <max. pts.>, <command>,
 * <minimum correlation coefficient>, <loop search>
 * where <max. pts.> = ALL or 3 or ... or n
 * <command> = MAX (maximum slope), MIN (minimum slope),
 * BEST (best correlation coeff), NONE, ALL
 * <loop search> = YES, NO (if YES, the data is searched for a minimum
 * position from which the linear regression
 * is performed - for cyclic tests only)
 LINEAR FIT = 5, 3, ALL, NONE, 0.99, YES

* Polynomial Regression
 * Format: POLY FIT = <column x>, <column y>, <max. pts.>, <order>
 POLY FIT = 5, 3, ALL, 4

* Strain Energy
 * Calculates the applied strain energy density to the system based on
 * the axial, hoop and torsional feedback.
 * Format: STRAIN ENERGY = <diametral strain column>, <axial strain column>,
 * <torsional strain column>
 * (note: this allows various strain measurement transducers to be used in
 * the calculation of strain energy)
 *
 STRAIN ENERGY = 16, 19, 32

* Permeability
 * Generates a permeability (and volume loss) profile file for the file.
 * Format: PERMEABILITY = <header>, <monotonic test sequence>
 *
 PERMEABILITY = 9, 1

OUTPUT FILE HEADER INDEX FOR MTM30.EXE/EXTRA30.EXE - PAGE 1 OF 1

0. STOP FLAG
1. INPUT TEST DATA
2. INPUT CALIBRATION DATA
3. TRANSDUCER ZERO VOLTAGES
4. TRANSDUCER GAGE LENGTHS
5. RAMP TO START
6. RAMP TO ZERO
7. HOLD PERIOD
8. TEST CYCLIC
9. TEST MONOTONIC
10. TEST PAUSED
11. TEST RESUMED
12. TRIGGERED EVENT

OUTPUT COLUMN INDEX FOR MTM30.EXE/EXTRA30.EXE - PAGE 1 OF 1

0. CYCLE
1. TIME (S)
2. INTERNAL PRESSURE FEEDBACK [V]
3. INTERNAL PRESSURE [PSI(P), KPA(P)]
4. EXTERNAL PRESSURE FEEDBACK [V]
5. EXTERNAL PRESSURE [PSI(P), KPA(P)]
6. DIFFERENTIAL PRESSURE [PSI(P), KPA(P)]
7. HOOP STRESS [PSI, MPA]
9. AXIAL LOAD FEEDBACK [V]
9. AXIAL FORCE [LBF, N]
10. AXIAL STRESS [PSI, MPA]
11. TORQUE FEEDBACK [V]
12. TORQUE [IN.LBF, N.M]
13. SHEAR STRESS [PSI, MPA]
14. DIAMETRAL EXTENSOMETER FEEDBACK [V]
15. DIAMETRAL EXTENSOMETER DISPLACEMENT [IN, MM]
16. DIAMETRAL EXTENSOMETER STRAIN
17. AXIAL EXTENSOMETER FEEDBACK [V]
18. AXIAL EXTENSOMETER DISPLACEMENT [IN, MM]
19. AXIAL EXTENSOMETER STRAIN
20. TORSIONAL EXTENSOMETER FEEDBACK [V]
21. TORSIONAL EXTENSOMETER ROTATION [RAD]
22. TORSIONAL EXTENSOMETER STRAIN
23. INTERNAL PRESSURE INTENSIFIER FEEDBACK (REMAINING VOLUME) [V]
24. INTERNAL PRESSURE INTENSIFIER VOLUME LOST [CU.IN, CU.CM]
25. EXTERNAL PRESSURE INTENSIFIER FEEDBACK (REMAINING VOLUME) [V] *
26. EXTERNAL PRESSURE INTENSIFIER VOLUME LOST [CU.IN, CU.CM] *
27. AXIAL LVDT FEEDBACK [V]
28. AXIAL LVDT DISPLACEMENT [IN, MM]
29. AXIAL LVDT STRAIN
30. TORSIONAL RVIT FEEDBACK [V]
31. TORSIONAL RVIT ROTATION [RAD]
32. TORSIONAL RVIT STRAIN
33. TEMPERATURE FEEDBACK [V]
34. TEMPERATURE [F, C]
35. STRAIN GAGE 1 FEEDBACK (OR USER DEFINED ANALOG INPUT) [V]
36. STRAIN GAGE 1 STRAIN
37. STRAIN GAGE 2 FEEDBACK (OR USER DEFINED ANALOG INPUT) [V]
38. STRAIN GAGE 2 STRAIN
39. STRAIN GAGE 3 FEEDBACK (OR USER DEFINED ANALOG INPUT) [V]
40. STRAIN GAGE 3 STRAIN
41. STRAIN GAGE 4 FEEDBACK (OR USER DEFINED ANALOG INPUT) [V]
42. STRAIN GAGE 4 STRAIN

* - NOT IN USE AT THIS TIME

VALID UNITS LIST FOR MTM30.EXE/EXTRA30.EXE - PAGE 1 OF 1

0. ANGLE - RAD, DEG
1. AREA - SQ.IN, SQ.MM
2. FORCE - LBF, N
3. LENGTH - IN, MM
4. PRESSURE - PSI(P), KPA(P)
5. MOMENT OF INERTIA - IN⁴, MM⁴
6. STRAIN - STRAIN, STRAIN
7. STRESS - PSI, MPA
8. TEMPERATURE - F, C
9. TEMPERATURE DIFFERENCE - F, C
10. TIME - S, S
11. TORQUE - IN.LBF, N.M
12. VOLTAGE - V, V
13. VOLUME - CU.IN, CU.CM
14. VISCOSITY - LBF.S/SQ.IN, N.S/SQ.M

UNITS INDEX - [ENGLISH], [METRIC]

APPENDIX C

Tubular Specimen Manufacturing Procedure

APPENDIX C

Tubular Specimen Manufacturing Procedure

C.1 INTRODUCTION

This appendix outlines the general procedure for manufacturing fiber reinforced tubular specimens using prepreg based material systems. The method consists of three main operations: a) composite tube fabrication, b) end tab fabrication and assembly, and c) integration of the tube and tab components. These operations are detailed in the following sections.

C.2 MOLD AND MANDREL PREPARATION

C.2.1 Resin Removal from External Molds

The basic components of the tube molding operation are shown in figure C.1. Before using the external molds (see figure C.1c), excess (hardened) resin from the previous specimen batch must be removed to maintain proper mold surface tolerances. The excess resin is deposited on the mold surfaces as a result of resin flow from the part during the consolidation (pressure) stage of the cure cycle. Since a mold release is used prior to curing, the excess resin typically flakes off without much physical effort. Resin residue on the internal mold surfaces should be completely removed by hand using Scotch-brite pads and/or Si-C grit papers (600 grit or higher). For the outer part of the mold, excess resin can first be removed using either a scraper, wire brush, or wire wheel, with the residual amounts being removed by the Scotch-brite pads. Excess resin inside the pin holes should be removed by reaming the hole, and

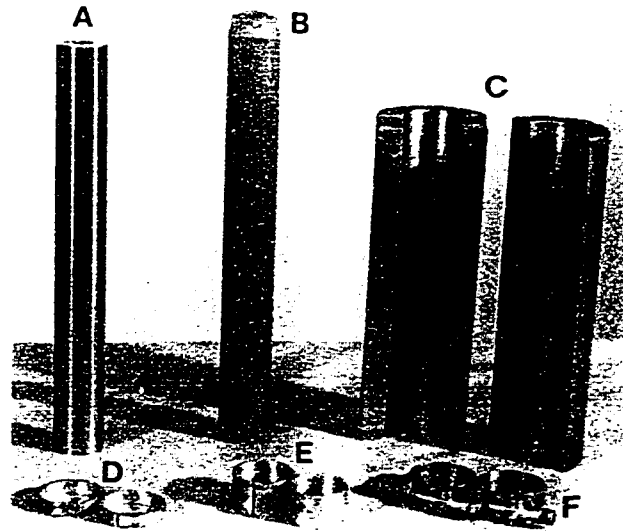


Figure C.1: *Mold components used for composite tube manufacturing; (a) steel mandrel without bladder, (b) steel mandrel with installed silicone bladder, (c) external stepped molds (2 part), (d) mandrel centering spacers, (e) clamp fittings, and (f) T-Bolt clamps.*

using compressed air to blow out any residue. Once all residue is removed, the mold surfaces should be thoroughly cleaned with acetone applied to a clean cloth.

C.2.2 Resin Removal from Fittings

The mandrel centering spacers (used to center the mandrel in the external mold) and clamp fittings (used to seal the bladder on the mandrel) must also be free of excess resin deposits to ensure proper tolerances and function (see figure C.1d-f). Since the spacer is used to provide accurate positioning of the mandrel inside the external mold, it should be cleaned by hand using Scotch-brite pads and/or Si-C grit papers (600 grit or higher). Excess resin on the outside of the clamp fittings can be removed using a scraper, wire brush, or wire wheel. The inside surface should be cleaned using Scotch-brite pads and/or Si-C grit papers (600 grit or higher). Once all residue is removed, the component surfaces should be thoroughly cleaned with acetone applied to a clean cloth.

C.2.3 Application of Release Agent

In order to facilitate the removal of excess resin after curing, a suitable release agent should be sprayed on the molds and fittings. Selection of an appropriate release agent will typically be a function of the resin system and mold material used (not all release agents work with all resins). For the 3M-1003 glass fiber/epoxy prepreg, Frekote release spray was found to be effective. Two applications of release agent should be made for the inside mold surfaces, with the molds being flipped in between applications to ensure that the top and bottom surfaces are covered. A single application can be made to the outer mold surface and to each side of the fittings. Release agents should NOT be applied to the mandrel since contamination of the prepreg may result.

C.2.4 Installation of Mandrel Bladder

The inflatable mandrel is composed of a machined steel mandrel with a fitted silicone rubber tube (Torr 1.25 in. ID x 1.375 in. OD - 50 Duro Shore A). The steel mandrel provides rigid support during the rolling operation, and is equipped with pathways for introducing compressed air, thermocouples and heater cartridges. A schematic of the mandrel is given in figure C.2. The surface of the mandrel is machined with small grooves which extend along the length and around the circumference of the mandrel. These ensure that supplied air is evenly distributed over the entire bladder surface after the lay-up is complete. At each end of the steel mandrel are un-grooved sections which provide a smooth surface for effective clamping and sealing of the silicone bladder.

The role of the bladder is to provide consolidation pressure to the prepreg material during curing, and to protect the mandrel core from excess resin flow. Depending on its condition from the previous cure cycle, the bladder may or may not be suitable for further use. If any surface anomalies are present, such as cuts, gouges or embedded resin, the bladder should be removed. If a bladder is to be re-used, ensure that the surface is free from excess resin and tape (remove by hand). If it is not to be re-used, a scalpel or utility blade can be used to cut the old bladder off of the steel mandrel. To prevent scoring of the mandrel surface at the clamping locations, the bladder should be removed by cutting the bladder from the inside outwards.

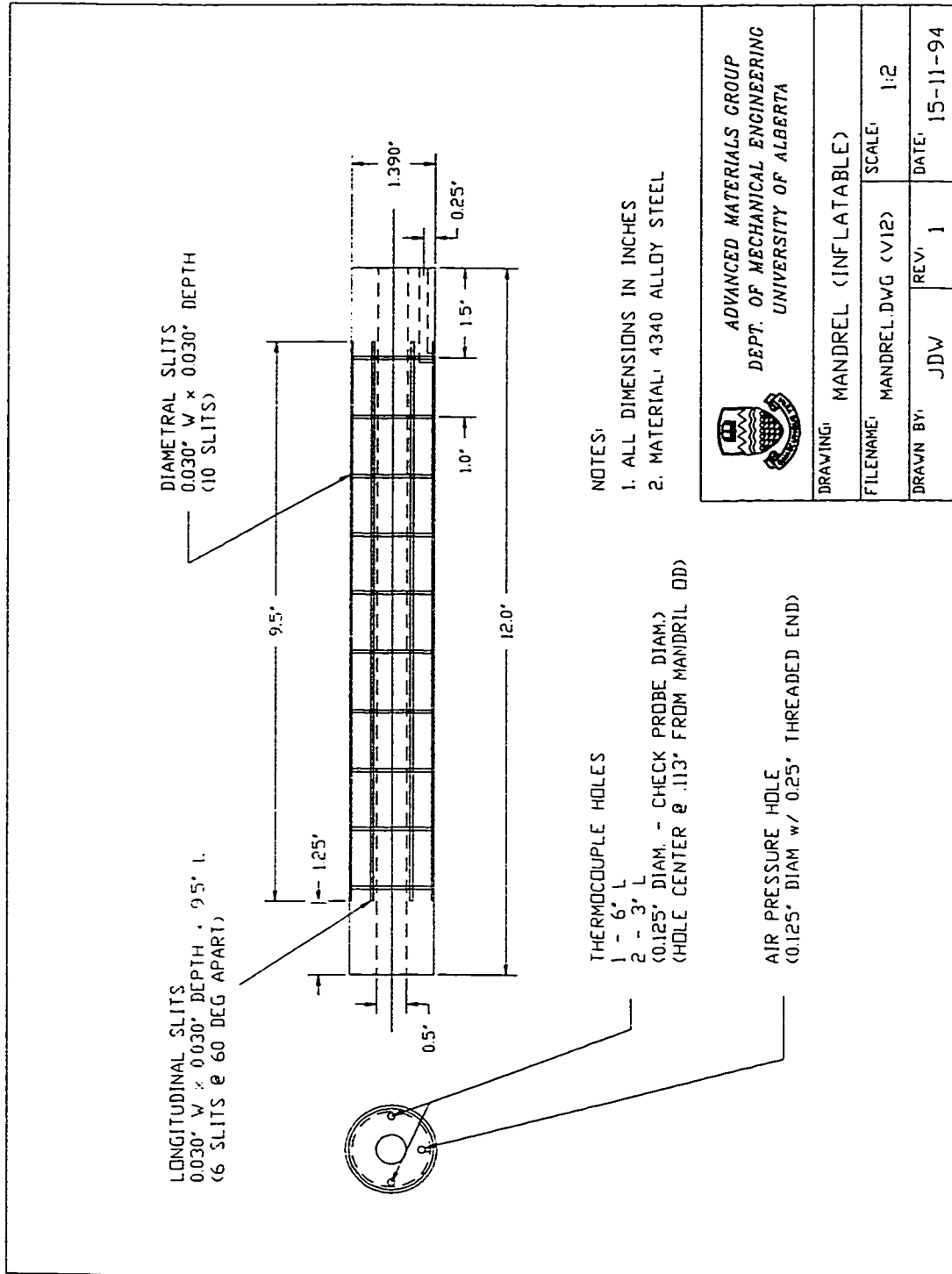


Figure C.2: Schematic of steel mandrel.

Installation of a new bladder is accomplished using the bladder vacuum tube system as shown in figure C.3. New bladder material is first cut to a length of 13.5 inches which will ensure protection of the ends of the mandrel from resin flow. Since the bladder tubing is received flattened in rolls, the cut bladder section should be opened up by squeezing the sides of the flattened roll. The bladder section is inserted into the vacuum tube with equal lengths protruding from each side. One at a time, the bladder ends are then opened up and folded over the ends of vacuum tube. The overlapping bladder material should be worked towards the center of the vacuum tube assembly to ensure proper deflation of the bladder inside. Deflate the bladder by applying a low vacuum to the vacuum tube using an appropriate source (vacuum pump or venturi tap). The deflated bladder surface on the inside of the vacuum tube should be smooth and free of any wrinkles or twisting. While maintaining the vacuum, insert the steel mandrel into the vacuum tube so that the bladder extends over the bottom of the mandrel by 1 to 1-1/2 inches (see figure C.3). Release the vacuum so that the bladder conforms to the mandrel surface. If using a venturi tap, be sure to remove the vacuum line before turning the water supply off since this will prevent water flow into the vacuum line (the bladder should be kept dry for the rolling process). Upon removal of vacuum, the bladder ends are unfolded off the vacuum tube onto the mandrel. The mandrel/bladder assembly is then removed from the vacuum tube, ready for mounting on the rolling table (see figure C.1b).

The bladder surface should be inspected after installation for any anomalies or defects. If there seems to be a concern, the bladder should be tested for leaks prior to its use. This can be done by mounting the clamp fittings on each end, and attaching an appropriate regulated air line. Using low pressure air (less than 20 psi) and limiting the supplied volume, inflate the bladder slightly then turn off supply. If the bladder does not hold the supplied air for more than 30 seconds, it should be replaced.

C.3 TUBE LAY-UP PROCEDURE

C.3.1 Mandrel Installation and Initial Wrapping

A rolling table is used to apply successive layers of prepreg onto the inflatable mandrel. Centering nuts are placed at the ends of the mandrel to allow for installation



Figure C.3: *Installation of silicone rubber bladder onto the steel mandrel using the vacuum tube assembly.*

on the rolling table. The mandrel support arm is rotated backwards for supported installation of the mandrel. In this position, the mandrel will be suspended off the table which will allow for easy installation and application of consumable layers. The mandrel (with its centering nuts) is installed by opening up and placing it in the threaded arm centers. The adjustable center is tightened just enough so that the mandrel is securely supported but is still free to rotate. The lock nut is then tightened to prevent release of the mandrel. At one end of the mandrel, equi-spaced markings (number of prepreg plies used) along the circumference should be made with a felt pen. This will be used to stagger successive layer starting points.

In order to facilitate easy removal of the mandrel from the part and to produce a quality finish free of surface anomalies, a number of initial consumable layers are applied to the mandrel surface. The particular surface finish required and final volume fraction of fibers in the part will depend upon the characteristics of the consumable layers, the prepreg system and the cure cycle. If the required prepreg system has excessive flow characteristics, the use of traditional bleeder cloth/perforated release film combinations may not be suitable due to difficulty in removal after cure. Through extensive testing, it was determined that a combination of peel-ply release fabric and release film should be used to produce the best dimensional tolerances and surface

finish. All consumable film and peel plies are dispensed in long rolls (typically 30 inches or longer). These products should be cut with a sharp scalpel or utility knife to prevent any edge distortion (do not use scissors).

The first layer applied to the mandrel surface is a 5.5 in. x 11 in. sheet of unperforated release film (Airtech A4000). With its long side along the mandrel axis, the film is affixed to the mandrel at each end using small pieces of Scotch Tape. The mandrel is rotated forward until the film overlaps itself. The surface should be smooth with the film held tightly. The film is affixed to itself on each end of the mandrel again by two small pieces of Scotch Tape. The tape should not be applied in the center section of the mandrel as this will leave impressions in the final part. In addition, one should maintain a consistent rolling direction for ALL layers including the consumables. If this is not followed, the prepreg layers will not tightly wrap onto the mandrel and separation will result.

The second consumable layer used is a 5.25 in. X 10 in. sheet of nylon release peel ply fabric (Precision Fabrics 51789/52006). This fabric produces a mat finish on the surface of the final tubular part, free of any large surface anomalies. Since the fabric material is prone to surface shifting, it must be succurely affixed to the previous release film layer. This can be accomplished by attaching a longitudinal strip of thin polyester tape (Airtech Flashbreaker 1) to the edge of the fabric. With the peel ply fabric laid on the flat glass surface of the rolling table, the polyester tape is unrolled along the longitudinal edge with 1/2 inch overlap on the fabric edge. By grasping the fabric and tape together, slowly peel the fabric and tape from the glass surface. By tightly holding each end of the tape, affix the fabric longitudinally to the mandrel as shown in figure C.4a (this should be applied to the opposite side of the release film overlap). The mandrel is rotated forward until the fabric ply overlaps itself and covers the exposed half of the polyester tape. The fabric should be temporarily held in place by two long pieces of Scotch Tape located at approximately 1.5 inches from each end of the fabric. The fabric is locked into place by wrapping two rotations of polyester tape at the ends (1/2 in. overlap) as shown in figure C.4b. The tape should be started just before the free end overlap which will suppress any fabric shifting. With the tape anchored, it is slowly unrolled as the mandrel is rotated forward. When both ends are affixed, the temporary Scotch Tape is removed. The mandrel is now prepared for rolling of the prepreg layers.

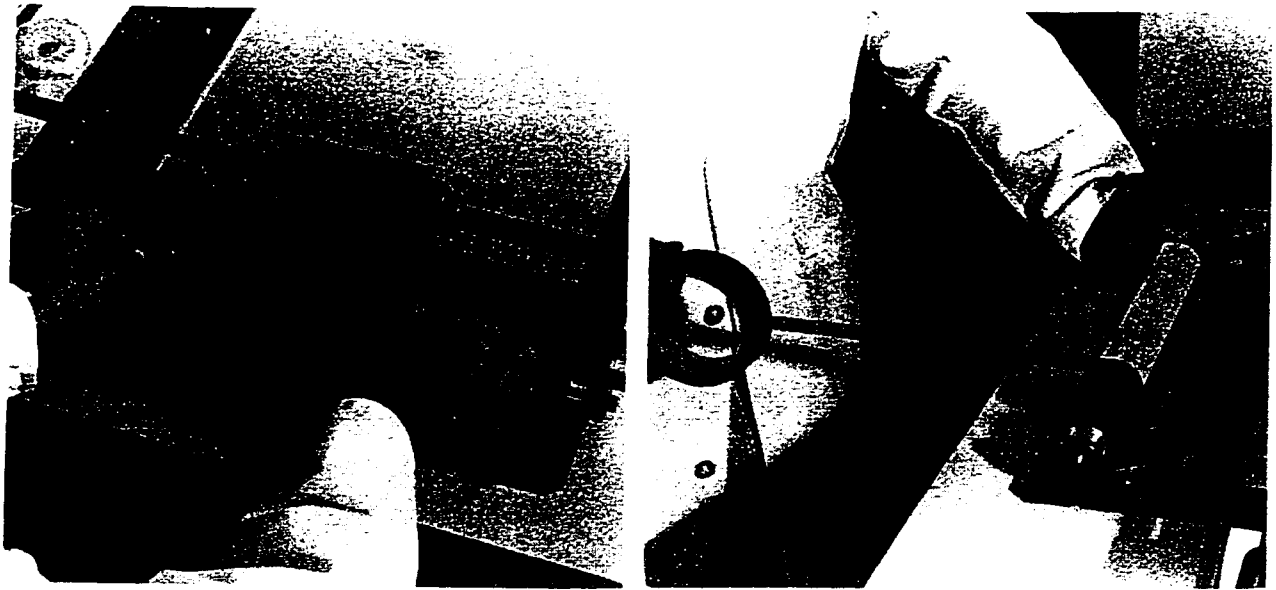


Figure C.4: *Installation and fixation of peel ply fabric; (left) affixing the fabric to the mandrel using an overlapping length of polyester tape, and (right) constraining the fabric layer by overwrapping the ends.*

C.3.2 Prepreg Cutting

Prepreg material is typically supplied in stock rolls with the unidirectional fibers oriented in the roll direction. Backing paper is used to separate the layers of the prepreg on its roll. Since active B-staged resins are used in prepreg materials, they should be stored at cold temperatures in order to prevent premature matrix curing. The use of over-aged prepreg material (which is characterized by increased stiffness and lack of tackiness) will result in poor interlaminar bonding and consolidation in the final part. If the material is suspected of being over-aged, it should be disposed of. In the (cold) storage environment, the prepreg should be kept in an evacuated airtight bag to prevent condensation on the material. Before using, the prepreg should be placed at room temperature for at least three hours.

Before the tube rolling operation begins, a complete series of prepreg patterns should be cut from the stock material roll using the appropriate stainless steel templates, and a sharp scalpel or utility knife (see figure C.5). An optional layer of release film can be applied to the surface of the prepreg before cutting to prevent contamination during handling. If a film layer is used, ensure that all entrapped air is removed by using a squeegee. For each layer, the template is aligned to the fiber direction of

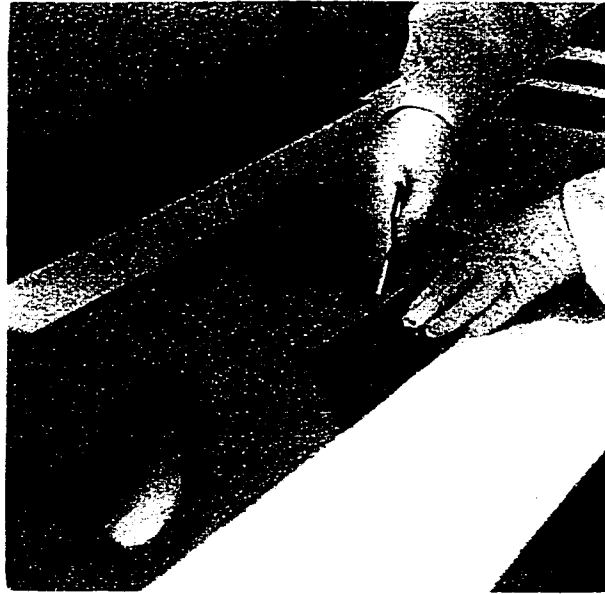


Figure C.5: *Cutting of prepreg layers using stainless steel templates.*

the roll by butting against a second template at the edge. The layer number should be marked on the backing paper for later identification. Particular attention should be made to the fiber orientation ($+\theta$ and $-\theta$) of each layer as it is cut and laid down, especially for symmetric laminates.

C.3.3 Tube Rolling

The rolling table is used to apply the prepreg patterns to the prepared mandrel. The rolling table consists of a flat glass surface, over which the traversing mandrel support arm is mounted on a linear track bearing. The mandrel support arm is designed to ensure the mandrel remains perpendicular to the rolling direction along the length of the table. As previously described, the mandrel is supported by the two support arm centers which allow it to rotate. The cut prepreg layer is precisely placed on the flat glass surface, and the mandrel is rolled over the pattern as shown in figure C.6. The prepreg pattern, thus, adheres and wraps around the entire mandrel as it is rolled.

A ground steel strip (prepreg placement guide) is bolted to the table below the glass plate, and is precisely adjusted so that it is perpendicular to the mandrel axis (and parallel to rolling direction). The placement guide is made thicker than the glass

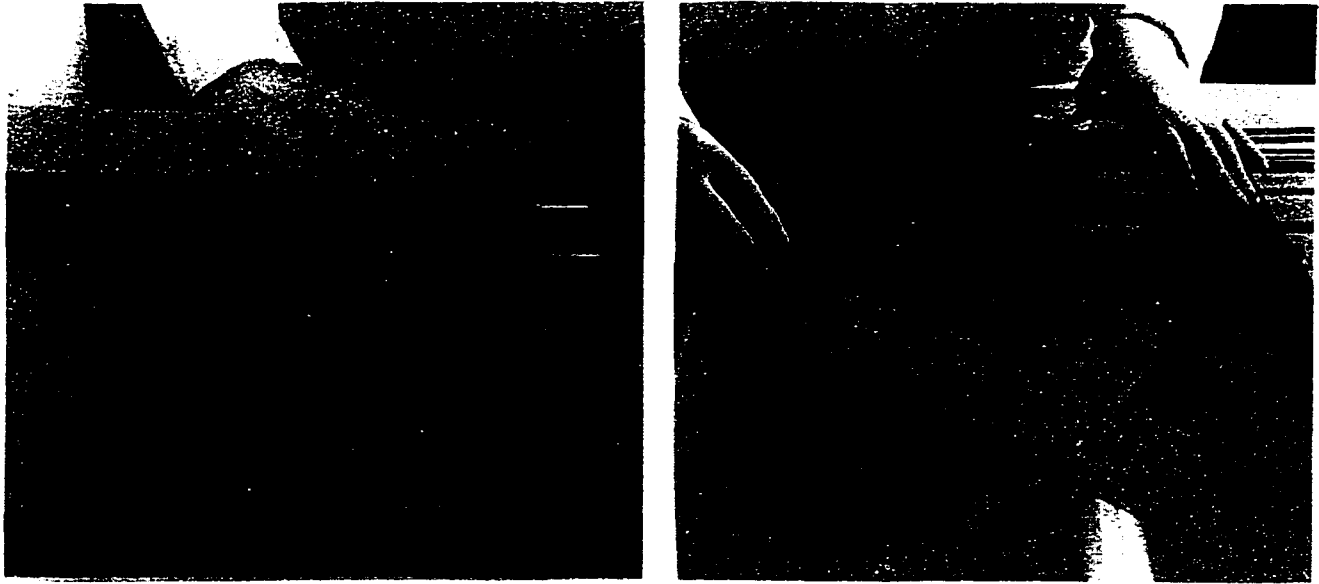


Figure C.6: *Rolling table operations; (a) alignment of prepreg sheet (with backing paper attached) and (b) rolling action.*

plate, in order to give a datum point for positioning the prepreg on the glass surface. Positioning plates butted against the placement guide are used to position and orient the prepreg patterns (see figure C.6a). Alignment of the table should be checked on a regular basis. A precision square can be used in conjunction with an unprepared steel mandrel (no bladder) to check and adjust the squareness between the mandrel support arm and the prepreg placement guide.

If a film layer was applied on the surface of the prepreg during cutting process, it should be removed first. The prepreg pattern is laid down on the surface of the glass with the backing side up. The backing side tends to have slightly more tackiness than the opposite side since it is protected. This fact is exploited to ensure that the prepreg will have a preferred affinity to adhere to other layers on the mandrel, and not to the table.

Once the pattern is located with the positioning plates, the backing is removed. The backing paper provides support for the prepreg during handling and positioning, and should not be removed until placement is complete. Unsupported prepreg will have a tendency to fray apart due to the very weak nature of the matrix interface. Proper angle orientation should be diligently observed. Once on the table, the mandrel is positioned over the start of the pattern. The mandrel is rotated so the marked

layer position approximately faces upward. By following the circumferential positioning of these markers, the butt joints of successive layers will be effectively staggered. Any anomalies that might occur due to the rolling process will be distributed.

The mandrel is lowered onto the start of the pattern and is rolled by rotating the end of the mandrel by hand (see figure C.6b). This ensures that some tension is placed on the pattern as it is rolled. The lay-up is compacted by rolling the specimen on the glass table a number of times while applying a moderate downward force on the arm. Rolling should be done only in the initial rolling direction to prevent any tendency of the prepreg to separate from the mandrel. Any fraying at the ends (which typically occur with off-axis layers) should be squeezed down by hand. Once the compaction is complete, and while the next layer is being positioned on the table, ensure the mandrel is off the table in the self-supporting position (i.e. by flipping the mandrel supports back over the support arm). If the lay-up is left on the table, the weight of the mandrel will cause distortion (flattening) in the prepreg.

It should be noted that the first prepreg layer is the most difficult to roll since it may have preference to adhere to the glass rather than the peel ply surface on the mandrel (multiple attempts are common). By using a scalpel, the start of the first layer can be lifted off the glass surface just after the roller has passed. This end can then be manually wrapped back onto the mandrel and held (anchored) by hand for the duration of the roll. Once the end is anchored by hand, the rolling process proceeds as usual. Since the adhesion to other prepreg layers is quite good, this procedure is typically not necessary for subsequent layers. The pattern placement and rolling operations are repeated until all required layers are applied to the mandrel.

C.3.4 Final Wrapping

In order to facilitate easy removal of the part from the external molds and to produce a quality finish free of surface anomalies, consumable layers are applied to the outside of the lay-up (the same materials used in section in section C.3.1).

The first layer applied to the prepreg surface is a 6 in. X 9 in. sheet of the nylon release peel ply fabric. By using slight hand pressure, the fabric layer can be wrapped around the prepreg with no supporting tape. The slight heating from handling is sufficient to fix the fabric in place. Smooth the surface by hand and

ensure that no wrinkling is present. The wrapped ends should slightly overlap the start (preferably by less than 1/8 in.).

The final layer applied is a 6 in. X 9 in. sheet of unperforated release film. It is wrapped on top of the peel ply surface to facilitate easy removal from the molds. The surface should be smooth with the film held tightly. The film is affixed to itself on each end of the mandrel by two small pieces of Scotch Tape at each end of the mandrel.

C.4 MOLD ASSEMBLY AND CURING PROCEDURE

C.4.1 *Mold Assembly*

Once the lay-up sequence completed, the mandrel is now ready to be placed into the external molds. The external (female) molds are used to shape the outer surface of the tubular part. These molds consist of a two-part construction and are made with hardened 4340 steel to ensure smooth surfaces and long life.

The internal diameter of the mold is precisely sized to allow for proper support for the expanding part. The sizing must be determined by trial and error, and is based on the final diameter of the lay-up and allowable pressure. A gap between the mold and part which is too large will require a large pressure to force the prepreg to the mold wall. High applied pressures, however, can cause excessive resin loss and failure of the bladder system. Pressures in excess of 100 psi cannot be supported by the present design.

The inside profile of the mold is stepped to accommodate the slight build-up of the lay-up ends during the rolling process (n.b. only for off-axis layers due to extensional/shear coupling at free ends). Without this step, proper consolidation of the gage section of the tube is impossible without excessive pressure. Locating pins are used to ensure proper alignment of the halves and must first be lubricated to ensure easy insertion and removal. This can be done by applying a thin lubricant (WD-40) to the inside of all pin holes with a cotton swab (excess on the mold surface should be removed).

Before the mandrel and lay-up are placed in the mold, the two centering rings are slid on both sides of the mandrel, and are butted against either side of the lay-up.



Figure C.7: *Installation of the mandrel (and lay-up) into the external mold.*

These rings are slit to allow for closure of the mold, and to allow for resin to escape during the curing stage. After the centering rings, the two clamping rings are slid on either side of the mandrel and are butted next to the centering rings. These rings are used to provide support for the T-Bolt hose clamps which seal the mandrel bladder. Without these clamp rings, a uniform seal cannot be obtained.

The mandrel assembly is placed in the first half of the mold marked "out" as shown in figure C.7. The mandrel should be placed in the mold with the thermocouple and air port openings oriented to the marked end of the mold. The mandrel should be centered over its length, allowing for approximately 1 in. overhang on each side of the mold. The second half of the mold is placed on top of the mandrel. Ensure that the orientation of the mold is correct (marked ends of the molds are placed together), and that the pin holes are aligned as close as possible. Apply a small lateral force by hand to close the mold together. Insert and tap the mold pins in the pin holes to ensure proper mold alignment.

Two circular mold clamps are placed on the outside of the mold to hold it together. When the mold clamps are tightened, any gaps which exist between the molds are eliminated. To complete the assembly operation, two T-Bolt hose clamps are slid over either side of the mandrel clamping rings, and are tightened by hand with a ratchet set in order to seal the internal bladder.

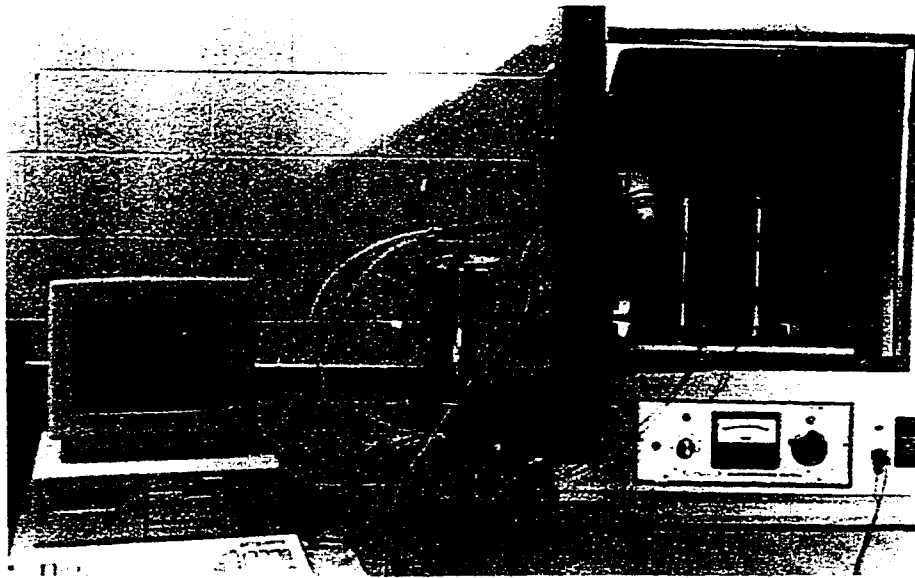


Figure C.8: *Polymeric composite tubular molding system (internally pressurized).*

C.4.2 Cure Cycle Procedure

The objective of the curing process is to provide heat and pressure to the part in order to provide resin flow, consolidation and final polymer cross-linking. The cure cycle is the programmed sequence of heating and pressure steps required to properly cure and consolidate the part. An air port is attached to the mandrel to provide the internal pressurization of the bladder. Uniform heating to the mold system is provided by an oven and internal heater cartridge. The oven provides a uniform heating source from the outside of the external mold while the cartridge heater, placed down the center of the mandrel, provides a uniform internal heating source. Up to three molds can be cured simultaneously with the current setup. The cure system assembly is shown in figure C.8.

In order to control the oven, three cartridge heaters and the applied pressure, a computer controlled cure system was developed. The oven temperature is controlled by an analog setpoint (open loop) while the cartridge heaters are operated by on/off control (pulsing closed loop). Thermocouples are placed in the mandrel to a) provide feedback to the cartridge heater system, b) provide a record of the actual molding temperature profile and c) trigger an alarm in the event of high mold temperatures (turn off system). An ice bath stored in a insulated thermos is used for the ther-

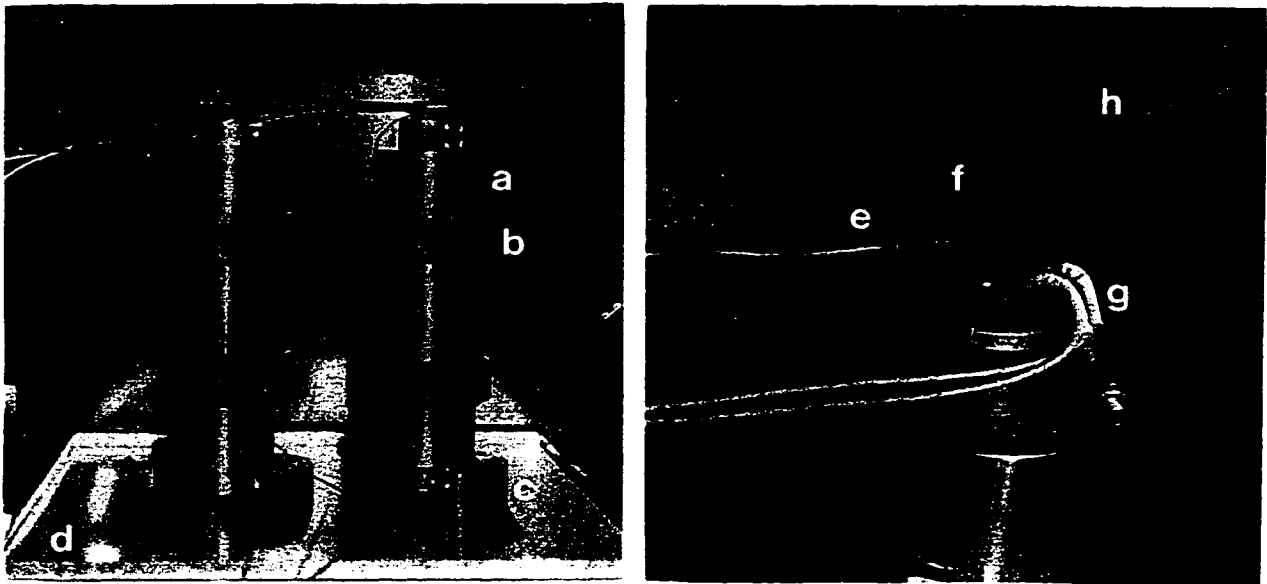


Figure C.9: *Details of mold assembly installation; (a) external part molds, (b) circular mold clamps, (c) split ring mold stands, (d) resin tray, (e) pressurized air line, (f) banjo nut attachment, (g) cartridge heater, and (h) thermocouple.*

mocouple reference point. Four trays of crushed ice are sufficient for monitoring the temperatures over the entire cure cycle (approximately 14 hours). The air pressure is automatically activated by the computer using a solenoid valve. The pressure level, however, must be manually set by adjusting the supply regulator.

Referring to figure C.9, installation of the mold is accomplished in the oven as follows. First, the cartridge heaters are inserted from the top, down the center of the mandrel. The heater wire is fed through a port to the outside of the oven. To prevent possible electrical shock, do not connect the power to the heater system until the final stages. The mold assembly is stood upright and supported on the external mold ends by a pair of circular split rings (which allow the protrusion of the mandrel to be free). The air line is fed from the outside of the oven through the oven port, and is attached to the mandrel with banjo nuts. The banjo nuts can be tightened using a ratchet set and simultaneously clamping the air port line with a pair of vise grips. The installation is completed by feeding the control thermocouple into the oven and inserting it into the mandrel. This sequence can be repeated for up to two more molds.

The proper air pressure is adjusted and locked at the regulator location. An air leak check is done to ensure that the banjo nuts and the mandrel bladder clamps are properly tightened. For the leakage test, the pressure solenoid valve can be activated manually using the control software. Air supplied to each mandrel is independently controlled by a series of manually operated flow valves. After each supply line is checked independently for leaks, all valves are opened for operation.

With the system assembly complete and the cartridge heaters attached to the main electrical supply, the oven is closed and set to remote program mode. The required cure cycle and setup is programmed into the computer via a set of ASCII textfiles (see Appendix D for samples). Once these files have been entered, the automated cure cycle can be initiated by the user. For the 3M-1003 prepreg system, the cure cycle is approximately 14 hours in length. Upon completion, the molds should be allowed to cool before removal and handling is attempted.

C.5 PART REMOVAL AND FINISHING

C.5.1 Part Removal

The mold is removed from the oven and disassembled in the reverse order as described in the previous section. Once the mold assembly is removed from the oven, the circular mold clamps and the mandrel bladder hose clamps should be removed first. With the clamps off, the mold assemblies are placed on a pair of wooden v-blocks at locations away from the pin holes. The mold is rotated so that the half marked "out" is facing upwards, and the pins are tapped out. The molds can be separated by prying the ends apart with a large screw driver or bar. Pay special attention not to pry on any ground mold surface. Once prying has separated the molds, it typically can be lifted off by hand. The mandrel can be separated from the remaining half of the mold by lightly tapping the mold face with a rubber mallet. Once the mandrel and cured part are removed from the external molds, the centering rings are removed from the mandrel by using a flat-end screw driver to break the accumulated resin bond between the ring and the cured tubular part.

The tubular composite part is pressed from the mandrel using an arbour press system. The mandrel is inserted into a support ring which is butted against the part.

This will provide the restraining force as the mandrel is pressed through the part. A series of rod extensions are used to force the mandrel through the entire length of the part. During the pressing operation, ensure that the mandrel is supported by hand underneath the press to prevent abrupt falling and damage to the mandrel. The internal consumable layers (peel ply and release film) are typically stripped from the part during the press operation, which facilitates its easy removal. Using a scalpel or utility knife and starting at one end of the tube (away from the gage section of the tube), the outer consumable layers must be removed by hand. The peel ply is typically embedded into the resin and may require some digging beneath the part surface to expose the fabric. Once a small amount of peel ply fabric is free, it can be peeled and removed from the remaining area of the part by hand.

C.5.2 Finishing

After the cured part is removed from the mandrel, the tube ends must be cut off and machined in order to provide a square and straight section for proper tab bonding. The ends are made square with the use of a rotatory sectioning device as shown in figure C.10. In this device, the tube is centered inside a rotating pipe section with a pair of three radially protruding bolts along the length of the tube. The pipe section is mounted to a block housing inside a bushing which allows the pipe section to rotate. A variable speed, DC motor is attached to the pipe section with a belt drive to rotate the structure. A rotary Dremel tool with a cut-off wheel is mounted on a stand at the opposite end of the device.

The center is initially set by lightly tightening the bolts on a wooden centering insert (see figure C.10 - left). The insert, which has a protruding rod with the same outside diameter as the tubular part, is located with respect to the pipe section and sets the proper position of the centering bolts. One set of radial bolts (along the length) is untightened, and the insert is removed. Using only these two bolts to clamp the part, centering is repeatedly assured.

Cut locations are first marked symmetrically on each side of the tube such that the final tube length will be 8 inches. The tube is inserted into the sectioning device partially extending from the end of the rotating pipe. The cut mark on the tube is aligned with the cut-off wheel, and the two clamp screws are lightly tightened to

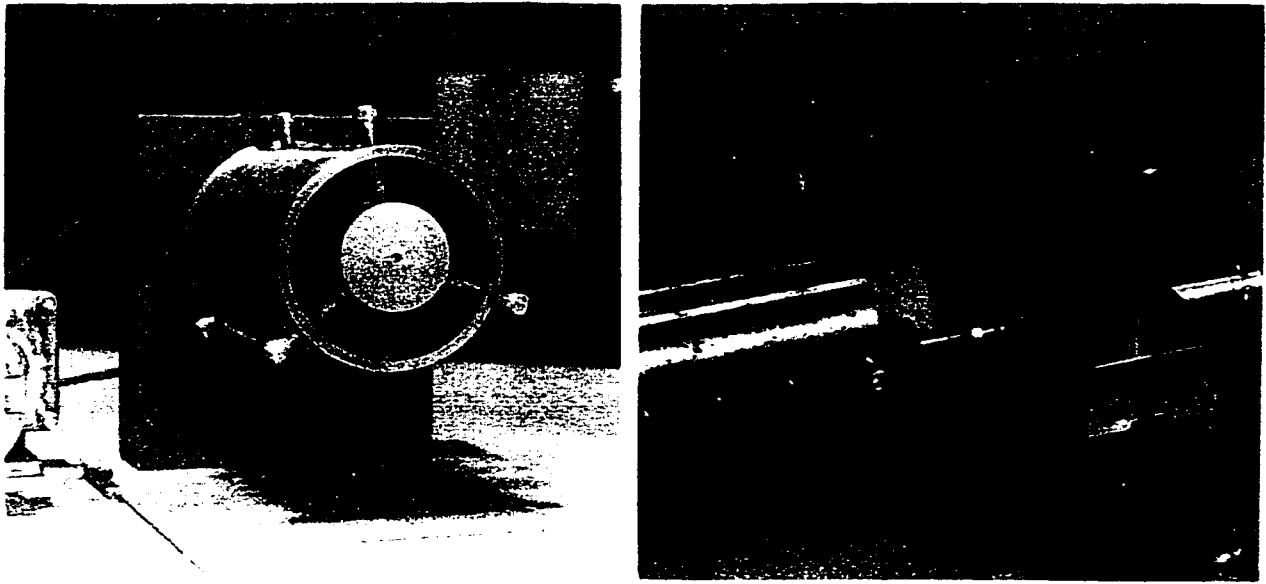


Figure C.10: *Tube sectioning apparatus; (left) initial center adjustment using wooden insert, and (right) cutting end of tube (both tubular part and cut-off blade are rotating).*

secure the tube in place. With the tubular part slowly rotating and the Dremel tool activated, the cut-off wheel is very slowly fed into the tubular part until sectioning is complete (see figure C.10 - right). Due to the hardness of the glass-fibers, the cut-off wheel will wear down and should be replaced when its diameter has decreased by $1/2$ (typically 6 cut ends). After the end of the tube is sectioned off, the rotation of the pipe clamp and cut-off blade is stopped and the specimen is removed. In order to maintain centering, ensure that only the previously tightened screws are untightened. Repeat the same procedure to section opposite end of the tube.

The final finishing activity is to machine off the steps on each end of the cured tube. This step is a consequence of the stepped external mold, and its removal is required to ensure that proper adhesive distribution occurs during end tab assembly (see next section). The machining process is performed in a lathe using conventional or carbide tools. One tube end is inserted into the three jaw chuck with a fitted wooden plug to prevent crushing with the other being supported by a center. The steps are subsequently machined and made flush with the gage section diameter. Only machine the steps at the ends of the tube (approximately $1/2$ inch). These machined areas will not affect the gage section as the ends are potted in tabs. It is recommended that the gage section area be protected from contamination by using a paper wrap.

Once the machining operation has been performed on both ends of the tube, measurement of the tube dimensions should be made before application of the tabs. The inside and outside diameters can be measured using a micrometer and bore hole gage, respectively. After taking measurements, the ends should be cleaned with an appropriate solvent (and clean cloths) to ensure proper bonding of the end tabs.

C.6 SPECIMEN ASSEMBLY

C.6.1 *Tab Preparation and Assembly*

The specimen design for the collet gripping system consists of a composite tubular part (with or without end reinforcement) with bonded aluminum end tabs. The purpose of the end tabs is to provide a method of attaching the composite tube to the testing machine gripping system without crushing the composite tubular wall. The tabs are made of 6061-T6 aluminum alloy, and are manufactured in two annular parts using a CNC lathe. A schematic of the tabs is given in figure C.11. The two concentric sections are pressed together to form an cylindrical annulus. The straight tubular part is potted in this annulus using a high shear strength epoxy adhesive. The adhesive is injected into the tab via four evenly spaced holes around its circumference near the top of the tab.

Before the tabs are assembled, the inside surface of the outer tab section and the outside surface of the inner tab section (i.e. the annular surface area) should be sand-blasted and cleaned as to enhance bonding of the tubular part. In order to ensure easy assembly and proper alignment, the mating surfaces should be protected prior to sand blasting as shown in figure C.12. The mating step of the inside tab section can be protected by a wrapping of polymer electrical tape. This tape is easy to apply and remove, and does not fall off during the sand blasting operation. The mating step of the outer tab section can be protected by inserting a tapered rubber stopper through the tab. This stopper will protrude from the back of the tab, and fit so that it covers the mating step on the inside.

After the sand-blasting operation, the tabs parts are blown with air to remove excess sand, and diligently cleaned with acetone applied to a clean cloth. To ensure the best bond possible, no residue should be left. The outer surfaces of the tab should

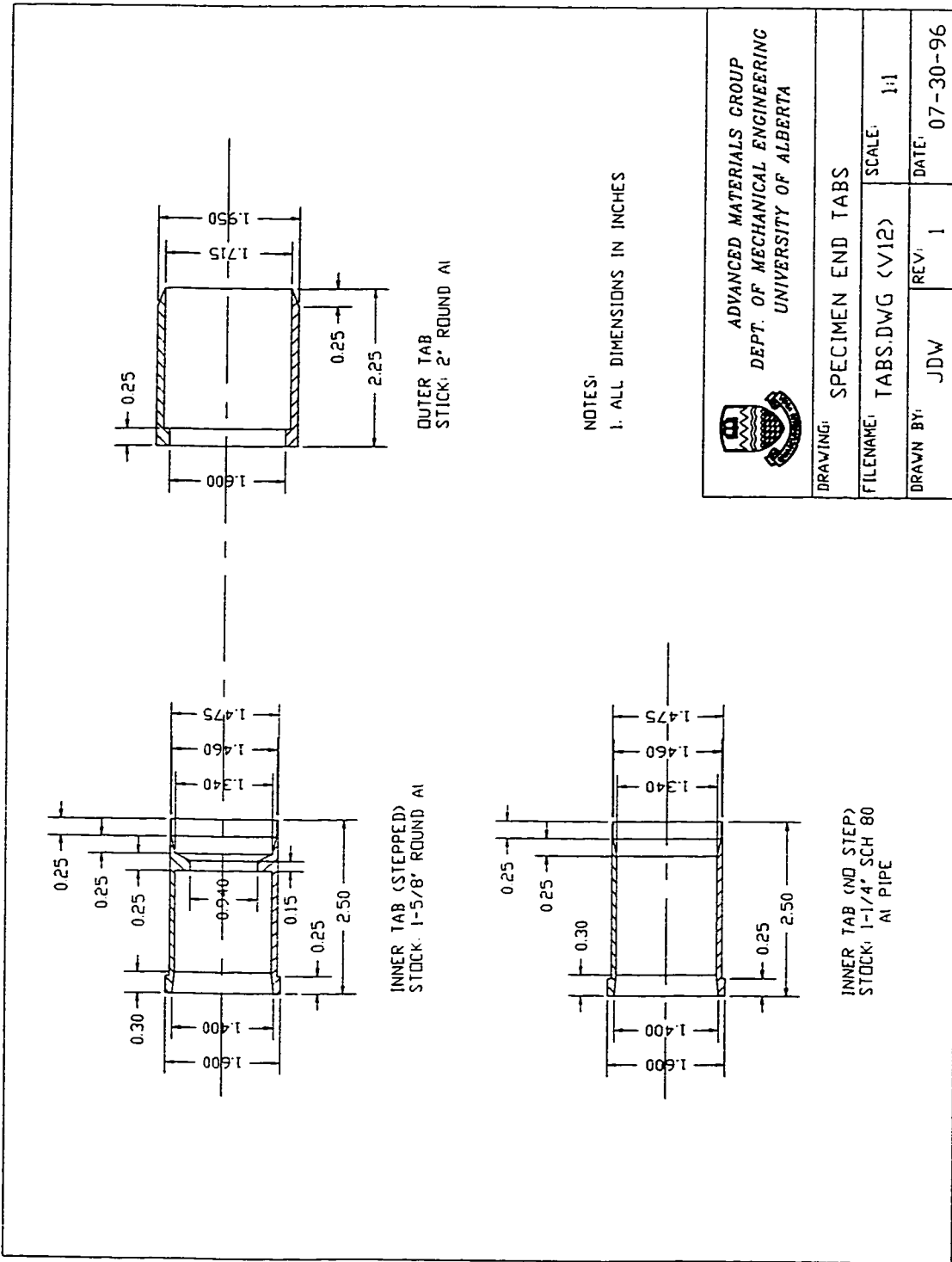


Figure C.11: Schematic of aluminum end tabs.

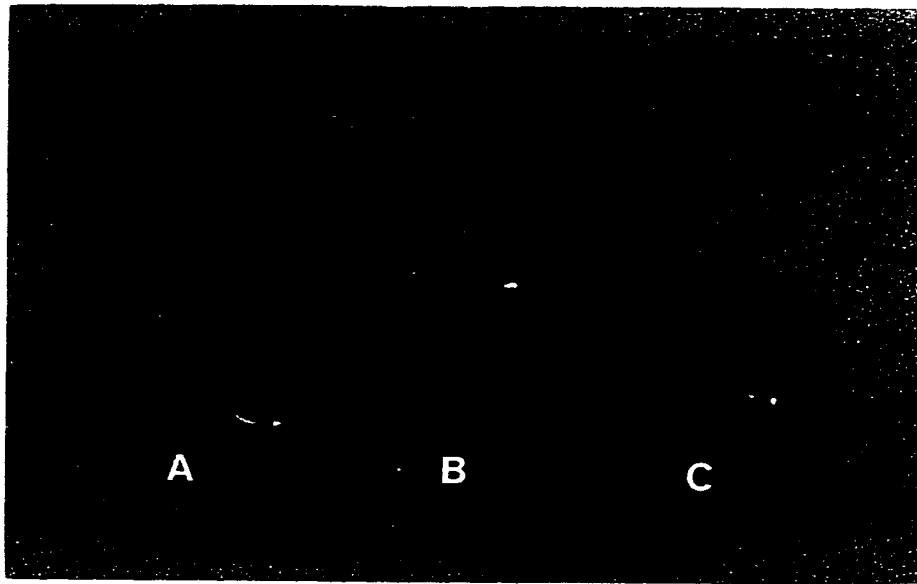


Figure C.12: *Inside and outside tab parts; (a) as machined, (b) with protection of mating surfaces for sand-blasting, and (c) after sand-blasting.*

also be cleaned to prevent grit contamination of the specimen assembly stands and the testing machine gripping system.

Once the inner and outer tab sections are blasted and cleaned, they are pressed together using a precision centering tool as shown in figure C.13. The centering tool is first inserted into the outer tab, followed by insertion of the inner tab. Using the arbor press, the outer tab section is pressed onto the inner tab section by applying force to the centering tool. Once the outer tab is seated, the centering tool can be removed by twisting.

C.6.2 Tab Bonding (Side A)

With the composite tube and end tab assemblies prepared, the tubular specimen can now be assembled. The tabs are bonded to the composite tubular part by first injecting an adhesive into the tab annulus, and then lowering the composite tube inside. Concentricity and alignment of the tube and tabs is ensured using an alignment stand, tab spacers, and a tube centering spacer as shown in figure C.14. This system effectively allows the precise attachment of tabs to any tubular geometry and material system.

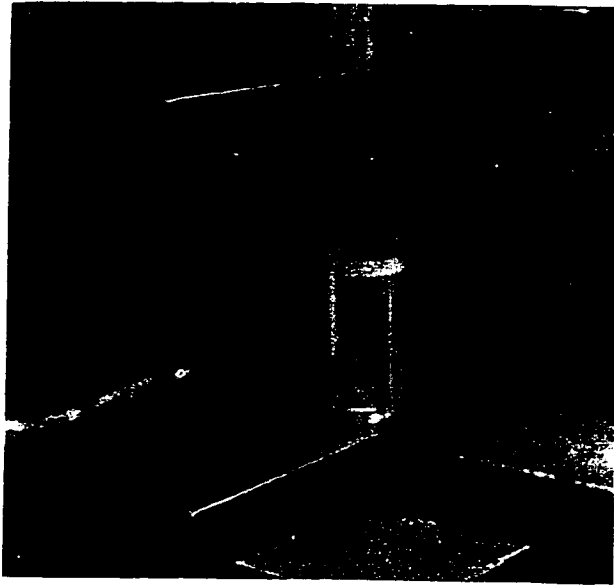


Figure C.13: *Pressing of the inside and outside tab sections.*

The tabs are adhesively bonded to the tubular part using 3M DP-460 structural adhesive. This product is a two part, high shear strength epoxy adhesive supplied in a 370 ml cartridge format. A 3M Scotch-Weld EPX applicator gun, EPX 2:1 plunger and EPX mixing nozzles are used to dispense the adhesive. The mixing nozzle ensures thorough mixing of the two part epoxy, and provides an efficient means of injecting the adhesive directly into the tab annulus.

Since the potted adhesive is forced out of the annulus during the assembly process, WD-40 lubricating liquid should be applied to any local surface of the alignment stand parts that are in the vicinity of the top of the tab. This will ensure easy assembly prior to potting, and easy removal of the tab and tubular part from the alignment stand after the adhesive has cured. The WD-40 fluid should be dispensed from the aerosol can into a container, so that it can be swabbed onto the required surfaces (i.e. do not spray directly as this may contaminate bonding surfaces). The lower section of the alignment stand (between 1 and 3 inches from the base), the top surface of the tab spacer and the inner transition section of the tab should be swabbed thoroughly. If lubricant enters inside the tab's annular area, it should be removed using a folded cloth corner with acetone prior to adhesive bonding.

The tab bonding procedure is as follows. The tab spacer is inserted into the unbonded tab, and the unit is slid onto the alignment stand rod and seated at its

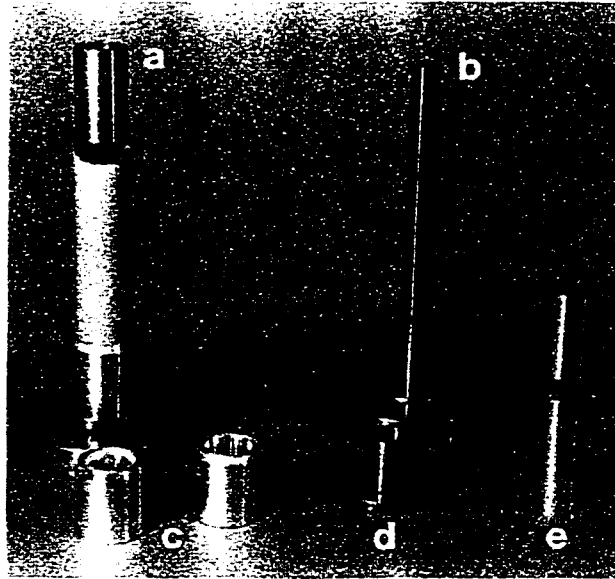


Figure C.14: *Specimen assembly components; (a) assembled alignment stand (first end tab), (b) alignment stand, (c) end tab assemblies, (d) tab centering spacer, and (e) tube centering spacer.*

base as shown in figure C.15. The first tab to be bonded should have no internal step. This allows for machining of the stepped tab after its attachment. In order to lower the viscosity of the potting adhesive and promote a more uniform flow around the composite tube, the alignment stand and tab assemblies are placed on a hot plate and moderately heated. When the temperature of the tab is warm to the touch but not excessively hot, the stand should be removed from the hot plate. Excessive heating will simply promote curing before potting can take place.

Before injecting the potting adhesive, the dispensing system must be assembled (i.e. adhesive cartridge, dispensing gun, plunger, and mixing nozzle). Just prior to attaching the mixing nozzle, the openings of cartridge cylinders should be punctured to ensure adhesive flow. Once the dispensing system is assembled, a ruler is placed on top of the plunger to measure the quantity of adhesive injected (based on plunger displacement). The objective is to supply the tab annulus with enough adhesive to completely immerse the tubular part when it is potted (overflow should occur). If insufficient adhesive is supplied, an incomplete bond may be formed from which there is no recourse (and the specimen might have to be scrapped).

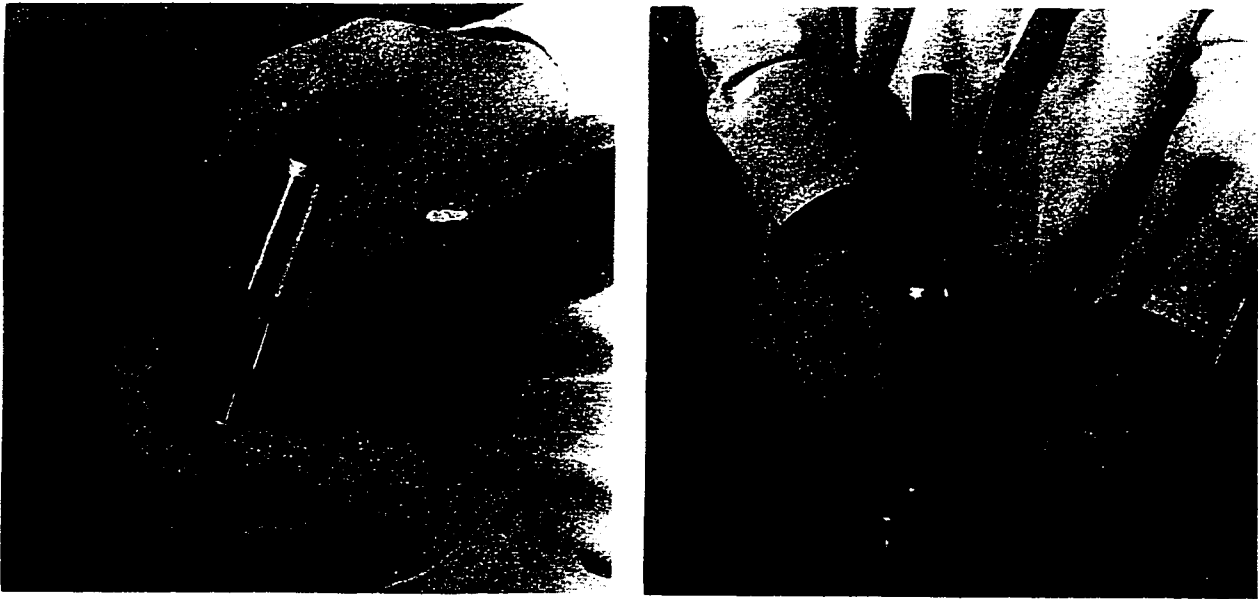


Figure C.15: *Alignment stand assembly; (left) insertion of centering spacer into tab, and (right) placement of tab/spacer assembly on alignment stand.*

For the current tab geometry, approximately 6 mm (plunger displacement) of adhesive cartridge stroke should be injected per tab hole as shown in figure C.16 (left). For other geometries and tubular wall thicknesses, the total volume of adhesive can be estimated by inserting a tube into a closed tab, and measuring the required volume using water from a marked syringe. This required volume is then divided by the effective cartridge cross-sectional area (total cartridge volume divided by its length) to derive the required plunger stroke.

Once adhesive has been injected into the four tab holes, the tab surface is wiped with a paper towel to remove any excess amounts. A length of polymer electrical tape is wrapped around the tab onto itself to seal the injection holes. To prevent adhesive leakage from the holes, a rubber strip constrained by a hose clamp is placed on top. The hose clamp should only be moderately tightened as not to distort the tab.

The composite tubular part is now potted before the adhesive sets (approximately 20 minutes at moderately elevated temperatures). To ensure that the composite tube is centered with respect to the tab, a stainless steel tube spacer is used. Since there is some variation in tubular part inside diameters, a range of tubular spacers is available for matching. The selected (closest fitting) spacer is partially inserted into the composite tube (approximately 2/3 of the tube length). A hose clamp is

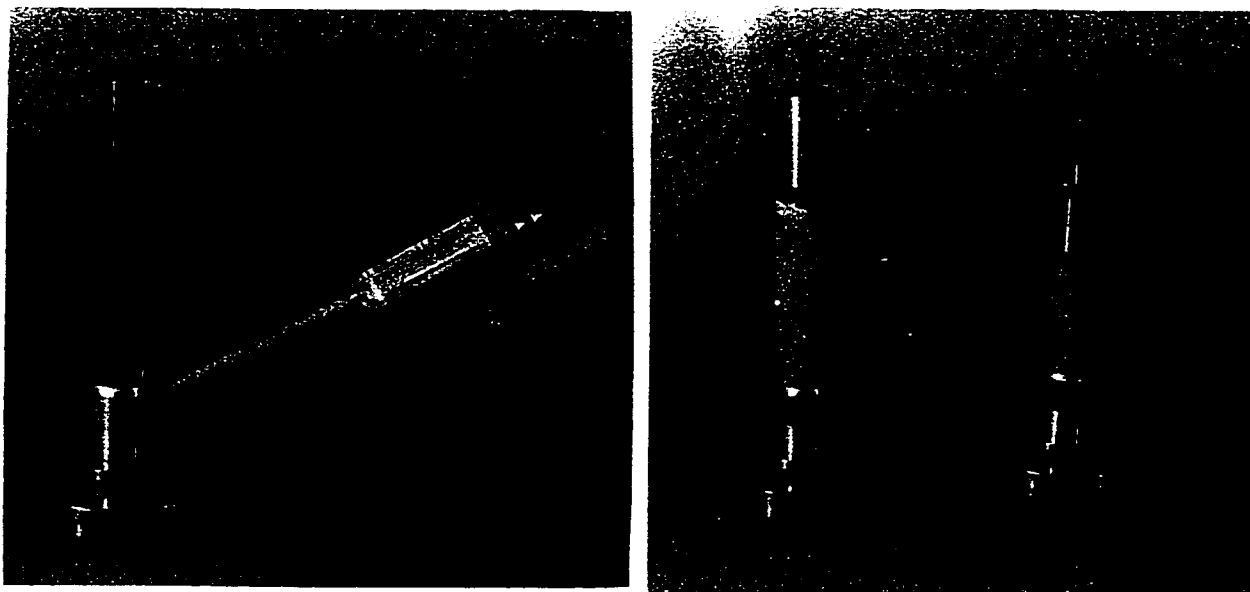


Figure C.16: *Tab bonding procedure; (left) injection of potting adhesive into the tab, and (right) completed tab potting (first and second tabs).*

used to suspend the spacer in the tube, and prevent it from falling inward towards the adhesive overflow. The spacer and tubular part are simultaneously slid onto the alignment stand rod, and lowered into the adhesive filled tab (see figure C.16 - right). As the descent of the tubular part occurs, the excess resin overflow on the outside should be continuously removed with paper towels. Since adhesive flow can occur quite quickly, paper towel sections (approximately 2 in. x 2 in.) should be pre-cut and readily available. When the tubular part has finished its descent and is seated, thoroughly wipe any excess at the tube/specimen interface and set aside to cure for 24 hours. The adhesive gun should be dis-assembled with the mixing nozzle disposed of.

Up to four ends can be simultaneously potted in one setup. For multiple stands, ensure that all accessories and supplies required (paper towel, tape, and hose clamps) are cut to size and readily available for use. Since volatiles evolve from the adhesive curing process, the bonding and curing of the tab ends should be performed in a fume hood.

C.6.3 Specimen Removal and Machining

After the adhesive has cured sufficiently for handling (24 hours minimum), the alignment apparatus must be dis-assembled. Since an overflow of adhesive will typically occur on the inside of the part, it becomes necessary to press the alignment stand rod off the bonded tab. The tubular spacer is first removed from the alignment rod and specimen, followed by the hose clamp and rubber strip on the tab circumference. The alignment stand base is then removed by un-bolting it from the rod portion. In order to remove the rod without damaging the specimen, the rod is pressed through the tab by bearing on the bottom of the end tab or end tab spacer (do not bear the load on the free specimen end). Various lengths of steel rod are used to push the rod completely through the specimen and out the bottom of the tab. If sufficient release agent was used (WD-40), the tab spacer can be removed from the specimen by hand. If not, the tab spacer can be manually pressed from the specimen using four pins inserted in pin-holes at the bottom of the spacer.

Any adhesive residue on either the stand rod or the tab spacer should be removed with a Scotchbrite pad or SiC grit paper (600 grit), and subsequently cleaned with acetone. The alignment stand can now be re-assembled for its next use.

The excess adhesive on the inside of the specimen tab must be machined off to allow for the attachment of the second tab and uninhibited insertion into the testing machine. Due to the geometry of the tab and spacer, the excess adhesive on the inside of the specimen will be deposited only on the aluminum tab surface (and not on the composite specimen). Thus, the composite tubular gage section will remain unaffected by any adhesive removal process. If sufficient release agent was used, the adhesive material should separate from the tab with minimal machining. To perform the machining operation, the specimen is placed in a lathe (cantilevered), and the excess adhesive is removed using a boring bar. Attention should be paid to avoid any contact with the composite material. When clamping the free end of the composite tubular part, use a fitted wooden plug to prevent crushing. After boring the inside tab surface, residue and roughness should be removed using fine grit paper (600 grit) as this surface is intended for pressure seal service.

Due to external adhesive overflow or leakage at the injection holes, there is often adhesive residue on the outer tab surface as well. Since the specimen is already setup

in the lathe, the adhesive residue on the outside surface can be removed by light filing and various grit papers. A center should be used to support the cantilevered specimen.

C.6.4 Tab Bonding (Side B)

To attach the second end tab, the previous procedure (for side A) is repeated. Instead of a tubular spacer, however, a second tab spacer is used to center the previously potted tab at the top of the alignment stand (see figure C.16 - right).

Once both specimen tabs are attached, two final (but optional) machining operations may be required. If a large clamping force is required for the specimen (e.g. for axial fiber dominated specimens), slits can be machined along the tabs in order to reduce the clamping stiffness. Using a milling machine, the specimen is clamped in v-blocks and machined using a slitting saw. Any number of slits can be imparted but ensure an even distribution around the circumference of the tab. To ensure the highest possible clamping force, these machined slits should penetrate through the tab wall (and partly through the adhesive) but should not touch the tubular part.

For tests with large torsional loads, a 1/4 in. keyway can be machined into each end of the specimen. This keyway matches a removable key located in the ends of the grip back plate. A milling machine with a 1/8 in. end mill cutter is used to machine the keyway. A special jig is used to hold the specimen in an upright position. Clamping force is applied only to both tab surfaces to prevent damage to the composite section. At least two passes with the end mill cutter is required, and a gage key should be continuously used to check the fit during the machining process.

APPENDIX D

Datafiles for Cure Cycle Control Program (CCCP.EXE)

1. Master Datafile
2. Cure Cycle Datafile - Cartridge Heaters (CURE36.DAT)
3. Cure Cycle Datafile - Oven (CURE36OV.DAT)
4. Control Datafile
5. Calibration Datafile

MASTER DATAFILE FOR COCP.EXE - PAGE 1 OF 2

START CALIB:

```
thermocouple #1 (0-Not Active, or Heater #) = 3
thermocouple #2 (0-Not Active, or Heater #) = 1
thermocouple #3 (0-Not Active, or Heater #) = 1
thermocouple #4 (0-Not Active, or Heater #) = 1
thermocouple #5 (0-Not Active, or Heater #) = 1
thermocouple #6 (0-Not Active, or Heater #) = 1
thermocouple #7 (0-Not Active, or Heater #) = 0
calibration datafile (thermocouple #1) = "CALIB.DAT"
calibration datafile (thermocouple #2) = "CALIB.DAT"
calibration datafile (thermocouple #3) = "CALIB.DAT"
calibration datafile (thermocouple #4) = "CALIB.DAT"
calibration datafile (thermocouple #5) = "CALIB.DAT"
calibration datafile (thermocouple #6) = "CALIB.DAT"
calibration datafile (thermocouple #7) = "CALIB.DAT"
```

END CALIB:

START CONTROL:

```
heater #1 active switch (Y/N) = "Y"
heater #2 active switch (Y/N) = "N"
heater #3 active switch (Y/N) = "Y"
heater #4 active switch (Y/N) = "N"
heater #5 active switch (Y/N) = "N"
heater #6 active switch (Y/N) = "N"
control thermocouple (for heater #1) = 3
control thermocouple (for heater #2) = 0
control thermocouple (for heater #3) = 1
control thermocouple (for heater #4) = 0
control thermocouple (for heater #5) = 0
control thermocouple (for heater #6) = 0
control datafile (heater #1) = "CONTROL.DAT"
control datafile (heater #2) = "CONTROL.DAT"
control datafile (heater #3) = "CONTROL.DAT"
control datafile (heater #4) = "CONTROL.DAT"
control datafile (heater #5) = "CONTROL.DAT"
control datafile (heater #6) = "CONTROL.DAT"
cure datafile (heater #1) = "CURE36OV.DAT"
cure datafile (heater #2) = " "
cure datafile (heater #3) = "CURE36.DAT"
cure datafile (heater #4) = " "
cure datafile (heater #5) = " "
cure datafile (heater #6) = " "
pulse frequency (in Hertz) = 2
```

END CONTROL:

START PRESSURE:

```
pressure line #1 (0-Not Active, or Heater #) = 0
pressure line #2 (0-Not Active, or Heater #) = 0
pressure line #3 (0-Not Active, or Heater #) = 0
pressure line #4 (0-Not Active, or Heater #) = 0
supply pressure (pressure line #1) = 70 psi
supply pressure (pressure line #2) = 0 psi
supply pressure (pressure line #3) = 0 psi
supply pressure (pressure line #4) = 0 psi
```

END PRESSURE:

MASTER DATAFILE FOR CCCP.EXE - PAGE 2 OF 2

START OUTPUT:

```
specimen description (heater #1) = "Thermal Gradient Test"
specimen description (heater #2) = " "
specimen description (heater #3) = "Thermal Gradient Test"
specimen description (heater #4) = " "
specimen description (heater #5) = " "
specimen description (heater #6) = " "
processing notes (heater #1) = "2 F/m and 300F cure cycle"
processing notes (heater #2) = " "
processing notes (heater #3) = "50W Cartridge"
processing notes (heater #4) = " "
processing notes (heater #5) = " "
processing notes (heater #6) = " "
output datafile (heater #1) = "therm36.ovn"
output datafile (heater #2) = " "
output datafile (heater #3) = "therm36.out"
output datafile (heater #4) = " "
output datafile (heater #5) = " "
output datafile (heater #6) = " "
```

END OUTPUT:

CURE CYCLE DATAFILE FOR CCCP.EXE - PAGE 1 OF 1
 CURE CYCLE FOR CARTRIDGE HEATERS (CURE36.DAT)

```

*
* Heating Information:
*
* 1. Heating Process - "HOLD", "RISE", "DECAY"
*
* The following is defined only for HOLD cycle steps:
* 2. Heating Duration Time in the form "hh:mm:ss"
*
* The following is defined only for RISE/DECAY cycle steps:
* 3. Heating Slope Type - "FORCED" (user specified), "NATURAL" (natural)
* 4. Heating Slope Ending Trigger Temperature
* 5. Units (C or F)
* 6. Heating Rate (only defined for FORCED RISE/DECAY)
* 7. Units (C/s, C/m, C/h, F/s, F/m, or F/h)
*
* Pressurization Information:
*
* 8. Pressurization Action - "ON", "OFF", "CONTINUE"
*   n.b. CONTINUE indicates the pressure will remain in the
*       same state as the previous step.
*
* The following is defined only for HOLD cycle steps:
* 9. Pressure Triggering Time in the form "hh:mm:ss" (used only
*   when the cycle is defined by HOLD)
*
* The following is defined only for RISE/DECAY cycle steps:
* 10. Pressure Triggering Temperature
* 11. Units (C or F)
*
* NOTE: When a field is not valid for the particular step, the
*       "-----" delimiter is included for parsing purposes.
*

```

START CURE:

```

RISE ----- FORCED 250.0 F 2.0 F/m --- -----
RISE ----- FORCED 285.0 F 1.01 F/m --- -----
DECAY ----- NATURAL 150.0 F ----- --- -----

```

END CURE:

CURE CYCLE DATAFILE FOR CCCP.EXE - PAGE 1 OF 1
 CURE CYCLE FOR OVEN (CURE36OV.DAT)

```

*
* Heating Information:
*
* 1. Heating Process - "HOLD", "RISE", "DECAY"
*
* The following is defined only for HOLD cycle steps:
* 2. Heating Duration Time in the form "hh:mm:ss"
*
* The following is defined only for RISE/DECAY cycle steps:
* 3. Heating Slope Type - "FORCED" (user specified), "NATURAL" (natural)
* 4. Heating Slope Ending Trigger Temperature
* 5. Units (C or F)
* 6. Heating Rate (only defined for FORCED RISE/DECAY)
* 7. Units (C/s, C/m, C/h, F/s, F/m, or F/h)
*
* Pressurization Information:
*
* 8. Pressurization Action - "ON", "OFF", "CONTINUE"
* n.b. CONTINUE indicates the pressure will remain in the
* same state as the previous step.
*
* The following is defined only for HOLD cycle steps:
* 9. Pressure Triggering Time in the form "hh:mm:ss" (used only
* when the cycle is defined by HOLD)
*
* The following is defined only for RISE/DECAY cycle steps:
* 10. Pressure Triggering Temperature
* 11. Units (C or F)
*
* NOTE: When a field is not valid for the particular step, the
* "-----" delimiter is included for parsing purposes.
*

```

START CURE:

RISE	-----	FORCED	325.0 F	2.0 F/m	----	-----	-----
HOLD	01:00:00	-----	-----	-----	----	-----	-----
DECAY	-----	FORCED	300.0 F	100.0 F/m	----	-----	-----
HOLD	12:00:00	-----	-----	-----	----	-----	-----
DECAY	-----	NATURAL	150.0 F	-----	----	-----	-----

END CURE:

CONTROL DATAFILE FOR CCCP.EXE - PAGE 1 OF 1

START CONTROL:

max. allowable temperature = 400 F

max. allowable temperature difference |SP-TC| = 400 F

END CONTROL:

START OUTPUT:

output file write increment = 30 s

output file temperature units = "F"

END OUTPUT:

START ANALOG_OUT: (open loop - heaters 1 & 2)

starting temperature = 190 F

heater calibration constant = 0.0091 V/C

END ANALOG_OUT:

START DIGITAL_OUT: (closed loop - heaters 3 to 6)

maximum allowable heater ON time = 10000 s

deadband temperature (on RISE) = 2 F

deadband temperature (on DECAY) = 2.5 F

maximum heater output = 1000 W

required heater output = 50 W

END DIGITAL_OUT:

CALIBRATION DATAFILE FOR COCP.EXE - PAGE 1 OF 1

START CALIB:

thermocouple reference voltage = 0 mV

thermocouple amplifier gain = 400

calibration equation output units = "C"

TC calibration polynomial coefficient (0th order) = 0.226001

TC calibration polynomial coefficient (1st order) = 25.488

TC calibration polynomial coefficient (2nd order) = -0.565494

TC calibration polynomial coefficient (3rd order) = 0.0146797

END CALIB:

APPENDIX E

Volume Fraction Worksheet

APPENDIX F

ANSYS Batch Files

1. Mechanical Analysis
2. Thermal Analysis

ANSYS BATCH FILE - TUBULAR SPECIMEN MODEL (MECHANICAL ANALYSIS) - PAGE 1 OF 5

C*** ANSYS FE TUBULAR SPECIMEN MODEL - MECHANICAL ANALYSIS

C*** 1/4 Cylinder Model [+/-45]s (1H:1A)

/FILENAME,P45_11

/TITLE,Tubular Specimen [+/-45]s (1H:1A)

/OUTPUT,P45_11,OUT

C*** Input Parameters

C*** Element Mesh Parameters

THDIVS=16

TABDIVS=5

ESIZE1=0.005

ESIZE2=0.1

C*** Applied Hoop and Axial Stresses

SIG_HOOP=1.0e6

SIG_AX=1.0e6

C*** Specimen Parameters

C*** note: layer angle given is in element C.S. which is rotated 90 to the pipe axis

C*** (ie. pipe winding angle is 90 - theta given)

SPEC_ANG=45

SPEC_WT=0.07

SPEC_LT=0.00875

SP_MRAD=0.8

C*** Tab Parameters

TAB_LT1=0.10

TAB_LT2=0.08

TAB_LT3=0.06

TAB_LT4=0.04

TAB_LT5=0.02

ADH_LT=0.025

C*** Keypoints Along Cylinder (Z Coordinate)

TAB_Z0=-0.25

TAB_Z1=-0.20

TAB_Z2=-0.15

TAB_Z3=-0.10

TAB_Z4=-0.05

TAB_Z5=0

SPEC_Z1=1.0

SPEC_Z2=2.0

C*** Calculated Parameters

N_AXIAL=SIG_AX*SPEC_WT

P_HOOP=SIG_HOOP*SPEC_WT/SP_MRAD

C*** *****

C*** PRE-PROCESSOR

C*** *****

/PREP7

C*** ELEMENT TYPE (Element 99 - Layered Plate Element)

C***

C*** Keyopt(2) = 0, constant thickness

C*** Keyopt(3) = 1, integration point strain printout

C*** Keyopt(4) = 0, no user subroutine for E.C.S.

C*** Keyopt(5) = 2, stress and strain results to be output

C*** Keyopt(6) = 2, layer solutions at int. points in layers LP1 and LP2

C*** Keyopt(8) = 0, store data for top/bottom layer only (post-processor)

C*** Keyopt(9) = 0, evaluate stress/strain at top and bottom of layer

C*** Keyopt(10) = 0, no material property matrices printed

C*** Keyopt(11) = 0, nodes located at midsurface

C*** use if necessary e.g. KEYOPT,1,9,1 <- Keyopt(9) = 1

ET,1,99,,,1,,2,2

ANSYS BATCH FILE - TUBULAR SPECIMEN MODEL (MECHANICAL ANALYSIS) - PAGE 2 OF 5

C*** MATERIAL CONSTANTS (define in Element C.S. where x - fiber direction,
 C*** y - transverse direction and z - out-of-plane)
 C*** All constants are defined in english units (ie. psi)

C*** 1. 3M-1003 E-Gl/Epoxy Composite
 C*** Note: define in Element C.S. where x - fiber direction,
 C*** y - transverse direction and z - out-of-plane
 MP,EX,1,6.05E06
 MP,EY,1,1.89E06
 MP,EZ,1,1.89E06
 MP,GXY,1,0.49E06
 MP,GYZ,1,0.66E06
 MP,GXZ,1,0.49E06
 MP,PRXY,1,0.3
 MP,PRXZ,1,0.3
 MP,PRYZ,1,0.4
 MP,ALPX,1,4.78E-06
 MP,ALPY,1,12.17E-06
 MP,ALPZ,1,12.17E-06

C*** 2. Epoxy Adhesive (isotropic)
 MP,EX,2,0.7E06
 MP,EY,2,0.7E06
 MP,EZ,2,0.7E06
 MP,GXY,2,0.26E06
 MP,GYZ,2,0.26E06
 MP,GXZ,2,0.26E06
 MP,PRXY,2,0.34
 MP,PRXZ,2,0.34
 MP,PRYZ,2,0.34

C*** 3. 6061-T6 Aluminium (isotropic)
 MP,EX,3,10.3E06
 MP,EY,3,10.3E06
 MP,EZ,3,10.3E06
 MP,GXY,3,3.8E06
 MP,GYZ,3,3.8E06
 MP,GXZ,3,3.8E06
 MP,PRXY,3,0.33
 MP,PRXZ,3,0.33
 MP,PRYZ,3,0.33

C*** REAL CONSTANTS (lay-up parameters)

C*** 1. TAB SECTIONS
 C*** Note: The tab section is compose of 5 stepped shell sections of
 C*** decreasing wall thickness from the grip to the gage section
 C*** which is used to simulate the aluminium tab. Each step is
 C*** represented by a separate REAL constant.

R,1,12,1,3,10
 RMORE
 RMORE,3,,TAB_LT1,2,,ADH_LT
 RMORE,1,SPEC_ANG,SPEC_LT,1,-(SPEC_ANG),SPEC_LT
 RMORE,1,SPEC_ANG,SPEC_LT,1,-(SPEC_ANG),SPEC_LT

R,2,12,1,3,10
 RMORE
 RMORE,3,,TAB_LT2,2,,ADH_LT
 RMORE,1,SPEC_ANG,SPEC_LT,1,-(SPEC_ANG),SPEC_LT
 RMORE,1,SPEC_ANG,SPEC_LT,1,-(SPEC_ANG),SPEC_LT

R,3,12,1,3,10
 RMORE
 RMORE,3,,TAB_LT3,2,,ADH_LT
 RMORE,1,SPEC_ANG,SPEC_LT,1,-(SPEC_ANG),SPEC_LT
 RMORE,1,SPEC_ANG,SPEC_LT,1,-(SPEC_ANG),SPEC_LT

ANSYS BATCH FILE - TUBULAR SPECIMEN MODEL (MECHANICAL ANALYSIS) - PAGE 3 OF 5

```

R,4,12,1,3,10
RMORE
RMORE,3,,TAB_LT4,2,,ADH_LT
RMORE,1,SPEC_ANG,SPEC_LT,1,-(SPEC_ANG),SPEC_LT
RMORE,1,SPEC_ANG,SPEC_LT,1,-(SPEC_ANG),SPEC_LT

R,5,12,1,3,10
RMORE
RMORE,3,,TAB_LT5,2,,ADH_LT
RMORE,1,SPEC_ANG,SPEC_LT,1,-(SPEC_ANG),SPEC_LT
RMORE,1,SPEC_ANG,SPEC_LT,1,-(SPEC_ANG),SPEC_LT

C*** 2. GAGE SECTION (composite tube only)
R,6,8,1,1,8
RMORE
RMORE,1,SPEC_ANG,SPEC_LT,1,-(SPEC_ANG),SPEC_LT
RMORE,1,SPEC_ANG,SPEC_LT,1,-(SPEC_ANG),SPEC_LT

C*** DEFINE CYLINDRICAL MODEL

C*** Explicitly define element orientation
LOCAL,11,1
ESYS,11

C*** Define Keypoints
CSYS,1
K,1,SP_MRAD,0,TAB_Z0
K,2,SP_MRAD,90,TAB_Z0
K,3,SP_MRAD,0,TAB_Z1
K,4,SP_MRAD,90,TAB_Z1
K,5,SP_MRAD,0,TAB_Z2
K,6,SP_MRAD,90,TAB_Z2
K,7,SP_MRAD,0,TAB_Z3
K,8,SP_MRAD,90,TAB_Z3
K,9,SP_MRAD,0,TAB_Z4
K,10,SP_MRAD,90,TAB_Z4
K,11,SP_MRAD,0,TAB_Z5
K,12,SP_MRAD,90,TAB_Z5
K,13,SP_MRAD,0,SPEC_Z1
K,14,SP_MRAD,90,SPEC_Z1
K,15,SP_MRAD,0,SPEC_Z2
K,16,SP_MRAD,90,SPEC_Z2

C*** Define Areas
A,2,4,3,1
A,4,6,5,3
A,6,8,7,5
A,8,10,9,7
A,10,12,11,9
A,12,14,13,11
A,14,16,15,13
AGLUE,ALL

C*** Define meshing parameters

C*** 1. Define tapered element spacing at transition from tab to gage
C*** along symmetry lines
KSEL,S,LOC,Z,TAB_Z5
KESIZE,ALL,ESIZE1

KSEL,S,LOC,Z,SPEC_Z1
KSEL,A,LOC,Z,SPEC_Z2
KESIZE,ALL,ESIZE2

LSEL,S,LOC,Z,((TAB_Z5+SPEC_Z1)/2)
LSEL,A,LOC,Z,((SPEC_Z1+SPEC_Z2)/2)
LDVA

```

ANSYS BATCH FILE - TUBULAR SPECIMEN MODEL (MECHANICAL ANALYSIS) - PAGE 4 OF 5

```

C*** 2. Define element divisions in tab steps along symmetry lines
LSEL,S,LOC,Z,((TAB_Z0+TAB_Z1)/2)
LSEL,A,LOC,Z,((TAB_Z1+TAB_Z2)/2)
LSEL,A,LOC,Z,((TAB_Z2+TAB_Z3)/2)
LSEL,A,LOC,Z,((TAB_Z3+TAB_Z4)/2)
LSEL,A,LOC,Z,((TAB_Z4+TAB_Z5)/2)
LESIZE,ALL,,,TABDIVS

```

```

C*** 3. Define element divisions along tube circumference
LSEL,S,LOC,Y,45
LESIZE,ALL,,,THDIVS

```

```

C*** Attach Area Attributes
ASEL,S,LOC,Z,((TAB_Z0+TAB_Z1)/2)
AATT,,1,1,11

```

```

ASEL,S,LOC,Z,((TAB_Z1+TAB_Z2)/2)
AATT,,2,1,11

```

```

ASEL,S,LOC,Z,((TAB_Z2+TAB_Z3)/2)
AATT,,3,1,11

```

```

ASEL,S,LOC,Z,((TAB_Z3+TAB_Z4)/2)
AATT,,4,1,11

```

```

ASEL,S,LOC,Z,((TAB_Z4+TAB_Z5)/2)
AATT,,5,1,11

```

```

ASEL,S,LOC,Z,((TAB_Z5+SPEC_Z1)/2)
ASEL,A,LOC,Z,((SPEC_Z1+SPEC_Z2)/2)
AATT,,6,1,11

```

```

C*** Select ALL entities
KSEL,ALL
LSEL,ALL
ASEL,ALL

```

```

C*** MESH and ROTATE NODEL C.S.
AMESH,ALL
NROTAT,ALL

```

```

FINISH

```

```

C*** *****
C*** SOLUTION
C*** *****
/SOLU

```

```

C*** 1. Apply Displacement Type Boundary Conditions

```

```

C*** Fixed End/Clamped End
NSEL,S,LOC,Z,TAB_Z0
D,ALL,UZ,0
D,ALL,UX,0

```

```

C*** No rotation at ends; No displacements in theta at ends
NSEL,S,LOC,Z,TAB_Z0
NSEL,A,LOC,Z,SPEC_Z2
D,ALL,ROTX,0
D,ALL,ROTY,0
D,ALL,ROTZ,0
D,ALL,UY,0

```

```

C*** Symmetry BC's along edges
NSEL,S,LOC,Y,0
NSEL,A,LOC,Y,90
D,ALL,ROTX,0
D,ALL,ROTZ,0
D,ALL,UY,0

```

ANSYS BATCH FILE - TUBULAR SPECIMEN MODEL (MECHANICAL ANALYSIS) - PAGE 5 OF 5

C*** Select ALL entities
NSEL,ALL

C*** 2. Apply AXIAL FORCE Loading
LSEL,S,LOC,Z,SPEC_Z2
SFL,ALL,PRES,-(N_AXIAL)
LSEL,ALL

C*** 3. Apply HOOP PRESSURE Loading
ASEL,ALL
SFA,ALL,1,PRES,P_HOOP

C*** Set Output
OUTPR,ESOL,LAST

C*** SOLVE MODEL AND SAVE RESULTS
SOLVE
SAVE

FINISH

ANSYS BATCH FILE - TUBULAR SPECIMEN MODEL (THERMAL ANALYSIS) - PAGE 1 OF 3

```

C*** ANSYS FE SPECIMEN MODEL
C*** 1/4 Cylinder Model [+/-45]s Thermal Loading

/FILNAME,P45_T
/TITLE,Tubular Specimen [+/-45]s Thermal Loading
/OUTPUT,P45_T,OUT

C*** Input Parameters

C*** Element Mesh Parameters
THDIVS=10
ZDIVS=16

C*** Specimen Parameters
C*** note: layer angle given is in element C.S. which is rotated 90 to the pipe axis
C***          (ie. pipe winding angle is 90 - theta given)
SPEC_ANG=45
SPEC_WT=0.07
SPEC_LT=0.00875
SP_MRAD=0.8

C*** Keypoints Along Cylinder (Z Coordinate)
SPEC_Z0=0
SPEC_Z2=2.0

C*** *****
C*** PRE-PROCESSOR
C*** *****
/PREP7

C*** ELEMENT TYPE (Element 99 - Layered Plate Element)
C***
C*** Keyopt(2) = 0, constant thickness
C*** Keyopt(3) = 1, integration point strain printout
C*** Keyopt(4) = 0, no user subroutine for E.C.S.
C*** Keyopt(5) = 2, stress and strain results to be output
C*** Keyopt(6) = 5, layer solutions at int. points in ALL layers
C*** Keyopt(8) = 0, store data for top/bottom layer only (post-processor)
C*** Keyopt(9) = 0, evaluate stress/strain at top and bottom of layer
C*** Keyopt(10) = 0, no material property matrices printed
C*** Keyopt(11) = 0, nodes located at midsurface
C*** use if necessary e.g. KEYOPT,1,9,1 <- Keyopt(9) = 1

ET,1,99,,1,,2,5

C*** MATERIAL CONSTANTS (define in Element C.S. where x - fiber direction,
C***          y - transverse direction and z - out-of-plane)

C*** 3M-1003 E-Gl/Epoxy Composite
C*** Note: define in Element C.S. where x - fiber direction,
C***          y - transverse direction and z - out-of-plane
MP,EX,1,6.05E06
MP,EY,1,1.89E06
MP,EZ,1,1.89E06
MP,GXY,1,0.49E06
MP,GYZ,1,0.66E06
MP,GXZ,1,0.49E06
MP,PRXY,1,0.3
MP,PRXZ,1,0.3
MP,PRYZ,1,0.4
MP,ALPX,1,4.78E-06
MP,ALPY,1,12.17E-06
MP,ALPZ,1,12.17E-06

C*** REAL CONSTANTS (lay-up parameters)
R,1,8,1
RMORE
RMORE,1,SPEC_ANG,SPEC_LT,1,-(SPEC_ANG),SPEC_LT
RMORE,1,SPEC_ANG,SPEC_LT,1,-(SPEC_ANG),SPEC_LT

```

ANSYS BATCH FILE - TUBULAR SPECIMEN MODEL (THERMAL ANALYSIS) - PAGE 2 OF 3

```

C*** DEFINE CYLINDRICAL MODEL

C*** Explicitly define element orientation
LOCAL,11,1
ESYS,11

C*** Define Keypoints
CSYS,1
K,1,SP_MRAD,0,SPEC_Z0
K,2,SP_MRAD,90,SPEC_Z0
K,3,SP_MRAD,0,SPEC_Z2
K,4,SP_MRAD,90,SPEC_Z2

C*** Define Areas
A,2,4,3,1

C*** Define meshing parameters

C*** Define element divisions along tube symmetry lines
LSEL,S,LOC,Z,((SPEC_Z0+SPEC_Z2)/2)
LESIZE,ALL,,,ZDIVS

C*** Define element divisions along tube circumference
LSEL,S,LOC,Y,45
LESIZE,ALL,,,THDIVS

C*** Select ALL entities
KSEL,ALL
LSEL,ALL
ASEL,ALL

C*** MESH and ROTATE NODEL C.S.
AMESH,ALL
NROTAT,ALL

FINISH

C*** *****
C*** SOLUTION
C*** *****
/SOLU

C*** 1. Apply Displacement Type Boundary Conditions

C*** Fixed End (No Clamping)
NSEL,S,LOC,Z,SPEC_Z0
D,ALL,UZ,0

C*** No rotation at ends; No displacements in theta at ends
NSEL,S,LOC,Z,SPEC_Z0
NSEL,A,LOC,Z,SPEC_Z2
D,ALL,ROTX,0
D,ALL,ROTY,0
D,ALL,ROTZ,0
D,ALL,UY,0

C*** Symmetry BC's along edges
NSEL,S,LOC,Y,0
NSEL,A,LOC,Y,90
D,ALL,ROTX,0
D,ALL,ROTZ,0
D,ALL,UY,0

C*** Select ALL entities
NSEL,ALL

```

ANSYS BATCH FILE - TUBULAR SPECIMEN MODEL (THERMAL ANALYSIS) - PAGE 3 OF 3

C*** 2. Apply THERMAL Loading
BF,ALL,TEMP,-250

C*** Set Output
OUTPR,ESOL,LAST

C*** SOLVE MODEL AND SAVE RESULTS
SOLVE
SAVE

FINISH